AFML-TR-70-295

HYPERVELOCITY IMPACT—MATERIAL STRENGTH EFFECTS ON CRATER FORMATION AND SHOCK PROPAGATION IN THREE ALUMINUM ALLOYS

Ronald F. Prater, Major, USAF

Air Force Institute of Technology

Doctoral Dissertation

TECHNICAL REPORT AFML-TR-70-295

December 1970

This document has been approved for public release and sale, its distribution is unlimited.

Air Force Materials Laboratory
Air Force Systems Command
Wright-Patterson Air Force Base, Ohio 45433

315

HYPERVELOCITY IMPACT -- MATERIAL STRENGTH EFFECTS ON CRATER FORMATION AND SHOCK PROPAGATION IN THREE ALUMINUM ALLOYS

Ronald F. Prater, Major, USAF

FOREWORD

This report is based upon a dissertation prepared by Major Ronald F. Prater for submission to the Air Force Institute of Technology as partial fulfillment of requirements for the degree of Doctor of Philosophy. The work was sponsored by the Material Physics Division, Air Force Materials Laboratory, under Project 7360, Chemical, Physical, and Thermodynamic Properties of Aircraft, Missile, and Spacecraft Materials, Task 736006, Impact Damage and Weapons Effects on Aerospace System Materials, and was performed during Major Prater's assignment to that division.

The author wishes to thank his AFIT faculty committee, headed by Prof. D. W. Breuer, for their guidance and assistance in completing this study. He also gratefully acknowledges the advice and assistance of the staff of the University of Dayton Research Institute, particularly Messrs. H. F. Swift and D. D. Preonas, for their professional advice regarding the experiments and to Messrs. H. Taylor, L. Shieverdecker, and E. Strader for their support in the operation of the AFML Hypervelocity Ballistic Range provided under Contract F33615-68-C-1138, Response of Materials to Impulsive Loading.

The manuscript was released by the author in November 1970 for publication.

This technical report has been reviewed and is approved.

Herbert M. Rosenberg

HERBERT M. ROSENBERG, Chief
Exploratory Studies Branch
Materials Physics Division
Air Force Materials Laboratory

ABSTRACT

The effects of material strength upon the transient response of thick aluminum targets to hypervelocity impact has been studied experimentally. Most experiments involved the normal impact of 2017 aluminum spheres at a velocity of about 7 km/sec. Material strength was varied by employing targets of 1100, 6061, and 7075 aluminum alloys. Flash x-ray techniques were used to measure accurately the rate at which the crater grew during the impact process. Definite material strength effects were detected, even between different heat treatments of the same alloy (7075-T0 and 7075-T6). Crater growth rates were also measured for 1100 aluminum in four separate ranges of projectile velocity from 2.3 km/sec to 7.0 km/sec. Comparison of these results with available theory indicates general agreement, but demonstrates that alterations to the theory will be required to obtain detailed agreement.

Free surface velocity and Hopkinson fly-off disk techniques were used to measure values of the peak normal stress at various distances from the impact point (between 1 cm and 10 cm) at several related angles away from the projectile trajectory. The results indicate propagation of a nearly spherical wave with constant stress amplitude out to 30° off axis. A large decrease in stress amplitude occurs at higher angles. The measurements of the variation of stress amplitude with distance into the target demonstrated significant non-hydrodynamic stress attenuation believed to be associated with propagation of an elastic relief wave from the rear of the impacting projectile. Comparisons with one-dimensional theory also indicate that the stress attenuation is sensitive to the loading history in the crater region. Numerical calculations yield reasonable agreement with experimental results, but many of the details are in question. Measurement of shock arrival time with quartz disk sensors confirmed the elastic-plastic behavior of the target material.

Contents

List of Figures

Figure		Page

Figure		Page
61	Comparative Performance of Disks on Three Thicknesses from 4.5 cm Thick Flat Plate Targets Using Dynafax Model 326 Camera	97
62	Comparative Performance of Disks of Two Thicknesses from 2.5 cm Thick Flat Plate Target Using Model 300 Camera	98
63	Comparative Performance of Disks of Two Thickness-to-Diameter Ratios	98
64	Design of Pin Probes	102
65	Photograph of Pin Probe and Components	102
66	Block Diagram -- Pin Probe Circuit	103
67	Piezoelectric Arrival Time Sensor Configuration	104
68	Block Diagram -- Quartz Sensor Circuit	106
69	Records of Quartz Arrival Time Sensors, Round 2857. Sweep Speed 1 μsec/cm with 1MHzTime Marks.	106
70	Optical Arrival Time Sensor Concept	108
71	Optical Time-of-Arrival Probe Streak Record Round 2837	108
72	Design of Multi-Faceted Targets -- End View	110
73	Photograph of 5-Faceted Target with Sensors Attached	110
74	Round 2779 Photo Sequence of Fly-off Disks on 3-Faceted Target	112
75	Variation of Free Surface Velocity with Shock Radius -- 1100-0 Aluminum Alloy 0 - 17.5° Off Axis	121
76	Variation of Free Surface Velocity with Shock Radius -- 1100-0 Aluminum Alloy 17.5 - 32.5° Off Axis	121
77	Variation of Free Surface Velocity with Shock Radius -- 1100-0 Aluminum Alloy 32.5 - 47.5° Off Axis	122
78	Variation of Free Surface Velocity with Shock Radius -- 1100-0 Aluminum Alloy 47.5 - 62.5° Off Axis	122
79	Variation of Free Surface Velocity with Shock Radius -- 1100-0 Aluminum Alloy 62.5 - 90° Off Axis	123

Figure | Page

Figure		Page

Figure		Page

List of Tables

List of Symbols

a	Constant used to fit analytic curves to experimental data, defined separately for each application.
A	Dimensionless constant used to fit exponential equation to crater growth data (equals final crater diameter or penetration divided by projectile diameter), or Area (cm^2)
b	Constant used to fit analytic curves to experimental data, defined separately for each application.
B	Dimensionless constant used to fit exponential equation to crater growth data.
B_{max}	Maximum Brinnell Hardness Number (BHN) in crater region.
c	Bulk sound speed (cm/sec)
C	Capacitance(farads)
d	Projectile diameter (cm)
D	Crater diameter (cm); also used as subscript to refer to the crater diameter, or Shock speed (cm/sec)
D_b	Diameter (cm) of base of debris spray plume
D_f	Final crater diameter (cm) for given round
D_{f_o}	Average final crater diameter (cm) for a given target type
D_g	Shock speed (cm/sec) in quartz disk.
D_m	Diameter (cm) of minimum neck of debris spray plume.
e	Specific internal energy (erg/gm),
$\hat{e}_x$, $\hat{e}_y$, $\hat{e}_z$	Unit vectors in Cartesian coordinate system.

E	Energy (ergs) in similarity blast wave theory.
E_o	Projectile energy (ergs).
E_t	Elastic modulus (dynes/cm^2) of target
f	X-direction piezoelectric constant (coulombs/cm^2-kilobar), or
	Dimensionless similarity pressure variable (Eq. 13).
g	Dimensionless similarity energy variable (Eq. 13).
G	Bulk Modulus (dynes/cm^2)
H	Subscript, implies value on the Hugoniot.
I	Subscript, implies value of impact point, or
	$I(\gamma)$ is integral defined in Eq. 22.
$k, \tilde{k}$	Constant, defined by specific application.
K	Bulk modulus (dynes/cm^2)
L	Length (cm)
M_d	Momentum of fly-off disk (gm-cm/sec)
n	Constant, defined by specific application, or
	As subscript, implies "normal to the shock front".
p	Crater penetration or depth (cm); also used as subscript to refer to crater depth, or
	Pressure (dynes/cm^2).
Q	Charge (coulombs).
r	Radial coordinate in cylindrical of spherical coordinate system.
r_o	Projectile (sphere) radius (cm).
r_c	Radius of L/D=1 cylinder equivalent in mass to sphere with radius r_o

r_p In flat plate target, the distance from the intersection of the trajectory of the projectile with the rear surface of the target out to a point on that surface.

$\vec{R}$ Vector from impact point to point of interest on the target rear surface.

R_o Scaling radius (cm) defined by Eq. 34.

R_p Radius (cm) of cylindrical projectile, Heyda model.

R_s Shock radius, distance (cm) from impact point to point of interest on the shock front.

R_{s_o} Projectile radius (cm) for sphere.

R'_s Adjusted shock radius (cm) for shifting coordinates in Karpov model.

s As subscript refers either to "shock" or "scaled" depending on application, or

Constant in linear Hugoniot (Eq. 27).

t Time (sec).

T Thickness (cm).

u Particle speed (cm/sec) in the solid material; also the radial component of the velocity vector for a particle in a spherical coordinate system.

v, v_p Projectile velocity (cm/sec).

v_d Fly-off disk velocity (cm/sec).

v_{fs} Free surface velocity (cm/sec).

V Specific volume (cm^3/gm), or

Electrical potential (volts).

x Coordinate in Cartesian system.

y Coordinate in Cartesian system.

Y	Yield strength (dynes/cm^2).
Y_o	Static yield strength (dynes/cm^2).
z	Coordinate in Cartesian and Cylindrical systems.
Z	Shock impedance (gm/cm^2-sec)
α	Angle between trajectory and $\vec{R}$ on five-facet target.
β	Angle between trajectory and $\vec{R}$ on three-facet target.
γ	Ratio of specific heats c_p/c_v; a constant in the perfect gas equation of state. Allowed to vary in some applications here.
Γ	Gruneisen factor in solid equation of state.
δ	Angle between shock front and free surface at point of reflection.
$\Delta(\rho)$	Non-similar portion of solid equation of state (Eq. 26).
ζ	Functional form of equation of state, such as $e = p\,\zeta(\rho)$, or
	Proportionality constant in Eq. 59.
η	Similarity variable, $\eta = r/R_s(t)$.
θ	Angle off-axis, i.e. the angle between the projectile trajectory and the line from the impact point to the point of interest.
μ	Compression, $\mu = \rho/\rho_0 - 1$
ρ	Density of compressed material (gm/cm^3).
ρ_o	Density of undisturbed material (gm/cm^3).
ρ_p	Density of Projectile (gm/cm^3), uncompressed.
ρ_t	Density of Target (gm/cm^3), uncompressed.
σ	Standard deviation.
σ_n	Normal stress, usually at the shock front (dynes/cm^2).

σ_H Peak stress at impact (one-dimensional plate impact equivalent, dynes/cm^2).

τ Exponential period for cr. er growth (sec), or

Shock transit time through quartz disk (sec).

τ_1 Time decay constant for quartz gauge (sec).

ϕ Dimensionless similarity particle velocity variable (Eq. 13).

ψ Dimensionless similarity density variable (Eq. 13).

HYPERVELOCITY IMPACT -- MATERIAL STRENGTH EFFECTS ON CRATER FORMATION AND SHOCK WAVE PROPAGATION IN THREE ALUMINUM ALLOYS

I. Introduction

The phenomena of the very high speed collision of solid projectiles with solid targets -- termed "hypervelocity impact" -- have been the subject of research for more than two decades. Only within the last few years, however, have the tools for really detailed study of such impacts been available. The advent of the modern, ultraspeed digital computers has made the application of detailed theory to this problem practical. Likewise, the development of advanced projectile launching techniques, such as the light gas gun, and the availability of submicrosecond electronic and optical instrumentation have made experimental studies of the dynamics of the impact processes feasible. While "post mortem" studies of hypervelocity impact abound in the literature, experimental studies of the dynamics of the impact events are rather rare even though they represent the most fruitful area for direct verification of theory. Both the difficulty and cost of performing accurate dynamic experiments have contributed to this situation. The direct correlation of theory with experiments has in the past contributed the most to understanding the phenomena involved and, hopefully, this trend will continue in the future.

In this dissertation one of the basic problems in hypervelocity impact -- the perpendicular impact of a sphere onto a thick target of like material -- was selected for study. The emphasis was on experiments and was directed toward studying two rather distinct and separable aspects of the problem -- the formation of the crater and the propagation of the induced shock wave into the target material. In particular, it was deemed important to investigate the effect of material strength upon the shock propagation phenomena since little dynamic information is available in this area and since only recently have the theoretical techniques been able to treat the effects of material strength. The target material used was aluminum; a range of material strengths was obtained by varying the alloy and heat treatment.

The experiments were conducted in two phases. The objective of the first was to measure the size and shape of the growing crater as a function of time after impact. Flash x-radiography and precise timing methods were employed to accomplish this. In the second phase, the objective was to measure the peak stress in the shock wave as a function of position in the target and to monitor the time history of the shock front (shock trajectory). The development of accurate optical techniques and arrival time gauges was required to obtain this data. The results obtained have been analyzed in terms of the phenomenology occurring and detailed comparisons have been made with existing computer solutions to similar impact events.

While this study is concerned with a very basic physical phenomena, the results have practical, although perhaps somewhat indirect, application in at least two areas. First, the effects of hypervelocity impact are important per se. A projectile moving at hypervelocity represents an extremely destructive device. It has a great amount of kinetic energy which, upon impact, is delivered in a concentrated form over a very small area of the target. As such, hypervelocity impacts represent a potential damage mechanism of high effectiveness. Weapons designed specifically to produce hypervelocity projectiles could represent a threat either to space vehicles or to ballistic missile reentry vehicles. Likewise, the natural hypervelocity fragments, micormeteoroids, represent a hazard to unprotected space vehicles. Since both space and reentry vehicles are important components in many of our military systems, the Department of Defense has sponsored broad research on hypervelocity impact effects for many years. Particularly good summaries of this research up to 1965 are included in the various Hypervelocity Impact Symposium Proceedings (Ref. 1 and 2). A good survey of hypervelocity impact research and its application to the hazards of micrometeroid impact is given by Cosby and Lyle (Ref. 3).

Hypervelocity impacts onto thick metal targets represent one class of problems involving the formation of cavities and propagation of diverging shock waves in solid materials. Such problems as the surface cratering produced by nuclear or conventional explosives, explosive forming for manufacturing operation, the formation of lunar craters, ballistic impacts into armor, etc., are all amenable to treatment by the numerical techniques originally developed to solve the hypervelocity impact problem. To the extent that this effort contributes to better understanding of or to increasing the confidence in the application of this body of theory, it also contributes to the study of these other important phenomena.

The remainder of this dissertation is devoted to a detailed discussion of the hypervelocity impact problem selected and the presentation of the results of the study. Chapter II discusses the physical phenomena of the cratering process and the formation and propagation of the shock waves in the medium. The numerical techniques currently used to study this problem are also discussed briefly. In Chapter III the experimental techniques and data handling for the crater growth studies are detailed. The results of the crater growth experiments are presented in Chapter IV along with an analysis of the results and correlation with available computer results. Chapter V contains a description of the experiments designed to study wave propagation while Chapter VI presents the results of this phase of the study and a discussion and analysis of the experimental data.

Existing and modified analytical, similarity-like theories designed to study the hydrodynamic phase of the wave propagation are presented in Chapter VII along with a detailed correlation of the experimental results with the analytical theories and the results of several numerical treatments of impact events. The conclusions and recommendations are summarized in Chapter VIII and the references are located in Chapter IX. The several appendices present the unprocessed experimental data and detail various aspects of the experiments.

II. Background and Theory

Probably the most fundamental multi-dimensional problem in impact physics is that of a compact projectile incident normal to the planar surface of an infinitely thick metal target of like material. If the projectile velocity is sufficiently high, say above the speed of sound in the target material, the impact results in the formation of a roughly hemispherical crater in the target and may be termed "hypervelocity" impact. An example is shown in Fig. 1 where the material was sufficiently ductile that lips or rims were formed on the crater. If the target is not infinitely thick, the stress waves produced by the impact will be reflected off the back surface as tensile waves and can produce fracture of the material -- spall -- as shown near the rear and in the corners of the target. Targets of intermediate thickness still produce reflected tensile waves, but these waves are attenuated to such an extent that they do not produce spall and, for sufficient thickness, do not affect the process of crater formation. This is defined as a quasi-infinite thickness.

At somewhat lower velocities (Ref. 3:63) the craters tend to be less hemispherical with the depth greater than the crater radius. The projectile tends to retain its identity although it may deform or fragment into small pieces; this is in contrast to the hypervelocity case where the projectile tends to merge with the target material in the plastic flow that occurs in the growing crater. In the limit of very low velocities, the more conventional ballistic effects such as deep penetration may be observed if the projectile strength is sufficiently high. These low velocity phenomena have been excluded from the research effort described here.

The final results of hypervelocity impacts, i.e. crater radius, depth, lip height, spall effects, etc., have been the subject of intensive experimental study over the past ten or more years. Wide varieties of materials have been impacted by projectiles of many shapes, sizes, and materials at velocities as high as 15 km/sec although data above 10 km/sec is very scarce. The results (Ref. 4 and 5)

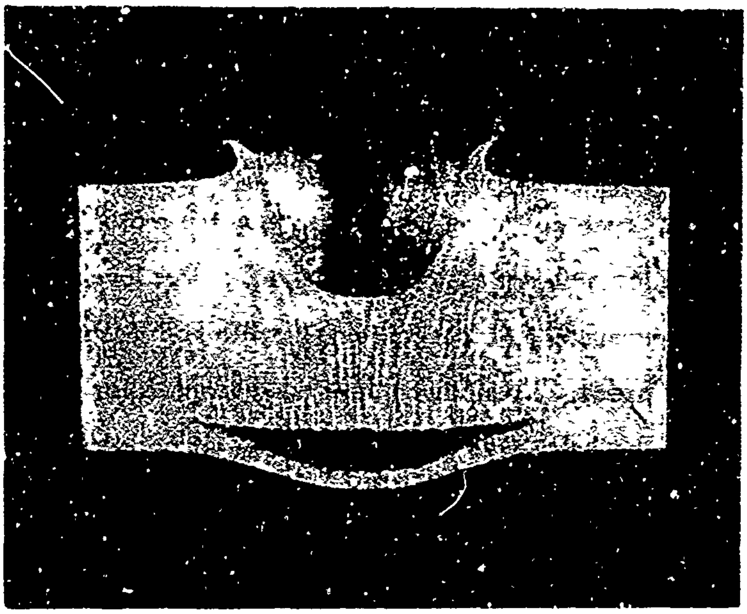

Fig. 1. Hypervelocity Impact Crater in Soft Aluminum

have been incorporated into several empirical equations relating crater depth to impact velocity, projectile and target densities, material strength parameters, target hardness, and a host of other potential independent variables. These and a wide variety of other empirical laws represent impacts reasonably accurately over restricted ranges of the independent variables. When extrapolated outside these limited ranges, these formulae yield widely divergent results.

The point of citing the vast empirical studies performed is merely to point out that post mortem studies of craters do not lead to fundamental understanding. These results cannot be confidently extrapolated to new situations or to new materials. Historically, this situation led to an emphasis on theory and fundamental understanding of the cratering process.

Crater Formation and Shock Wave Propagation

Recent studies (Ref. 3:64; 6:684-685; 7:1-3, 14) have yielded the following phenomenological picture of the crater formation process. The process has been divided into four phases for ease of description, but it should be borne in mind that this division is arbitrary and that there is a smooth transition between phases. Figure 2 illustrates these phases.

Transient Stage. (Stage 1 in Fig. 2) Immediately upon impact the pressures at the points of contact are much greater than the material strength so that the material behaves as a compressible fluid and the pressures are the same as those that would be produced by a one-dimensional impact (such as a flat plate impact). The initial pressure can reach several megabars for certain impacts. These pressures can be calculated by appropriately applying the Rankine-Hugoniot jump conditions if the equations of state of both target and projectile are known. Immediately, rarefaction waves originating at the projectile edge advance through the shocked region, decreasing the pressure and creating lateral flow. This phase ceases in a very short time, essentially when the projectile has contacted the target across its whole face and rarefaction waves have reached the shock generated by the original contact. This phase generally lasts a small fraction of a microsecond during which strong shock waves propagate only a very short distance into the target.

Penetration Stage. (Stage 2) During this stage the shock remains attached to the growing crater since the velocity of the incoming projectile is still greater than the shock velocity in the target material, i.e. an "equilibrium" condition is reached where the shock in the target is stationary with respect to the moving projectile-target interface. This shock front is thin and contains a very high energy density. This phase can still be considered hydrodynamic since the pressures are much greater than the material strengths. The penetration stage is of importance when the impact speed is several times the sound speed. In the range of projectile velocities accessible to experiments (in metal targets) the duration of this phase is so short that it can generally be ignored.

Cavitation. (Stage 3) Release waves and lateral flow slow the projectile and allow the shock wave to detach from the growing crater boundary and proceed into the target. The exact structure of the shock wave so generated, i.e. the loading

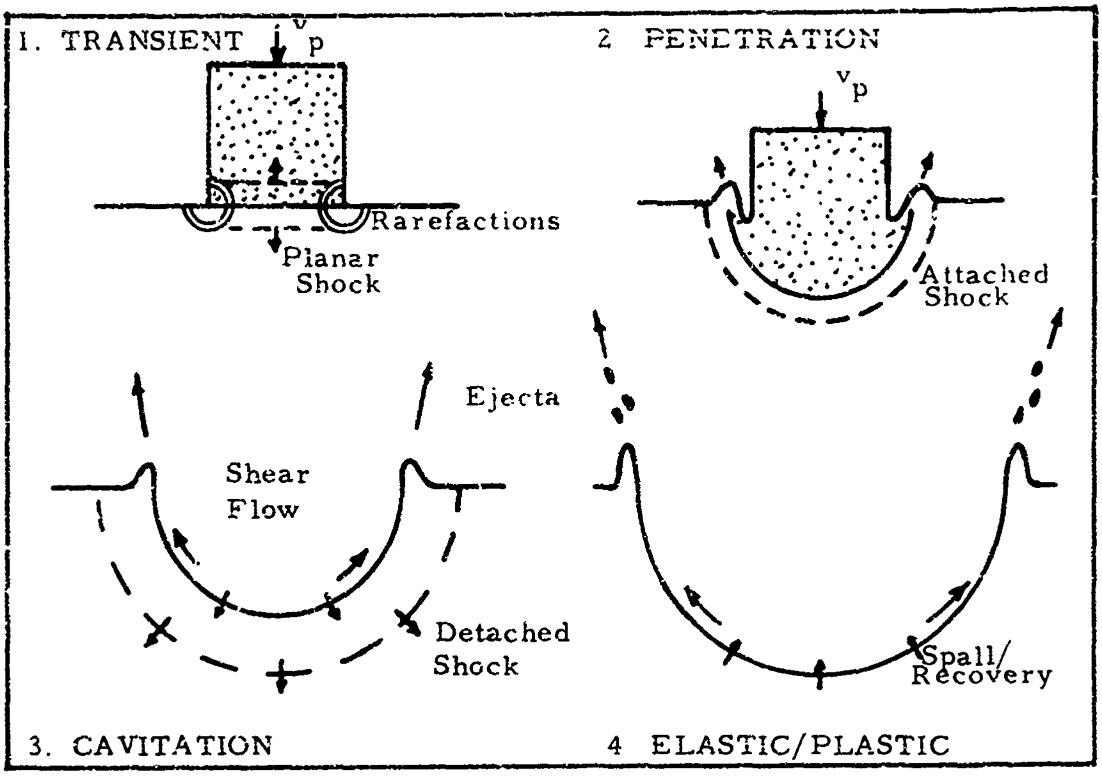

Fig. 2. Four Stages of Hypervelocity Impact Crater Formation

history, is quite complicated since it is governed by events taking place in the region of the expanding cavity. In addition, the shock wave is attenuated rapidly due to the roughly spherical divergence created by the geometry. The net effect is that the impact creates a compressive stress wave with neither the constant amplitude nor well-defined duration that results from the impact of a flat plate on a flat surface.

In addition, the shock wave generated by the impact travels through the projectile, reflects off its rear surface and creates unloading waves (elastic as well as plastic in a material with strength) which then propagate through the compressed material in the target. Even though the behavior of the compressed shock wave is essentially hydrodynamic at this point, material strengths cannot be neglected since the tensile yield strength determines the amplitude of the elastic unloading wave while the values of the bulk modulus, K, and shear modulus, G, in the compressed material determine the elastic wave velocity.

Meanwhile, the material near the crater face is subjected to strong shear forces in the presence of substantial heating or melting (or vaporization at very high impact velocities) which results in the ejection of much of this material from the crater at high velocity.

Elastic-Plastic Stage. (Stage 4) In this final phase, the crater growth and stress wave propagation become completely uncoupled. The crater continues to grow by plastic flow and elastic deformation. The crater growth is finally arrested by the strength of the target material. If there has been significant elastic deformation, it is possible for the crater to recover (decrease in size) to its final size and shape. For certain types of materials, fracture and spall can occur during this final phase. In extreme cases such as rocks, the fracture and spall can obscure the form of the crater.

In addition, the unloading waves generated in the region of the crater catch up with the compressive plastic wave front in this phase and contribute to further reduction of its amplitude. A combination of unloading and spherical divergence eventually reduces the shock wave amplitude to the point where it becomes an acoustic disturbance.

During these stages of growth the pressure in the region of the growing crater changes drastically. Upon impact the stresses become very high -- megabars in many cases. During the second stage of growth the stresses are sustained at high, although not maximum, level by the continued loading of the impacting projectile. During the third stage the stresses decay due to rarefaction processes and geometric attenuation in the material. Finally the stress may go into tension, creating spall and fracture phenomena, and perhaps some elastic recovery of the crater. For different impacts, the details may change drastically, but the overall processes are the same.

Previous Experimental Studies

The measurement of events occurring during the formation of an impact crater represents a very difficult task. In the typical impact, the complete crater formation process lasts only several tens of microseconds. The initial propagation of the shock and early phases of the cratering last only a few microseconds or less. Most of the interesting phenomena occur either inside the solid target or are obscured by the ejecta from the crater. The placement of measuring devices in the path of the shock or growing crater disrupts the cratering process, sometimes making measurements impossible to interpret. At the earliest times the pressures are so high that they cannot be measured directly. All of these difficulties explain, perhaps, why such a small number of experimental studies of transient cratering phenomena have been performed.

Some of the earliest studies of transient phenomena were conducted by Kineke and his coworkers at the Ballistics Research Laboratory. In Ref. 8 Kineke studied the external ramifications of the impact of a 0.18 gram steel disk onto a lead target at a velocity of 5.01 km/sec by means of sequential flash radiographs. Lead is so opaque to the x-rays that only a "shadowgraph" of ejecta and growing crater lip could be obtained. A crude estimate of ejecta velocity was obtained and crater growth was studied by measuring the minimum diameter of the apparent crater lip in each radiograph. The results showed a rapid increase in diameter for the first 100 μsec followed by a slower rise to a peak at 400 μsec and by a slight decline at later times. No direct connection of these lip growth rates to crater growth rates was attempted. Additional measurements of crater growth rates under nearly identical impact conditions were made with 1100-0 aluminum (flash radiographs) and Lucite® (streak camera). The complete cratering process lasted about 10 μsec in aluminum and about 60 μsec in Lucite®.

In a later study (Ref. 9) additional data on steel disks impacting lead were presented. The studies appear to involve considerable errors in the determination of the time interval between impact and the x-radiograph. Projectile orientation at impact also may have influenced the scatter in the results. In addition the time of arrival of the shock front at various depths in the target was measured by means of a series of holes in the target perpendicular to the impact. These holes were back lighted and viewed with a streak camera. Blanking of a hole indicated shock arrival. Again timing with respect to impact was somewhat inexact. Both the response time of the pinholes and their effect upon the stress propagation must be determined before this technique could yield accurate data.

Frasier and Karpov have studied impacts into wax targets. Wax has several advantages for this type of study: (1) can be internally instrumented; (2) has low dilatational wave velocity; and (3) acts like a very soft, ductile metal under impact. Their initial studies (Ref. 10) involved using the emf generated by a wire moving in a magnetic field to monitor material motion within the target. Fine wires were imbedded in the wax and the output was monitored on oscilloscopes. This data allows calculation of the pressures within the target. Additional data resulted from continuing studies (Ref. 11) in wax, in which piezoelectric (tourmaline disks) pressure gauges and flash radiographic methods were employed in addition to the induction wire technique. This group was able to get peak particle speed, shock propagation speed, and peak radial stress on axis as a function of distance from impact using the wire induction gauges. In addition, wires along the target surface yielded displacement-time histories perpendicular to the target face. The piezoelectric gauges yielded qualitatively good results. Flash radiography was employed to obtain the crater growth history. The results of the wire gauge technique indicated good agreement with theoretical predictions. Details of the experimental techniques are contained in References 10 and 11.

The most complete (and nearly the only) dynamic studies performed on hypervelocity impacts into metals were accomplished by Gehring and his co-workers at GM Santa Barbara (Ref. 12). They employed both flash x-rays and optical measurements to follow the crater growth in 1100 aluminum and several other metals. These results are discussed in more detail in Chapter IV. They also performed a series of ballistic pendulum experiments (where the thick target was mounted on the pendulum) to determine the momentum transfer to the target due to impact. Charest (Ref. 13) performed a series of experiments using "fly-off disks" to measure the pressures at various depths in the material. This technique is described in Chapter V and Charest's results are described in Chapter VI.

More recently Billingsley (Ref. 14 and 15) studied the axial pressure variation in 6061-T6 aluminum and copper in the hypervelocity impact region. He obtained the pressure indirectly by measuring the free surface velocity at the target rear using a high speed framing camera. This technique imposes severe limits on the measurements, essentially restricting the acquisition of accurate data to the very high pressure (hydrodynamic behavior) regime. The experimental technique and results are discussed in detail in Chapters V and VI respectively. The results are not of sufficient accuracy, nor do they correspond to sufficient depth into the target for assessing the effects of material strength on the shock wave propagation.

Other related studies, such as those of impacts and explosions in Lucite® by Kinslow (Ref. 16) and impacts into water by Stepka (Ref. 17) have also yielded useful information on transient impact effects. These efforts do not represent, however, the more extensive study of transient cratering phenomena that would seem to be so desirable for correlation with the sophisticated computer calculations of impacts now available. On the whole it appears that the amount of experimental information on transient cratering phenomena is rather limited, especially considering the many, many post mortem studies that have been done in the field. The situation is about the same with regard to experimental studies of hypervelocity impact generated shock wave propagation in metals. Data are available in only very limited cases that involve on-axis measurements and are not sufficient to provide information on material strength effects.

As outlined in Chapter I, the experimental program to be described in detail later in this study was specifically designed to remove the major deficiencies noted above and to represent a significant new contribution to the area of dynamic cratering experiments. The crater growth experiments reported here yielded more new data on growth rates in metals than was available, <u>in toto</u>, before and provide a significant increase in accuracy. This is the first study to employ a systematic variation of material strengths and projectile velocities. These data are the first available where the effects of material strength on crater growth dynamics have been studied experimentally.

In similar fashion, the experimental studies of shock wave attenuation were planned to provided more accurate data than has been available in the past and represents the first systematic experimental study of material strength effects. They also represent the first reported direct experimental measurements of the angular variation of shock wave attenuation in metals.

Hypervelocity Impact Theory

Early attempts to treat the cratering portion of the impact process theoretically were concerned with determining the final crater depth and not with the entire history of the process. Consequently these theories were rather crude and indeed many times were semi-empirical. In every case grossly simplifying assumptions were made to obtain results. In many cases the assumptions were not even physically correct, the only justification for their use being that they yielded correct results over some restricted range of the independent variables. Herrmann and Jones (Ref. 4:7 ff) give a good summary of the various simplified theories for predicting final crater size. The analytic treatment of the dynamic crater growth has proven intractable in general and extremely difficult in the few specialized cases where any success has been achieved.

Several researchers have attempted to apply gas dynamic theory to the shock wave propagation part of the problem. In each case the problem has been considerably simplified by reducing it to a one-dimensional radial geometry and assuming that the impact is simulated by a point source explosion at the origin. The material behavior is assumed to be purely hydrodynamic. Using these assumptions Rae and Kirchner (Refs. 18, 19, and 20) applied similarity theory to obtain a description of the shock wave propagation behavior. Even here, however, it was necessary to modify the theory since solid materials, even in the hydrodynamic regime, behave in a fundamentally nonsimilar fashion. Even though Rae and Kirchner's technique does not yield particularly good agreement with theory, its development leads to good insight into the behavior of materials and the spherically expanding shock wave problem. Consequently, this theory is discussed in detail in Chapter VII and an alternative formulation designed to bring the results in closer agreement with experiments is discussed.

Another technique, similar to the above except that the density distribution behind the shock front is an assumed rather than derived quantity, was applied by Zaker (Ref. 21) and further developed by Bach and Lee (Ref. 22). An even more complicated blast wave theory was developed by Heyda (Ref. 23). Again, the theories are based on so many simplifying assumptions that they have only limited usefulness. None of these analytical approaches consider material strength effects.

Numerical Hydrodynamic Solutions. Not until the advent of the "hydrodynamic codes" did theory begin to treat the complete history of cratering and shock propagation in any detail. This numerical technique involves solving the two-dimensional, axisymmetric equations of compressible, inviscid fluid flow on a high speed digital computer using numerical finite-difference methods. An artificial viscosity is introduced to spread any discontinuities, such as a shock front, out over a finite distance so that the numerical techniques remain stable. The basic assumption is made that the pressures in the problem are sufficiently higher than material strengths so that the flow is purely hydrodynamic. Thus the hydrodynamic codes treat the problem only through part of the cavitation phase of the crater formation process. Some auxiliary argument or assumption is necessary to lead to a final prediction of crater diameter.

The numerical hydrodynamic method was pioneered in the field of hypervelocity impact by Bjork (Ref. 24) as early as 1959. He applied the "particle-in-cell (PIC)" method that was introduced by the Los Alamos Scientific Laboratory in the early 1950's (Ref. 25). Other groups followed shortly in developing this type of technique and applying it to a variety of impact problems. Notable among these groups were those of Walsh (Refs. 26 and 27) and Riney (Ref. 28) who performed extensive studies of hypervelocity impact problems using these numerical techniques. Since purely hydrodynamic behavior was a fundamental assumption of these codes, those aspects of crater formation and shock propagation that were strength dependent were necessarily ignored.

The most successful attempts to apply these codes to practical problems where final crater dimensions were of interest appealed to the principle of "late stage equivalence" first expounded by Walsh (Ref. 27:4) and Dienes (Ref. 29). The principle was developed from a combination of hydrodynamic code calculations and dimensional analyses. This principle states in effect that if, at any time during the formation of craters resulting from two different impacts, the pressure profiles (in scaled coordinates) are the same, then the resulting crater formation due to this pressure pulse (again in scaled coordinates) will be the same. The scaled coordinates arise from similarity and dimensional analysis arguments. Thus, if the pressure profile in a certain impact calculation can be matched at some time with the profile in another calculation for which experimental determination of final crater size is available, then the final crater size may be determined for the first calculation by application of the late stage equivalence principle -- the result is a combined theoretical experimental technique.

While the late stage equivalence principle was a great step forward in the hypervelocity impact field, it has not represented a panacea. It requires the assumption that viscous effects and heat conduction are negligible (Ref. 26:4). Bjork (Ref. 30:175-181) expresses some well reasoned reservations regarding late stage equivalence, especially in the lower end of the hypervelocity regime where material strengths play a more important role. In addition, this approach does not specifically treat material strength dependence, so the effects of material behavior models cannot be explored.

Numerical Methods Including Material Strength. Since 1965 continued improvements have been made in the numerical treatment of hypervelocity impact problems. For purposes of economy and improved accuracy the particle-in-cell methods have generally been replaced by new computational methods. In addition all the codes now include a rather general axisymmetric, two-dimensional treatment of the impact with material strength included. This work was pioneered by Wilkins (Ref. 31) who first formulated the mathematical treatment of the two-dimensional elastic-plastic problem in Lagrangian coordinates using numerical techniques.

These calculations are very demanding upon the computer used; they require vast amounts of memory storage and a very fast machine to be considered practical. The computers of the late 1960's have now met these requirements. Consequently many organizations are employing or developing this technology for application to a wide spectrum of problems. Codes have been written in Eulerian and Lagrangian coordinates and combinations thereof and three-dimensional codes are currently under development. Various models of material behavior have been incorporated in the codes.

The key to experimentally verifying the computer results lies in appropriate measurements of the transient phenomena that occur during the event -- in this case the crater formation. At very high velocities there is general agreement that late stage equivalence holds. With the advent of strength codes which can now follow crater growth to termination, experiments of transient phenomena at velocities near the lower end of the hypervelocity regime where material strengths play a dominant role have proved both feasible and fruitful.

Supporting Calculations

In view of the emphasis placed upon the comparison of experiments with numerical calculations in this study, a series of problems corresponding directly to portions of the experimental program was performed* by Shock Hydrodynamics,

*Sponsored as a subcontract by the University of Dayton Research Institute. Mr. M. Rosenblatt was principle investigator for the subcontractor. Additional comparison of numerical and experimental results beyond those reported herein are planned as a joint UDRI/AFML effort.

Inc. (Ref. 32). The calculations employed STEEP, a two-dimensional Eulerian computer code that includes an elastic-plastic formulation of material strength effects. This code is representative of the currently available techniques. The material model used employs a sharply defined yield condition (von Mises), but allows the yield strength and shear modulus to vary with temperature (thermal softening) and accounts for work hardening. Allowance is made for a pressure dependent phase change from solid to liquid. There was no consideration of strain rate effects. The hydrodynamic equation of state (the calculation divides the stress tensor into a hydrodynamic part and a deviatoric part) is that commonly known as the LASL equation of state (Ref. 32:4).

Three calculations were performed as indicated in Table I. In each case the projectile was a .635 cm diameter aluminum sphere of the same alloy as the target impacting the target normally. The calculations were chosen such that a comparison of Cases A and B would reveal effects of material strength while a comparison of Cases A and C would indicate the effects of impact velocity.

In an Eulerian calculation such as this, the problem (in r-z space) is broken into discrete elements called zones. In general, the use of finer zoning yields a more accurate calculation, but increases computer storage requirements and running time. For this problem, the origin was located at the point of contact between the projectile and target at zero time. The coordinate system (zones) then remained fixed and the calculation allowed mass to flow from zone to zone.

The region of space within one centimeter of the origin was zoned quite finely ($\Delta r = \Delta z = .0635$ cm). Beyond this each Δz was made 2-1/2% larger than its previous neighbor. This yielded good resolution in the immediate vicinity of the impact point while keeping the total number of zones in the problem to a manageable number. The coarse zoning that resulted at large radii had little effect upon the processes occurring in the region of the growing crater. Unfortunately, it did contribute to somewhat poor resolution in the shock wave propagation data at the larger radii.

Table I

Numerical Calculations of Impacts in Aluminum

Case	Projectile Velocity (km/sec)	Target: Aluminum Alloy	Density (gm/cm^3)	Nominal Yield Stress (kilobars)	Nominal Shear Modulus (kilobars)
A	7.0	1100-0	2.71	0.31	259
B	7.0	7075-T6	2.80	4.14	270
C	4.0	1100-0	2.71	0.31	259

The craters produced in 1100-0 aluminum (Cases A and C) grew so slowly that the calculations were terminated before crater growth had completely ceased. For Case A the calculation was carried out to 14 μsec after impact, for Case B to about 13 μsec, and for Case C to 6 μsec. For Case B, the 7075-T6 aluminum, the crater growth had essentially ceased by the time the calculation was terminated. In each case, the calculations showed substantial effects due to the material strength (and velocity) in the region of the growing crater. The effects of strength on shock wave propagation deep into the target were somewhat less conclusive due to the early termination of the calculations.

The calculations indicate the general existence of a three-peaked stress pulse propagating into the medium. The first pulse is clearly compressive and a result of the projectile-target impact. Rosenblatt (Ref. 32:47) suggests that the second peak is probably associated with a shear wave while the third peak may be created by the late time flow on the crater surface. While not experimentally verified, the possible existence of three waves in the material is an interesting phenomenon worthy of further investigation.

The details of the results of crater formation are discussed in Chapter IV in conjunction with related experimental results. Likewise, the results of the calculations concerned with shock wave propagation are considered in detail in Chapter VII.

Summary

Hypervelocity impact in thick metal targets is an extremely complex phenomenon. The several stages of impact commonly considered, initial, transient, cavitation, and elastic-plastic, allow a consistent phenomenological description of the impact effects.

Experiments to measure the dynamics of such an impact are very scarce. Almost without exception, those experiments that have been performed were used to explore the impact phenomenology, not to produce quantitative data on such events as crater growth and shock wave propagation. This study was designed to at least partly fill this void by providing accurate measurements of crater growth and shock wave attenuation using refined experimental techniques. The effects of material strength upon the impact phenomena have been emphasized although the study also includes data on the effect of projectile velocity on crater growth and on the angular variation of the peak normal stress in the target.

Efforts to develop the theory of hypervelocity impact have centered upon the use of numerical finite-difference techniques -- the so called hydrodynamic codes. Recent advances have allowed the inclusion of material strength effects in the numerical theory. Specific calculations, using a two-dimensional strength code, were performed by Shock Hydrodynamics, Inc., for direct comparison with several of the experiments included in this study.

III. Crater Growth -- Experimental Techniques

The dynamics of hypervelocity impact cratering in solids involves two features -- cavitation and shock propagation -- which become remarkably separate and distinct phenomena shortly after the initial contact of the projectile and target. The earliest phase of the crater formation where the shock wave remains attached to the growing cavity surface is of such short duration and occurs at such high pressures that it is not amenable to direct experimental investigation. Following shock wave detachment, however, the cavitation region becomes clearly distinguishable; it represents a region of stress relaxation and gross material flow. The shock wave travels further into the target, is attenuated by geometric and rarefaction processes, and eventually becomes an acoustic wave. These phenomena are not really uncoupled physically since the state of the material in the cavitation region is determined by the passage of the shock wave, and the decay of the shock wave is largely dominated by rarefactions originating in the cavity region. Nevertheless, the phenomena are sufficiently different that each represents a fruitful field for experimental investigations of the impact process. The experimental study of impact cavitation provides a good test of our theoretical understanding of hypervelocity impact and, in particular, of the numerical techniques used to predict analytically the dynamic crater formation.

Experimental Methods

In metals, craters produced by hypervelocity impacts grow very quickly. If a 0.318 cm diameter aluminum sphere with a velocity of 7 km/sec normally impacts a flat aluminum target, all the essential features of the cavity formation are complete within about 20 μsec. Consequently the requirements on experiments to investigate this process are rather stringent. The experiments must provide a record of the position of the free cavity surface to less than 0.1 cm even though the surface may be traveling at velocities nearly as high as that of the incident projectile. Likewise the times of various events with respect to the time of impact must be known to less than a microsecond.

During the crater formation, substantial quantities of debris (the debris "plume") are thrown at high velocity out of the crater and obscure any attempt to look directly into the growing crater by optical means. The most obvious way of "seeing" inside the target is with x-rays; a commercially available device known as a "flash" x-ray unit provides a pulsed x-ray source of sufficient intensity and short enough duration to fulfill the experimental requirements if properly employed. Materials such as copper, lead, iron, etc. have such high x-ray absorption cross sections that they cannot be used with x-ray equipment currently available to this investigator. The several alloys of aluminum, however, have cross-sections sufficiently low that good flash radiographs can be obtained. In addition, aluminum is a relatively well characterized material, easily machinable, and inexpensive in bulk, so that it represents a nearly ideal material for this study.

Except for the work of Smith (Ref. 34) of AFML, only very limited studies of the internal crater growth in metals using flash x-radiography techniques have been discovered in the literature -- those by Gehring (Ref. 33) and by Kineke (Ref. 8). Gehring initially produced data for the impact of a steel disk into 1100-0 aluminum. That data will be discussed in Chapter IV. Later Gehring and co-workers at GMDRL (Ref. 12:201) employed a high speed framing camera to obtain backlighted silhouette (shadowgraph) photographs of the plume emitting from the front surface of the target. He then used measurements of the base of this plume to infer the diameter of the crater as a function of time. Kineke also used flash x-radiography to examine the internal crater dimensions as well as the emitted debris plume and to infer crater growth rates from this data (Ref. 8:339ff). His projectiles were steel disks accelerated by explosive techniques. Smith (Ref. 34) applied the flash x-radiograph technique to a study of crater growth in 1100-0 aluminum at the AFML facility. The relation of the crater dimensions to the characteristics of the debris plume was obtained from high speed framing camera records. Portions of the experimental and data reduction techniques used were developed in collaboration with the author. Smith obtained enough crater growth data on 1100-0 aluminum to assign a smooth experimental form to the crater growth; to suggest that Gehring's early data might be incorrect; and to indicate that the relation of the base diameter of the debris plume to the crater diameter might not be as direct as was previously believed.

The crater growth experiments described here represent a considerable extension of Smith's research in direct measurement of crater dimensions as a function of time. The work incorporates new or modified experimental and data reduction techniques, although it is based upon the techniques employed by Smith. Enough data was obtained to provide crater growth rates for several aluminum alloys of different static strengths and for 1100-0 aluminum at several projectile velocities and to explore further the correlation between the debris plume and the crater diameter. The techniques employed in obtaining this data are detailed in the remainder of this section.

Design and Construction of Experiments

Light Gas Gun Facility. All of the experiments reported here were performed at the Air Force Materials Laboratory Hypervelocity Ballistic Range which consists of a two-stage light gas gun with associated instrumentation and support equipment. The range is pictured in Fig. 3 and described in considerable detail in Reference 35 so that only the most essential information will be repeated here. The light gas gun is a device for accelerating small projectiles to exceedingly high velocities -- in this case 0.635 cm diameter aluminum spheres can be accelerated to a velocity of over 7.5 km/sec and smaller projectiles can be accelerated to even higher velocities.

The gun provides the acceleration in a two-stage process. A shell containing conventional propellant accelerates a heavy piston down the 40 mm pump tube compressing hydrogen gas to extremely high pressures in the central breech. When the compression becomes sufficiently high, a diaphragm in the central breech ruptures allowing the compressed hydrogen to expand into the launch tube. The launch package, consisting of a spherical projectile and a five-piece plastic carrier (sabot), is initially located in the launch tube near the

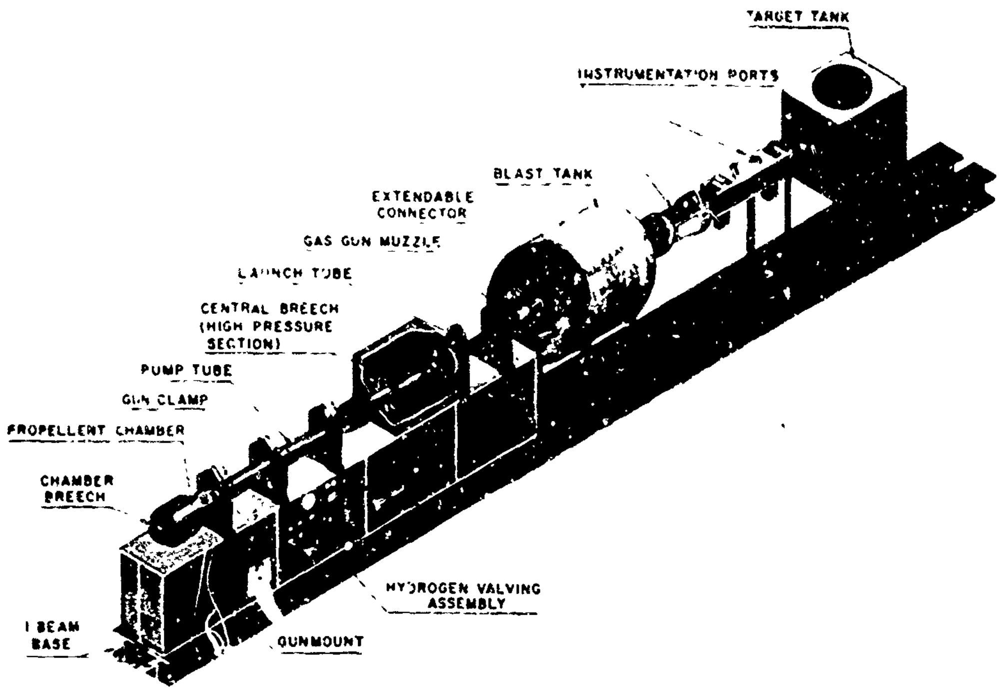

Fig. 3. AFML Hypervelocity Ballistic Range

central breech. The expanding hydrogen pushes the launch package down the launch tube, accelerating the whole package to the desired velocity. The light gas gun operating cycle is depicted schematically in Fig. 4 and a typical launch package is pictured in Fig. 5. The sabot pieces which have become slightly separated from the projectile due to aerodynamic forces are stopped on the far side of the blast tank by allowing them to impact a steel plate while letting the projectile pass unhindered through a small hole in the plate. The projectile proceeds down range past the instrumentation where its velocity and integrity are measured (Ref. 35:13-18) until it impacts the target located in the center of the target tank. The range is evacuated to a pressure of approximately 20 torr (20 mm of Hg) to prevent velocity degradation and aerodynamic ablation of the projectile while maintaining proper operation of the sabot stopping technique.

Flash X-ray and Target Geometry. The primary experiments conducted were designed to obtain flash radiographs of the growing crater in aluminum

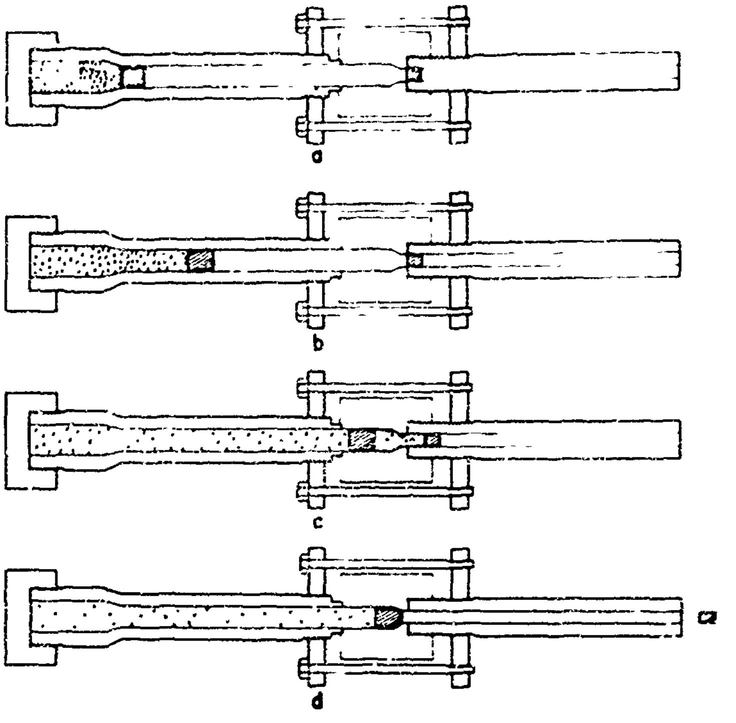

Fig. 4. Operating Cycle of Adiabatic Compression Light Gas Gun Hypervelocity Launcher.

Fig. 5. Typical Segmented Sabot Launch Packages with Aerodynamic Separation.

targets such that the time dependence of both the crater diameter and depth would be determined. The cost of operating the gas gun dictated that as many flash x-ray data points as possible be obtained on each round. In addition there is, historically, substantial scatter in data obtained from hypervelocity impact experiments. It is almost always advisable to obtain sufficient data for a statistical treatment of the results. Consequently, all available flash x-ray equipment, ten separate sources in all, was used in most experiments; the units were fired in a pre-determined time sequence. All of the x-ray units were of the type called Fexitron® manufactured by the Field Emission Corporation. Each of the four available 300 kV (Model 2710) units produces enough integrated x-ray flux and has enough penetrating power to provide a good radiograph through several inches of aluminum. The remaining four 150 kV (Model 235) and two 105 kV (Model 231) units have considerably less penetrating ability and their use was limited to thinner target sections. Consequently the 300 kV units were located so as to produce profile views of the growing crater -- yielding both depth and diameter -- while the remaining x-ray sources were placed to produce views through the rear of the target. The four 300 kV x-ray sources were arranged around the target tank in circular fashion in a plane perpendicular to the projectile trajectory.

The six remaining lower energy x-ray units were attached to a mounting plate located on the rear of the target tank as shown in Fig. 6. They were aimed nearly parallel to the projectile trajectory such that the x-rays would penetrate the target and impinge upon film placed in front of the target. Plastic windows were used in the target tank to allow easy penetration by the x-rays. Since the x-ray units provide a rather broad beam, large quantities of lead and careful placement were required to provide shielding of the film for any given x-ray unit from the direct emissions of the remaining nine units. It was also necessary to provide some shielding from the scattered x-rays produced by the 300 kV units. The geometric arrangement of the x-ray sources with respect to the target and film holders (cassettes) is illustrated in Fig. 7. In the early experiments, the

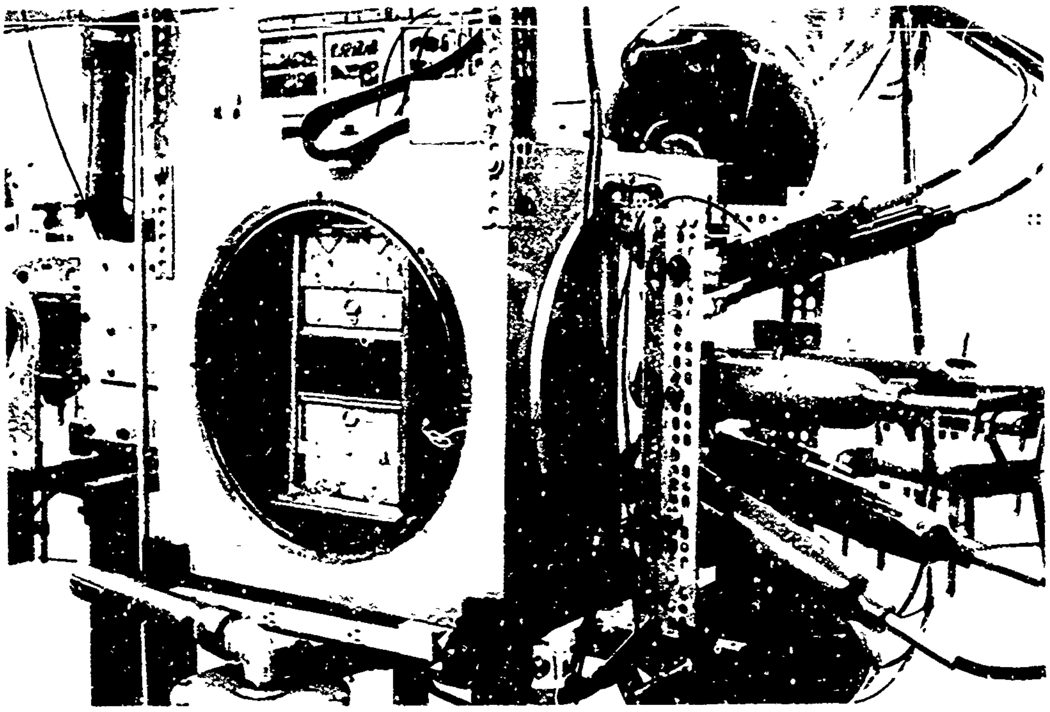

Fig. 6. Target Tank and Instrumentation Area of AFML Hypervelocity Range Showing Arrangement of Flash X-Ray Equipment.

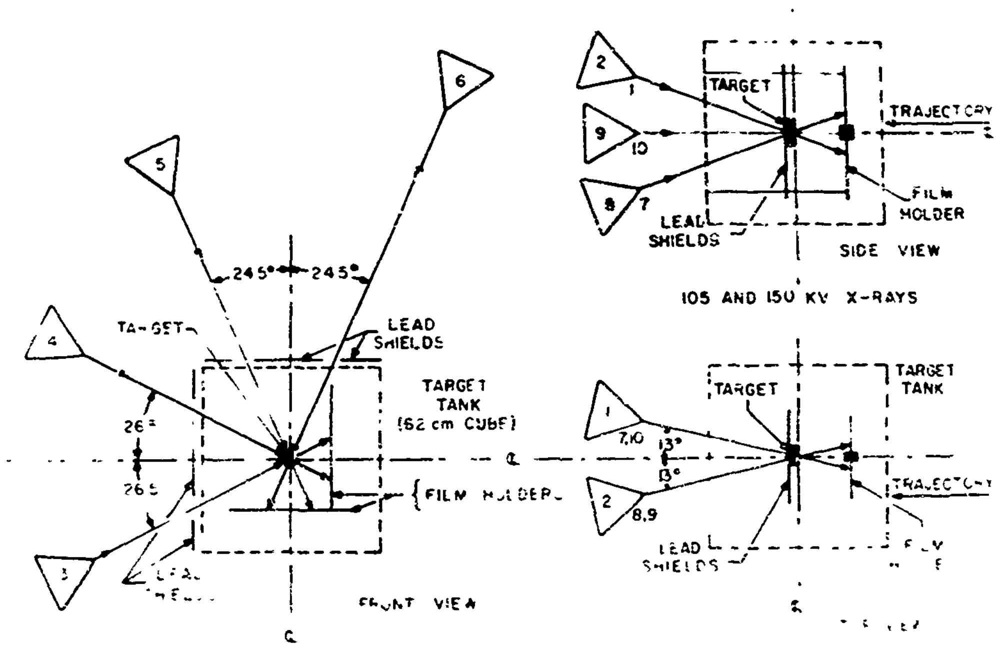

Fig. 7. Geometrical Arrangement of Flash X-Ray Equipment and Film Holders.

150 kV units were not available, but the geomerry was essentially the same with that exception.

A special target and film cassette holder described in detail by Smith (Ref. 34:34-37) and illustrated in Fig. 8 was used to insure proper and repeatable alignment of the target and film holders. Additional cassette holders were installed in the target tank to yield repeatable alignment of the films used with the 300 kV x-ray sources. The front panel (nearest the gun muzzle) holds the film cassette for the 105 kV and 150 kV x-ray sources. The panel and cassette each contain a 2.5 cm diameter hole through which the projectile must pass. This cassette is shielded from debris spray by a thin sheet of acrylic plastic. The rear panel holds both the target (bolted to its front surface) and a lead shield on the rear. This lead shield has a 5.0 cm diameter hole at its center immediately behind the target; it is a shadow shield to prevent the 105 kV and 150 kV sources from interfering with the image produced by each of their neighbors. Most of the shielding for the 300 kV x-ray sources was arranged external to the target tank.

In most cases the targets to be radiographed were quite thick so that deposited x-ray energy was at a premium. Consequently pairs of ultrafast experimental flourescent screens provided by E. I. du Pont de Nemours & Co. were used in conjunction with Kodak Royal Blue® Medical X-ray Film to obtain maximum exposure. One screen was placed on each side of the film in intimate contact with the emulsion layer on that side. Development was performed with Kodak X-ray Developer and the process was monitored visually.

Two x-radiographs obtained during a cratering event are shown in Fig. 9 to illustrate typical results obtained with the techniques described above. Note that the silhouette radiograph, typical of channels 3 through 6, yields rather clearly defined information on both crater depth and diameter. The rear illuminated radiograph, typical of channels 1, 2, and 7 through 10, contains

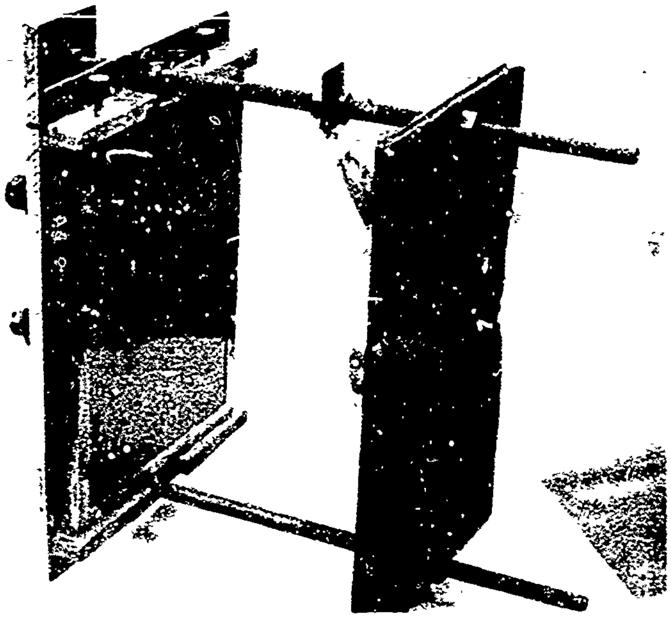

Fig. 8. Target and X-Ray Cassette Mount.

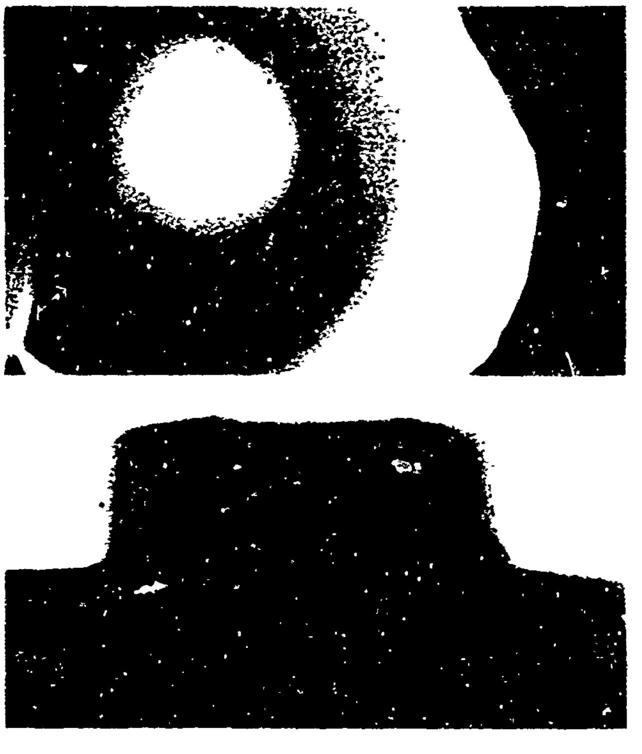

Fig. 9. Typical X-Radiographs of Growing Crater, Round 2692.

information on the crater diameter only -- and even that is less well defined because of the effect of the crater lips on the radiograph.

Sequencing and Timing. The electrical signal initiating all x-ray events for these experiments was derived from a thin switch placed directly upon the face of the target and activated by the projectile impact. The switch consisted of a 50 μm Mylar® sheet separating the grounded target from a 25 μm thick aluminum foil electrode which was held at high electrical potential by a pulse forming network (PFN). Penetration of the Mylar® insulator by the projectile caused arc over to the target and the generation of a very fast rise time signal. This signal was used to activate a bank of time delay generators each of which created a pulse to fire one x-ray unit. Both the switch signal and signal to the x-ray pulser were delivered to the time recording system so that the time between impact and x-ray firing was accurately known.

In addition, to achieve even greater accuracy, special spark gap switches were mounted directly on the x-ray tube heads. These switches (Ref. 36) are activated by the ionization created by the actual x-ray beam and, when properly adjusted, produce signals accurately indicating the time of x-ray firing (15 ± 5 nsec delay after x-ray initiation).

A block diagram of the timing and synchronizing electronics for a single x-ray channel is shown in Fig. 10. The timing system used to record the electrical signals supplied by the thyratron drivers has been described in detail elsewhere (Ref. 35:18-19). It consists basically of a set of xenon flash tubes whose optical output is viewed with a 16 mm Fastax Oscillographic Camera operating in a streaking mode. The zenon tubes are driven far past their breakdown voltage by the signals provided to the timing system. The result is a light pulse with very fast rising intensity (<0.1 μsec) which is viewed and recorded by the camera. Accurate timing marks are added to the film by a mechanical light chopper. The relative times between any two events as indicated by flashes from the zenon tubes can then be computed to an accuracy of 60 nsec. In addition, the

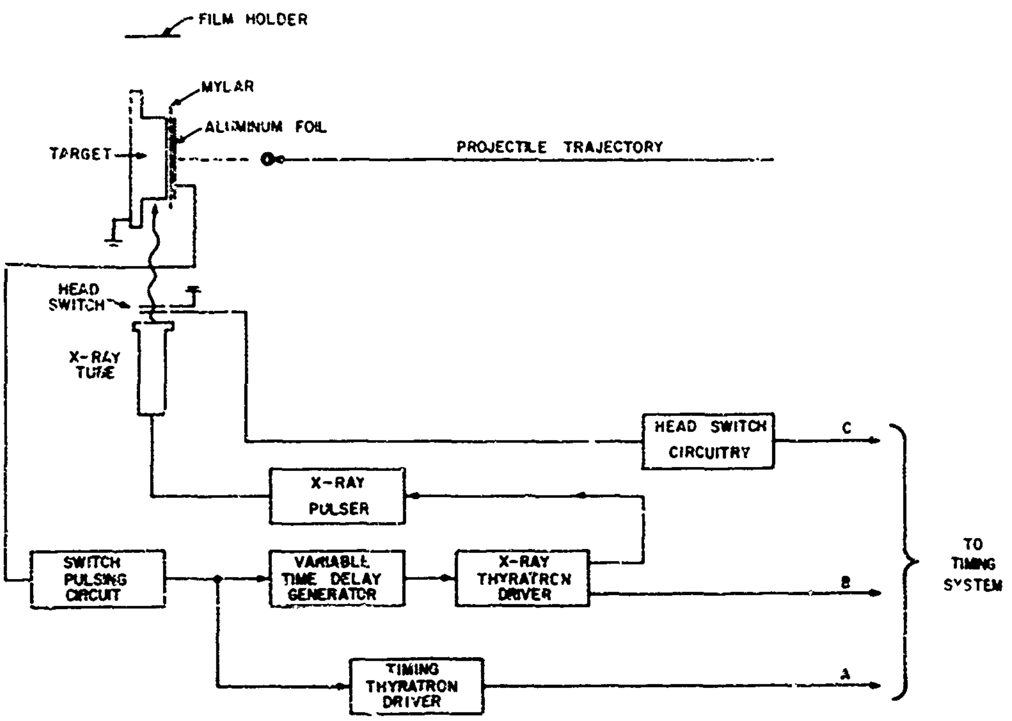

Fig. 10. Block Diagram of Flash X-Ray Electronics.

velocity of the projectile can be recorded on this same film record by noting the times the projectile passed the two velocity recording slits whose images are located perpendicular to the film travel (Ref. 35:13-16). The projectile velocity can be measured to an accuracy of ±0.25%.

Although the errors involved in recording the timing data are small, the uncertainties introduced by time delays in the electronic circuitry must be considered. Referring to Fig. 10, the switch pulsing circuit and timing thyratron driver introduce a delay between the closure of the aluminum/Mylar® switch (impact) and the signal A to the timing system. In a number of experiments this delay was measured with a fast oscilloscope and a photomultiplier tube monitoring the output of the xenon flash tube and found to be nearly constant at 0.35±0.05 μ sec.

Use of a calibration curve for the variable time delay generator to determine the time between the input to the time delay and the output to the x-ray pulser is a very unreliable and inaccurate procedure. Therefore two independent measurements of the time of x-ray firing were made for each channel, namely the signal B indicating the input to the x-ray pulser and the signal C derived from the x-ray head switch. The x-ray head switches proved considerably less than 100% reliable since the adjustment of the voltage and separation between the plates in the switch is critical. Enough data was obtained over a number of shots, however, to determine the average delay between signals B and C for each x-ray channel. In several instances, neither signal B nor C was available on the timing system record. The time between input and output of the time delay generator was used, with appropriate corrections, to obtain the time of the x-ray -- a less exact procedure.

Framing Camera Experiments. A slightly modified experimental arrangement was necessary for those rounds where framing camera records of the plume expanding off the front surface of the target were desired. In order to correlate the diameter of portions of this plume with x-ray records of the growing craters, it was necessary to obtain an unobstructed and back-lighted view of the target in silhouette. For these experiments, x-ray channels 3 and 4 were not used and the film cassette and holder for these channels were removed from the target tank. A very high intensity spark light source (Ref. 37) was used in conjunction with a collimating lens to provide a back-lighted field of view of even illumination. The camera employed was a Beckman & Whitney Model 300 rotating mirror high speed framing camera capable of recording 48 frames at a maximum framing rate of 4.5 million frames per second. The framing rate was determined by using an electronic counter to count the number of pulses per second generated by a magnetic pickup on the mirror turbine shaft. The camera was located to view the target along a line from the camera to the light source as illustrated in Fig. 11. To obtain an unobstructed view of the target, it was also necessary to move the impact switch about 10 cm in front of the target face and construct a switch consisting of two thin aluminum foil electrodes separated by a Mylar® sheet. The time of impact could then be calculated knowing the target-switch separation and the

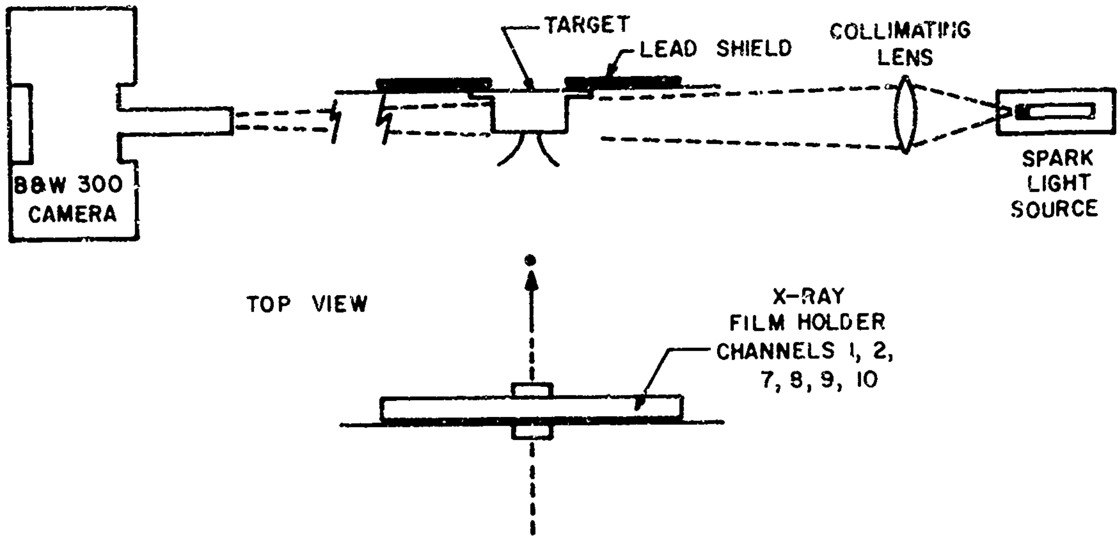

Fig. 11. Experimental Setup for Framing Camera Photographs and Flash X-Radiographs.

projectile velocity. The resultant determination of impact time was slightly less accurate than when the switch was mounted directly on the target face.

With this arrangement it was possible to obtain the framing camera record and eight flash radiographs from one impact event. The single frame taken from the framing camera record of Round 2524 and shown in Fig. 12 is typical of the photographs generated by this technique and nicely illustrates the front surface plume phenomena. Methods of obtaining quantitative data from these films are described later in this chapter.

Target Materials and Design

Target and Projectile Materials. As mentioned previously, favorable x-ray absorption characteristics and other practical considerations dictated the choice of aluminum alloys as the target materials for this study. All the target

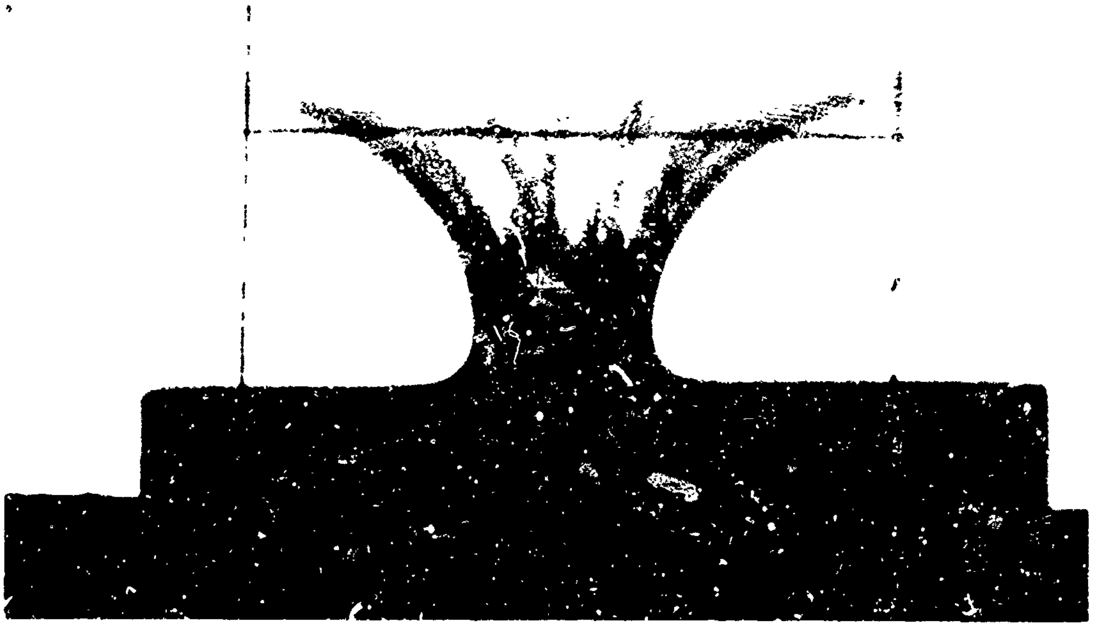

Fig. 12. Single Frame from Framing Camera Record of Round 2524.

materials used except for the 6061-T6 were obtained from well characterized billets (Ref 38). The materials used and their pertinent properties are shown in Table II. The 6061-T6 was obtained from local commercial sources. The values shown for this alloy are from the supplier.

The 1100-0 is a very soft ductile alloy of nearly pure aluminum and therefore represents one end of the material strength regime. At the other extreme, the T6 heat treatment of the 7075 alloy is the hardest, most brittle aluminum commonly available. The strength of the 6061-T6 alloy lies nearly midway between these two extremes and consequently represents another good test of the effects of material strength upon the hypervelocity impact processes. Finally, the T0 heat treat of the 7075 alloy provides a direct comparison between two cases of identical alloy composition but substantially different strength properties. The materials selected for the targets used in this study represent a very wide range of material strengths -- as such the results obtained should provide a good test

Table II

Prrnerties of Materials Employed

Alloy	Static Yield Strength (psi)	Static Yield Strength (kilobars)	True Stress to Fracture (psi)	Brinnell Hardness kg/mm^2
1100-0 Al	3,800	0.26	26,400	24
2017-T4 Al	40,000	2.76	100,500	---
6061-T651 Al	40,000	2.76	---	95
7075-T0 Al	13,000	0.90	48,400	60
7075-T6 Al	70,500	4.86	98,500	148

of any strength dependent hypervelocity impact cratering theory.

Finally, in all cases but one, projectiles were made from 2017 aluminum, a malleable alloy in common use for the production of high quality spheres. In this study it has been assumed that the strength of the projectile does not affect the impact results. This assumption is conservative since the pressures felt by the projectile material are at all points many times greater than the static yield strength. The density of the projectile does, however, affect the impact conditions. Therefore, one series of experiments used 0.18 gram spherical steel projectiles to duplicate the results obtained by Gehring (Ref. 12:201).

Target Design. The targets were cylindrical in shape as shown in Fig. 13 and had a small flange for mounting to th ,et holder. The thickness and diameter of the target proper were variables that were chosen to be as large as possible while still yielding acceptable radiographs. If the targets are too thin, reflections from the target rear will eventually interact with the growing crater and affect its further growth. Likewise reflected waves from the sides of a target that is too small (or for an impact that is too far off center) can affect the growing crater. Targets were chosen such that the shock wave had to traverse a sufficient distance so that its reflected components were very weak by the time they reached

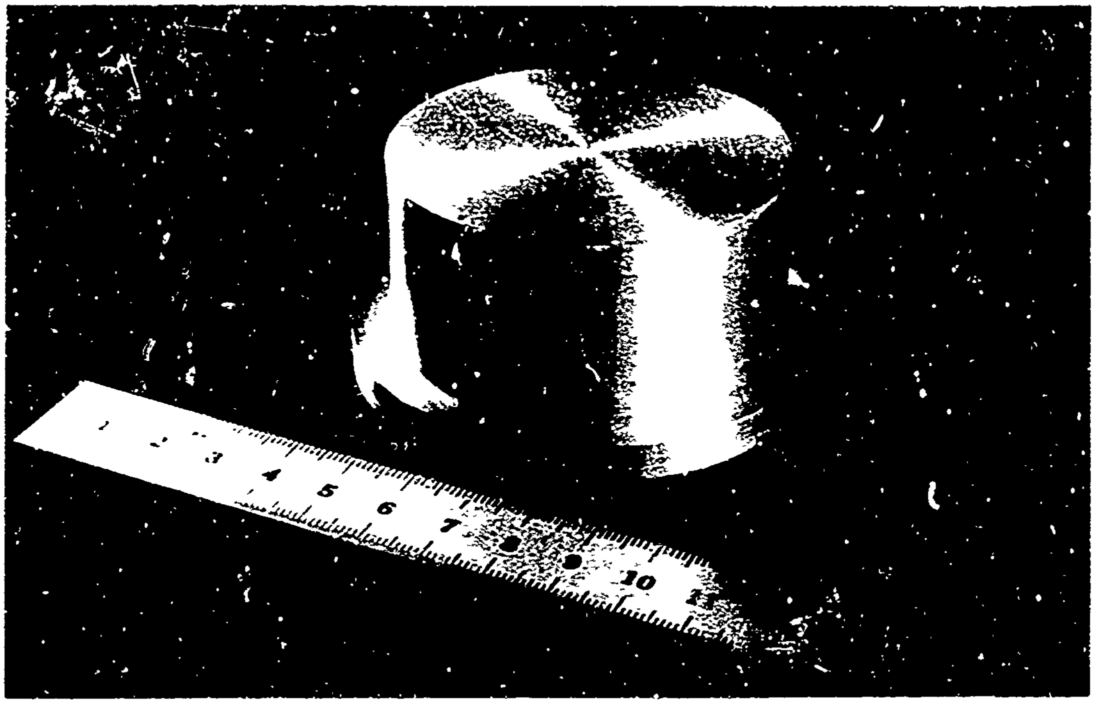

Fig. 13. Typical Crater Growth Study Target.

the growing crater region. In most cases the target thickness was six projectile diameters or more -- a thickness which can be defined as "quasi-infinite", meaning that the final crater appears as it would in an infinitely thick target. For further information on this phenomena, refer to Appendix A -- Reduction of Data Obtained from Crater Growth Flash X-Rays.

In several cases, it was necessary to use undersized targets to obtain good x-radiographs of very early-time craters where the crater dimensions were still quite small. For these rounds, the final crater was affected by reflected waves, and the data obtained was valid only up to a time after impact corresponding to the start of the interaction of the reflected wave with the growing crater. These special rounds were treated separately in the data reduction process. Whenever possible, these thin targets were backed by a thin (0.625 cm) sheet of acrylic plastic which reduces the magnitude of the reflected wave without substantially attenuating the x-ray flux.

Data Reduction Methods

Flash X-ray Films. X-radiographs must be analyzed carefully to obtain valid dimensional data. The most important factor to consider is that the geometry of each x-ray channel is different; the varying distances between each source, target, and film result in a different magnification being recorded by each channel. Even for a given channel the geometry (and magnification) was altered somewhat from round to round by changing target sizes and exact location on the target holder. It is not sufficient to merely calibrate each x-ray channel; the changing target requirements dictate that some dimensional reference be included in the record of each round for each x-ray channel.

The inclusion of a length reference such as a rod or scale in each record was impractical since each channel viewed the scene from a different angle. A good distance reference in one channel tended to shield all information from adjacent channels. For those channels (3 through 6) viewing the target in profile, there were occasions when the target did not completely fill the field of view of the x-ray. In these cases, the diameter of the target could be used as a distance reference. The results obtained agreed well with the more general technique described below.

Based upon Smith's experience (Ref. 34:40) the best available reference points are the final dimensions of the crater themselves. After each experiment was conducted, but before the target or holder were moved in any way (only the film cassettes were removed, reloaded, and replaced in register with their original positions) a set of radiographs of the final, static target was taken. Separate measurements were then made of the crater depth and/or diameter on both sets of radiographs -- those taken during the impact event and those taken later. The crater diameter or depth read from the films obtained during the impact was then divided by the same dimension from the radiographs obtained after the event to obtain the appropriate ratio. In this fashion, no direct calculation of magnification factor for each channel was necessary.

in presenting the results of any set of experiments, the ratios obtained were multiplied by the mean final crater depth or diameter for that case. This procedure also results in some smoothing of the data since the mean value of the final dimensions are used to normalize the data. Small variations from the mean values actually realized in the final crater dimensions are averaged by this process of presenting the data. The method is discussed in more detail in Appendix A -- Reduction of Data Obtained from Crater Growth Flash X-Radiographs.

Several techniques were attempted to obtain the best method of making the required measurements on the x-ray films. The use of a scanning photodensitometer was attempted, but the lack of contrast in the films, the granularity introduced by the use of intensifying screens, and the type of measurement required precluded the effective use of this instrument. The best way to read the films was without magnification on a variable intensity light table as shown in Fig. 14. Attempts to magnify the images resulted in an unacceptable loss of contrast and accompanying difficulty in interpreting the image.

The crater diameter and depth in the profile radiographs were measured with respect to the undisturbed target surface as illustrated in Fig. 15. The reference line AA on the reader was aligned with the image of the undeformed target surface lying near the outer edges. Dividers and a scale were then used to determine visually the crater diameter as observed along the line AA and the depth as measured along the line BB to the intersection with line AA.

For the radiographs taken through the target rear, two separate readings of the diameter were made along the lines DD and CC on the reader as indicated in Fig. 15. The author and at least two other operators read each film. The readings were averaged to obtain the final measurements and the multiple readings were used to determine the accuracy and reproducibility of this technique. In addition, each radiograph was assigned a subjective rating of quality: good, fair, or poor. On x-radiographs with good image quality, dimensions could be measured reproducibly to ± 0.5 mm while with poor images this error was increased to ± 1.0 mm.

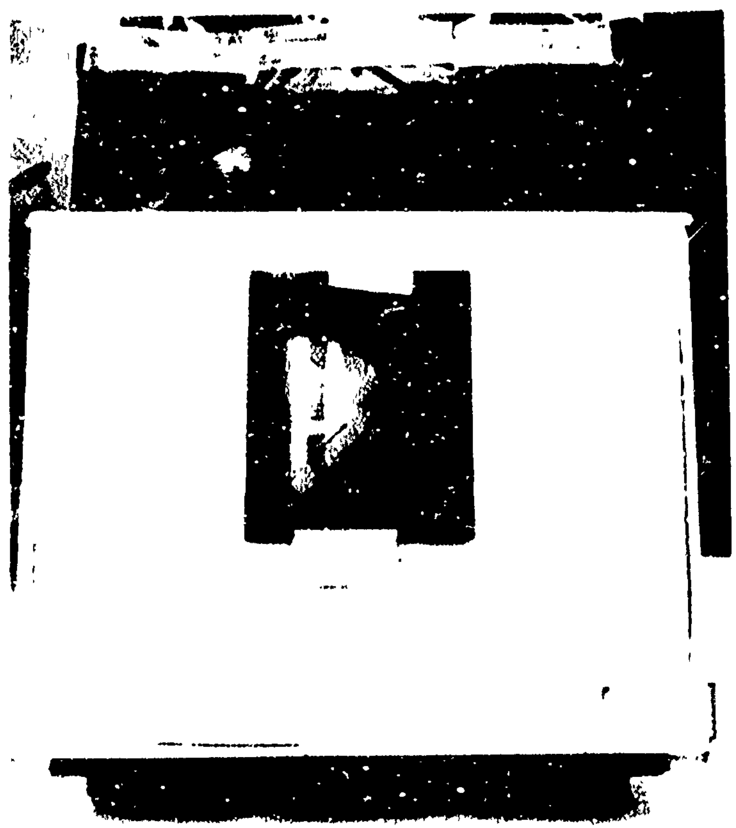

Fig. 14. Light Table for X-Ray Film Reading.

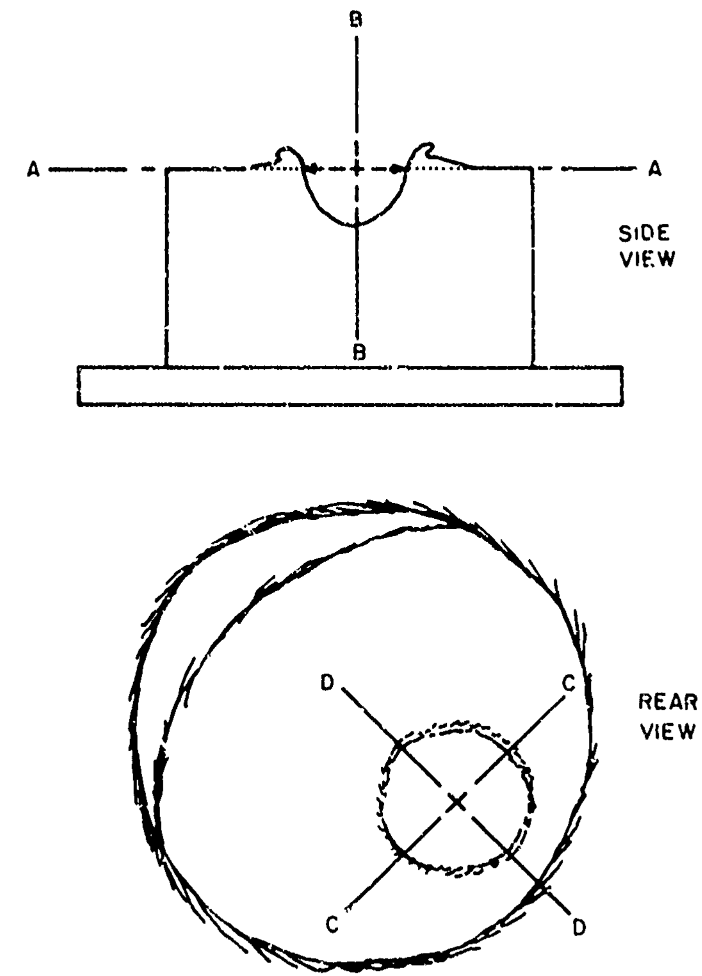

Fig. 15. Diagrams of Flash Radiographs of Craters.

Inaccuracies can arise through difficulties in interpreting the images. The use of the ratioing technique of presenting the data helps to alleviate this interpretation difficulty since a given operator tends to interpret both the final radiographs and those taken during the event in the same fashion.

Framing Camera Films. B&W Model 300 framing camera photographs of the front surface debris plume were obtained in several experiments for comparison with crater diameter histories obtained from flash x-ray data. These photographic records were read, i.e. translated into numerical data, in a special purpose automated system available at this facility (Ref. 39). In this application, the system produces the x-y coordinates of various points selected in each frame. The film is placed upon a micrometer driven two-dimensional microscope stage located at the object plane of a projection microscope. The image is projected upon a ground glass screen that provides a pair of perpendicular cross hairs for a fixed reference position. The film is adjusted so that some reference line in each frame is aligned with the fixed reference on the screen. The operator then selects points for reading, moves the point under the cross hair by turning the micrometer dials, and records both the x and y coordinates (with respect to the reference chosen for each frame) on IBM cards by activating a switch.

Considerable interpretation is required to obtain data from this type of experiment since the character of the debris plume changes with target material. In some cases, the general shape may even change as a function of time during an impact. Fig. 16 illustrates the major features of the debris plume and indicates the points at which measurements of x-y coordinates were made on each frame. The point 9 at the target corner was chosen as the origin with the x-axis lying along the target surface. The distance between the markers 7 and 8 was measured before the experiment and used to determine the magnification in the framing camera record, Two separate pairs of points were obtained from each frame, each pair yielding the diameter of a certain portion of the plume at that time. The diameter of each portion could then be obtained as a function of time from all the frames.

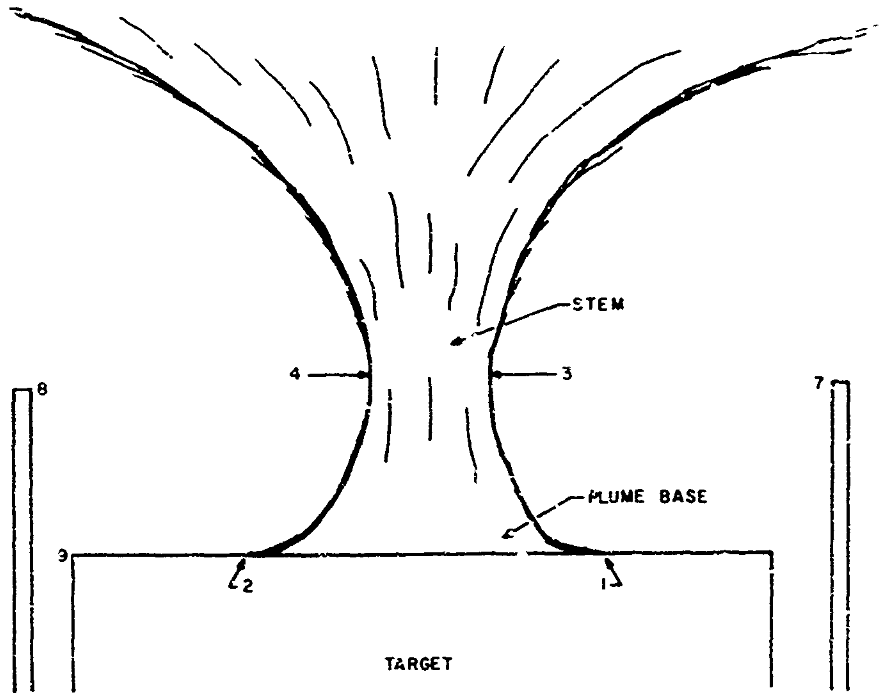

Fig. 16. Primary Features of Debris Plume.

The pair of points 1 and 2 represent the outer limits of the base of the plume, probably corresponding to an outward propagating bulge in the target material. In some experiments, it was difficult to measure these positions accurately since the silhouette of the plume base was nearly tangent to the target surface at these points. The character of the plume base varied considerably for the different targets used in this study.

The points labeled 3 and 4 represent the minimum diameter of the stem as determined by the operator. In general, the curve of the outline of the stem was such that these points were relatively easy to determine. The height of this minimum diameter point above the target surface varies somewhat as a function of time.

Two separate measurements of plume diameter as a function of time were thus obtained for each experiment. These measurements were judged to include the most distinctive features of the plume and probably represented the only diameters that could be measured with any consistency from experiment to experiment.

Summary

Hypervelocity impacts into solids produce two features -- cavitation and shock propagation -- each of which is amenable to separate experimental study. Experiments to study the cavitation or cratering processes have been described. Techniques were developed to provide up to ten sequential flash x-radiographs of growing cavities in several aluminum alloys; the required impacts were produced by a light gas gun at the AFML Hypervelocity Ballistic Range. Electronic and optical techniques were used to obtain accurate measurement of x-ray flash times with respect to the impact of the target. Additional experiments were designed to yield ultra-high speed framing camera pictures of the debris plume that is emitted from the crater on the impacted side of the target. Data reduction techniques were developed that removed the distortion inherent in flash x-radiographs and which relieved difficulties in interpreting the radiographs. The flash x-ray experiments produced a record of crater depths and diameters as a function of time. The framing camera record provided a time history of the diameter of two distinctive features related to the debris plume.

IV. Crater Growth -- Experimental Results

The experimental techniques described in the preceding chapter were employed in an extensive study of the growth of craters in aluminum alloys under hypervelocity impact conditions. Flash x-ray techniques were used to determine the dimensions of craters as a function of time after impact. A high speed framing camera was used to study the dynamics of the front surface plume created by a hypervelocity impact and to determine the relation of this phenomenon to the crater growth. The remainder of this chapter describes the results obtained and presents an analysis of this data including comparisons with previous experimental information and recent numerical calculations of hypervelocity impact events.

Experimental Program

The experiments were selected to study several effects. First and foremost was the effect of target strength upon the crater growth. This was achieved by using three separate aluminum alloys with different heat treatments as targets while keeping the projectile velocity constant (see Table II). Numerical calculations employing a purely hydrodynamic flow model of material behavior will predict identical crater growth rates for all aluminum alloys. This is incorrect since the final sizes of the craters in these alloys are drastically different. The new numerical procedures that include material strength effects (described in Chapter II) do predict different crater growth rates for these alloys (Refs. 40:12, 41:18 and 42). The experiments described below are, to the author's knowledge, the first set conducted on several alloys of one basic material and are specifically applicable to direct correlation with the results of numerical calculations and to studying the effects of material strength upon crater growth.

Outside of this facility, the only reported flash x-ray measurements of the internal dimensions of growing craters in metals are those by

Gehring (Ref. 33) who first applied the flash x-ray technique to hypervelocity impact studies. Gehring's results indicate substantial rebound (elastic recovery) in the crater dimensions after growth, a process opened to question by Smith's results (Ref. 34). Consequently, one set of experiments in this study -- steel projectiles impacting aluminum targets at 5 km/sec -- was conducted to compare directly with Gehring's results and investigate the existence of crater rebound further.

It also appeared desirable to investigate the effects of projectile velocity upon crater growth. therefore four sets of experiments using 1100 aluminum targets were performed at velocities ranging from 2.3 km/sec to 7 km/sec. These experiments explore the regime where material strength effects are expected to dominate the cratering process more and more as the velocity is lowered. Table III describes the eight sets of crater growth data obtained with flash x-ray techniques.

Several authors, including Kineke (Ref. 8) and Gehring (Ref. 12) have measured the diameter of the front surface plume produced during an impact event and have inferred information regarding the crater diameter from these measurements. Smith (Ref. 34) found indications that the correlation between plume and crater diameter was not as good as might be expected. Therefore, it was decided to explore this correlation further and framing camera photographs of plume growth were obtained for cases 1, 4, 7, and 8.

The experimental program consisted of 39 new, successful rounds conducted in two phases. The first group of experiments employed 0.318 cm diameter spherical projectiles. After further launch technique development, the remainder of the experiments were conducted using 0.635 cm diameter projectiles. The experiments are tabulated in Table IV.

In each case, the actual projectile velocity was held sufficiently close to the nominal velocity that no attempt has been made to scale the results

Table III

Classification of Crater Growth Experiments

Case Number	Projectile Material	Nominal Projectile Velocity (km/sec)	Aluminum Target Material
1	2017 Al	7.0	1100-0
2	2017 Al	5.2	1100-0
3	2017 Al	4.2	1100-0
4	2017 Al	2.3	1100-0
5	Tool Steel	5.0	1100-0
6	2017 Al	7.0	6061-T6
7	2017 Al	7.0	7075-T0
8	2017 Al	7.0	7075-T6

with velocity for any single case. This results in errors well within the experimental errors that arise from other sources.

Flash X-ray Results

Nearly two hundred flash x-radiographs of growing craters were obtained in this study. All data was analyzed according to the procedures described in Chapter III. Histories of crater diameter, D, and penetration (depth), p, were obtained for each of the eight cases considered. The data was normalized with respect to the projectile diameter, d, to facilitate size scaling and comparisons of the results. Cases 1 and 8 contain information obtained from experiments conducted with both 0.318 cm and 0.636 cm diameter projectiles. When scaled in the manner described, the results are indistinguishable with respect to projectile size.

For each set of data a least squares technique was used to obtain an analytical representation of the form:

Table IV

Tabulation of Crater Growth Experiments

Round Number	Projectile Diameter (cm)	Projectile Material	Velocity (km/sec)	Target Material (Aluminum)	Target Thickness (cm)	Number of Data Points
1043	0.3175	Al	2.22	1100-0	2.49	FC only
1044	0.3175	Al	2.34	1100-0	2.54	5
1045	0.3175	Al	2.32	1100-0	2.54	4
1049	0.3175	Al	2.3e	1100-0	2.27	5
2384[1]	0.3175	Al	6.90	1100-0	3.38	5
2385[1,2]	0.3175	Al	7.05	1100-0	2.38	-
2386[1]	0.3175	Al	7.04	1100-0	2.38	5
2387[1]	0.3175	Al	7.0e	1100-0	3.18	3
2502	0.3175	Al	7.45	7075-T0	2.54	2
2503	0.3175	Al	7.16	1100-0	2.54	3
2504	0.3175	Al	7.22	1100-0	2.54	4
2505	0.3175	Al	7.14	1100-0	2.54	4
2506	0.3175	Al	7.15	7075-T0	2.54	2
2507	0.3175	Al	7.35	7075-T0	1.59	6
2508	0.3175	Al	7.16	7075-T0	2.54	3
2509	0.3175	Al	7.29	7075-T6	2.54	4
2510	0.3175	Al	7.20	7075-T6	2.54	3
2511	0.3175	Al	7.25	7075-T6	2.54	3
2515	0.3175	Al	5.40	1100-0	2.54	6
2516	0.3175	Al	5.03	1100-0	2.54	5
2517	0.3175	Al	5.07	1100-0	2.54	6
2519	0.3175	Al	7.27	7075-T0	2.54	2
2520	0.3175	Al	7.27	7075-T6	2.54	2 FC
2521	0.3175	Al	7.30	1100-0	2.54	2 FC
2523	0.3175	Al	7.28	7075-T0	2.54	FC only
2524	0.3175	Al	5.16	1100-0	2.54	FC only
2525	0.358	Steel	4.92	1100-0	2.54	5
2526	0.358	Steel	5.26	1100-0	5.08	2
2527	0.358	Steel	5.03	1100-0	3.81	4
2528	0.358	Steel	5.13	1100-0	5.08	4
2684	0.635	Al	6.63	6061-T6	2.54	7
2685	0.635	Al	7.0e	6061-T6	4.13	8
2686	0.635	Al	7.01	6061-T6	3.18	5

Table IV (Continued)

Round Number	Projectile Diameter (cm)	Material	Velocity km/sec	Target Material (Aluminum)	Thickness (cm)	Number of Data Points
2688[3]	0.635	Al	6.70	6061-T6	4.01	10
2689	0.635	Al	6.90	1100-0	4.44	6
2692	0.635	Al	6.98	7075-T6	2.16	9
2693	0.635	Al	6.98	7075-T6	3.56	3
2694	0.635	Al	6.80	6061-T6	3.56	8
2696[4]	0.635	Al	6.96	1100-0	5.08	7
2698	0.635	Al	4.19	1100-0	3.02	5
2700	0.635	Al	4.03	1100-0	4.45	7
2702	0.635	Al	4.08	1100-0	3.30	8
2704	0.635	Al	4.20	1100-0	3.30	7

e indicates estimated projectile velocity
FC indicates framing camera experiment
(1) Experiments performed by Smith (Ref. 34) at this facility.
(2) Time base very uncertain and data did not agree with other experimental results -- data not used.
(3) Time base incorrect. Each data point shifted by 5.08 μsec resulted in good agreement with remainder of experimental data.
(4) Small pieces of sabot cap hit crater area several microseconds after projectile impact. Effects of cap impact on crater formation appear negligible, because they occur after the x-rays were obtained.
(5) All aluminum projectiles were 2017 alloy.

$$\left(\frac{D}{d}\right) \text{ or } \left(\frac{p}{d}\right) = A - B\, e^{-\frac{(t/d)}{(\tau/d)}} \qquad \text{(Eq. 1)}$$

where A and B are dimensionless constants and (τ/d) is a quantity with dimensions μsec/cm that represents an exponential period for the crater growth process, i.e., it indicates how fast the crater is approaching its final size. The values A and B were picked based upon the physical argument that, at the very earliest times, the projectile penetrates the target with very little deceleration.

At 7 km/sec the projectile is half imbedded in the target ($D/d = 1$ and $p/d = 0.5$) at t/d 0.71 μsec/cm. Consequently, on the scale shown, it is not unreasonable to assume that the D/d and p/d intercepts at $t/d \cong 0$ are 1.0 and 0.5 respectively. Likewise, at late times the D/d or p/d ratios must assume a constant value identified with the final crater diameter or depth respectively. Consequently the following values were selected:

A =(Final crater diameter or penetration)/(Projectile Diameter)

$$B = \begin{cases} A - 1 \text{ for } D/d \\ A - 1/2 \text{ for } p/d \end{cases}$$

The constant (τ/d) was then determined using the least squares criteria. A related form of analytical fit was used by Smith (Ref. 34). The values of these constants for each case and the standard deviation for each curve are given in Table V. The dashed lines in these figures give a measure of σ, the standard deviation of the fit in each case.

In several cases it was possible to obtain slightly better fits to the data with a Prony series expression in the form:

$$(D/d) \text{ or } (p/d) = \sum_{i=1}^{n} a_i e^{k_i (t/d)} \qquad \text{(Eq. 2)}$$

where the k_i are constants selected empirically and the a_i are determined using a computer and a generalized least squares technique. The fits achieved were not sufficiently better, however, to employ these rather complicated expressions in place of the very simple analytic expression actually used.

The experimental data points obtained as well as the analytic curve fit to each set of data points are shown for Cases 1 through 8 in Figures 17 through 32. The data points shown as circles were derived from x-ray films rated as average or good. Those points marked with triangles were from the poorer x-radiographs and were expected to show more scatter -- though little difference is actually noted. The detailed data from these experiments are included in Appendix B.

Table V

Constants for Crater Growth Curves

$$(D/d) \text{ or } (p/d) = A - Be^{-(t/d)/(\tau/d)}$$

Case	A	B	τ/d (μ sec/cm)	Standard Deviation of fit, σ
1 - Diameter	5.20	4.20	15.6	[illegible]
Penetration	2.89	2.39	14.5	.08
2 - Diameter	4.42	3.42	14.9	.13
Penetration	2.52	2.02	14.7	.14
3 - Diameter	3.94	2.94	13.0	.16
Penetration	2.27	1.77	18.2	.18
4 - Diameter	2.60	1.60	14.7	.11
Penetration	1.56	1.06	20.4	.11
5 - Diameter	6.03	5.03	32.3	.13
Penetration	5.02	4.52	21.3	.18
6 - Diameter	4.14	3.14	8.6	.12
Penetration	2.07	1.57	7.7	.08
7 - Diameter	4.27	3.27	13.0	.09
Penetration	2.48	1.98	14.4	.13
8 - Diameter	3.38	2.38	7.9	.10
Penetration	1.63	1.13	7.5	.09

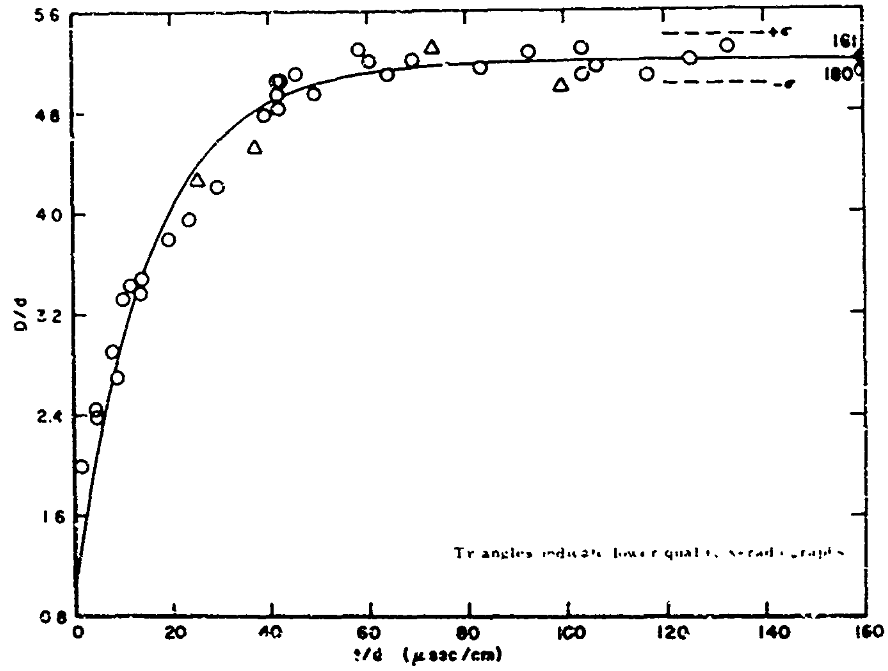

Fig. 17. CASE 1. Normalized Crater Diameter vs Normalized Time for 1100-0 Aluminum Target and Aluminum Projectile at 7.0 km/sec Nominal Velocity.

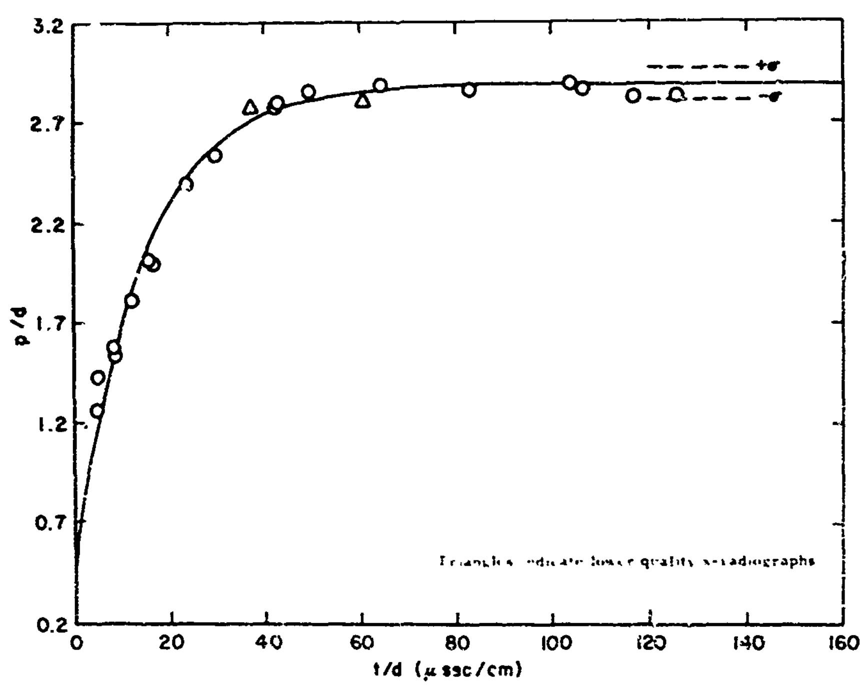

Fig. 18. CASE 1. Normalized Crater Penetration vs Normalized Time for 1100-0 Aluminum Target and Aluminum Projectile at 7.0 km/sec Nominal Velocity.

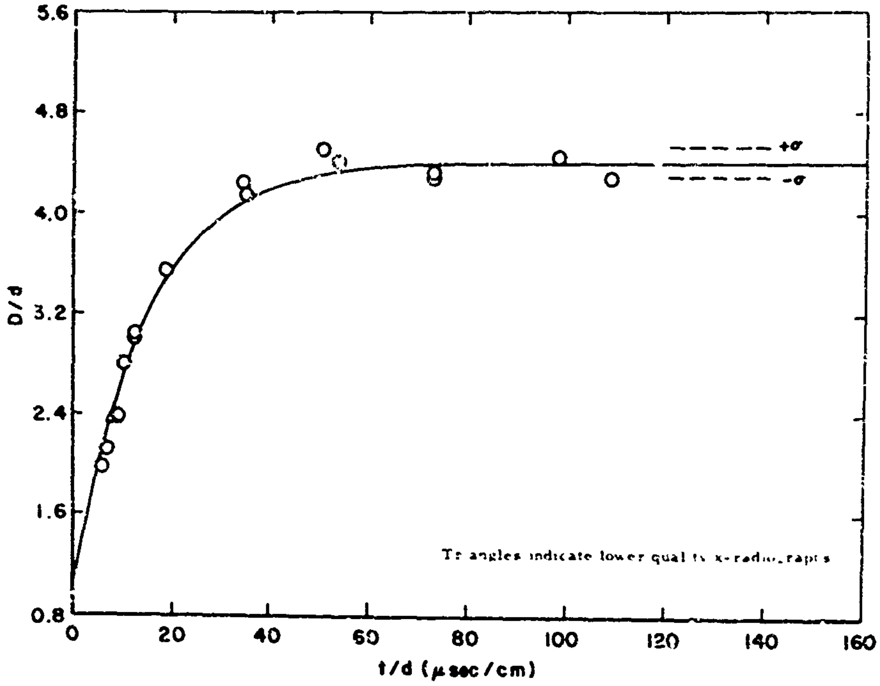

Fig. 19. CASE 2. Normalized Crater Diameter vs Normalized Time for 1100-0 Aluminum Target and Aluminum Projectile at 5.2 km/sec Nominal Velocity.

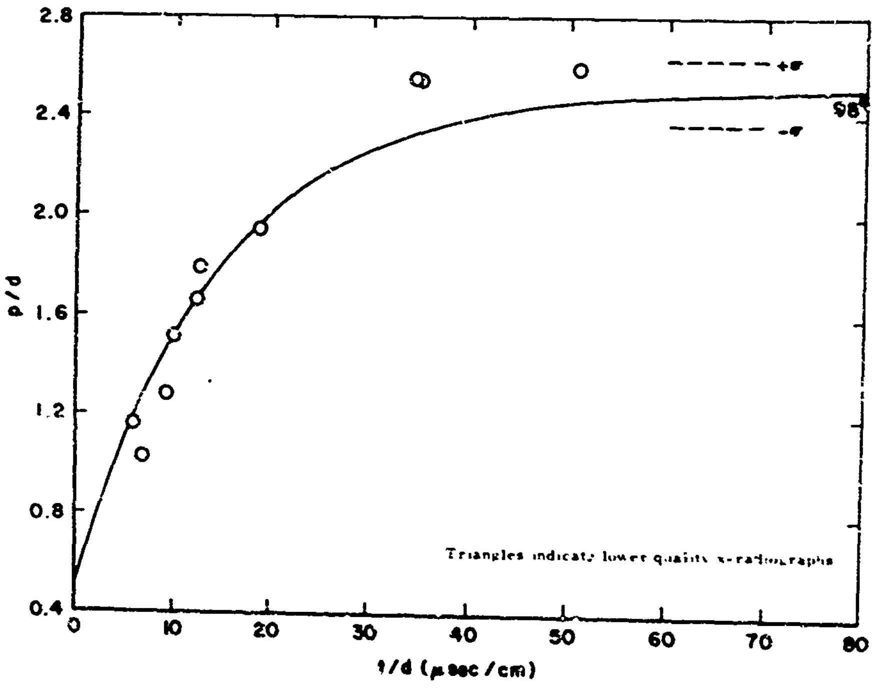

Fig. 20. CASE 2. Normalized Crater Penetration vs Normalized Time for 1100-0 Aluminum Target and Aluminum Projectile at 5.2 km/sec Nominal Velocity.

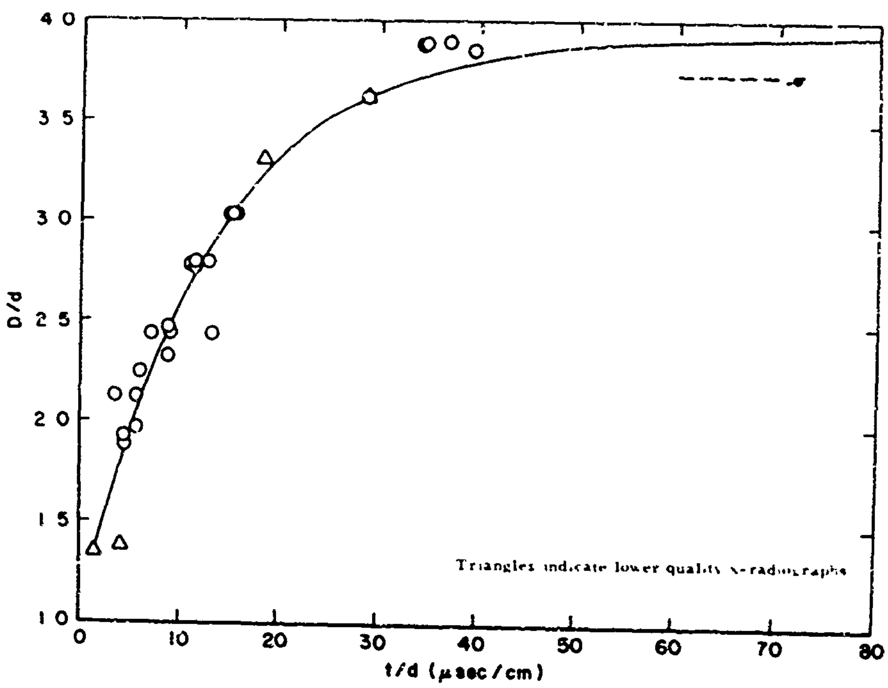

Fig. 21. CASE 3. Normalized Crater Diameter vs Normalized Time for 1100-0 Aluminum Target and Aluminum Projectile at 4.2 km/sec Nominal Velocity.

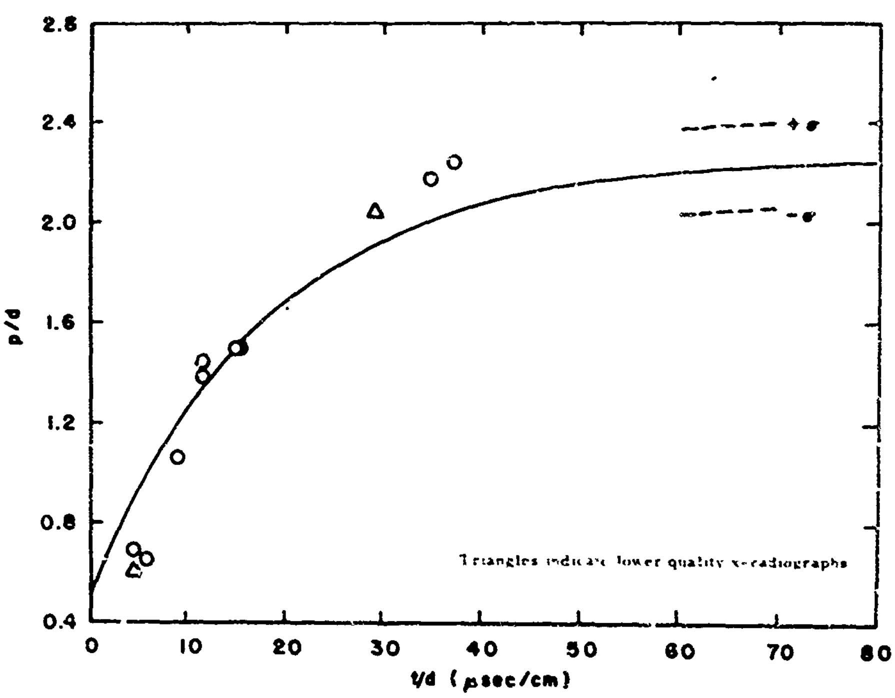

Fig. 22. CASE 3. Normalized Crater Penetration vs Normalized Time for 1100-0 Aluminum Target and Aluminum Projectile at 4.2 km/sec Nominal Velocity.

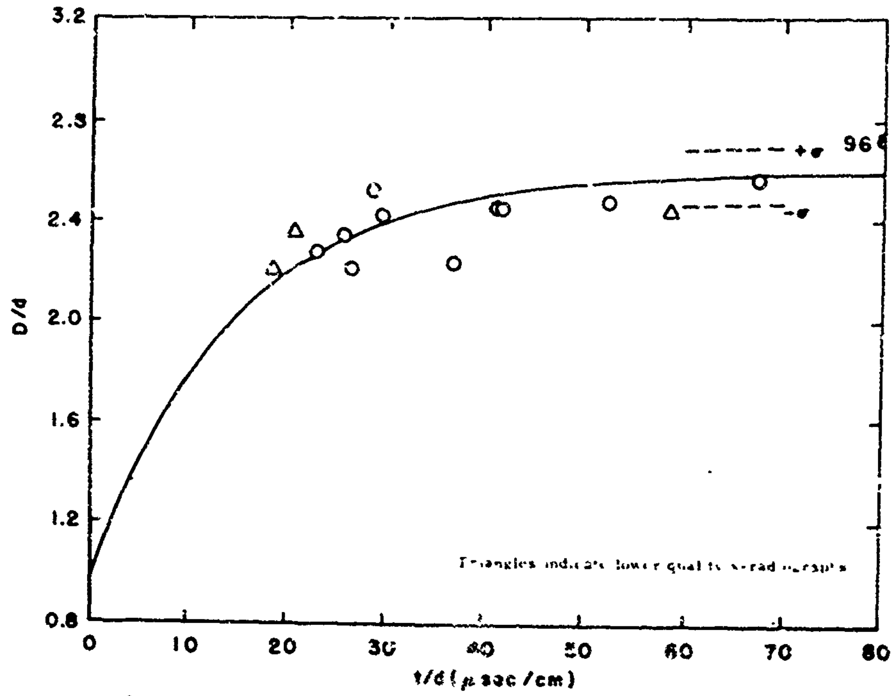

Fig. 23. CASE 4. Normalized Crater Diameter vs Normalized Time for 1100-0 Aluminum Target and Aluminum Projectile at 2.3 km/sec Nominal Velocity.

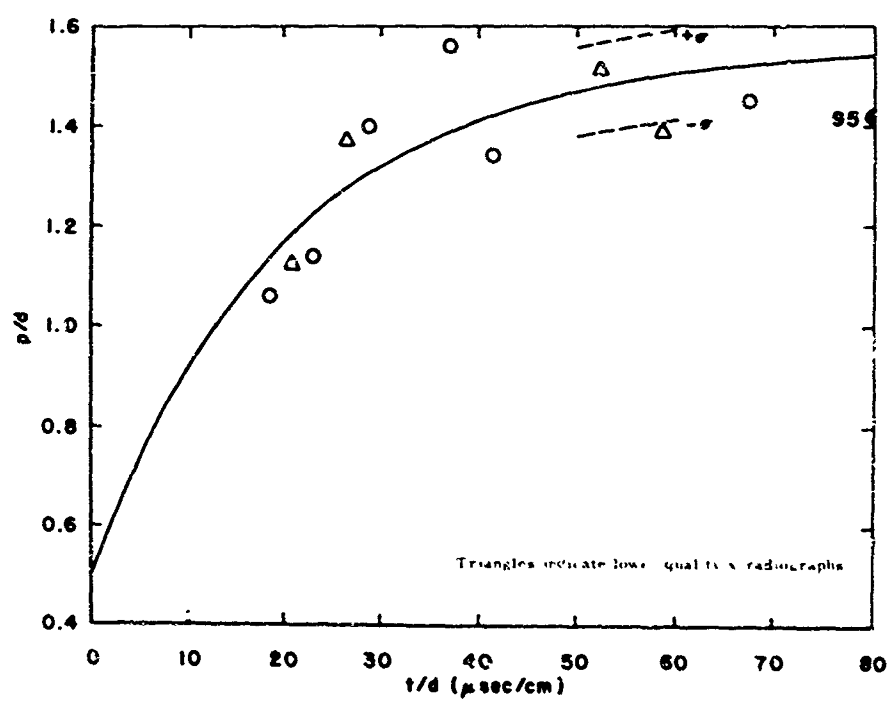

Fig. 24. CASE 4. Normalized Crater Penetration vs Normalized Time for 1100-0 Aluminum Target and Aluminum Projectile at 2.3 km/sec Nominal Velocity.

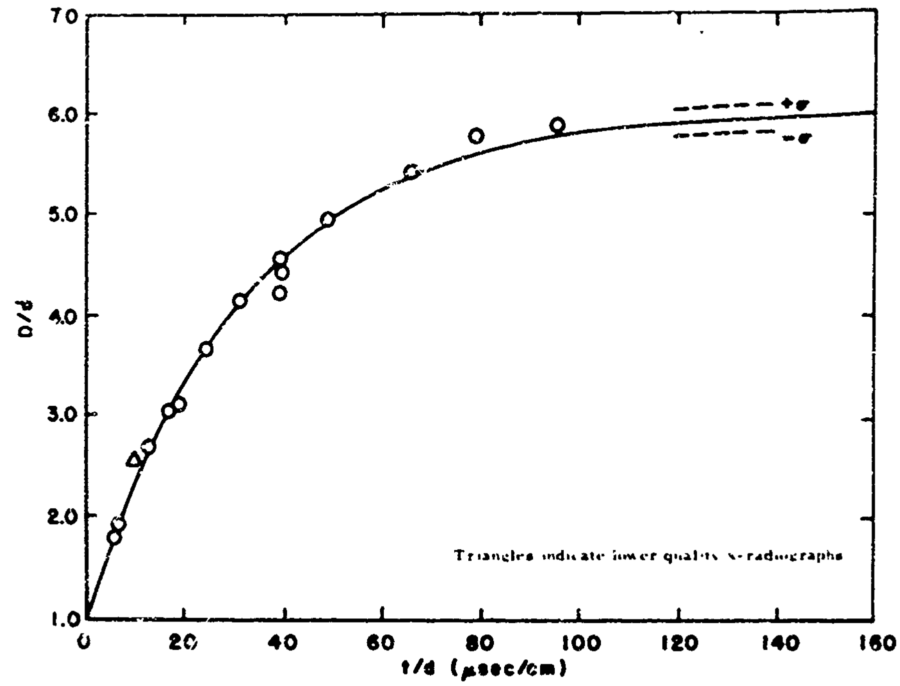

Fig. 25. CASE 5. Normalized Crater Diameter vs Normalized Time for 1100-0 Aluminum Target and Steel Projectile at 5.0 km/sec Nominal Velocity.

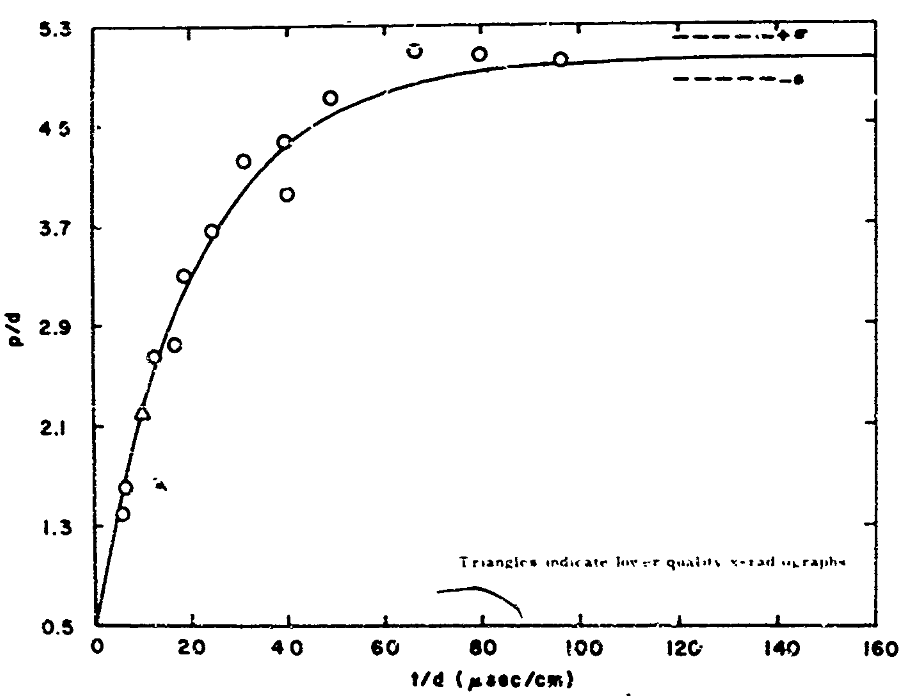

Fig. 26. CASE 5. Normalized Crater Penetration vs Normalized Time for 1100-0 Aluminum Target and Steel Projectile at 5.0 km/sec Nominal Velocity.

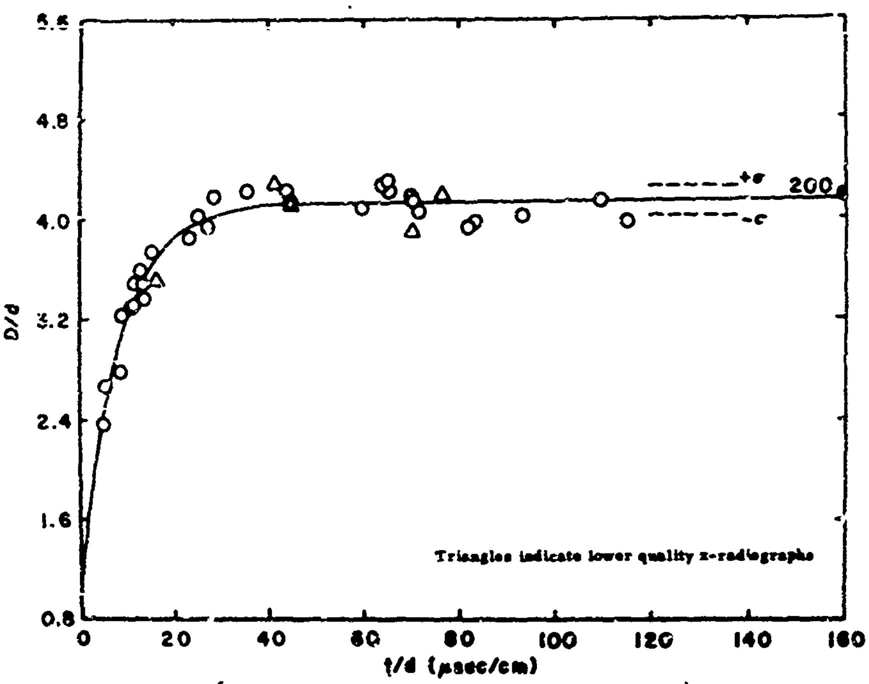

Fig. 27. CASE 6. Normalized Crater Diameter vs Normalized Time for 6061-T6 Aluminum Target and Aluminum Projectile at 7.0 km/sec Nominal Velocity.

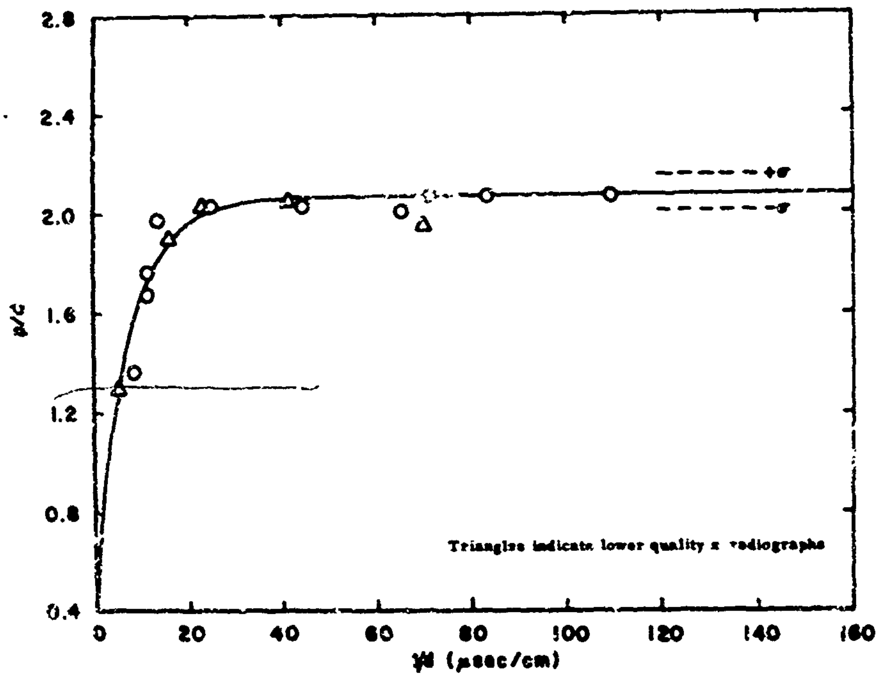

Fig. 28. CASE 6. Normalized Crater Penetration vs Normalized Time for 6061-T6 Aluminum Target and Aluminum Projectile at 7.0 km/sec Nominal Velocity.

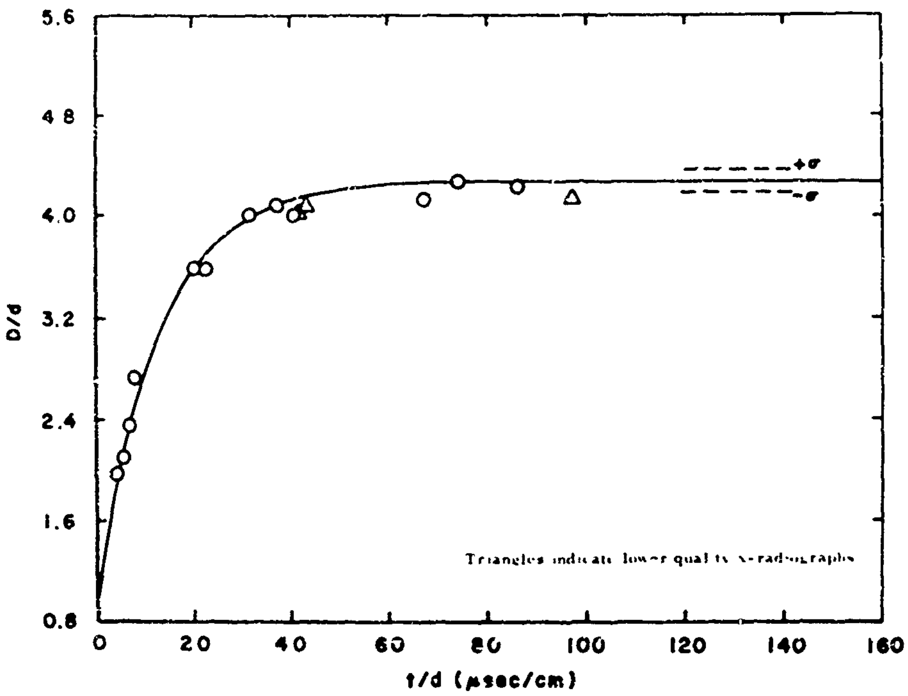

Fig. 29. CASE 7. Normalized Crater Diameter vs Normalized Time for 7075-T0 Aluminum Target and Aluminum Projectile at 7.0 km/sec Nominal Velocity.

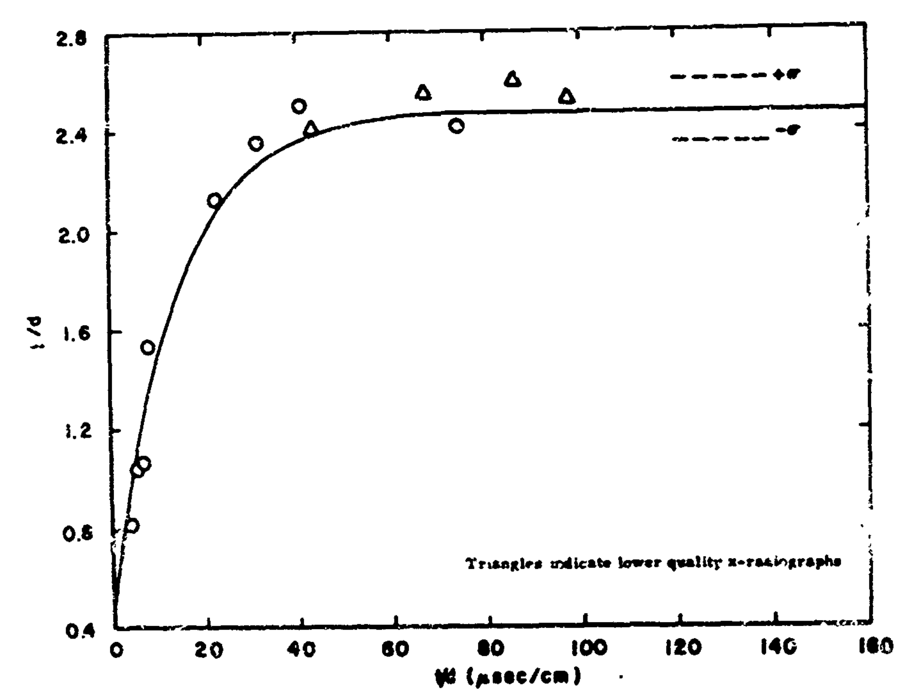

Fig. 30. CASE 7. Normalized Crater Penetration vs Normalized Time for 7075-T0 Aluminum Target and Aluminum Projectile at 7.0 km/sec Nominal Velocity.

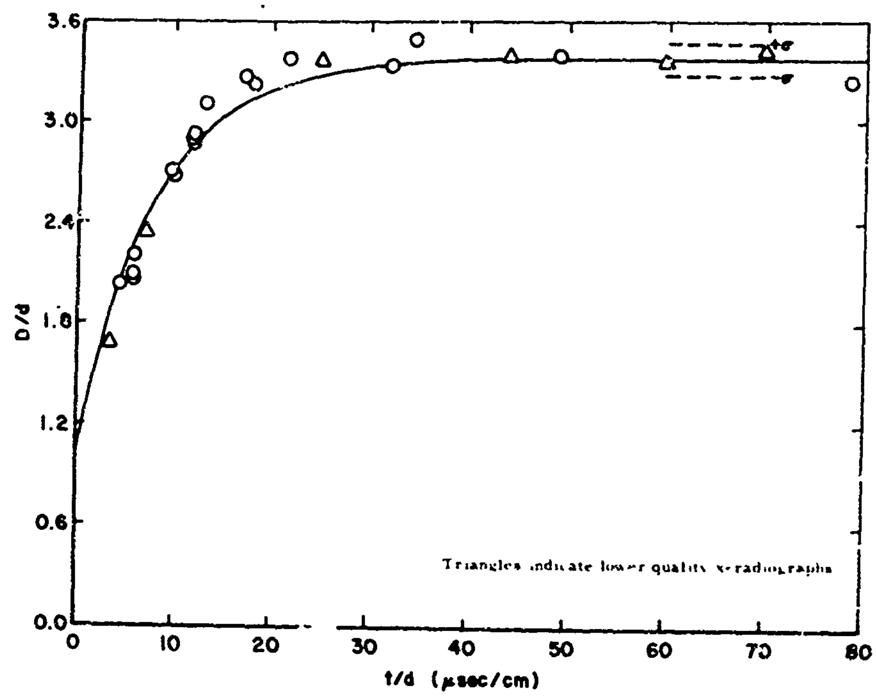

Fig. 31. CASE 8. Normalized Crater Diameter vs Normalized Time for 7075-T6 Aluminum Target and Aluminum Projectile at 7.0 km/sec Nominal Velocity.

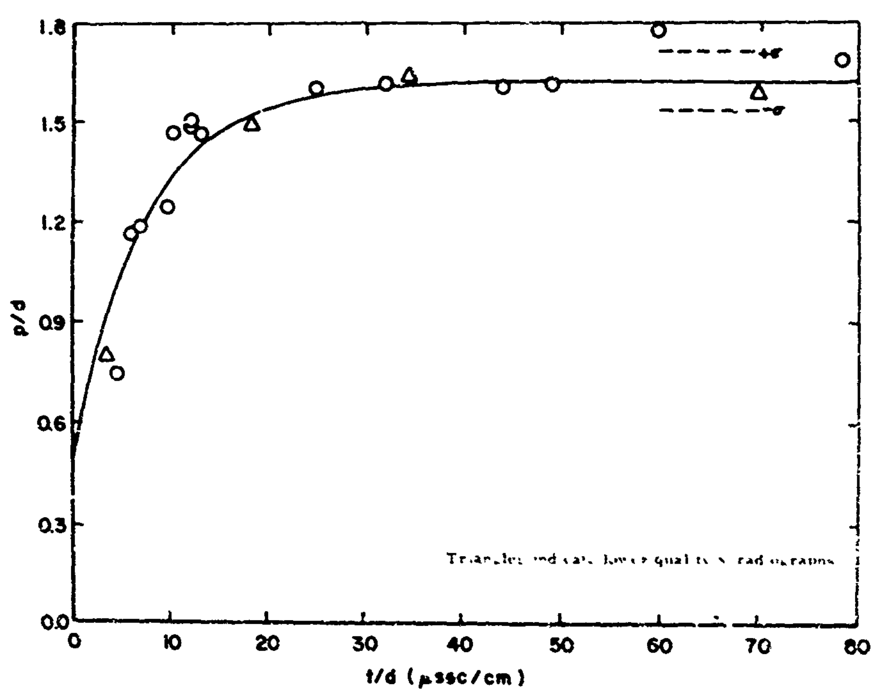

Fig. 32. CASE 8. Normalized Crater Penetration vs Normalized Time for 7075-T6 Aluminum Target and Aluminum Projectile at 7.0 km/sec Nominal Velocity.

The data of Case 1 (1100 Al target) was obtained from the highest quality x-radiographs -- those showing the largest craters and highest contrast. As craters became smaller due to lower projectile velocities (Cases 2, 3 and 4), the x-radiograph quality decreased. This is most readily apparent in the data of Case 4 where the projectile velocity was very low, 2.3 km/sec, and the projectiles were all 0.318 cm spheres. The craters were small for these experiments and the data shows considerable scatter. All data points obtained in the program are reported except those that could be deleted for specific, identifiable causes or which exceeded three times the standard deviation of the analytic curves described below. Points which lie outside the range of the plots are indicated by darkened circles.

The accuracy of the reported time from impact for any point is a function of the measurement technique used. If the timing signal was derived from the ionization switch on the x-ray source, the times are accurate to approximately 0.2 μsec while if the signal was derived from the x-ray source trigger signal, the accuracy was about 0.7 μsec. In a few cases, neither of these signals was available and an estimate of the time was made from other sources. Appendix B lists the estimated accuracy of the time as well as the source of timing signal for each flash x-ray data point.

Analysis

These results yield a good deal of quantitative information about the crater growth process in aluminum and the qualitative model of the various phases of the growth discussed in Chapter II. In addition to the primary phenomena of material strength effects, the experiments yielded data related to such effects as variation in the crater growth with velocity, strength effects, and the existence of rebound during the growth process. Each of these is discussed below.

Velocity Dependence. Everything else being constant, it is expected that the final crater size will increase as a function of the projectile impact velocity since more energy is available to the process. A great deal of effort has been spent in studying this velocity scaling law, which is usually written in the form:

$$p/d = kv_p^n \qquad \text{(Eq. 3)}$$

where k may describe properties of the target and projectile, but is not a function of v_p.

It is usually assumed (in the hypervelocity regime) that the crater diameter, D, is simply twice the penetration p. The values of the constant n range all the way from 1/3 to 2/3; from a momentum dependence to an energy dependence. The most generally accepted value for impacts that are truly hypervelocity is $n = 0.58$ based upon combined numerical and analytical studies by Walsh and Dienes (Ref. 42). Thus assuming that $n = .58$, the results of the present study for penetration into 1100-0 aluminum yield $(p/d)_{final} = (0.96 \pm .03)v_p^{.58}$ and $(D/d)_{final} = (1.66 \pm .06)v_p^{.58}$ for the diameter. These relations are in agreement with Halperson's data (Ref. 43). Nothing is revealed, of course, about the dynamics of the crater formation.

The results of Cases 1 through 4 illustrate the growth of craters in 1100-0 aluminum created at four different projectile velocities ranging from 7.0 km/sec in the hypervelocity regime down to 2.3 km/sec, which is in the ballistic impact regime. The curves derived from these results are shown in Figs. 33 and 34. From these, three phases of crater growth can be discussed. At early times (roughly $t/d < 10$) for the three higher velocity cases, the behavior is dominated by hydrodynamic processes and the crater grows at a high rate. Later ($10 < t/d < 40$) the target strength becomes increasingly important and slows the crater growth completely.

At the lowest velocity, when the peak pressures are so low that no true hydrodynamic phase should be encountered, target strength should affect crater growth from the onset. The data obtained at 2.3 km/sec (see Figs. 23 and 24, Case 4) is not of sufficient accuracy to establish the behavior at early times --

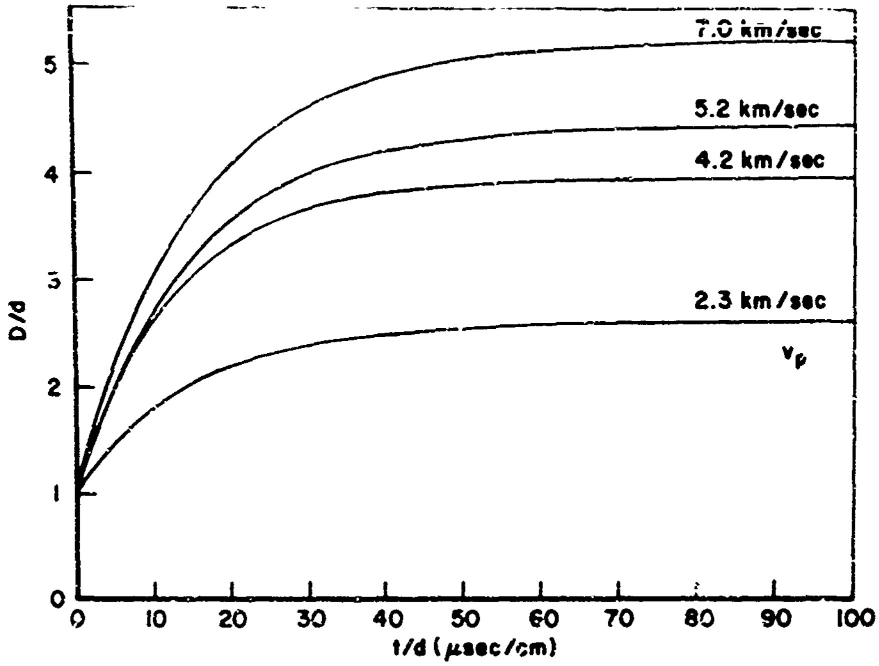

Fig. 33. History of Crater Diameter in 1100-0 Aluminum at Four Projectile Velocities.

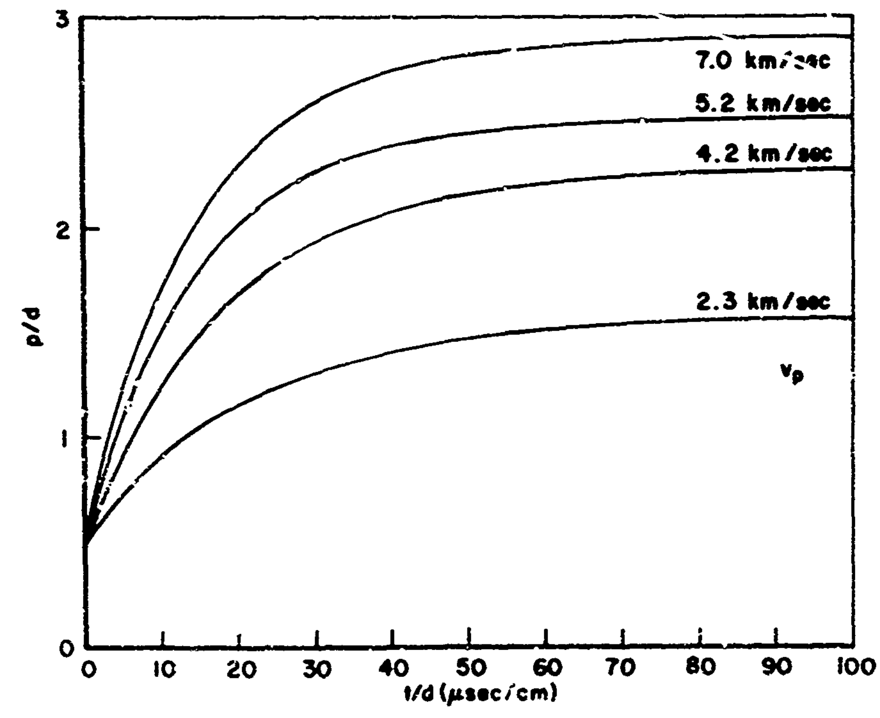

Fig. 34. History of Crater Penetration in 1100-0 Aluminum at Four Projectile Velocities.

in fact no readable data was obtained at $t/d < 18$. The exponential curve derived from this data is likely to be rather inaccurate and should not be taken to imply any more than a general trend. Indeed, the justification for the use of the exponential form to fit the Case 4 data must be based upon analogy with the Case 1, 2, and 3 data, not upon direct evidence.

The variation of the crater diameter growth time constant $(\tau/d)_D$ with projectile velocity is either small or non-existent over the range of velocities considered here. Since this time constant represents a measure of the relative growth rate, i.e., $D(t)/D_{final}$, this is a reasonable result. The absolute growth, as indicated in Fig. 33, is higher at the higher projectile velocities as expected.

The data indicates an increase in $(\tau/d)_p$ with decreasing projectile velocity, a somewhat unexpected result. Again, however, the absolute growth rates (see Fig. 34) appear in the correct order. The data for Cases 3 and 4 are so sparse at early times for the penetration measurements that it is likely that large errors were associated with the determination of $(\tau/d)_p$ here. It is therefore possible that the values of τ/d do not depend upon the projectile velocity over the range considered.

Crater Shape. At hypervelocities there is a strong tendency for the craters formed to be approximately hemispherical in shape. Even though the experiments conducted here extend only into the lower end of the hypervelocity impact region (v_p was never more than fifty per cent above the sound speed in the target material) this trend is clearly evident in the results of Fig. 35. The data are taken from the crater growth curves for Cases 1 through 4. A perfect hemispherical crater would grow along the dashed line. For the 1100-0 aluminum targets, there is a tendency for the penetration to exceed the crater radius by about ten per cent. The data for the 4.2 km/sec projectile velocity case indicate that the crater shape changes during the growth process at the lower velocities. The growth data on the 2.3 km/sec projectile velocity case are sufficient to substantiate this trend. The data for Cases 1 and 2 (7.0 and 5.2

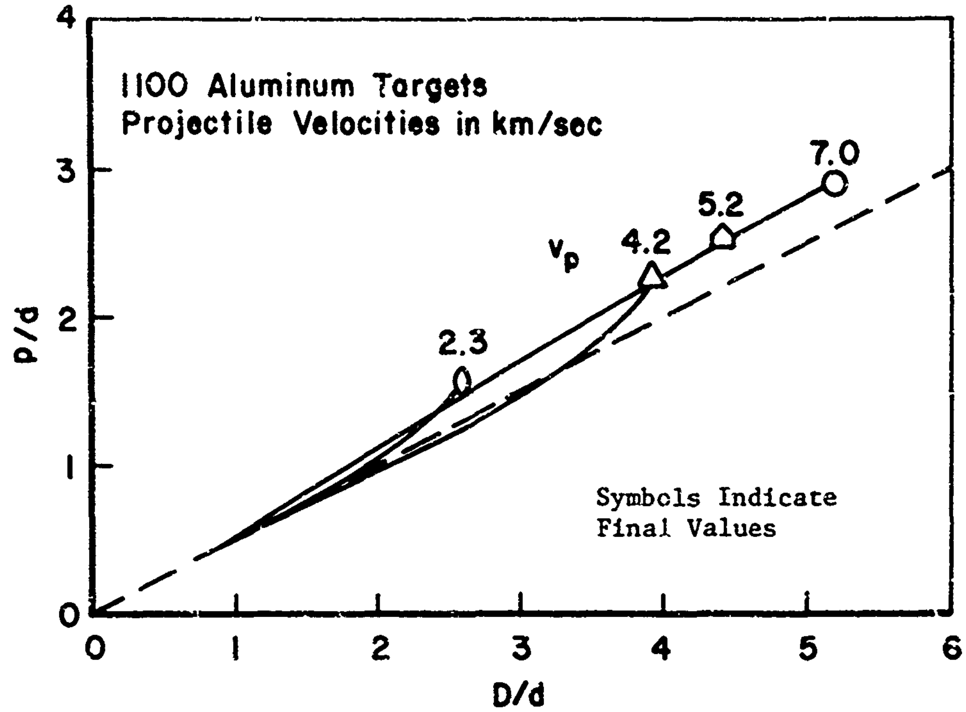

Fig. 35. Crater Shape During Growth -- 1100-0 Aluminum Target at Four Projectile Velocities.

km/sec projectile velocity) lie along the same curve.

Figure 36 shows equivalent crater shape data for the four alloys of aluminum used, all with a projectile velocity of 7.0 km/sec nominally. The harder alloys form more nearly hemispherical craters. At these velocities, the crater shape remains nearly constant during the growth process. On these figures, all craters "start" at the point D/d =1, p/d =1/2 corresponding to the projectile half imbedded in the target and continue along the lines shown to the end points marked with data symbols.

Target Strength. Cases 1, 6, 7, and 8 were conducted to explore the effects of material strength upon the crater growth rates in aluminum. The curves derived from the experimental data are redrawn in Figs. 37 and 38. The results agree quite well with the four phase description of impact cratering described previously. The earliest penetration phase ·. ·. short at the impact velocities studied her hat no information was acquired on this phase. The

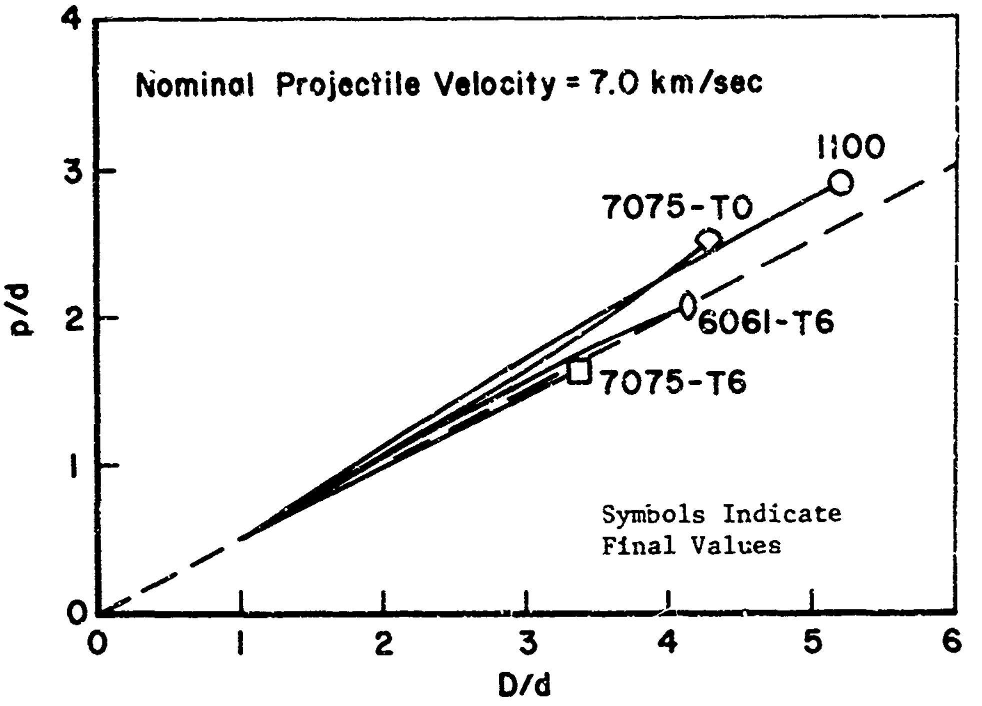

Fig. 36. Crater Shape During Growth -- 7.0 km/sec Projectile Velocity with Four Aluminum Alloy Targets.

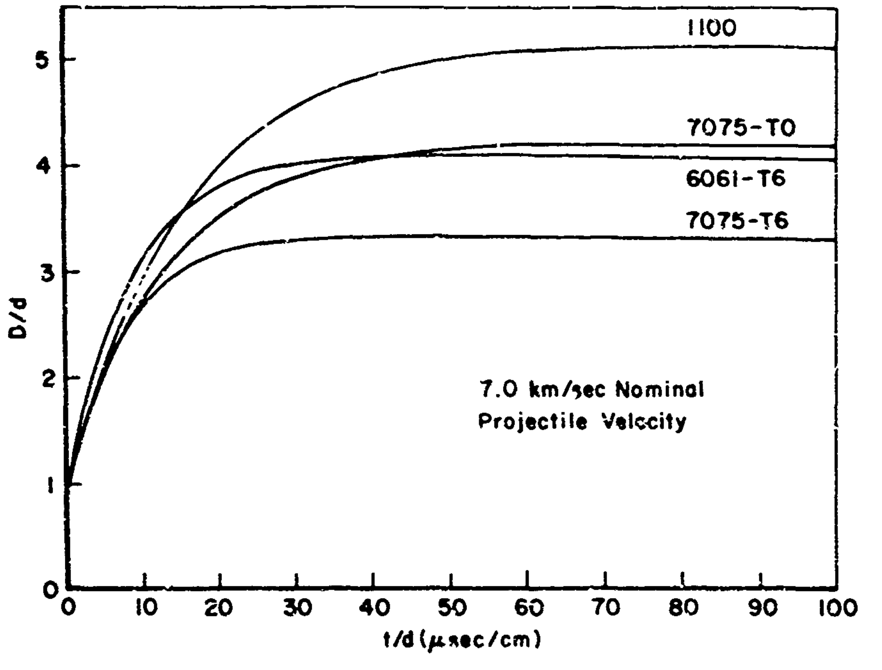

Fig. 37. Comparison of Crater Diameter Growth for Four Aluminum Alloys.

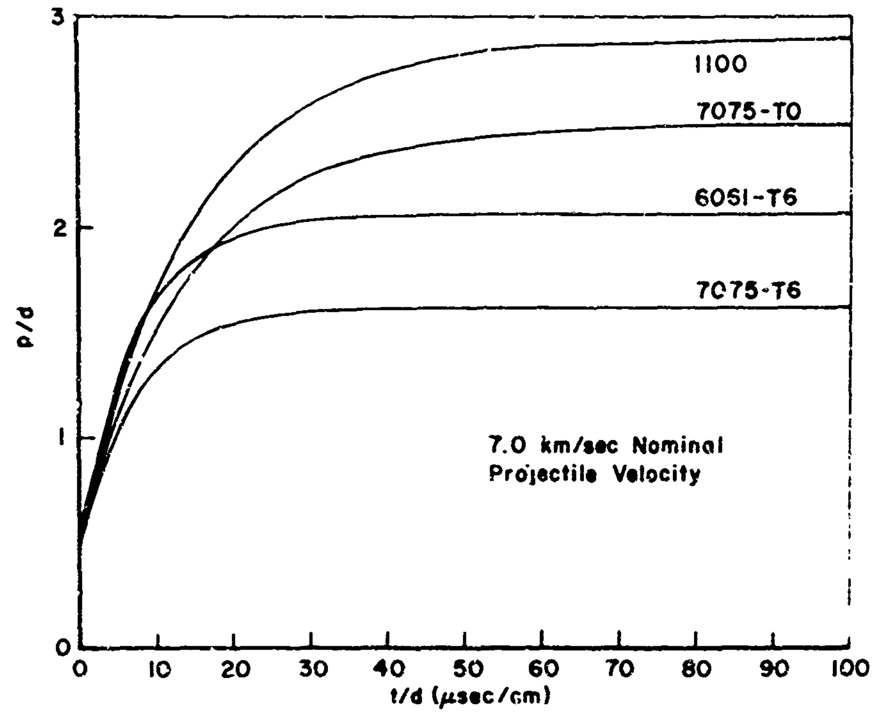

Fig. 38. Comparison of Crater Penetration Growth for Four Aluminum Alloys.

hydrodynamic phase, where pressures greatly exceed any material strength (specifically where the pressure is substantially greater than the deviatoric components of the stress tensor), is of relatively short duration, but definitely exists at the 7.0 km/sec impact velocities. The peak pressure at impact is nearly one megabar. This phase is illustrated rather clearly on Fig. 37 where the craters in all four alloys are shown to grow at nearly the same rate until $t/d \approx 8$.

In the region $8 < t/d < 25$, material strength begins to dominate, slowing the growth. Finally in the region $t/d > 25$, the crater growth is arrested completely. As expecred, the stronger materials result in smaller craters and the strength seems to affect the growth earlier in the process.

A brief examination of the variation of the final crater diameter and penetration with the yield strength, Y_o, of the target material yielded the following approximate scaling laws for a projectile velocity of 7.0 km/sec.

$$(D/d)_{final} \cong 0.45\, Y_o^{-.2}$$

$$(p/d)_{final} \cong 0.23\, Y_o^{-.2} \qquad \text{(Eq. 4)}$$

where Y_o is in kilobars.

These relations can be considered only approximate since the scatter of the experimental data around the values predicted by these equations is relatively large and may not be valid at other projectile velocities. Additional correlation of final crater size with material properties is discussed in Appendix A.

Likewise, it was determined that the time constants, τ/d, varied with the yield strength as follows: $(\tau/d)_D \cong (\tau/d)_p \cong 0.86\, Y_o^{-.2}$. Hence

$$D_{final}/\tau \cong 0.39 \text{ cm}/\mu\text{sec}$$

$$p_{final}/\tau \cong 0.20 \text{ cm}/\mu\text{sec} \qquad \text{(Eq. 5)}$$

This implies that, at least to first order, the growth speed, insofar as it is characterized by the time constant, τ, remains about the same independent of the material yield strength. This conclusion is consistent with the data shown in Figs. 37 and 38. (See Appendix H for further discussion and dimensional analysis implications.) The greatest deviation from this result is displayed by the 6061-T6 alloy which tends to grow slightly faster than these scaling laws would predict. The slightly higher density ($\sim$3%) of the 6061-T6 may explain in part this tendency toward faster crater growth.

Crater Rebound and Previous Experimental Results. The application of flash x-ray techniques to the measurement of crater formation in solid materials has received only limited attention in the past. The earliest information was obtained by Gehring (Ref. 33) who used 1100-0 aluminum targets. These data as well as new results in wax targets were reported in Ref. 8. Later studies by Holloway (Ref. 44) and by Frasier, Karpov, and Holloway (Ref. 11) were related to more extensive studies of the hydrodynamic behavior of the crater formation and shock propagation in wax.

Each of these sets of data indicated that significant "rebound" occurred during the crater formation, that is the crater grew beyond its final dimensions during the middle stages of its growth process and relaxed to its final configuration at later time. Frasier's data indicates that, in wax there is little rebound in the crater diameter, but that the crater depth grows to 35% larger dimensions than its final configuration (Ref. 11:137-138). Frasier attributes this to the high compressibility of the wax, but indicates that the rebound in metals should be expected to be less pronounced.

Gehring's data is shown in Fig. 39 and compared with the results obtained in this study for Case 5, a steel projectile with 5.0 km/sec velocity impacting an 1100-0 aluminum target at normal incidence. Gehring's experiments, conducted in 1960 when hypervelocity projection techniques were not as well developed and when flash x-radiography was a relatively new technology, involved the impact of an 0.18 gram steel disk, traveling at 5 km/sec, upon a 2S aluminum (1100-0 aluminum equivalent) target. In attempting to compare the results, the diameter of an equivalent mass sphere of steel, $d = 0.358$ cm, was used to scale the data. The differences in final penetration are rather large and apparently due to projectile shape -- a disk as opposed to a sphere. The disk impact results in rather significant attenuation of the on-axis pressures in the target due to the rapid onset of rarefaction from the rear of the disk, thereby resulting in decreased penetration. On the other hand, the crater diameter is determined largely by other processes such as the shear flow that occurs at late time and its final value appears not to be a sensitive function of the projectile shape.

Gehring's data indicates substantial crater rebound, both in diameter and depth. The data obtained here (Figs. 25 and 26) indicates no such trend.

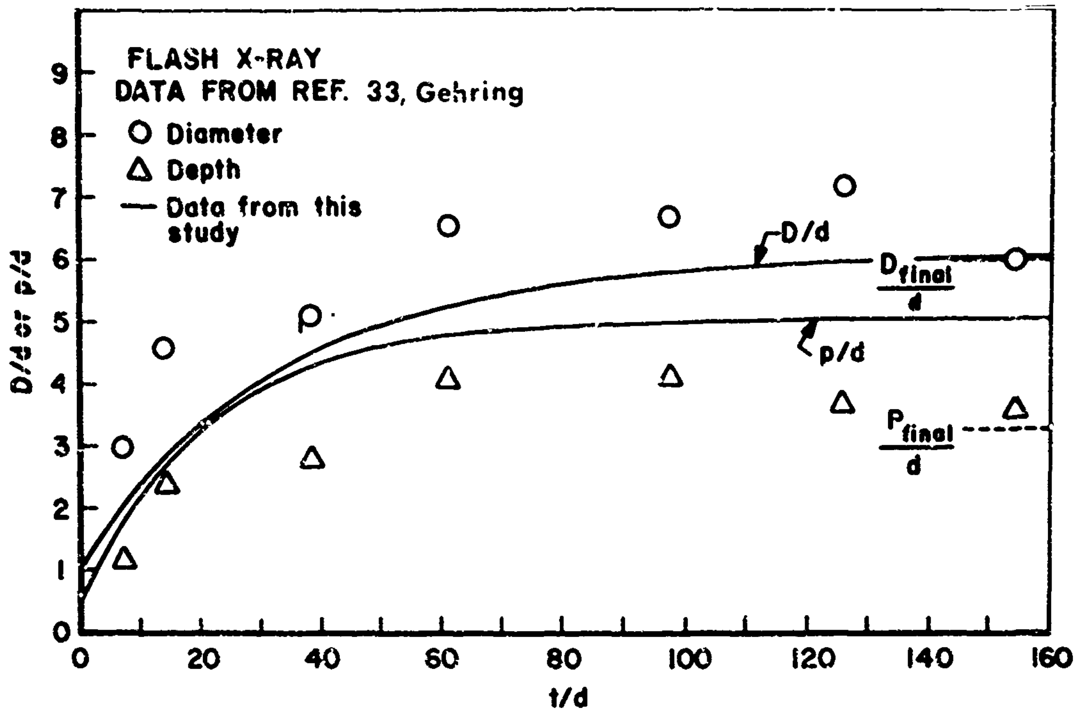

Fig. 39. Comparison of Experimental Flash X-Ray Crater Growth Data with Gehring's Results (Scaled).

The impacts of aluminum spheres into 1100-0 aluminum targets at 7.0 km/sec (Figs. 17 and 18) clearly indicate that no measurable rebound phenomena occurs for either the crater diameter or depth (penetration) to within the accuracy of these experiments, which is roughly ±4%. At lower velocities in this target material (Cases 2, 3, and 4) the data is less complete, but again there is no indication of any crater rebound. The data for the harder aluminum alloy targets (Cases 6, 7, and 8) show definite evidence that no rebound occurs. Those results clearly indicate that crater rebound is not a typical feature of the impact of spherical projectiles into aluminum targets.

The only remaining explanation for the large rebound measured by Gehring and shown in Fig. 39 is the difference in the shape of the projectile used. No attempt was made to explore projectile shape effects in this study.

Framing Camera Results

As mentioned before, several researchers have used framing camera measurements of the front surface plume to determine crater growth rates. It is very desirable to have a technique such as this available since most metallic targets do not lend themselves to flash x-ray studies because of x-ray absorption properties. Smith (Ref. 34) obtained results with framing camera photographs that indicated a lack of good correlation between the growth of the plume or outside dimension of the crater lips and the growth of the inside diameter of the crater. Smith's work has been extended here to additional impact situations and newly developed film reading and data reduction techniques have been applied to yield more accurate results.

The results obtained are presented in Figs. 40 through 44 for the five cases where data was obtained. For Case 1, Gehring's framing camera data employing .476 cm diameter spherical projectiles (from Ref. 12) is superimposed for comparison. They agree quite well with the framing camera data obtained in this study for what was termed the "plume minimum". However, the agreement of framing camera data with the flash x-ray data is only qualitative at best. Gehring obtained results out to later times ($t/d > 100$) which indicate that the "plume minimum" exhibits a rebound behavior of some five to ten percent. In the case of this very soft and ductile 1100-0 aluminum target, the "plume minimum" seems to represent the outside diameter of the crater lips -- an exact correlation with the history of the inside crater diameter need not occur.

For the hardest material studied, Case 8, 7075-T6 aluminum, shown in Fig. 44, the framing camera data extends to relatively late times when equilibrium values have been achieved. Here there is no evidence of any rebound phenomena. Also the correlation between framing camera and x-radiographic records of crater growth is quite poor. In this hard alloy, the crater lips actually fracture and are ejected away from the target at late time although this does not seem to complicate the interpretation of the framing camera

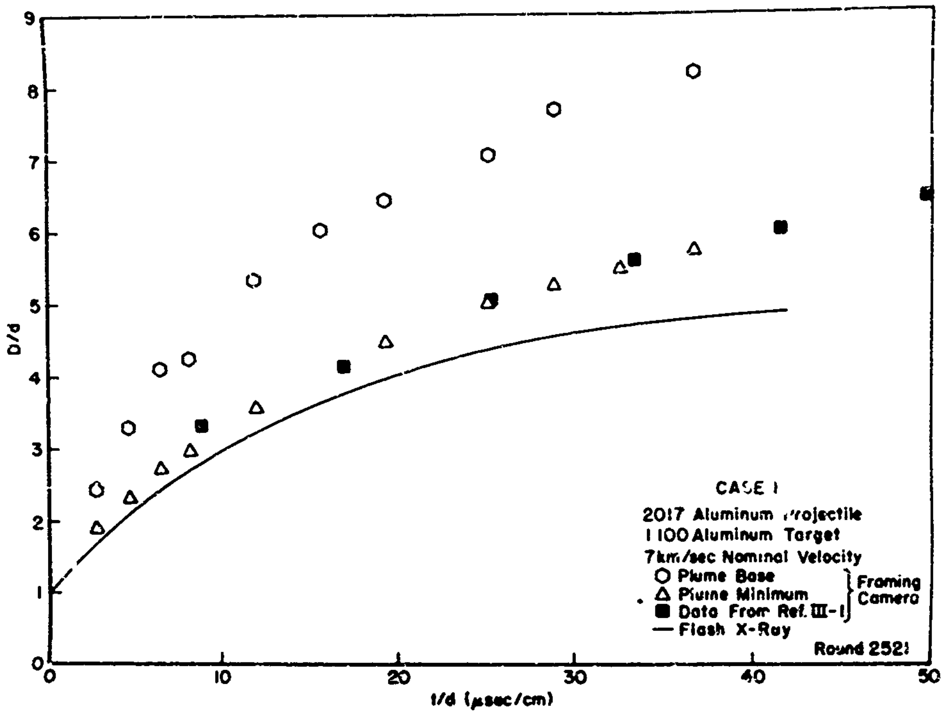

Fig. 40. Comparison of Framing Camera and Flash X-Ray Data on Crater Growth -- Case 1.

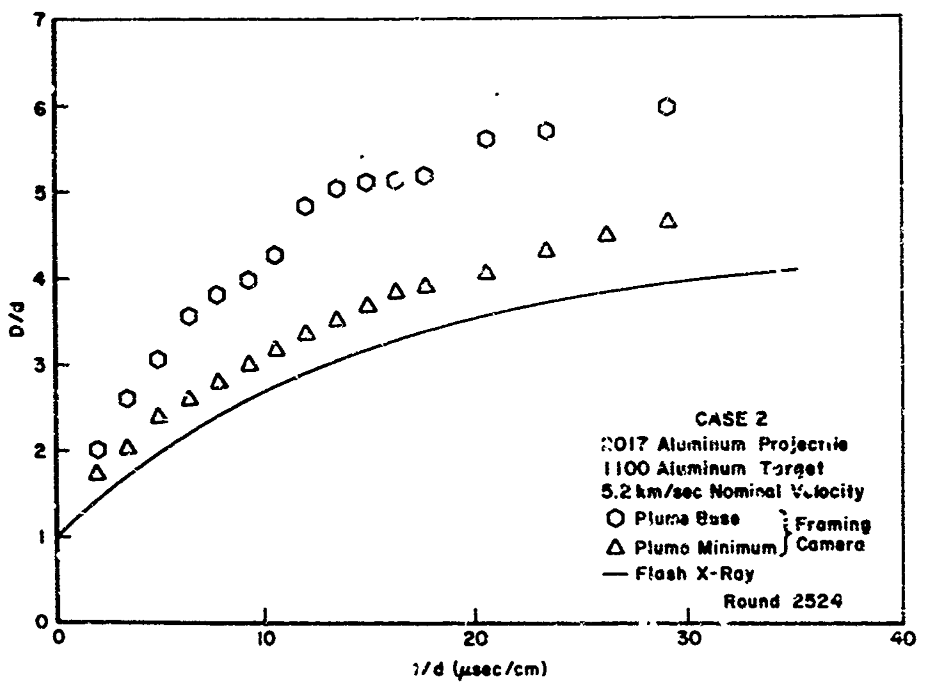

Fig. 41. Comparison of Framing Camera and Flash X-Ray Data on Crater Growth -- Case 2.

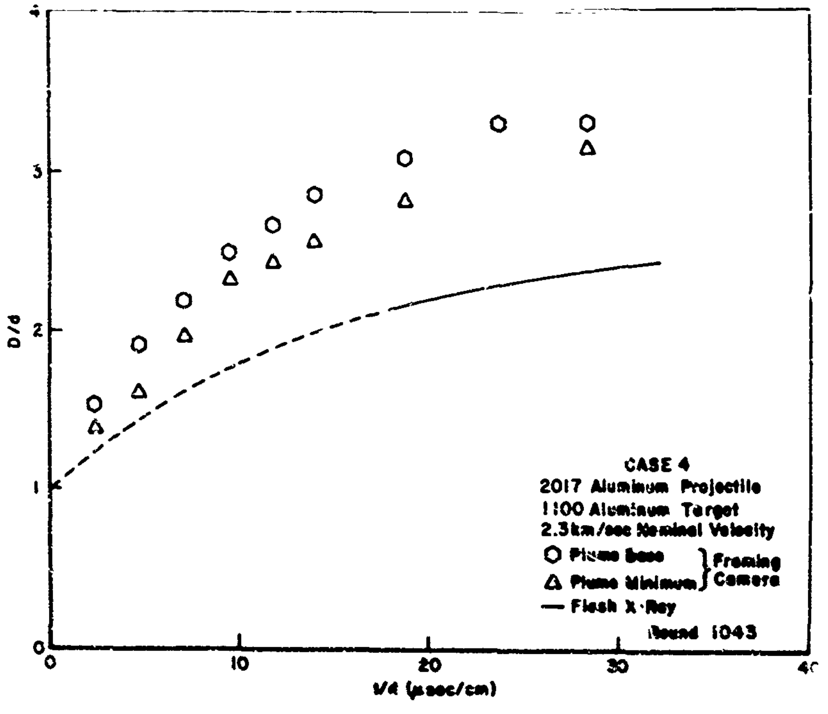

Fig. 42. Comparison of Framing Camera and Flash X-Ray Data on Crater Growth -- Case 4.

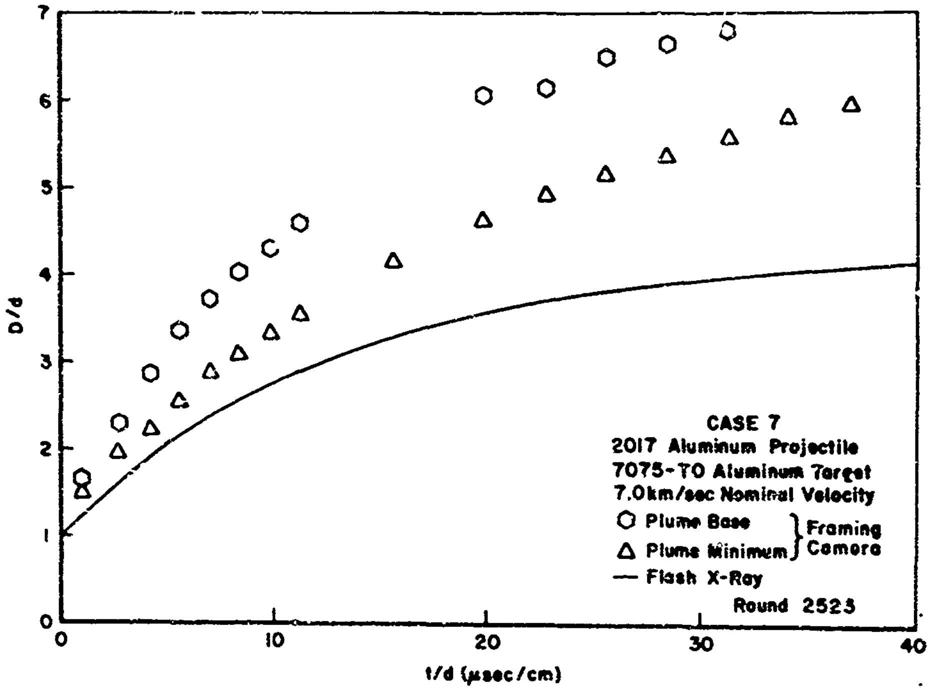

Fig. 43. Comparison of Framing Camera and Flash X-Ray Data on Crater Growth -- Case 7.

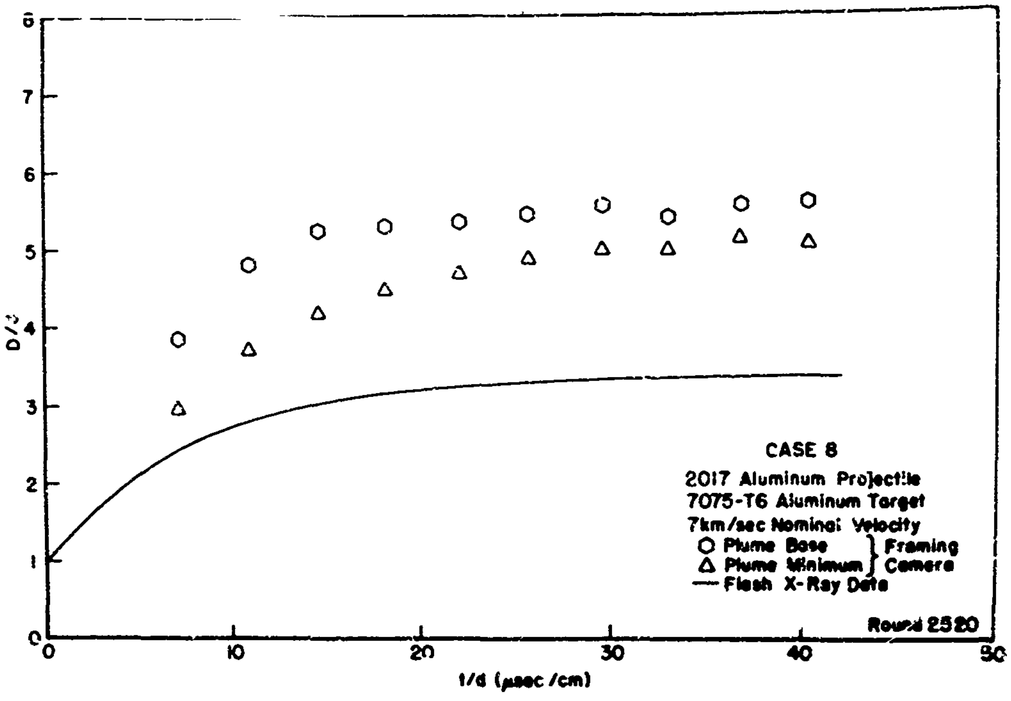

Fig. 44. Comparison of Framing Camera and Flash X-Ray Data on Crater Growth -- Case 8.

records.

The remaining data presents essentially the same picture; it is possible to obtain good records of the growth of the front surface plume, but the correlation of this data with crater growth data obtained using flash x-rays is only qualitative at best. The measurements of the "plume base", that is the diameter of the region of deformation on the target surface, show roughly the expected behavior, but little correlation with the crater diameter. There is not much likelyhood that any quantitative information regarding crater diameters can be obtained from measurements of the plume base.

The ag eement between the framing camera data on the plume and the flash x-ray data or crater internal diameter may be improved by assuming that both diameters grow according to the exponential law discussed previously with the same time constant τ. The magnitude of the diameter is found from (D/d) final. That is, assume that

$$\left(\frac{D}{d}\right) \quad 1 + a\,(1 - e^{-t/\tau}) \qquad \text{(Eq. 6)}$$

and where the framing camera data takes the form

$$\left(\frac{D}{d}\right)_{\substack{\text{plume}\\\text{diameter}}} \quad 1 + b\,(1 - e^{-t/\tau}) \qquad \text{(Eq. 7)}$$

In these equations the quantity (1 + a) represents the final measured value of D/d for the crater diameter and the quantity (1 + b) represents the very late time value of D/d for the plume minimum which can be obtained from the framing camera record. Eq. 7 is then solved for $e^{-t/\tau}$ and substituted into Eq. 6 to obtain

$$\left(\frac{D}{d}\right)_{adj} = 1 + a\left[\frac{(D/d)\text{ plume diam} - 1}{b}\right] \qquad \text{(Eq. 8)}$$

When adjusted in this manner, the modified results lie within fifteen percent of the value calculated from the curve derived from flash x-ray data. This indicates that, to first order, framing camera records of the plume growth can be used to infer the value of the exponential period τ/d, of the crater. This scaling technique is not completely successful since some minor differences are noted in the shapes of the x-ray and framing camera derived curves. Practical difficulties exist in that some "equilibrium" or nearly final value of the "plume minimum" diameter must be known to apply the scaling. In Cases 2, 4, and 7 this information was not available.

All in all, the determination of crater growth rates from framing camera records leaves much to be desired, although for the aluminum alloys used here, this approach does yield at least a qualitative picture of the process. Under other conditions or with other materials, the correlation between the plume and crater diameter histories might be very different.

Correlation With Numerical Results

Only in recent years have numerical schemes been available for predicting the behavior of materials subjected to hypervelocity impact where the effects of material strength could be included. In fact, through the last (Seventh) Hypervelocity Impact Symposium in 1965 no such results had been reported although several groups were developing the required techniques at that time.

Computer programs have since become available for handling this type of problem (see Chapter II). Due largely to the expense involved, the number of thick target impact calculations performed has been rather limited. One set of calculations by Rosenblatt (Ref. 32) was commissioned to complement this research study. Results are available at this time on three separate problems, each involving the normal impact of an 0.635 cm diameter aluminum sphere onto a thick aluminum target: (1) 7.0 km/sec projectile velocity, 1100-0 alloy target; (2) 4.0 km/sec projectile velocity, 1100-0 alloy target; and (3) 7.0 km/sec projectile velocity, 7075-T6 alloy target.

The results of an earlier calculation by Rosenblatt (Ref. 41) for the impact of a large aluminum cylinder on a 6061-T6 aluminum target are also available as are two calculations by Dienes (Ref. 40) involving the impact of aluminum spheres onto two targets, 1100-F and 2014-T6 aluminum, at 7.35 km/sec velocity. In each of these cases only limited detail is available. Even though the latter two sets of calculations were not designed to match the experimental conditions reported here, they still yield interesting results and are included, appropriately scaled, for completeness. In the following sections, the portions of the calculations described above that deal with the dimensional history of the crater are compared with experimental results and discussed.

Results of Rosenblatt. The preliminary numerical results obtained by Rosenblatt (Ref. 41) and specifically designed to correlate with the experimental results of Cases 1, 3 and 8 of this study are shown in Figs. 45, 46 and 47 respectively. For comparison purposes, both the experimental points obtained in

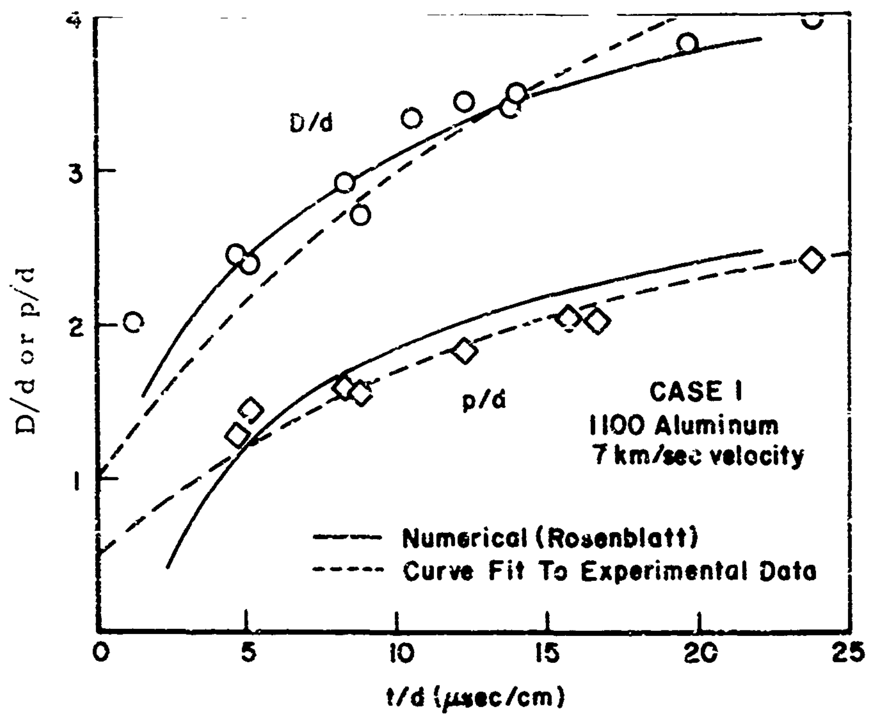

Fig. 45. Comparison of Numerical and Experimental Results on Crater Growth -- Case 1.

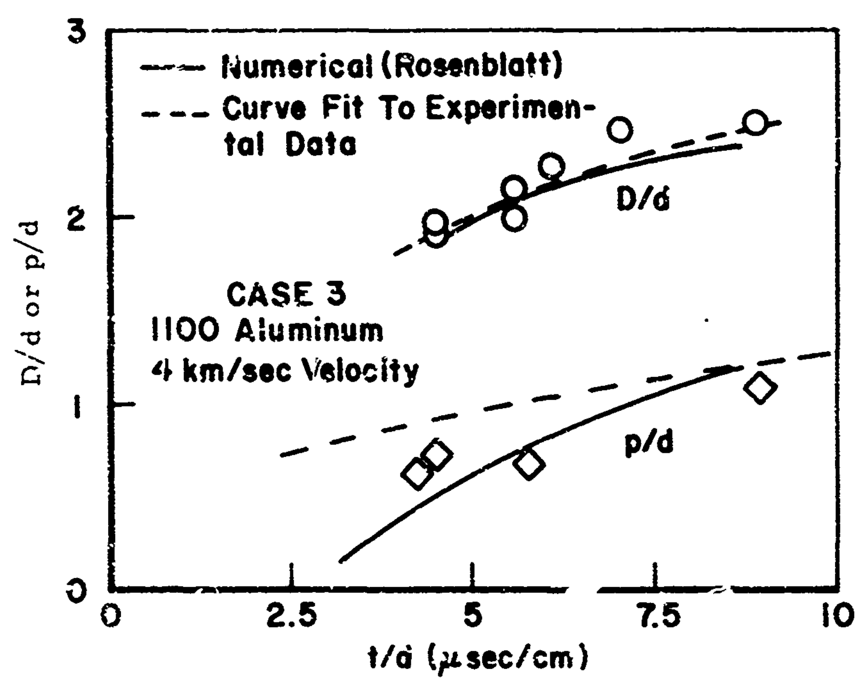

Fig. 46. Comparison of Numerical and Experimental Results on Crater Growth -- Case 3.

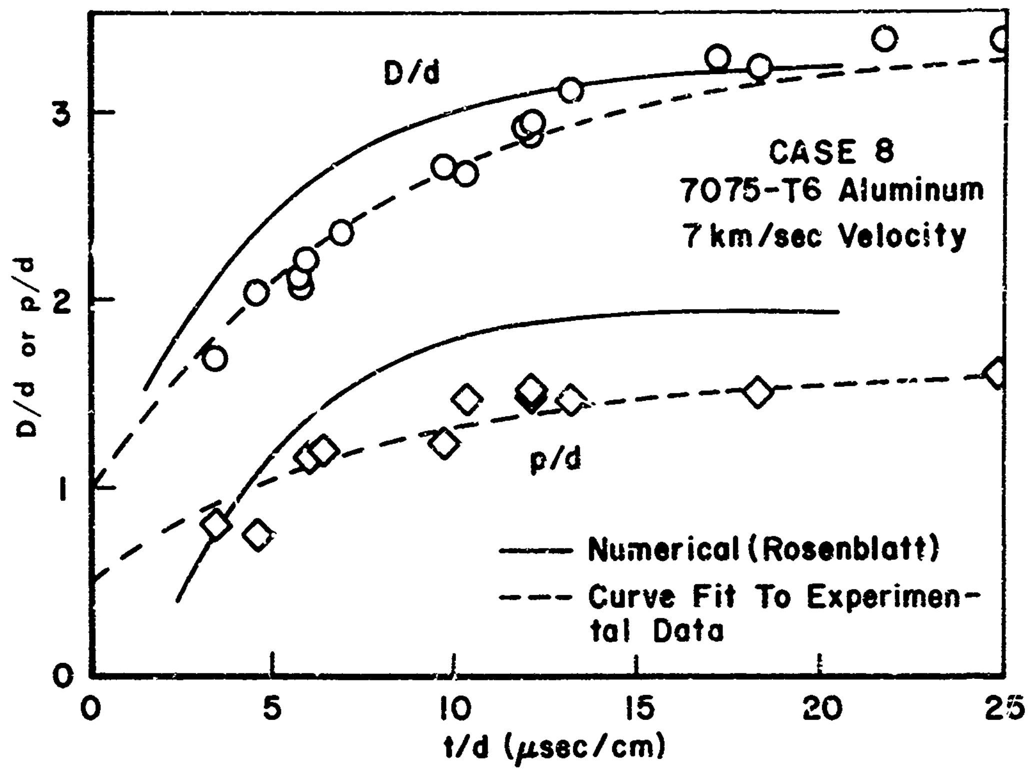

Fig. 47. Comparison of Numerical and Experimental Results on Crater Growth -- Case 8.

this study and the curve fit to this data with an exponential form are shown on these plots -- see Table V.

Note that little claim is made for the accuracy of the curve fit to the experimental data at very early times when $t/d < 4$ since it was very nearly impossible to obtain data during that phase. For Case 1, the agreement in penetration history out to the point where the calculations were terminated is quite good. The divergence at early time may be due to a question of interpretation in the numerical calculations as to what constitutes the bottom of the crater until the projectile is completely consumed.

For the crater diameter, the agreement is considerably poorer, although that is not immediately obvious from the few data points shown. The dashed line is in fact, better because it is derived from data that extends to much later times but which is not shown. The final value of D/d for Case 1 is 5.20 experimentally and even though craters in 1100-0 aluminum continue to grow for a very long time ($t/d > 60$) the trend is clear -- the numerical calculation for D/d will likely not agree with the correct final value as evidenced by the slope of the growth lines at $t/d = 15$, and certainly the growth exponential period will not be correct.

In the region of the crater lips and sides, there is considerable plastic flow and hence a great deal of plastic work with resultant material heating. It is possible that this failure to predict the correct history of the crater diameter is due to a poor model for thermal softening in the computer program. Since little is known about thermal softening (variation in yield strength with temperature) under these shock loading conditions, a simple model of the variation was used in the calculations. It was assumed that the yield strength, Y, varied linearly with temperature between Y_o at room temperature and zero at the melting temperature of the material. Calculations by Rosenblatt with a modified thermal softening model failed to confirm this explanation of the incorrect prediction of late time crater diameter history. It may be that the thermal softening properties of 1100-0 aluminum are more non-linear than had been expected or that some other processes are affecting the calculations.

At lower projectile velocity (Case 3, Fig. 47) the experimental data is less complete, but the trends are about the same. In the region $4 < t/d < 8$ the agreement between numerical calculations and experimental points is quite good. For these conditions, crater growth continues to as late as $t/d = 60-70$. Consequently, it is difficult to tell from the available information whether crater final dimensions will be predicted correctly.

In each of these calculations in 1100-0 aluminum it would have been better to carry the calculation to the point where crater growth was essentially complete. However, lack of funds dictated that the calculations be terminated as soon as the information on shock wave propagation required for the second phase of this effort was obtained.

The 7075-T6 aluminum alloy has such a high strength that the crater growth terminates relatively quickly as evidenced in Fig. 47. In this case, the numerical calculations were carried nearly to the point of completion of the crater growth. The prediction of the final crater diameter of D/d = 3.25 compared with the experimental value of D/d = 3.38 is excellent. In fact the complete history of the crater diameter is good although there seems to be a slight tendency for the code to overestimate the diameter in the region 5 < t/d < 15. Several explanations are plausible, including the possibility that the calculations are underestimating the effects of strain rate or viscosity at early times. In any event, the difference is rather small (< 10%) and is undoubtedly due in part to the lack of accurate knowledge about the properties of the target material.

The experimental penetration data need explanation. The 7075-T6 alloy is so brittle that the entire region of the crater displays fracture phenomena after the impact event. A typical crater produced in this series is illustrated in Fig. 48. The crater lips are completely spalled and ejected from the target. Likewise the sides and bottom of the crater are rough and jagged. Inside the crater, the degree of surface roughness is typically two millimeters or so for craters produced by 0.635 cm diameter aluminum spheres impacted at 7 km/sec.

After the impact, any measurement of final crater diameter by conventional means is meaningless since the whole lip region has spalled away. In contrast, the flash x-radiographs of craters in this material, even those taken after the impact, show a smooth wall appearance -- obviously the result of "averaging" the mass in the fractured region of the crater walls. Consequently, the final crater diameter D/d = 3.38 used to obtain a fit to the experimental data (Table V) was obtained by direct measurement of the final crater diameter in x-radiographs with the target diameter as a dimensional reference.

The same procedure was followed in obtaining the final p/d = 1.63 used in Table V. In this case independent measurements of final crater depth are possible (Appendix A) and yield the average value p/d = 1.87. For

Fig. 48. Crater in 7075-T6 Aluminum Alloy
Illustrating Fracture Phenomena.

these measurements, depths are measured to the deepest portion of the crater bottom -- hence the difference in p/d of 0.24 (1.5 mm for the .635 cm diameter projectile) obtained from these two techniques is apparently due to the large fracture zone created in this alloy.

In view of these results, the history of crater depth in 7075-T6 aluminum predicted by numerical techniques and shown in Fig. 47 may not be as bad as it appears at first glance. It is likely that the x-radiographic data are related to the upper surface of the fracture zone on the crater floor while the numerical technique is predicting the deepest portion. The final value of p/d 1.95 predicted numerically agrees quite well with measured results.

Another interesting result of these calculations is the history of the ratio of crater penetration to crater diameter illustrated in Fig. 49. Again the dashed line indicates how the crater would grow if it were perfectly hemispherical at all times. In the region $D/d > 2.5$, the results for 1100-0

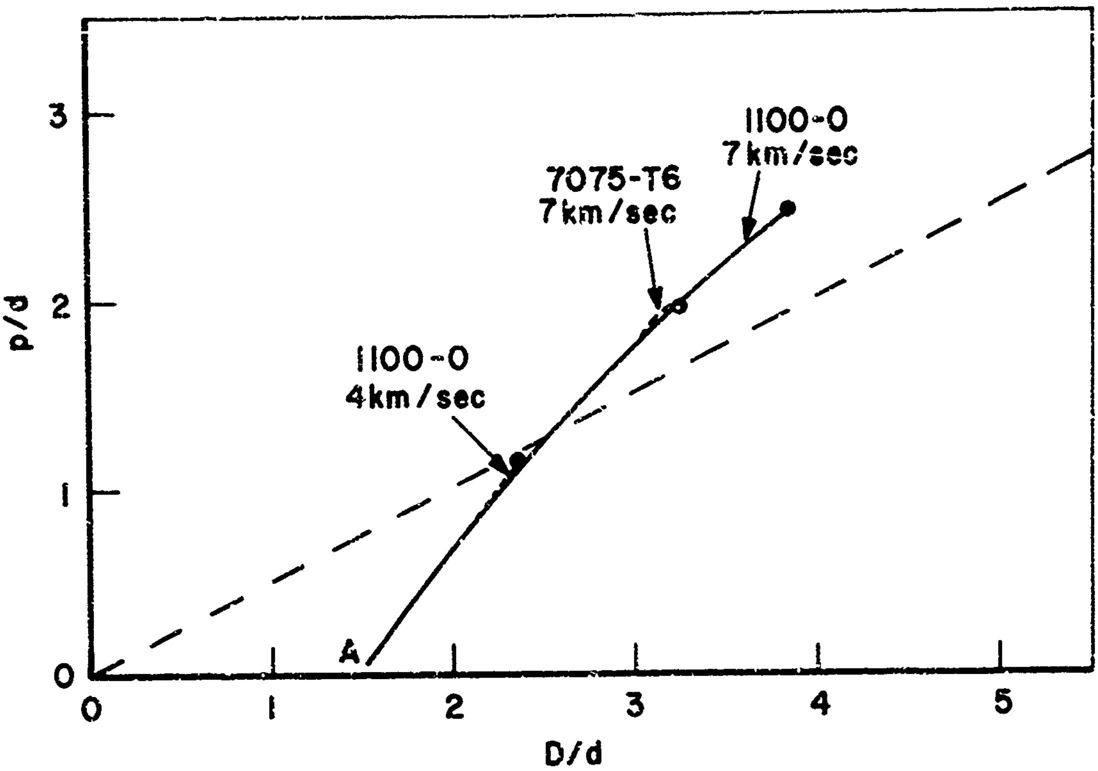

Fig. 49. History of Crater Penetration to Diameter Ratio -- Numerical Results of Rosenblatt.

aluminum agree rather well with the experimental data (see Figs. 35 and 36). The results for 7075-T6 aluminum display some minor lack of agreement, again probably related to the fracture zone in this hard alloy.

All in all, the numerical results of Rosenblatt show relatively good agreement with the experimental crater growth data with a few exceptions. In the softer aluminum there appears to be a tendency to predict crater diameters that are too small at late times. Although it is perhaps naive to generalize from the data available, there seems to be a tendency for the computer results to yield crater growth rates that are somewhat too high at early times ($t/d < 5$).

Other Numerical Results. In Ref. 40 Dienes presents the results of two hypervelocity impact calculations performed with a strength version of the OIL code, a two dimensional Eulerian formulation that included perfectly plastic and viscous effects. The calculations involved the normal impact of 0.4763 cm diameter spheres at a velocity of 7.35 km/sec onto 1100-F and

2014-T6 aluminum targets with yield strength corresponding to 0.75 kilobars and 2.39 kilobars respectively. The results are presented in Fig. 50. The experimental data obtained in this study is represented by the solid lines. The final crater size for several alloys is also shown.

The crater growth (penetration) Dienes obtained for the 1100-F aluminum agrees well in shape but not in magnitude with the data of this study. The material reported by Dienes has a yield strength larger than the 0.26 kb of the annealed 1100-0 alloy used here, yet he reports a larger value of D/d, 3.06, opposed to the value of 2.89 obtained in Appendix A. It appears therefore that Dienes' calculations tend to underestimate the role of the material strength in halting the crater growth by almost 20 percent, i.e., the crater penetration is about one fifth less than that predicted numerically.

The predicted behavior of the 2014-T6 alloy during the roughly hydrodynamic behavior phase, $t/d < 15$, follows the experimental data for the 1100-0 aluminum very closely. The strength of the 2014-T6 alloy is just slightly less than that of the 6061 T6 alloy used in this study, so the general late time behavior of the crater formation is 2014-T6 aluminum predicted by Dienes is still somewhat high.

Finally, the results of one other calculation are available. Rosenblatt (Ref. 41) calculated the normal impact of an 8 cm diameter by 8 cm high right circular cylinder of 6061-T6 aluminum upon a thick target of like material. The projectile velocity was 7.35 km/sec. The diameter of an equivalent mass sphere was used to scale this data which is shown in Fig. 51. Again the general agreement with experimental data is relatively good except for the region $t/d < 5$. The effects of the difference in projectile shape seem quite trivial for this situation.

<u>Summary</u>

Flash x-ray techniques have been used to obtain experimental measurements of the growth of craters in aluminum targets subjected to hypervelocity

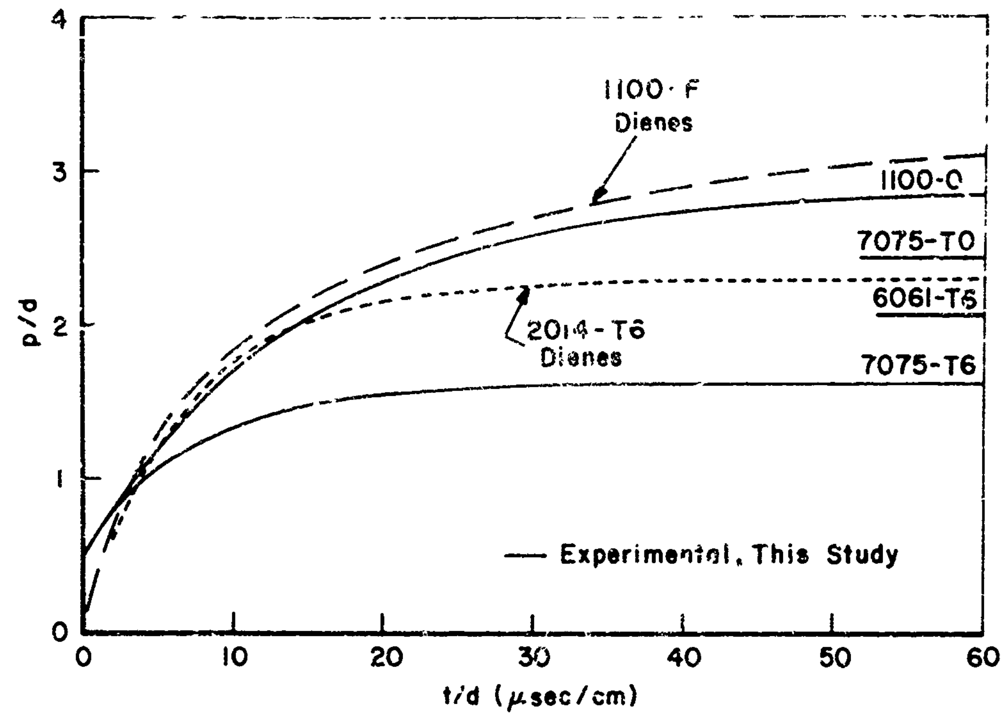

Fig. 50. Comparison of Numerical Results of Crater Growth with Experimental Data.

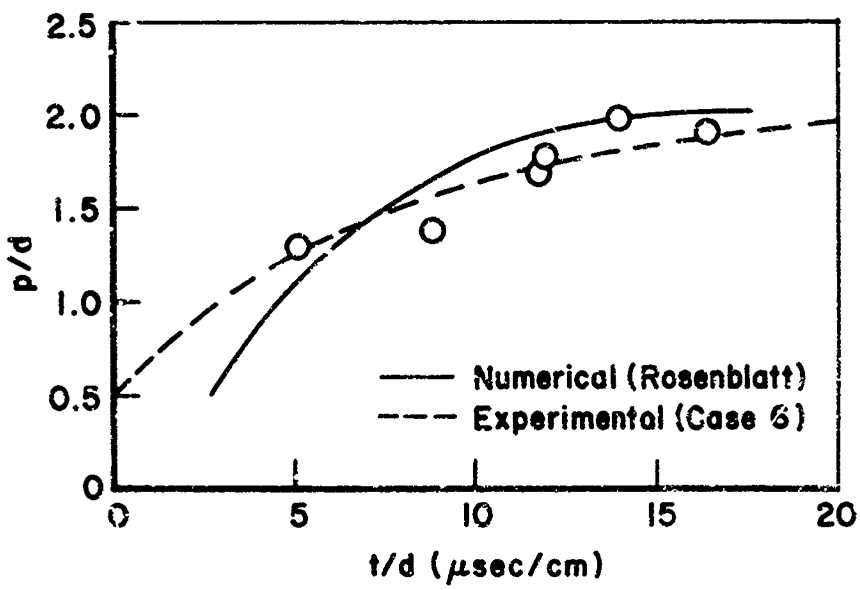

Fig. 51. Calculation of Crater Growth -- Impact of Cylinder on 6061-T6 Aluminum at 7.35 km/sec by Rosenblatt.

impacts. Data on both crater diameter and penetration (depth) were obtained for four alloys of widely varying static strength properties: 1100-0, 6061-T6, 7075-T0, and 7076-T6. In all cases the projectiles were aluminum spheres with velocities of approximately 7 km/sec. Additional data were obtained for 1100-0 aluminum targets impacted by projectiles with velocities of 5.2, 4.2, and 2.3 km/sec. One additional combination, a steel projectile impacting an 1100-0 aluminum target at 5 km/sec was studied to explore crater rebound phenomena. In each case a simple exponential growth law whose coefficients could be related to the projectile size and final crater parameters was found to yield a good fit to the experimental data.

Additional information was obtained in the form of high speed framing camera photographs of the expanding front surface debris plume produced during the impact process for four situations. Measurements were made of the history of the narrowest portion of this plume. When properly scaled, this data yields a rough correlation with the inside crater diameter history as obtained from the flash x-ray studies, but there is no good evidence that plume measurements can be used to obtain reliable measurements of the crater growth histories.

Finally, the experimental crater growth results are compared with the results of several numerical calculations of hypervelocity impact events. The results show generally good agreement between theory and experiment, but point to several areas where the theoretical behavior is in question.

V. Shock Propagation -- Experimental Techniques

While cavitation data is important to the understanding of crater formation in thick metal targets, it represents only a part of the picture. The hypervelocity impact also generates a strong shock wave which propagates into the target. From a practical point of view, studies of impact damage are generally concerned with the effects that take place at material interfaces or the rear of the target, such as spall, debonding, or delamination, depending upon the character of the material. It is the characteristics of the shock wave that determine the mode and extent of this damage.

The initial features of the shock wave are determined by the loading occurring in the region of the growing crater. The shock wave travels outward from that region through virgin material, changing in character as it moves. The shock wave decays in amplitude due to: (1) the roughly spherical divergence from the impact point, (2) release waves generated near the impact region, and (3) attenuation related to the strength properties of the target material. Experimental data on shock propagation variables provide additional understanding of the overall impact processes and valuable information for correlation with theoretical predictions of impact.

For these reasons, the second phase of this study is concerned with experiments designed to obtain data on selected features of the shock wave generated by hypervelocity impact. The remainder of this chapter describes several types of experiments and the techniques used to obtain data.

Experiment Selection

Requirements. In studying the propagation of shock waves created by by hypervelocity impact experiments, the values of the flow quantities at the shock front are of particular interest. These values reflect the effects of all factors involved -- divergence, relaxation, strength -- but involve measurements at only one point as opposed to the measurement of a field quantity. If the Hugoniot curve of the material is known, the measurement of any variable behind the shock front (such as σ_{n_H}, the normal stress; ρ_H, density; u_H, particle velocity; D_H, shock velocity; and e_H, specific internal energy, where the subscript H refers to the Hugoniot values at the shock front) allows calculation of all the others through the Rankine-Hugoniot jump conditions. Likewise, the peak values of such quantities as normal stress generally occur at the shock front and tend to be most accurately predicted by available numerical techniques. It follows that measurement of one of the Hugoniot values is the most useful in studying shock propagation and in comparing theory with experiment.

Early analytical calculations (see Chapter VII) and a variety of two-dimensional numerical calculations have shown that, for a hypervelocity impact normal to a plane surface, the shock wave propagates in a nearly spherical fashion. The results obtained indicate that on the axis (i.e., directly ahead of the projectile) the flow quantities are little affected by the presence of the free surface at the target front. The analysis of most numerical calculations and all experimental measurements heretofore has been restricted to the on-axis case. Clearly as the angle off axis becomes large, the flow quantities will differ greatly from their on-axis values because of the free surface. Since this study is concerned with the two dimensional aspects of the impact problem, it is imperative that measurements be made as a function of angle away from the axis. The problem studied here is restricted to normal impact on a plane surface and the results are assumed to be axisymmetric about the projectile trajectory. There is, consequently, no azimuthal variation in the above quantities. The geometry of the impacts studied and the associated nomenclature are shown in Fig. 52.

In solids, shock wave propagation is a non-linear process. The shock front changes speed as it progresses -- in a way that is related to the peak pressure behind the shock. Consequently, the position history of the shock front, shock radius (R_s) versus time (t), known as the shock trajectory is a useful experimental quantity since it contains much of the history of the shock propagation. Unfortunately, the behavior of most solids is such that the shock trajectory is a less sensitive

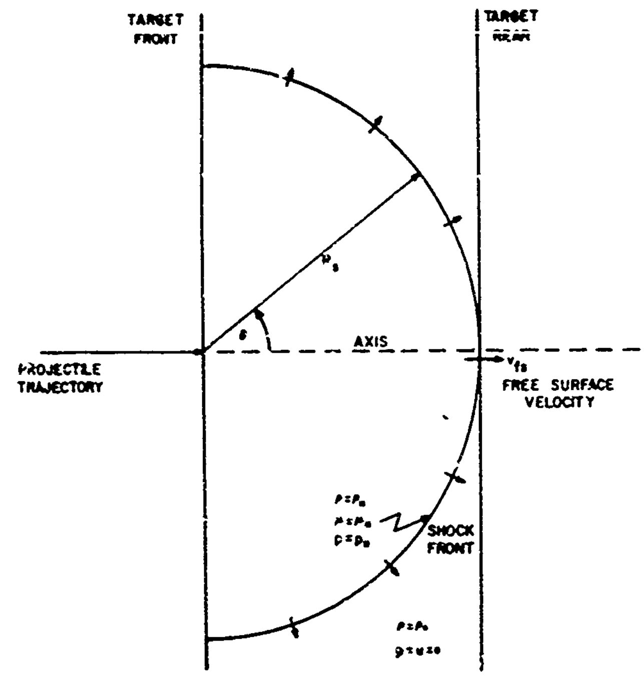

Fig. 52. Impact Generated Shock Wave Propagation in Solid Target.

measure of the flow variables than is, say, the peak normal stress.

The number of rounds fired in any study must be restricted because the light gas gun range is expensive to operate. Measurement of a quantity at a variety of distances from impact, at several angles, and for several target materials could quickly become prohibitive unless care were taken in the experiment design. Experience has also indicated that it is highly desirable to obtain enough data points that behavior trends can be established statistically. Consequently, it is essential that each experiment be designed to yield multiple data points.

In summary, the objective of this phase of the experimental program was to obtain direct measurements of at least one of the shock variables directly behind the shock wave (Hugoniot value) as a function of distance from the impact point (R_s) and the angle off trajectory (θ). A secondary objective was to obtain direct measurements of the shock trajectory. A normal impact and axial symmetry about the projectile trajectory were assumed.

Techniques. Many techniques have been developed for measuring the flow properties during shock wave propagation in one-dimensional (flat plate) experiments. The existence of the curved wavefront and tangential stresses in the hypervelocity impact problem makes the application of most of these techniques infeasible. Techniques reported in the literature include quartz (piezoelectric) crystal gauges, Manganin wire, capacitance probes, streak camera/reflected wire systems, and velocity interferometers. Each was rejected because the required development was prohibitive.

The method selected requires the measurement of the peak velocity of the target rear surface. It then yields a measure of the material velocity, u_H, behind the shock front based upon the usual free surface approximation for plane waves:

$$v_{fs} \cong 2\, u_H \qquad \text{(Eq. 9)}$$

where v_{fs} is the peak velocity of the free surface. Observation of the free surface velocity at some point on the rear surface of the target then allows a direct calculation of all the material variables behind the shock front through the Rankine-Hugoniot relations and the equation of state.

In many of the experiments conducted, the free surface motion was observed directly with a high speed framing camera and the surface velocity was derived from the framing camera record. In this application, framing cameras lack sufficient accuracy to follow the complete velocity history of the free surface; however, they can yield good data on the final surface velocity when the surface is accelerated to a high velocity quickly and does not then decelerate significantly. At high stresses (above about 70 kb in aluminum) the surface is accelerated to v_{fs} and continues to move at this velocity, fracturing into many small particles. At lower stresses, the residual strength of the material is such that the surface will slow down following its initial acceleration. The technique described above then fails to yield accurate results.

A modified technique based upon work by Hopkinson and described by Rinehart (Ref. 45:78-80) was required for the lower stress regions. This technique simply allows a thin disk of the same material as the target to substitute for the "free surface". An essentially zero strength bond between the disk and target rear surface allows the disk to continue to travel with maximum velocity v_{fs} after the actual rear surface has begun to decelerate. This "fly-off disk", or "momentum trap," technique was first applied to hypervelocity impact problems by Charest (Ref. 13).

Several techniques for measuring the time between impact and the arrival of the shock front at a given point on the target were developed with varying degrees of success. These include a high voltage contact pin, a quartz piezoelectric probe, and an optical fiber cut-off device. This portion of the experiments was considered secondary to the free surface velocity measurements.

Materials. The target materials selected were consistent with the materials used in the crater growth portion of this effort. The experiments were conducted using three alloys of aluminum: 1100-0, 6061-T651, and 7075-T6. These materials should have nearly the same hydrodynamic behavior, but a wide range of strength properties varying from soft and ductile to hard and brittle. (See Table II). The projectiles were again 2017 aluminum spheres, all of .635 cm diameter in this case. The projectile velocity was nominally 7.0 km/sec.

Direct Free Surface Velocity Measurements

As mentioned previously, at sufficiently high stresses, an accurate measure of the material velocity behind the shock front can be obtained by directly monitoring the target free surface velocity at a point. This technique has been used many times for one-dimensional impact studies, although a framing camera is not a common instrument for measuring velocities in this application. Recently Billingsley (Refs. 14 and 15) has applied the technique to the determination of peak on-axis normal stress in aluminum and copper targets. He used flat plates for the targets, varying the plate thickness to obtain the stress (or material velocity) at various radii from the impact point and measured free surface velocity from framing camera photographs.

Split Cylinder Targets. Because of the desire in this study to determine the shock decay as a function of angle off axis it was necessary to use a completely different target geometry. This new design consisted of a cylinder of material cut along the axis of the cylinder. The result is a "split cylinder" or half-cylinder which is then impacted in the center of the flat face. Typical split-cylinders before and after impact are shown in Fig. 53. In all cases the cylinder was quite small so that very good aiming accuracy was required to impact the target near the correct point. Consequently, these experiments were conducted in a small target tank installed just behind the blast tank on the AFML Hypervelocity Ballistic Range; a procedure which allowed the target to be placed much nearer the gun barrel.

The target was mounted in a holder as illustrated in Fig. 54. The front of the holder and the flat side of the target faced the light gas gun muzzle. The holder was mounted directly on the bottom plate of the small target tank for easy access. The sides of the holder were made of transparent plastic and were replaced after each experiment. Lines for film reading reference and magnification determination were placed directly on the plastic. The Beckman and Whitley Model 300 camera used in these experiments was sufficiently far away from the target, about 10 meters, that no parallax corrections were required using this arrangement. The characteristics of the Model 300 camera and associated data reduction techniques are described in Appendix G.

The target was back-lighted using a custom-made spark light source (Ref. 37) that provides a very intense light pulse of controlled duration. In these experiments, the light duration was about 70 μsec, sufficiently short to prevent rewrite on the Model 300 camera film record. A lens placed between the light source and target was used to focus a large fraction of the available light into the camera lens. With this arrangement good results were obtained using Kodak Tri-X film with standard development in Acufine®.

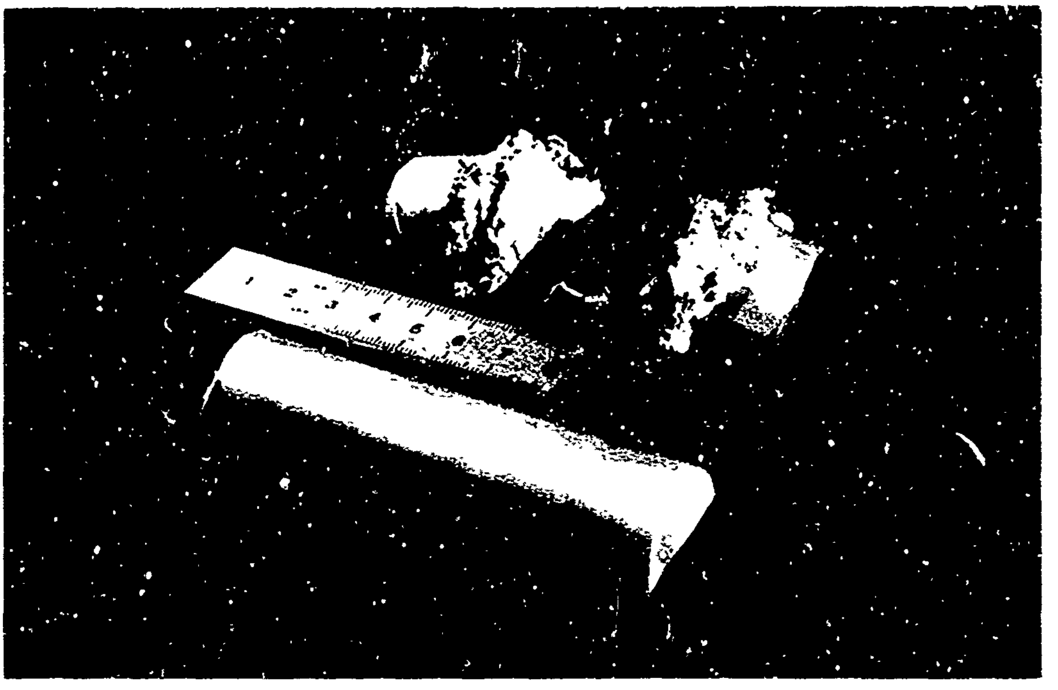

Fig. 53. Typical Split Cylinder Target -- Before and After Impact.

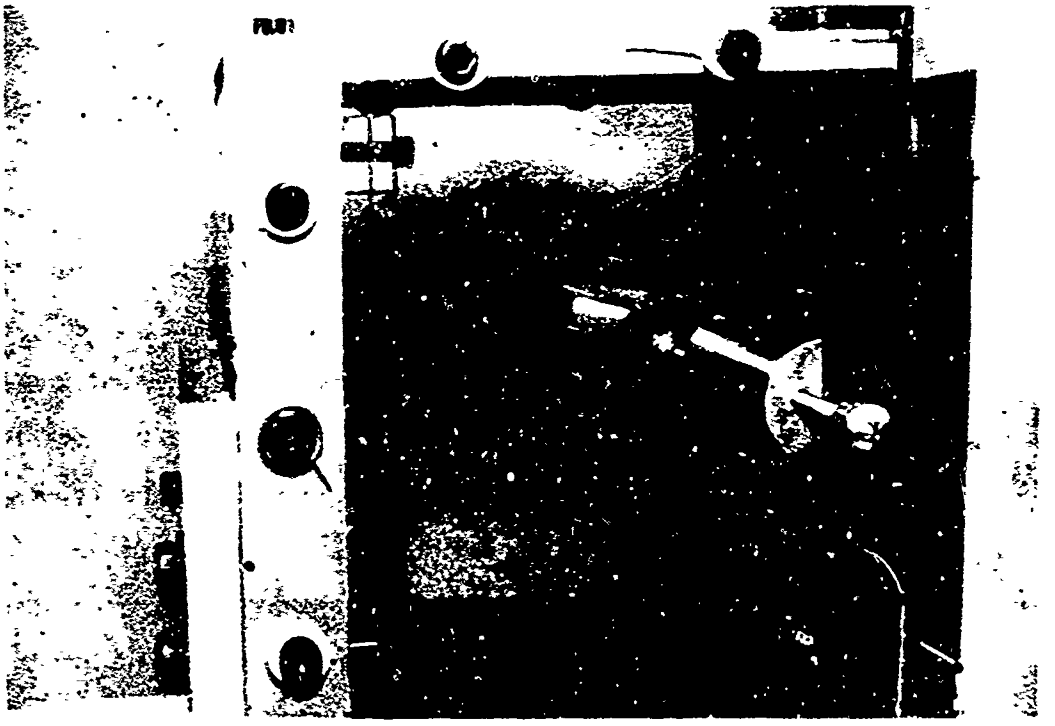

Fig. 54. Holder for Split Cylinder Targets.

The overall layout of this series of experiments is illustrated in Fig. 55. The placement of the target precluded using the normal range system for measuring projectile velocity, so another system was employed. A pair of flash x-rays were taken of the projectile in flight. The time between the x-rays was measured by using an oscilloscope to monitor the trigger signals to each x-ray unit. The distance the projectile traveled between the two x-ray pulses was obtained from the double exposed x-ray film record. This system yielded velocity measurements accurate to about 5%. A thin foil switch (see Chapter III) consisting of two layers of 25 μm aluminum foil separated by a sheet of 50 μm Mylar® was attached to the rear of the sabot stopping plate. The signal derived from this switch when the projectile penetrated it was used to trigger time delay generators which provided signals at the appropriate time to actuate the x-ray sources and to turn the spark light source on. As with the crater growth experiments, all timing was critical since the events of interest were completed in a few tens of microseconds.

In most cases, the Model 300 camera record of the event contained several frames showing the projectile approaching the target. This data was used to obtain another measure of the projectile velocity, again accurate to about 5% (see Appendix G).

Free Surface Trajectory. The film records obtained from the experimental setup described above yielded a silhouette, back-lighted view of the curved target surface. The sequence of photos shown in Fig. 56 is typical of the type of information obtained. The films show the maximum dimension of the expanding surface. Therefore, the point of impact along the axis of the target is unimportant. The accuracy of impact in the vertical direction (perpendicular to the target axis and the projectile trajectory) is quite important, however, since an off-center impact alters the distance from impact to the point upon the rear surface where motion is measured. Likewise, the direction in which a given particle leaves the rear surface is less well defined if the shock wave does not impact the rear surface almost normally. A detailed description of the effects of off-center impacts

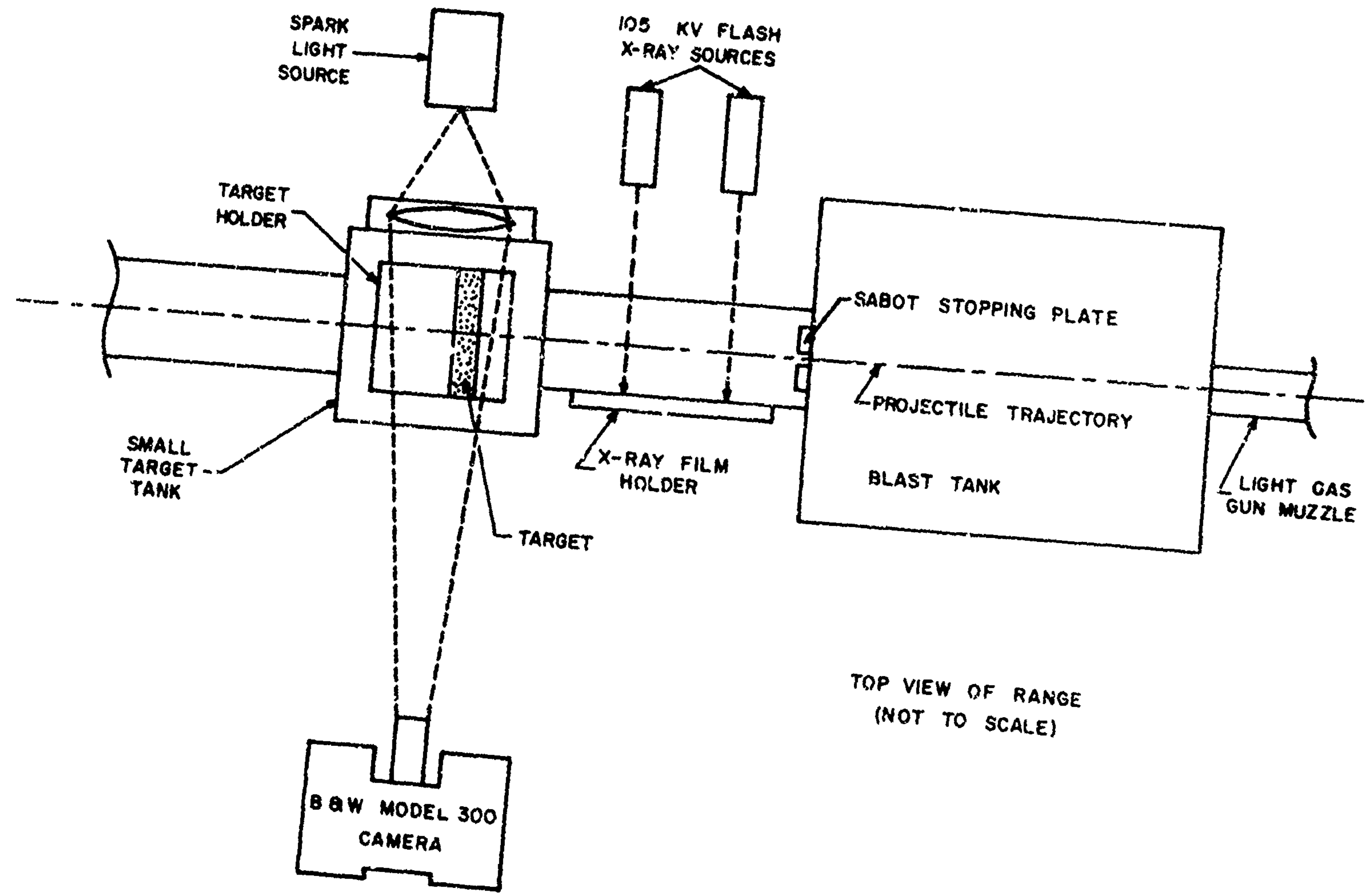

Fig. 55. Arrangement for Free Surface Velocity Experiments.

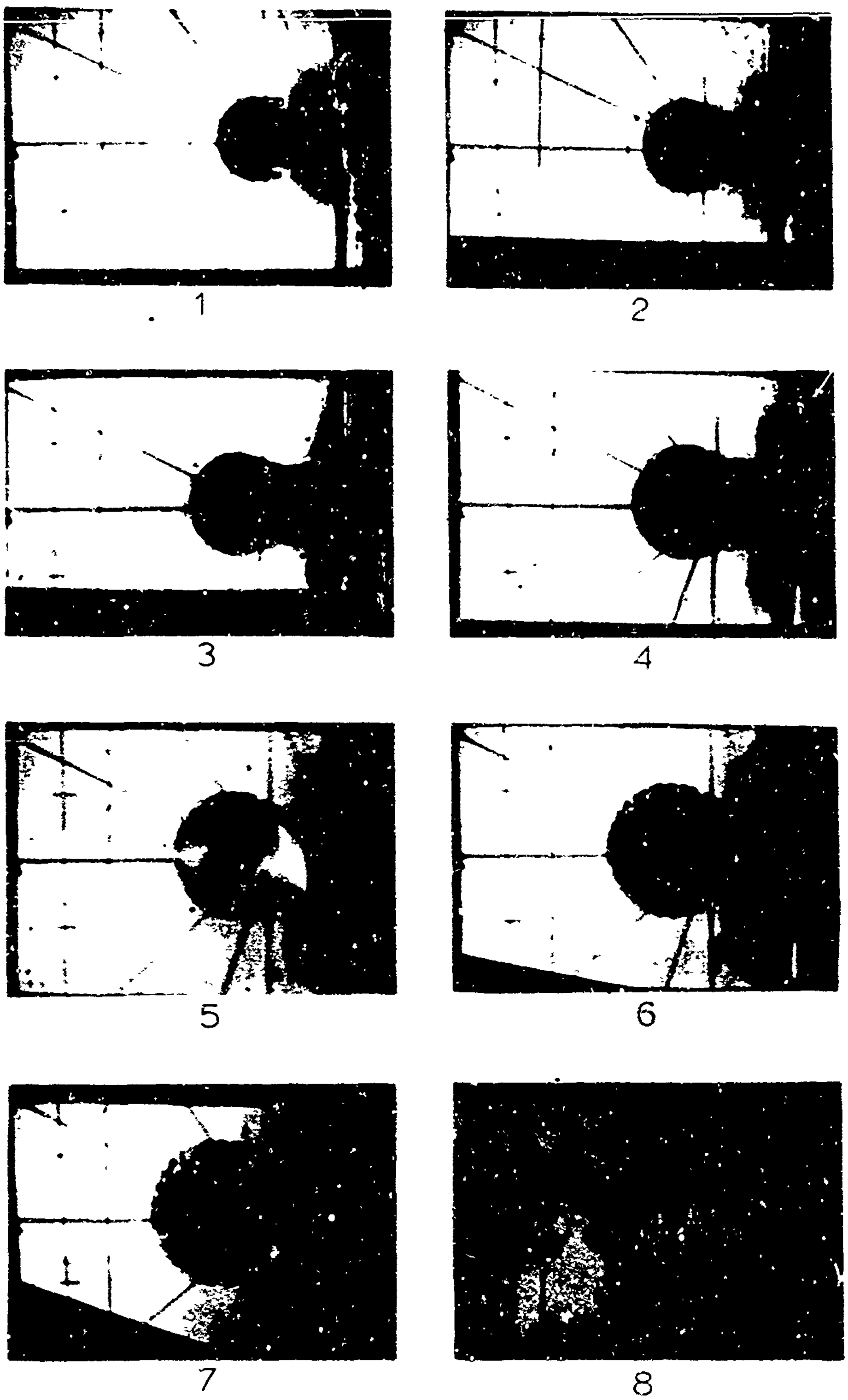

Fig. 56. Round 2772. Expansion of Free Surface Obtained With B & W Model 300 Framing Camera.

and methods for reducing the data from the split cylinder targets are contained in Appendix C.

Briefly, the study of rear surface trajectories for slightly off-center impacts involved placing solid material barriers (rods or wires parallel to the target axis) in the path of the expanding rear surface such that points on the surface were "marked" and their subsequent motion could be determined. This technique is also described in Appendix C and is related to the debris cloud "dissection" techniques developed by Swift et al. (Ref. 46) to study the dynamics of thin plate impact. The results indicate that for relatively well centered impacts, the particle trajectories pass through the axis of the target. Distances from impact to the rear surface (R_s) must, however, be calculated from the actual impact point.

Even though sophisticated techniques have been developed for obtaining and reducing the data from the split cylinder targets, the data still shows some scatter. This is inevitable because these targets are quite small -- ranging in diameter from 2.0 to 3.2 cm -- and the Model 300 camera records can provide position data accurate to only about ± 0.1 cm at the magnification employed under good conditions. On the smaller targets this can result in inaccuracies in measuring the impact to surface distance of as much as 20%. In a small number of cases, for shock radii of less than 1.25 centimeter, flat plate targets were employed in a setup like that described above. Measurement of the leading edge velocity of the expanding rear surface then yielded a single value for free surface velocity <u>on axis</u> only.

The methods described above have resulted in a relatively accurate technique for measuring free surface velocities as a function of both shock radius and angle off trajectory for those cases where the peak of the stress pulse reaching at the rear surface unequivocably exceeded the dynamic yield strength of the material. At lower stress levels, other techniques must be employed as described below.

Fly-off Disk Technique

The primary technique used for measuring peak shock wave properties at various points in the target was the fly-off disk technique mentioned earlier. All measurements made in the region of pressures or stresses where material strengths might affect the processes were obtained with this technique. The basic theory of operation of a fly-off disk is explained in Appendix D which also includes a discussion of the validity of the free surface approximation, $v_{fs} \approx 2\,u$, the effects of the stress wave amplitude, shape, and duration on disk performance, and the Hugoniot data necessary to derive the material properties behind the shock front from the disk velocity.

Technique Evaluation Experiments. The initial effort was devoted to a short development program to optimize experimental techniques and applications of instrumentation and to explore the factors which might affect fly-off disk performance. A simplified target geometry -- a flat plate -- was employed in a configuration illustrated in Figs. 57 and 58. A row of disks was placed on a vertical line on the target rear surface directly behind the anticipated impact point. The bolt shown in Fig. 57 was used as an alignment and distance reference in reading the photographic record of the experiment. Both framing cameras (described in Appendix G) were used in the development tests, always with the target back-lighted and with a pulsed light source to provide sufficient illumination and prevent rewrite. With the Model 300 camera, the spark light source mentioned before was used. For use with the Dynafax Model 326 camera, a xenon flash tube source (Beckman & Whitney Model 358) provided a nearly constant intensity light pulse of ~2 milliseconds duration. Either light source was triggered by an uprange foil switch activated by projectile penetration. For a description of the framing cameras and techniques used to reduce the data obtained, refer to Appendix G.

The purpose of these development experiments was to investigate: (1) fly-off disk attachment, (2) disk diameter-to-thickness ratio (i.e. edge) effects, (3) disk tumbling, (4) disk thickness effects, (5) projectile velocity scaling, and

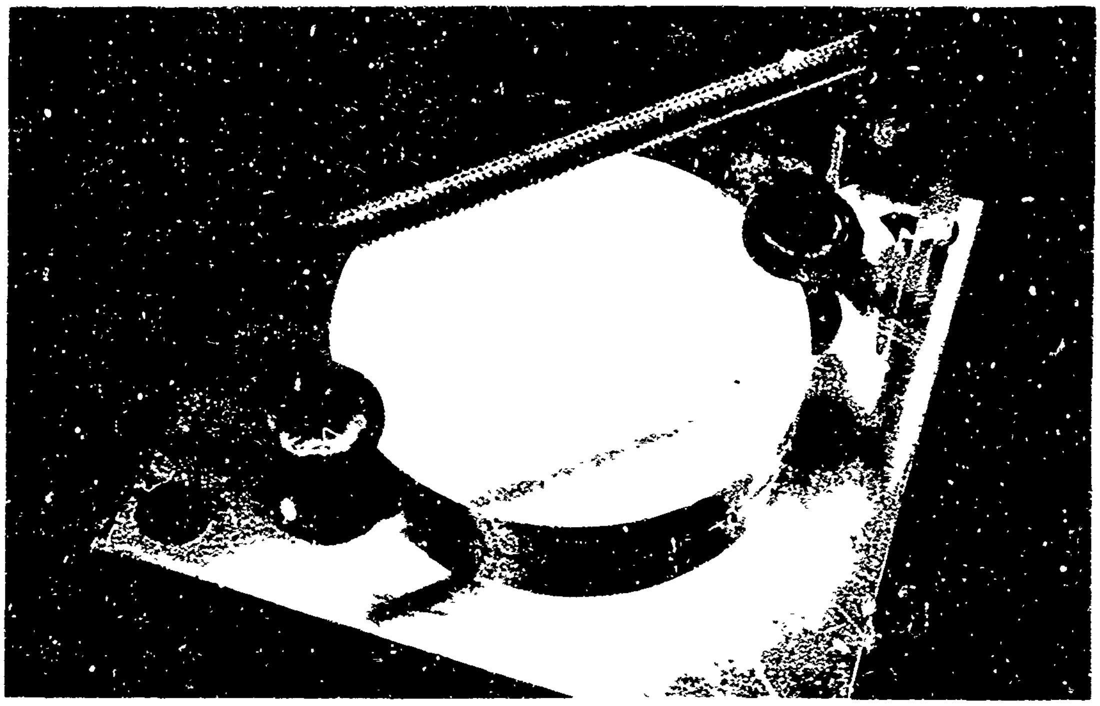

Fig. 57. A Rear View of Flat Plate Target on Holder With Fly-off Disks Attached.

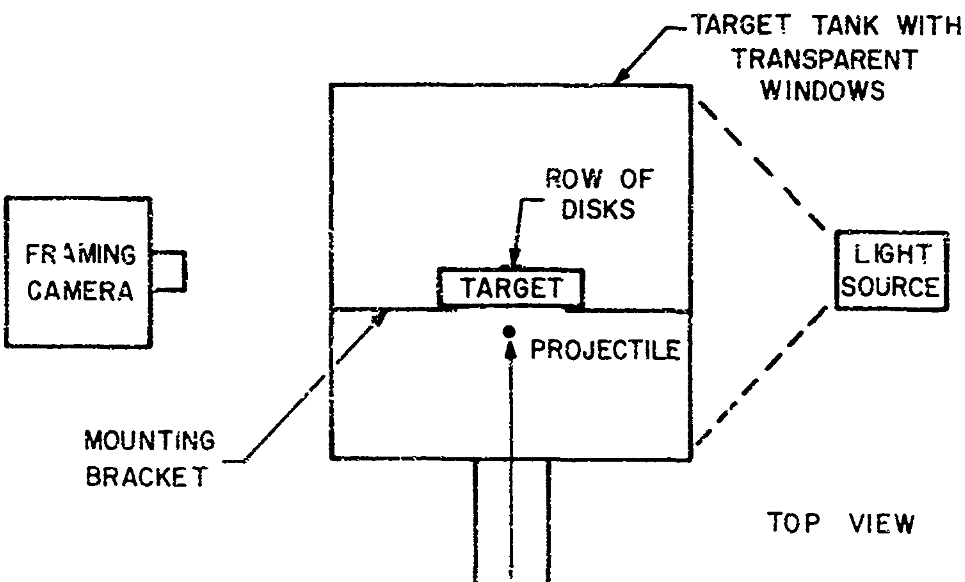

Fig. 58. Diagram of Experimental Arrangement for Fly-off Disk Development Effort.

(6) reproducibility. Due to the geometry, these experiments were not expected to yield velocity data as a function of angle off axis since the leading edge of the shock front did not intersect the rear surface normally. The data was interpreted by comparing the results of separate rounds where parameters were varied. For those disks located on axis, the shock impact is normal to the disk and valid data is produced. The on-axis data obtained in this sequence is included in the data reported in Chapter VI.

A total of ten successful impact events were conducted in this development series. The characteristics of each round fired are described in Table VI. The series successfully demonstrated the application of available instrumentation and the fly-off disk technique to the measurement of shock properties. The raw data from this series has been included in Appendix F for completeness along with several other flat plate impacts described later.

Development Results. The framing camera sequences shown in Figs. 59 and 60 were typical of those obtained in this experimental program. The data obtained from these and other photographs were used to evaluate various aspects of the performance of the fly-off disk technique.

Data taken from Rounds 2619, 2620, 2621, 2639, and 2640 were used to determine the effect of disk thickness on the measured velocity. The results are shown in Fig. 61. The variable r_p, which represents the distance from the projection of the impact point onto the target rear surface out to the location of the disk, yields a measure of both shock radius and angle off trajectory for each point -- consequently it is the comparison of the two curves that is important. The results show that the 600 μm (24 mils) thick disk is measuring reduced velocities -- due possibly to two effects: (1) edge effects created by the larger thickness-to-diameter ratio of the 600 μm disks, and (2) these thick disks may be averaging a rather sharply peaked stress pulse. This data as well as that obtained in Round 2642 (at reduced projectile impact velocity) indicates that 300 μm and 130 μm thick disks yield essentially the same performance to within experimental error. Similar results were obtained using 2.54 cm thick

Table VI

Description of Fly-off Disk Development Rounds

Round No.	Projectile Velocity (km/sec)	Target Thickness (cm)	Camera Model	Number of Disks	Remarks
2587	6.69	4.51	326	5	Exploratory shot
2610	6.56	1.27	300	9	
2614	6.93	2.49	300	11	
2618	7.02	2.54	300	11	Note (1)
2619	7.20	4.42	326	9	
2620	7.03	4.42	326	10	
2621	6.93	4.42	326	10	
2639	7.14	4.45	326	12	
2640	7.07	4.45	326	6	Note (2)
2642	5.42	4.45	326	8	Velocity Scaling

(1) Sabot cap hit target -- data did not appear to be affected.

(2) Included bent flyers to check performance of poor attachment, etc.

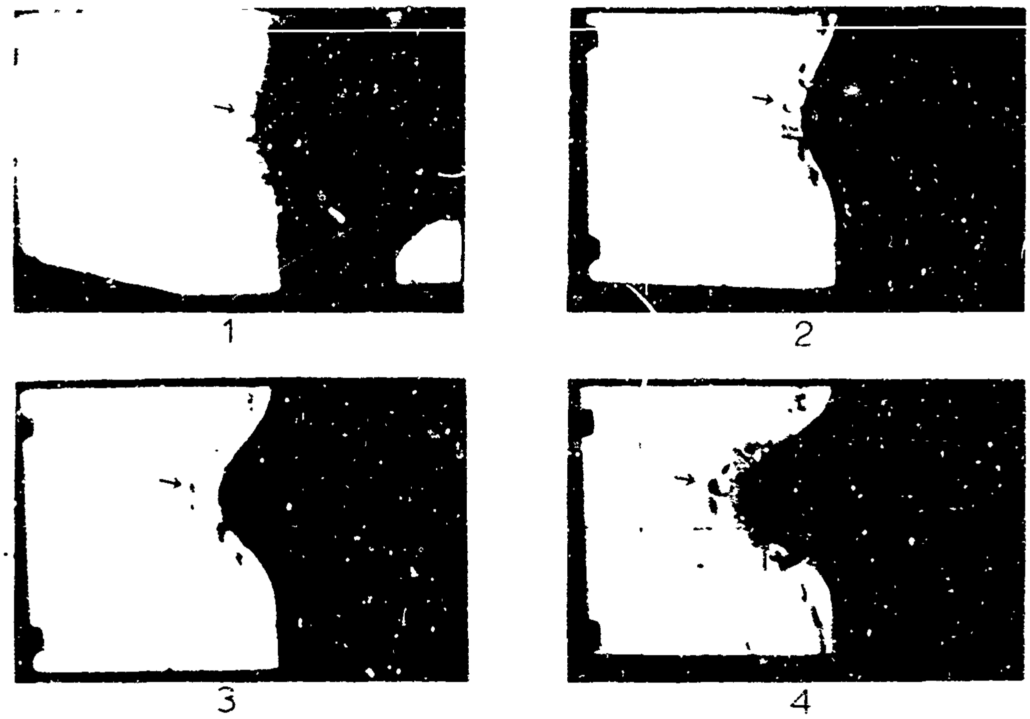

Fig. 59. B & W Model 300 Camera Sequence Fly-off Disk Motion on 2.54 cm Thick Target -- Round 2618.

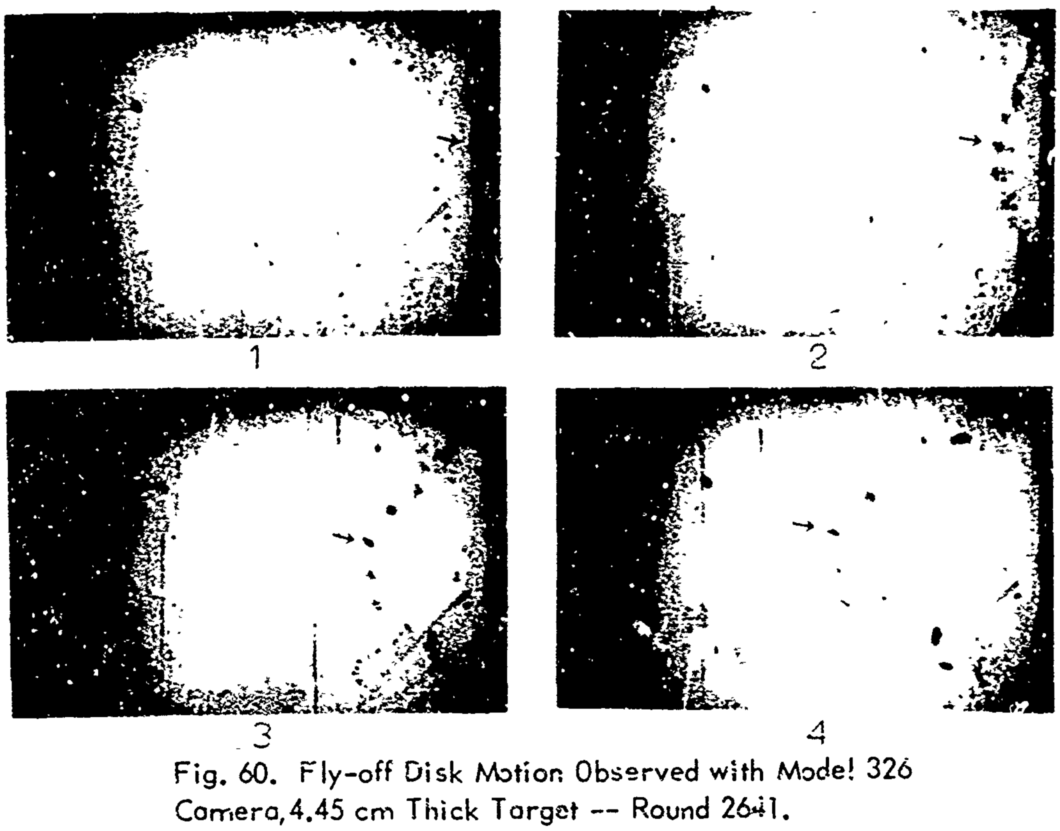

Fig. 60. Fly-off Disk Motion Observed with Model 326 Camera, 4.45 cm Thick Target -- Round 2641.

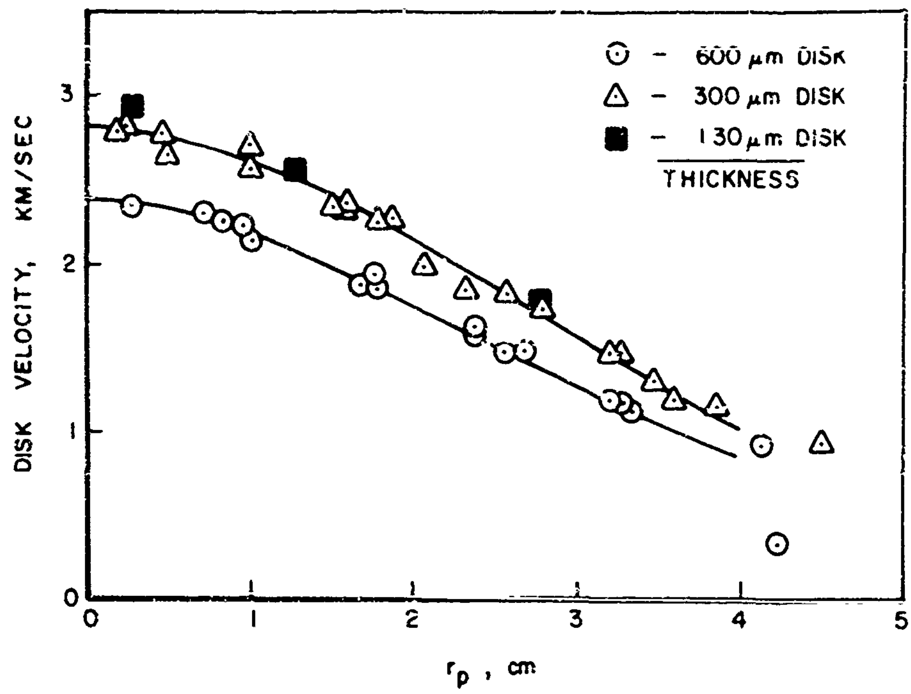

Fig. 61. Comparative Performance of Disks of Three Thicknesses from 4.5 cm Thick Flat Plate Targets Using Dynafax Model 326 Camera.

targets as shown in Fig. 62. In this case the disk velocity data was obtained using the Model 300 framing camera.

Figure 63 shows the effects of using disks with like thickness, but different thickness-to-diameter ratios. For this particular comparison, the data does not indicate a significant difference in performance due to this effect. The somewhat larger scatter in the data is related to the greater difficulties encountered in following the motion of the small .316 cm diameter disks during the film reading.

On these same experiments, two different methods were used to attach the disk to the target: Dow Corning silicon based high vacuum grease and Eastman 910®, a quick setting adhesive with high tensile strength. Over the range of stresses seen in these experiments, the disk performance was unaltered by attachment method.

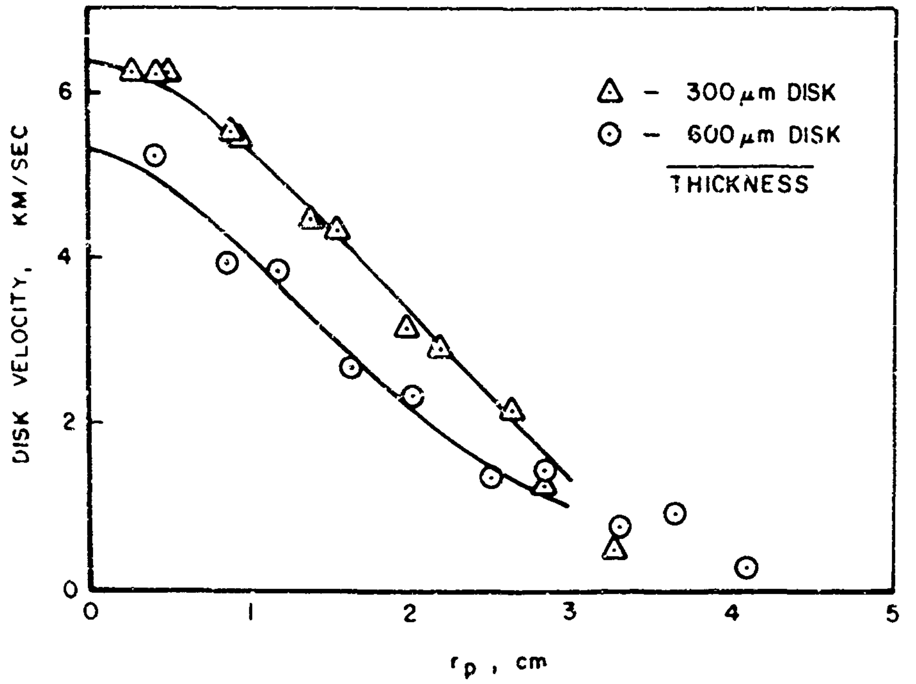

Fig. 62. Comparative Performance of Disks of Two Thicknesses from 2.5 cm Thick Flat Plate Target Using Model 300 Camera.

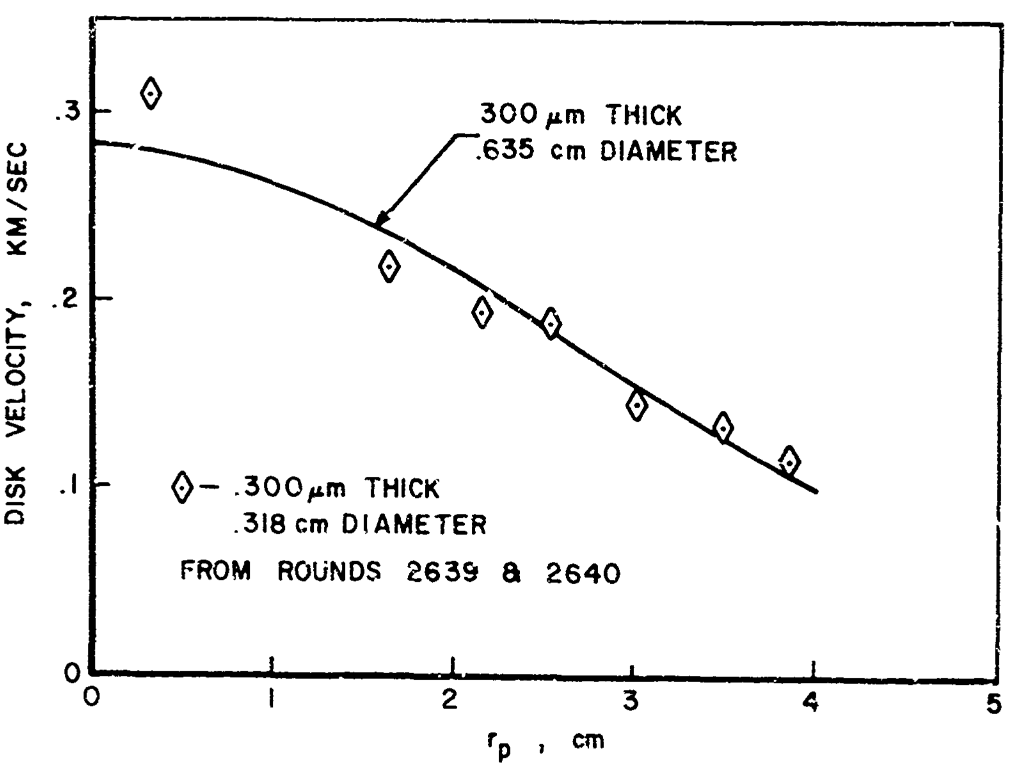

Fig. 63 Comparative Performance of Disks of Two Thickness-to-Diameter Ratios.

A standard fly-off disk configuration was selected for the main experimental program on the basis of the results presented above. The disk size selected was .635 cm in diameter and 250 μm (10 mils) thick since the development program proved the performance of this size and also showed that smaller disks were difficult to follow in the film records in some cases These experiments also demonstrated that the results were reproducible from round to round with a scatter of a few per cent. The vacuum seal grease was used exclusively in the remainder of the program, providing a bond of essentially zero strength.

Tumbling of the disks was observed in some of the experiments, particularly where the shock wave interacted with the disk at high angle. The maximum tumbling rate observed was 6000 radians per second. In that case the energy stored in the form of rotation was equivalent to the translational kinetic energy corresponding to a disk moving at ~10 meters/sec. Rotation rates of this magnitude were observed only when the disk velocity was relatively high (>150 meters/second) so that the error introduced by tumbling could amount to only a few per cent as an upper bound. In practice, the tumbling observed in later experiments on multi-faceted targets was much lower -- more than an order of magnitude less than that described above -- such that the effect on the measured disk velocity was negligible.

Comments regarding the scaling of the fly-off disk results with projectile velocity and on the effect of the angle of incidence of the shock wave with the disk upon its performance are contained in Appendix E.

The development experiments resulted in confidence in the fly-off disk technique and well controlled procedures -- both in the experiment and in the data reduction -- for application of this technique to the main experimental program that followed.

Shock Arrival Time Measurement Techniques

The second portion of this phase of the experimental effort involved measurement of the arrival time of the impact generated shock wave at selected distances from the impact point. The collection of data at various depths yields the relation between the shock radius, R_s, and the time, t, known as the "shock trajectory". As with the other shock property measurements, it was desirable to measure the shock trajectory as a function of angle off axis. The shock trajectory is an interesting quantity since it is one of the fundamental relations predicted by certain theoretical treatments of hypervelocity impact processes. Consequently an accurate measure of shock trajectory helps to verify the theoretical predictions. Since the shock trajectory is related to the variation in shock speed, it is not as sensitive a measure of the shock propagation as is the material velocity or shock stress.

To be useful, it was necessary to measure the time between impact and shock arrival to an accuracy of a few tenths of a microsecond. In addition, it was necessary to be prepared for the existence of an elastic precursor for stresses below 100 kilobars in some of the materials used, and to insure that the time of arrival of the plastic front was recorded. Furthermore, it was essential that the method used be relatively inexpensive since many measurements were contemplated. As a result, two techniques were developed and used -- a high voltage discharge switch employed in the high stress regime and a piezoelectric probe used for the lower stress experiments. Exploratory research was performed on a third, optical technique.

Pin Probes. The primary range timing instrumentation used a Fastax® streaking camera to record optical signals derived from high voltage discharges through small xenon flash tubes. Other applications of this timing system have already been discussed in Chapter III and Ref. 35:18-19. In this application, the target was electrically grounded and an electrode (a "pin") was placed against the rear surface, but separated from it by a 127 μm (5 mil) thick sheet of Mylar® insulation, at the point where the shock wave arrival time was to be monitored. The pin and target were then connected to a pulse forming network and power supply which placed a potential of some 500 volts between the pin and target. Shock wave arrival at the rear surface moved this surface, puncturing the Mylar®

and causing an electrical discharge between the pin and the target. The fast rise time signal produced was then monitored on an oscilloscope and, as a redundant measurement, with the range Fastax® system. The target impact signal was obtained from a foil switch attached directly to the target face (as described for the x-ray experiments in Chapter III). This signal was recorded on the range Fastax® system and was used to trigger the scopes used to monitor pin probe signals.

At high stresses, the rear surface moves at velocities of roughly 0.1 cm/ μ sec and the rear surface will contact the pin within less than 0.05 μ sec after the shock wave reaches the rear surface. Likewise the rise time of the pulse generated by the pin circuit is less than 0.1 μsec. The impact switch measured impact to an accuracy of ± 0.05 μ sec as indicated in Chapter III. The net result is that this system is capable of measuring shock time-of-arrivals to an estimated accuracy of less than 0.2 μsec not counting whatever errors might be introduced in the recording apparatus.

At lower stresses, two potential problems arise: (1) the wave may exhibit an elastic precursor which could cause the pin switch to close early, and (2) the Mylar® insulation will offer mechanical resistance to the movement of the target surface thereby slowing the time response of the system and destroying its accuracy. The application of this design was therefore restricted to those experiments where the expected stresses were above approximately 50 kilobars.

The design of the probes is illustrated in Figs. 64 and 65. They were manufactured from cloth phenolic and designed such that the pin was held against the Mylar® insulation by a spring. The head of the "pin" was relatively sharp to ensure clean penetration of the Mylar®. The pin probe was attached to the target with Eastman 910® adhesive. The block diagram of the discharge pin measuring system for shock wave arrival time is shown in Fig. 66.

Piezoelectric Arrival Time Sensor. A shock wave arrival time sensor operating upon the piezoelectric effect in quartz was developed for application at lower pressures (Ref. 47). The probe is a simple, inexpensive, and easily

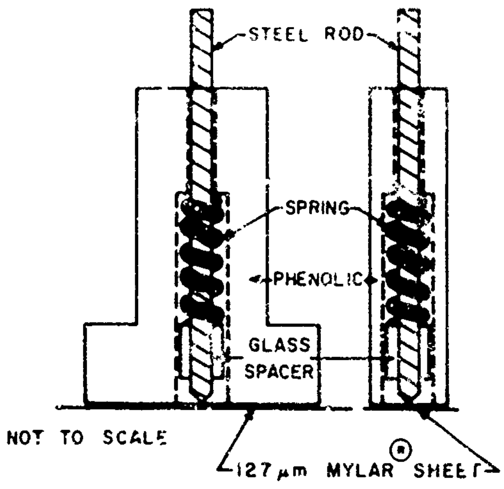

Fig. 64. Design of Pin Probes.

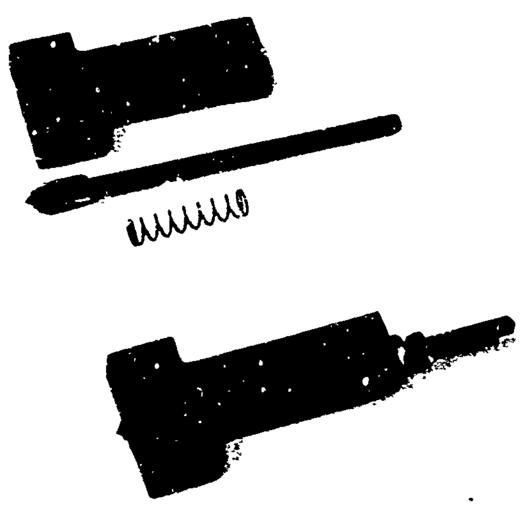

Fig. 65. Photograph of Pin Probe and Components.

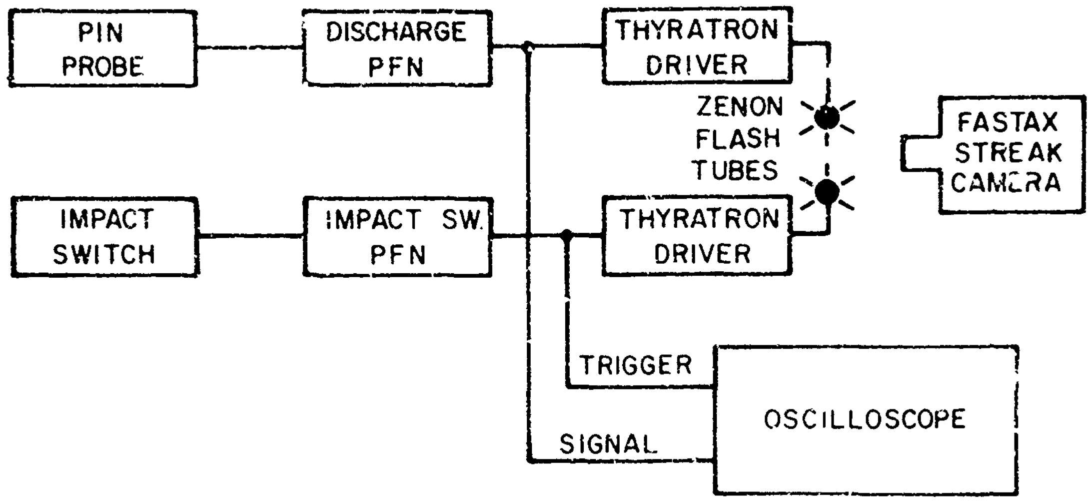

Fig. 66. Block Diagram -- Pin Probe Circuit.

mounted device which produces a real-time voltage output designed to yield not only timing information, but a qualitative indication of the normal stress during the critical rising portions of the stress pulse.

The sensor consists of an X-cut quartz crystal of 0.25 mm thickness and 6.35 mm diameter cemented between a flat surface on the target and a short aluminum rod of like diameter (see Fig. 67). Compression of the quartz disk by the shock wave produces a piezoelectric charge separation between the crystal faces that is proportional to the applied stress. The charge magnitude, Q (coulombs), can be computed from the following once the shock wave has reached the second surface:

$$Q = f A \sigma_n$$

Where σ_n is the normal stress (kilobars), A is the area of the crystal (cm^2) and f the X-direction piezoelectric constant (coulombs/cm^2 - kilobars). The

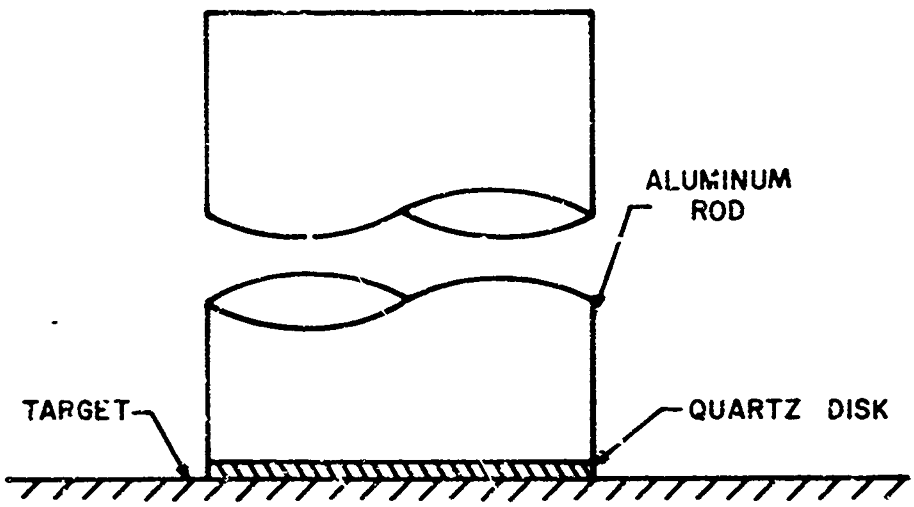

Fig. 67. Piezoelectric Arrival Time Sensor Configuration.

resultant open circuit voltage observed by an oscilloscope whose input is connected between the target and rod becomes:

$$V = \frac{Q}{C} = \frac{fA\sigma_n}{C}$$

where C is the capacitance (farads) of the crystal and detecting system.

The sensor produces a finite rise time signal due to the time required for the shock wave to traverse the crystal thickness, T. This rise time, τ_1, which represents the fundamental sensor resolution time is then $\tau_1 = T/D_g$ where D_g is the shock speed in quartz -- in this case τ_1 was on the order of 50 nsec.

The length of the backup rod determines the time interval during which the pressure pulse can be recorded unambiguously. The aluminum rod was employed as the rear electrode of the sensor and, in addition, extended the recording time of the quartz disk. The recording time can be calculated approximately by calculating the double transit time of the shock wave through the rod, assuming that it moves at sonic velocity. For the 2.5 cm long rod used here, the recording time is roughly 10 μsec, much longer than is required to obtain arrival time signals.

As a stress measuring device, this sensor yields only a qualitative picture of the stress variation. Rarefractions from the edges of the crystal, multiple reflections in the crystal, and any combined states of stress that might exist in the crystal make a quantitative interpretation of the results impractical. In addition, the exponential leakage of the charge on the crystal through the detecting circuit limits the accuracy of any pressure-time measurement -- although in this application the decay time constant is so large ($\sim 10^{-4}$ sec) that the leakage has little effect.

The production of these sensors was simple and inexpensive. One end of an aluminum rod was ground flat and a quartz crystal was cemented to the rod with Eastman 910® adhesive. A center conductor of a coaxial cable was attached to one end of the rod and the outer conductor was grounded to the target. The completed rod and crystal assembly was then cemented to the target. The crystals were obtained from Valpey-Fisher Corporation, Holliston, Massachusetts. The cost of materials in each sensor was less than two dollars.

A block diagram of the electrical circuit employed is shown in Fig. 68. The signal for triggering the oscilloscopes was derived from a foil discharge switch as described previously. A precision time mark generator (Tektronix Type 184) was used to provide calibrated timing for each oscilloscope trace. On each event, one oscilloscope was set up separately, using a fast sweep to measure precisely the time between the impact signal and the first time mark. Typical sensor records are shown in Fig. 69. Reading accuracy for these records depends, of course, on the sweep speeds used in a given experiment. The accuracy was generally about 1% of full scale on the oscilloscope plus the response time of the sensor.

<u>Optical Fiber Sensor.</u> One additional shock arrival time measuring tech-

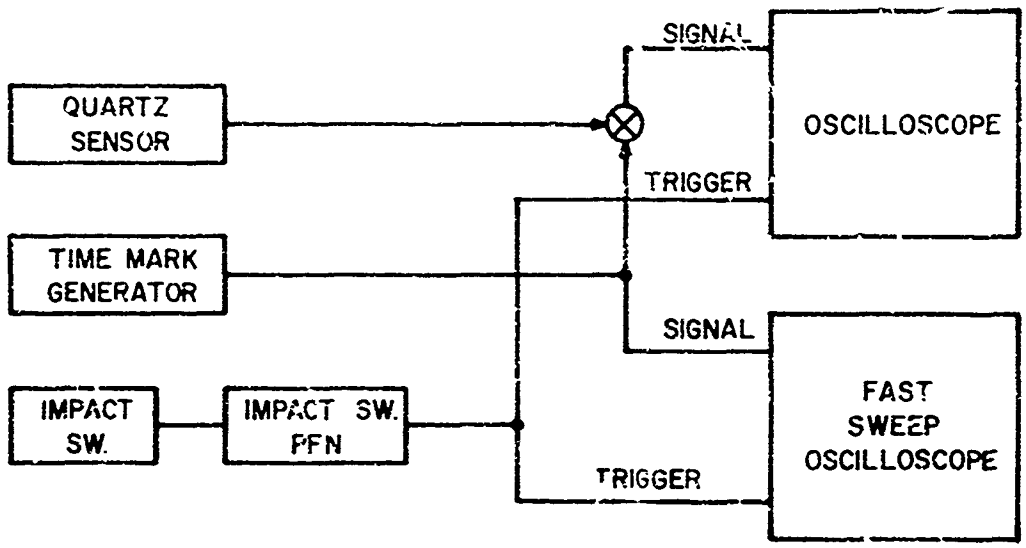

Fig. 68. Block Diagram -- Quartz Sensor Circuit.

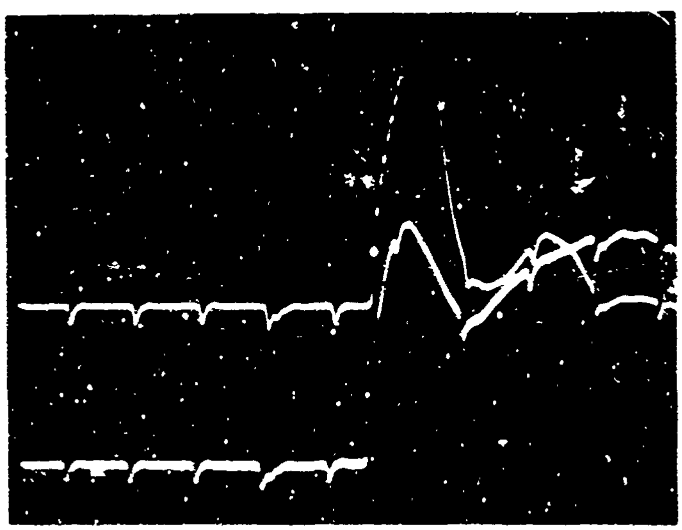

Fig 69. Record of Quartz Arrival Time Sensors, Round 2857. Sweep Speed 1 μ sec/cm with 1MHz Time Marks.

nique was investigated and pursued to the point where practical application is promising. This particular technique was, however, developed so late in the program that it was used on only two experiments. The technique is represented schematically in Fig. 70. One end of an optical fiber is illuminated with a strong light source while the other end is viewed with a streck camera. The light source is pulsed to avoid rewrite on the camera record. The center portion of the optical fiber touches the target surface where an arrival time measurement is desired and is backed by a knife edge. Rear surface motion on the target severs the fiber, extinguishing the light on the end viewed by the streak camera. Impact time is recorded directly by another fiber viewing the impact flash and monitored by the streak camera in the same manner as the probe fibers.

In principle, this technique is capable of measuring the arrival times quite accurately -- to better than 0.1 μsec. Several practical problems, however, prevented successful application to this study. The major difficulty was concerned with the control of the intensity of the light transmitted through the fibers. A record obtained during an impact event (Round 2837) is shown in Fig. 71. Agreement between this record and results obtained with quartz probes was promising, but not really satisfactory. The discrepancy is apparently due to the lack of control over the intensity of the light from each fiber -- resulting in blooming or fading on the streak record. The use of glass instead of plastic fibers and increased manufacturing quality control could hopefully alleviate these difficulties.

Multi-Faceted Targets

The bulk of the experiments in this series were performed at pressure levels where fly-off disks were required to obtain reliable peak rear surface velocity measurements. In this case, it was necessary to provide targets with flat surfaces at the point where the disk (or arrival time probe) was to be mounted. Each target was designed such that the distance from the nominal impact point to each of the flattened rear surfaces was equal. Surfaces were provided at selected angles off axis so that the angular variation of surface velocities and arrival times could be determined.

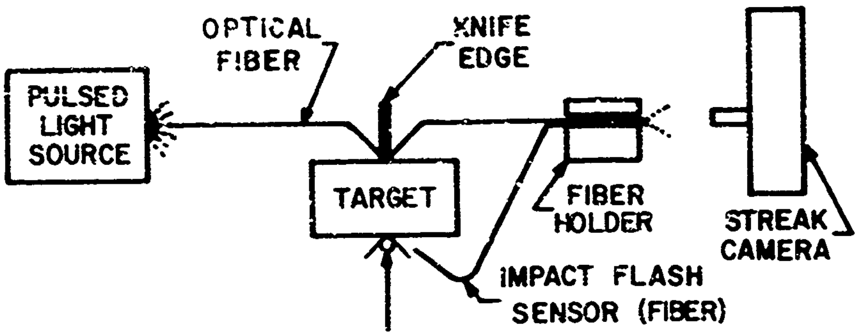

Fig. 70. Optical Arrival Time Sensor Concept.

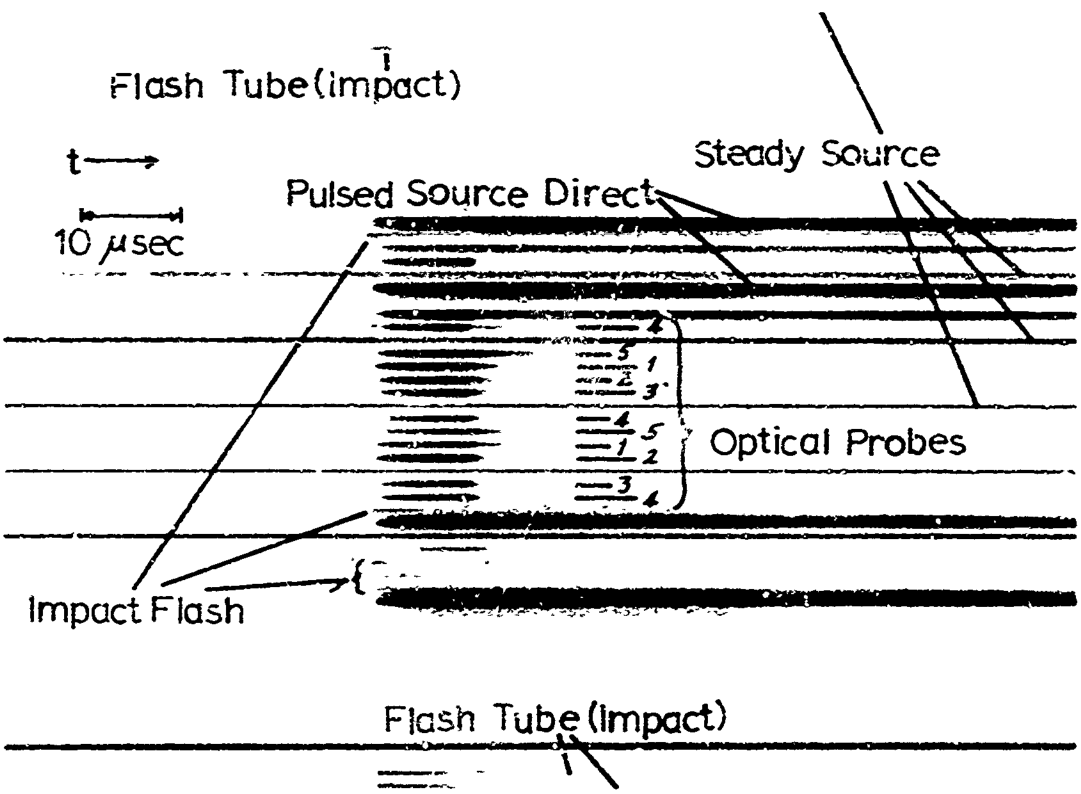

Fig. 71. Optical Time-of-Arrival Probe Streak Record. Round 2837.

The target design is shown in Fig. 72. For the smaller radius targets only three facets were provided at the indicated angles because of the small width of the facet at these sizes. Each facet was machined parallel to the long axis of the target and for the complete length of the target to allow the framing cameras an unobstructed side view of the disks.

This design ensures that the shock wave impacts each free surface and disk normally, provided the actual impact is near the nominal impact point. Targets with three facets were used for those targets with radii between 1.45 cm and 1.9 cm. Targets with five facets ranged in radius from 1.75 cm to 10.0 cm, providing some overlap with the three-facet design.

The target in Fig. 73 is shown attached to a mounting plate which is installed vertically in the range. The projectile impacts the front of the target through a 7.8 cm diameter hole in the mounting plate. After installation, the light gas gun was aligned with the nominal impact point marked on the target front ensuring impact near that point. The details of determining actual distances from the rear impact point to the point of rear surface measurement are described in Appendix C.

Also shown in this photograph are the installation of the fly-off disks and quartz arrival time sensors on each facet. Before installation of these devices, the rear surface was prepared by carefully polishing and cleaning the area where the sensors were to be attached. The fly-off disks were prepared from sheet aluminum with a sheet metal punch. The disks were then flattened in a custom built die. Finally the disks were polished by hand, yielding a flat, smooth surface. A micrometer was used to sample the thickness of the disks, ensuring that their thickness remained 250 μm $\pm$ 20 μm. After attachment, the positions of the disks and arrival time sensors were carefully measured and recorded.

Since the three-faceted targets were rather small and a closely controlled impact point was desired, these targets were installed in the small target tank on the AFML Hypervelocity Ballistic Range in a manner almost identical to that described earlier in this chapter for the split cylinder targets

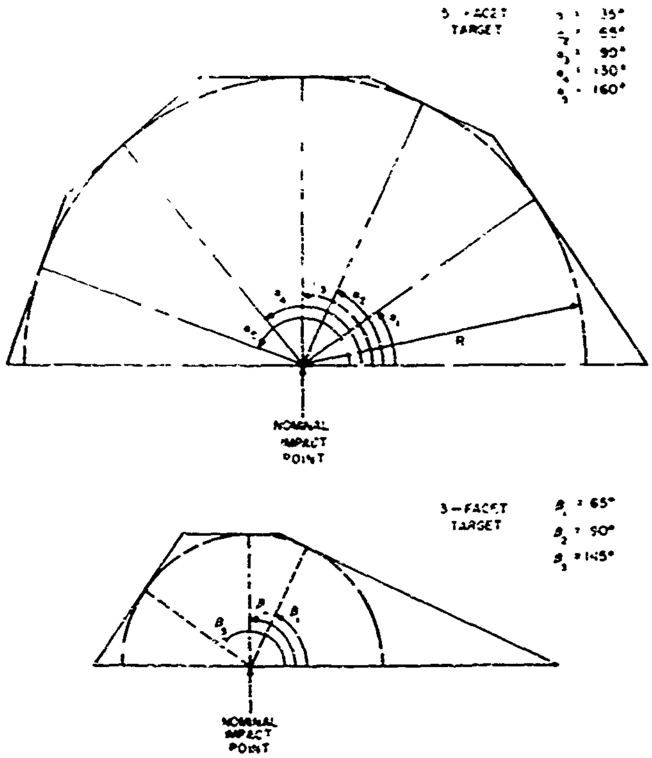

Fig. 72. Design of Multi-Faceted Targets -- End View.

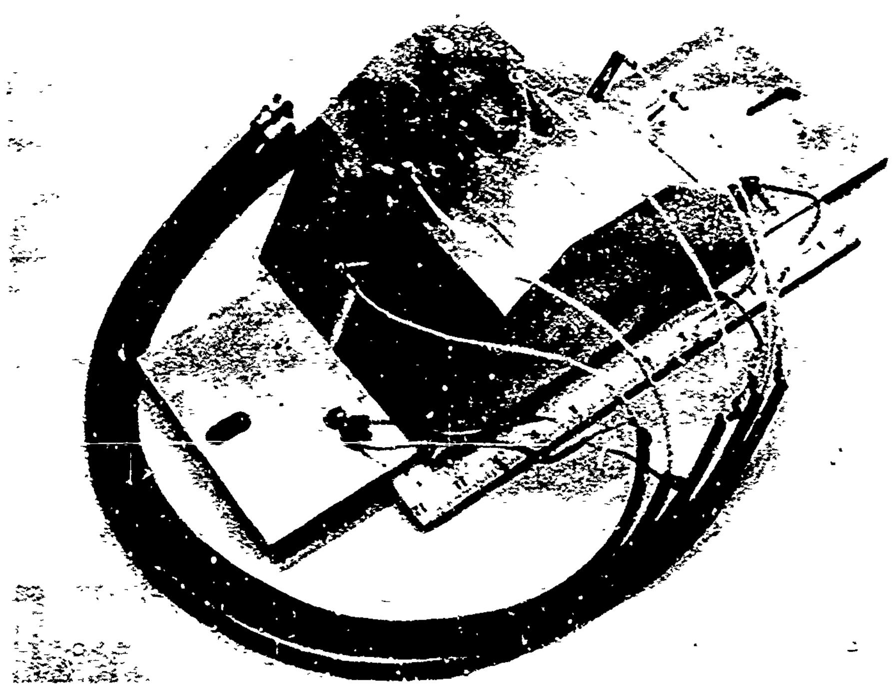

Fig. 73. Photograph of 5-Faceted Target With Sensors Attached.

(see Fig. 55). All framing camera records were obtained from the Model 300 camera. The light source and velocity measuring x-ray sources were triggered by a foil switch placed on the rear of the sabot stopping plate. Framing camera records of the incoming projectile were used to check the x-ray measurement of projectile velocity and to determine the vertical component of the impact coordinate at the target face. The impact coordinates were also obtained by measurement on the target after impact -- modestly accurate determination of the impact point (±2 mm) could be made even on completely penetrated targets. Errors in these measurements undoubtedly contributed to the scatter in the data from these targets. A typical sequence of frames from the Model 300 camera is shown in Fig. 74. Fly-off disk and arrival time experiments were performed separately on these targets to avoid crowding the target rear and creating interactions between the two types of measurements.

For the larger five-faceted targets, the experiments were moved back to the main target tank and set up in a geometry as shown in Fig. 58. The choice of camera-light source combination employed depended, of course, upon the radius of the target installed.

The framing camera setup and arrival time sensor instrumentation for these experiments has been described previously. A foil switch directly on the target face provided a trigger signal for the camera light source and for the arrival time sensor instrumentation. The impact point was determined by direct measurement on the recovered target (see Appendix C). Projectile velocity was measured on the standard range Fastax® system.

Summary

The decay of the peak shock wave normal stress generated by hypervelocity impact is of great importance in understanding the impact dynamics and effects of material strength as well as determining the validity of numerical calculations of impact events. Two techniques have been developed for measuring peak free surface velocity -- and consequently Hugoniot stress -- as a function

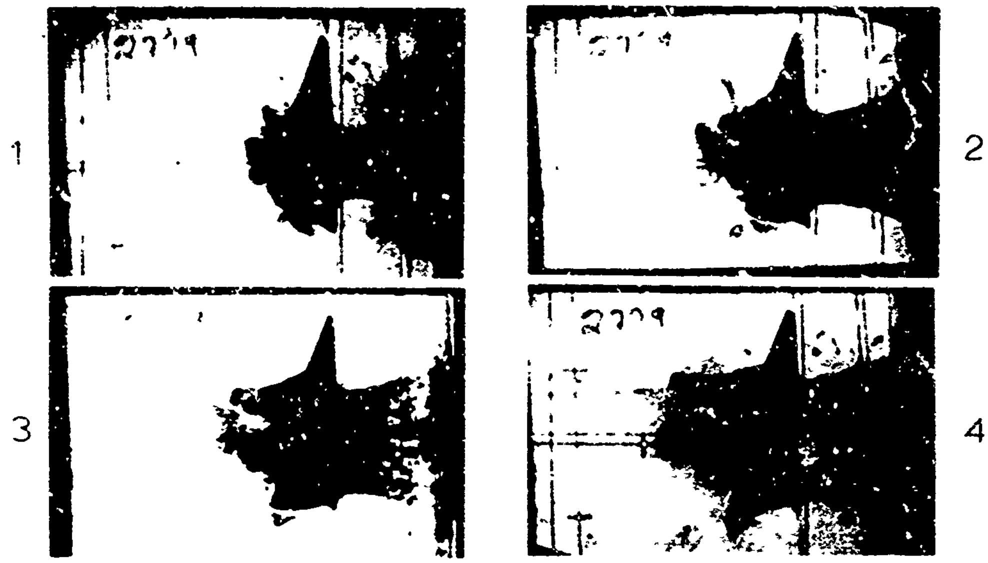

Fig. 74. Round 2779 Photo Sequence of Fly-off Disks on 3-Faceted Target.

of distance from the impact point and angle off the target axis (projectile trajectory). Direct measurement of the rear surface motion of a "split-cylinder" target was employed when expected stresses were greater than approximately 50 kilobars. At lower stresses, thin "fly-off disks" were attached to the target rear surface. The velocity imparted to the disks by the shock wave interaction then yielded a measure of the peak free surface velocity. In each case high speed framing cameras were employed to measure the velocity of the particles in question.

In addition, two methods were developed for determining the time between impact and arrival of the shock wave at a given point on the target. One method -- the pin probe -- employed a high voltage discharge through an insulating sheet penetrated by the shock wave to produce an arrival signal. The second technique -- a quartz piezoelectric sensor -- yielded a direct, active voltage signal that corresponded to shock arrival time. These arrival time sensors were employed in experiments to determine the shock wave trajectory, R_s vs t.

VI. Shock Propagation -- Experimental Results

The experimental techniques described in the previous chapter have been applied to a study of shock wave propagation in three aluminum alloys. Major emphasis was placed in measuring the peak normal stress across the shock front through measurements of free surface velocities or fly-off disk velocities as appropriate. Considerable success was achieved in this endeavor. Secondary effort was placed upon measurement of the shock trajectory using time-of-arrival probes. The remainder of this chapter presents a description of the experimental program, the results obtained, and a discussion of the results. The comparison of the results with hypervelocity impact theory is contained in the following chapter.

Experimental Program

The primary experiments, those involving measurements of peak normal stress, were designed to study the effects of material strength upon the shock propagation and to explore the variation of stress as a function of angle off axis. Neither of these features of a normal hypervelocity impact has received systematic experimental study before. Only with the advent of the numerical techniques that include strength terms in a two-dimensional geometry as described in Chapter II has it even been possible to calculate these effects -- and these numerical techniques are a relatively recent development, dating from about 1965 in their early forms. The experimental data obtained here provide a realistic test of the ability of these numerical techniques to predict impact results.

The results of the crater growth experiments presented earlier provided data on the effects that occurred in the region of the crater and provided several useful comparisons with numerically generated results. The data described in this chapter yields analagous information on the behavior of the material in regions far removed from the crater where the shock wave propagated away from the impact point at high speed. The combination of both types of results provides a more complete set of experimental impact data.

Previous studies of shock wave propagation in solids under the two-dimensional conditions created by hypervelocity impact have been performed by Charest (Ref. 13) and by Billingsley (Ref. 14). Charest used techniques similar to those employed here to measure the on-axis normal stress in 1100-0 aluminum targets. Billingsley obtained limited stress data in 6061-T6 aluminum as well as other metals using only measurements of free surface velocity. The lowest stresses he could accurately monitor were therefore restricted by the technique employed. The emphasis in his study was on the very high stresses and the comparison of those data with numerical, pure hydrodynamic calculations. The present study extends the available data over a wider range of stresses for a wider variety of aluminum alloys in addition to providing off-axis data. It is hoped also that the refined experimental techniques used have resulted in an improvement in the accuracy of the data produced.

The experimental program was performed at the AFML Hypervelocity Ballistic Range and consisted of over seventy successful rounds on the light-gas gun. All experiments were conducted with a nominal projectile velocity of 7.0 km/sec although actual projectile velocities ranged from 5.8 km/sec to 7.3 km/sec. In each case the projectile was a 0.635 cm diameter sphere of 2017 aluminum alloy. Three aluminum alloys were selected for target materials on the basis of their widely varying strength properties and the availability of quality material: 1100-0, 6061-T6, and 7075-T6. The properties of these materials have been described in Chapter III in conjunction with the crater growth experiments (Table II). The experiments conducted in this portion of the program correspond to Cases 1, 6, and 8 of the crater growth experiments. Whenever the target configuration and available equipment would allow it, both stress and time-of-arrival experiments were performed on the same round. Those experiments that yielded data are listed in Table VII.

Table VII

Tabulation of Shock Propagation Experiments

Round Number	Target Material	Target Type	Target Radius (cm)	Projectile Velocity (km/sec)	Instru-mentation
2719	1100-0	5	4.00	6.95e	D-D
2720	1100-0	5	4.00	6.30	D-D
2726	1100-0	C	1.60	6.92e	FS
2728	1100-0	C	1.60	6.95	FS
2729	1100-0	C	1.45	6.89	FS
2730	1100-0	C	1.25	6.82	FS
2733	1100-0	3	1.60	6.17	D-300
2734	1100-0	5	2.50	6.53	D-300
2750	7075-T6	C	1.00	6.09	FS
2752	7075-T6	C	1.45	6.09	FS
2760	7075-T6	FP	1.25	5.80e	FS
2763	1100-0	FP	1.25	6.56e	FS
2766	7075-T6	C	1.60	6.75	FS
2767	7075-T6	C	1.45	6.67	FS
2769	7075-T6	C	1.25	6.80	FS
2772	6061-T6	C	1.60	6.98	FS
2774	7075-T6	C	1.00	6.71	FS
2775	6061-T6	3	1.75	6.77	D-300
2776	6061-T6	3	1.90	6.92e	D-300
2777	7075-T6	3	1.90	6.77	D-300
2778	7075-T6	3	1.75	6.56	D-300
2779	1100-0	3	1.90	6.80	D-300
2780	1100-0	3	1.75	7.01	D-300
2781	7075-T6	FP	1.25	7.01e	FS
2784	7075-T6	3	1.90	6.80e	ET
2785	6061-T6	3	1.90	7.05	ET
2787	7075-T6	3	1.75	6.71	ET
2789	6061-T6	3	1.75	6.68	ET
2791	1100-0	3	1.75	6.71e	ET
2796	6061-T6	5	1.75	7.05	D-300

Table VII (Cont'd)

Round Number	Target Material	Target Type	Target Radius (cm)	Projectile Velocity (km/sec)	Instru-mentation
2797	7075-T6	5	1.75	6.98	D-300
2798	1100-0	FP	1.25	6.70	FS
2799	6061-T6	5	2.50	7.01e	D-300,QT
2801	7075-T6	5	2.50	6.46	D-300
2804	7075-T6	5	4.00	6.70e	QT
2806	6061-T6	5	4.00	6.70e	QT
2807	1100-0	5	4.00	6.46	QT
2809	1100-0	5	4.00	6.77	D-D, QT
2811	1100-0	5	4.00	6.99	ET, QT
2815	1100-0	5	2.00	6.74	QT
2817	1100-0	FP	1.25	6.35	FS
2818	1100-0	5	2.50	6.89	D-300
2820	1100-0	C	1.60	6.19	FS
2821	7075-T6	5	3.00	6.85	QT
2822	7075-T6	5	2.00	6.98	D-300, QT
2823	7075-T6	5	8.00	7.00	D-D
2824	7075-T6	5	8.00	6.95	D-D, QT
2825	7075-T6	5	6.00	6.41	D-D
2826	7075-T6	5	10.00	6.71	D-D, QT
2827	7075-T6	3	1.60	7.10	QT
2828	6061-T6	5	3.00	6.31	QT
2829	6061-T6	C	1.45	6.46	D-300
2831	7075-T6	C	1.60	7.10	D-300
2832	7075-T6	5	3.00	6.95	QT
2833	1100-0	3	1.45	6.52	QT
2834	1100-0	5	3.00	7.12	D-300, QT
2836	1100-0	5	10.00	6.45	D-D, QT, OT
2837	6061-T6	5	6.00	6.26	D-D, QT, OT
2838	6061-T6	5	10.00	5.93	D-D, QT
2842	6061-T6	5	8.00	5.89	QT, OT

Table VII (Cont'd)

Round Number	Target Material	Target Type	Target Radius (cm)	Projectile Velocity (km/sec)	Instru-mentation
2851	1100-0	5	5.00	6.43	D-D, QT
2854	7075-T6	5	5.00	6.61	D-D
2857	7075-T6	5	4.00	6.45	QT
2859	7075-T6	5	4.00	6.44	D-D
2860	1100-0	5	8.00	6.77	D-D
2863	6061-T6	5	8.00	6.70	D-D
2864	1100-0	5	6.00	[illegible]	D-D, QT
2865	6061-T6	5	4.00	[illegible]	D-D, QT
2867	1100-0	5	3.25	6.67	D-300
2869	7075-T6	5	3.25	6.89	D-300

e -- Estimated projectile velocity.
D-D -- Fly-off disks measured with Dynafax framing camera.
D-300 -- Fly-off disks measured with B&W 300 camera.
ET -- Electrical pin time-of-arrival probes.
QT -- Quartz time-of-arrival probes.
OT -- Optical fiber time-of-arrival probes.
FS -- Free surface motion measured with B&W 300 camera.

Target Type:
5 -- Five faceted target.
3 -- Three faceted target.
C -- Split cylinder target.
FP -- Flat plate target.

Stress Measurement Results

Over 240 data points were obtained from either direct measurements of free surface velocity or fly-off disk velocity employing the techniques described in Chapter V. The experiments emphasized obtaining data on the two aluminum alloys 1100-0 and 7075-T6 which represent the lower and upper bounds of strength properties for the available materials. Somewhat less complete data was obtained on the 6061-T6 alloy which has intermediate strength properties.

For each alloy, the disk velocities were measured at five different nominal angles, 0°, 25°, 40°, 55°, and 70°, with respect to the trajectory (axis). Actual impact points did not generally correspond with the nominal impact point, hence a distribution of angles was actually achieved.

The measurements of free surface velocity taken from the split cylinder targets were made at a variety of angles. The data for each alloy has been broken into five angle ranges for presentation. The ranges were determined by the actual angular distribution of the data and by consideration of the nominal angles. The ranges are: (1) 0° - 17.5°, representing points nearly directly behind the impact point; (2) 17.5° - 32.5°; (3) 32.5° - 47.5°; (4) 47.5° - 62.5°; and (5) 62.5° - 90° with the nominal angles lying roughly in the centers of these ranges.

The method for calculating stress from the measured disk or free surface velocity and the assumptions employed in these calculations are discussed in detail in Appendix G. It consists essentially in assuming that the disk or surface responds ultimately to the peak normal stress and in employing the velocity doubling rule, i.e., that the free surface (or disk) velocity is equal to twice the material velocity ($v_{fs} \cong 2u$). The aluminum Hugoniot data required for the calculation was obtained from Ref. 48 which also corresponds very closely to the Hugoniot data used in the numerical calculations to be described in Chapter VII.

Presentation of Results. Each experiment was designed such that the nominal projectile velocity would be 7.0 km/sec and so that the expanding shock front (assumed spherical) would strike the free surface or disk where measurements were being made at normal incidence (i.e. the incidence angle, δ, between the shock front and rear surface being zero). In no case were the nominal conditions achieved exactly. Every data point presented below was corrected for these deviations from nominal performance by means of the scaling relation

$$v_{fs_{scaled}} = (v_{fs_{measured}} / \cos \delta) \cdot (3.471 - 0.353\, v_p)$$

where v_p, the actual projectile velocity, was given in km/sec. This scaling law is largely empirical and is explained and justified in detail in Appendix E. The law is believed to be quite accurate over the small range of the variables employed in this study.

Measurement errors can arise from a variety of sources. While most of these sources have been discussed previously, the major ones are summarized here for comparison:

a. Impact Point. Can be determined to about ±.03 cm in large targets, but to only about ±.05 cm in small targets where significant deformation of the whole target occurs. For the split cylinder targets, impact can be determined to approximately ±.1 cm.

b. Impact Point to Rear Surface. A physical measurement that can be made to an accuracy of about ±0.3 mm.

c. Framing Camera Speed. Accurate to ±1 count, amounting to a percentage error varying from ±0.1% to ±0.03% depending upon the camera speed.

d. Disk or Free Surface Velocity. Accuracy varies depending upon image quality, travel distance, camera speed, etc. An rms error is computed in the data reduction program and varies from about ±0.5% to over ~10% depending on circumstances. This rms error is reported for each data point in Appendix F.

e. Camera Magnification. A potential systematic error estimated to amount to approximately 1.5% for those films taken with the B&W 300 camera and approximately 2% for films taken with the B&W 326 camera.

f. Conversion of Free Surface Velocity to Stress. Less than 1% -- see Appendix F.

The data obtained is shown in graphical form in Figs. 75 through 89 displaying both free surface velocity (or disk velocity) versus shock radius, R_s, and peak normal stress, σ_n, versus shock radius for the three aluminum alloys in five angle ranges. The detailed data from each round are included in Appendix F. Estimated errors have been calculated for several data points based upon the above sources and are shown in Fig. 75. These can be considered typical for the bulk of the data presented in the remaining figures.

Velocity-Distance Relations. The most obvious feature of the data is that the measured free surface or disk velocity decreases exponentially with increasing distance into the target and that the decay law changes sharply at some distance into the target which varies with the target material. This behavior is emphasized by the straight lines shown on each plot of velocity versus R_s. In each case the straight lines were obtained from a least squares fit to the data in the region indicated. The consistency between all the sets of data is startling and strongly emphasizes the essential correctness of this dual decay law behavior. The change in behavior of the decay law is believed to be associated with release waves generated in the region of the crater. The different position of this knee in the curve for different alloys indicates that the effect is also material strength dependent, i.e., that non-hydrodynamic attenuation is occurring at this point. This aspect of the data is discussed in more detail later in this chapter.

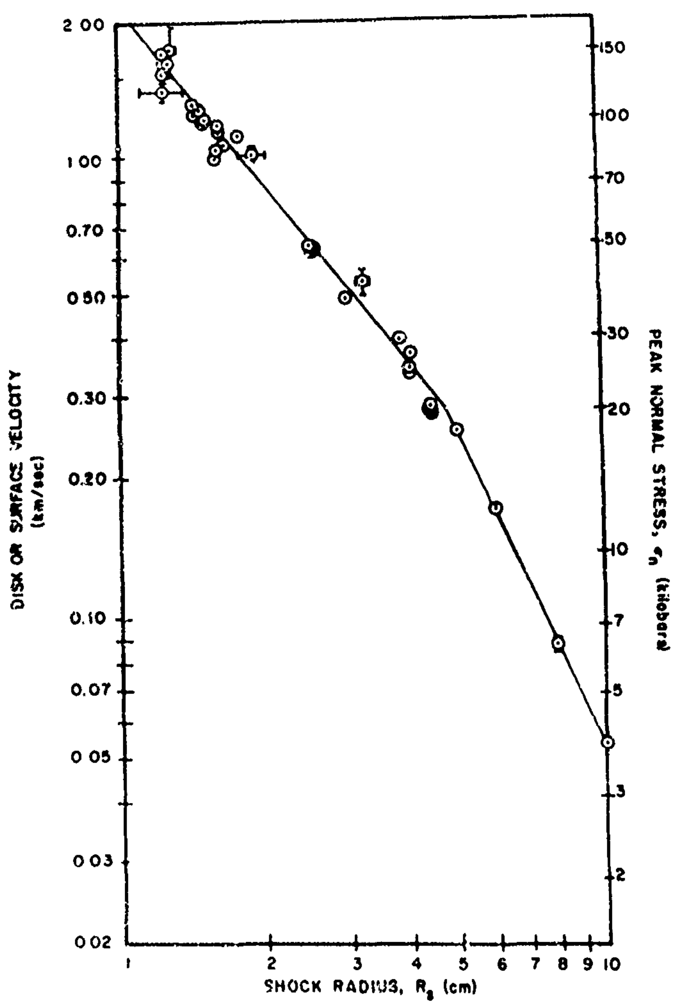

Fig. 75. Variation of Free Surface Velocity with Shock Radius -- 1100-0 Aluminum Alloy 0 - 17.5° Off Axis.

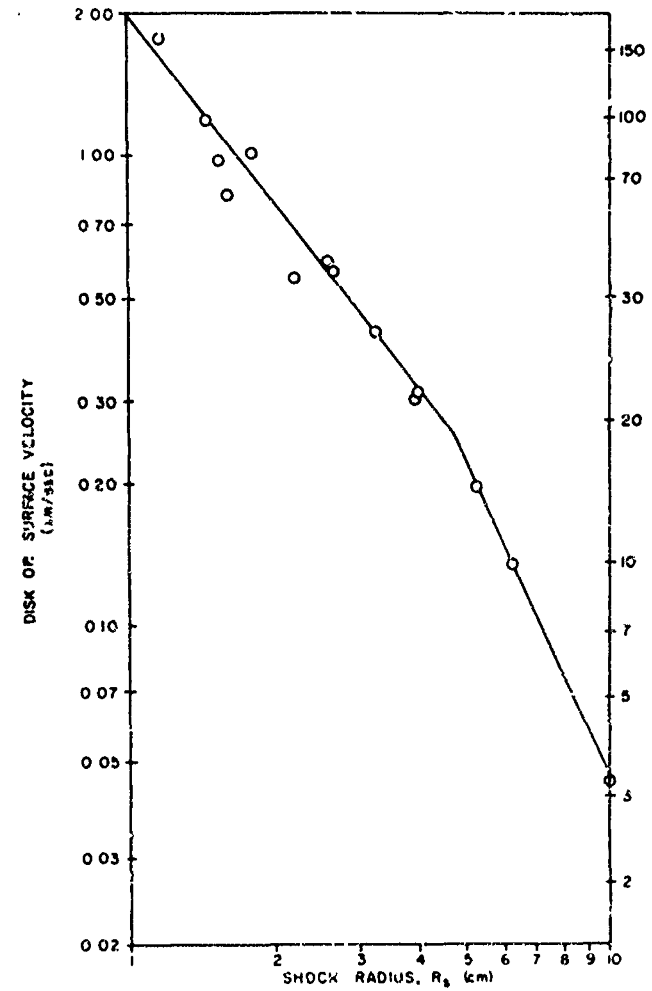

Fig. 76. Variation of Free Surface Velocity with Shock Radius -- 1100-0 Aluminum Alloy 17.5 - 32.5° Off Axis.

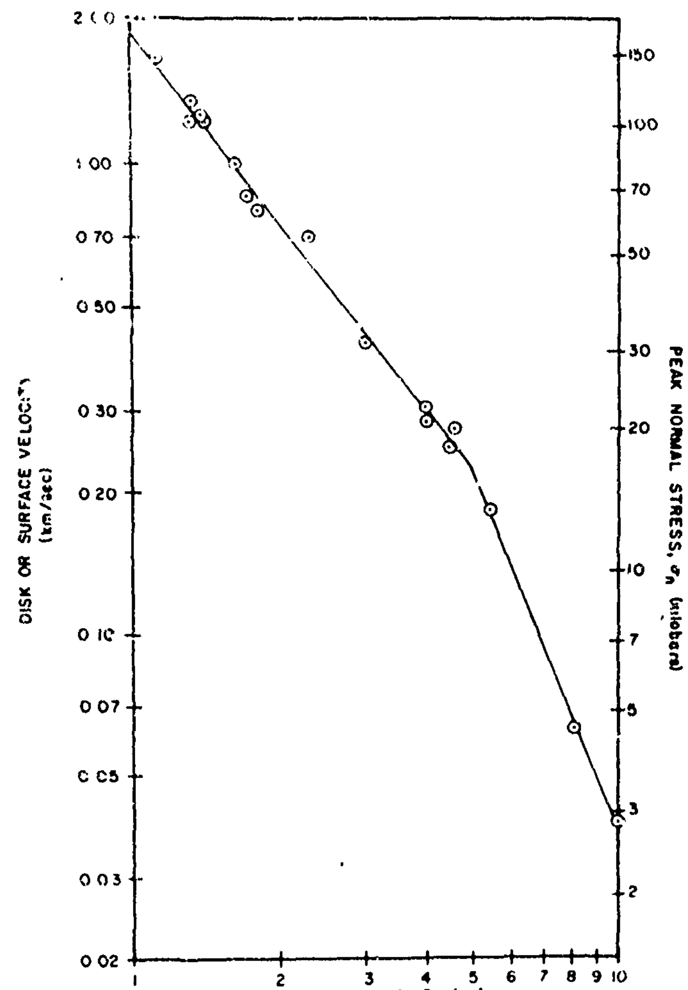

Fig. 77. Variation of Free Surface Velocity with Shock Radius -- 1100-0 Aluminum Alloy 32.5 - 47.5° Off Axis.

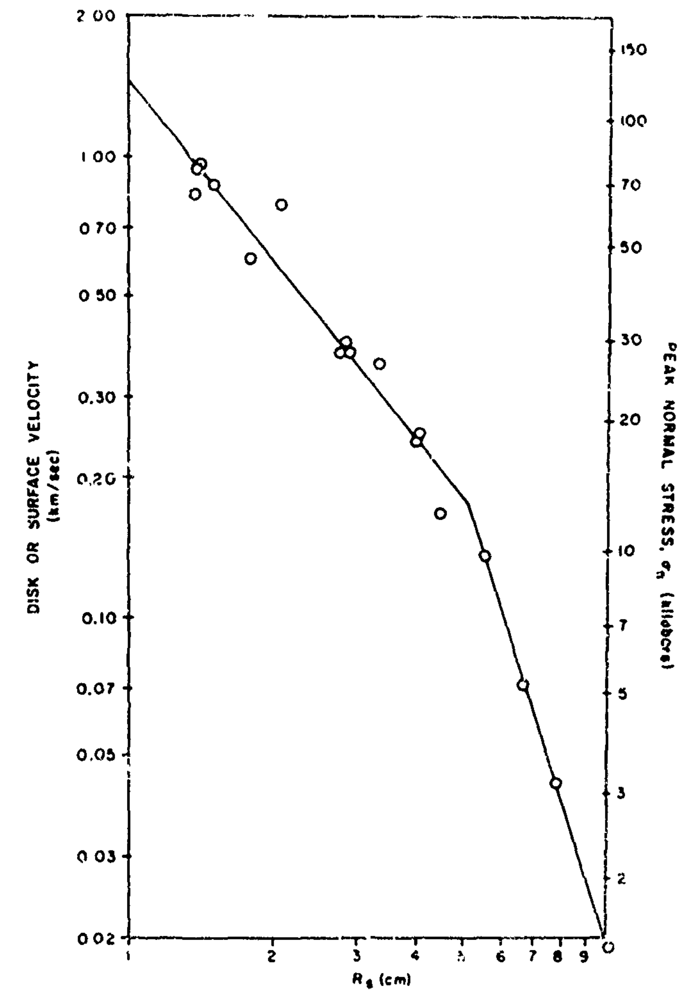

Fig. 78. Variation of Free Surface Velocity with Shock Radius -- 1100-0 Aluminum Alloy 47.5 - 62.5° Off Axis.

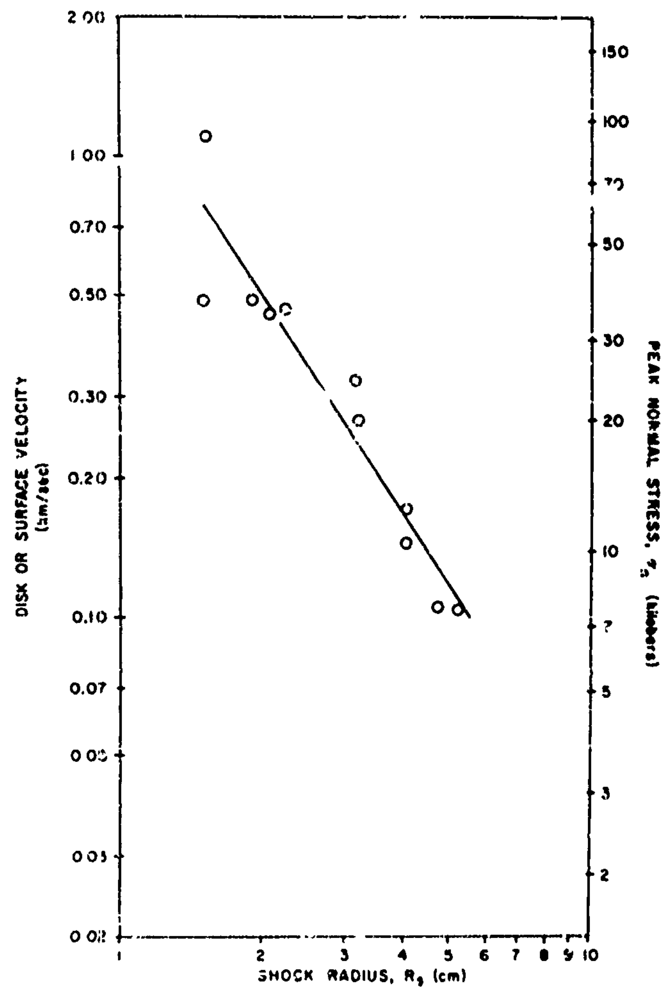

Fig. 79. Variation of Free Surface Velocity with Shock Radius -- 1100-0 Aluminum Alloy 62.5 - 90° Off Axis.

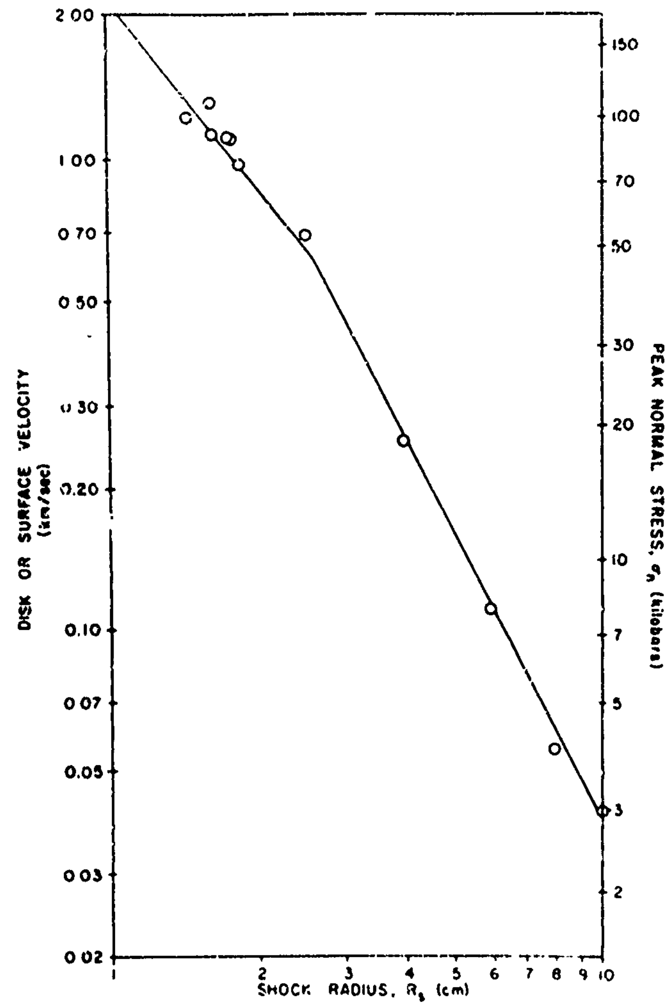

Fig. 80. Variation of Free Surface Velocity with Shock Radius -- 6061-T6 Aluminum Alloy 0 - 17.5° Off Axis.

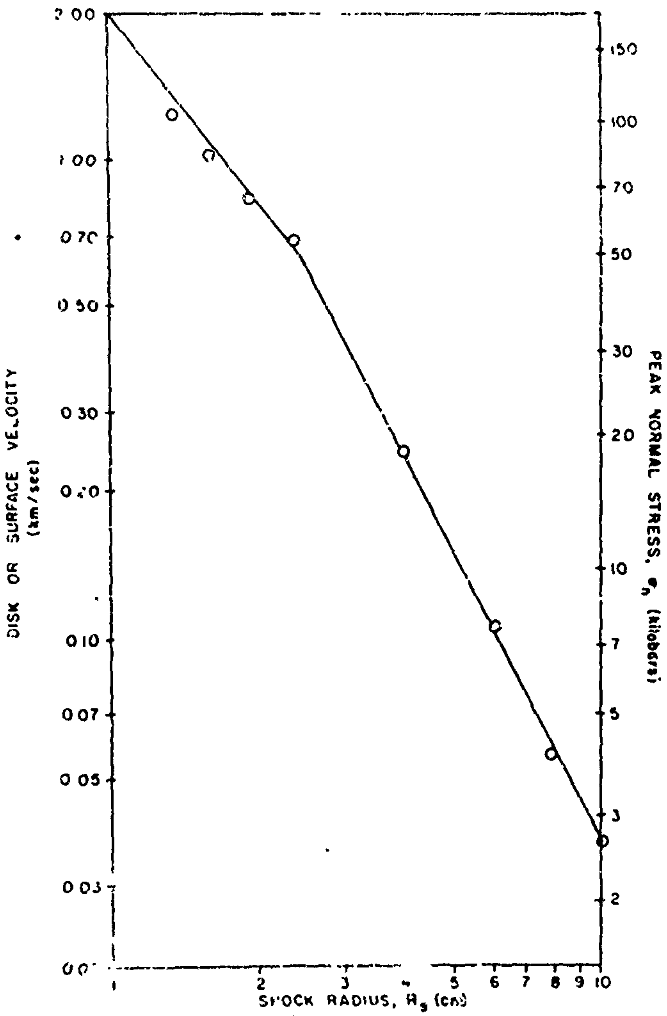

Fig. 81. Variation of Free Surface Velocity with Shock Radius -- 6061-T6 Aluminum Alloy 17.5 - 32.5° Off Axis.

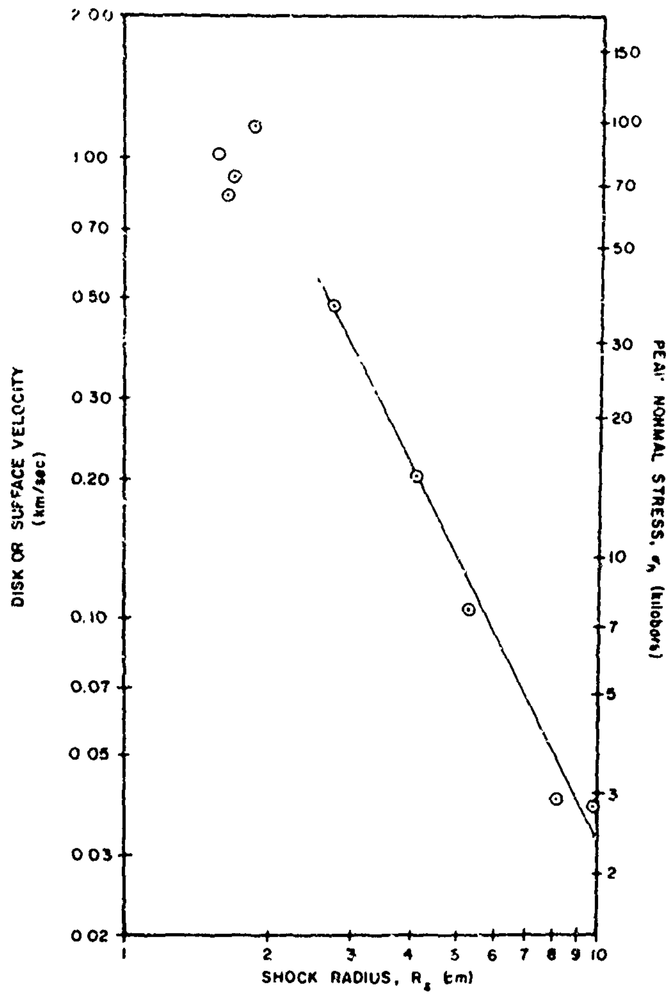

Fig. 82. Variation of Free Surface Velocity with Shock Radius -- 6061-T6 Aluminum Alloy 32.5 - 47.5° Off Axis.

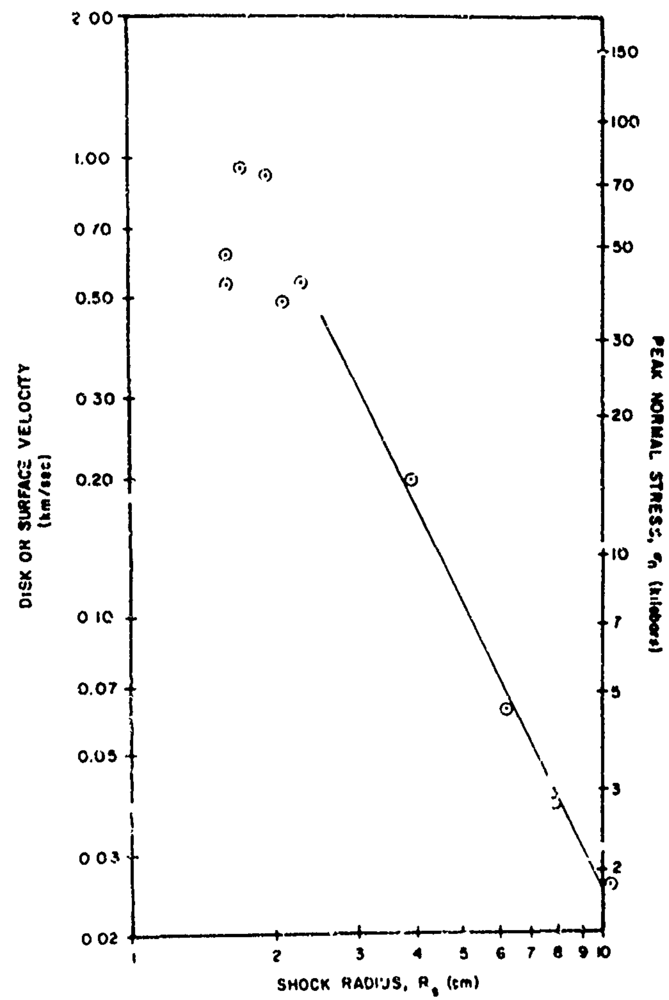

Fig. 83. Variation of Free Surface Velocity with Shock Radius -- 6061-T6 Aluminum Alloy 47.5 - 62.5° Off Axis.

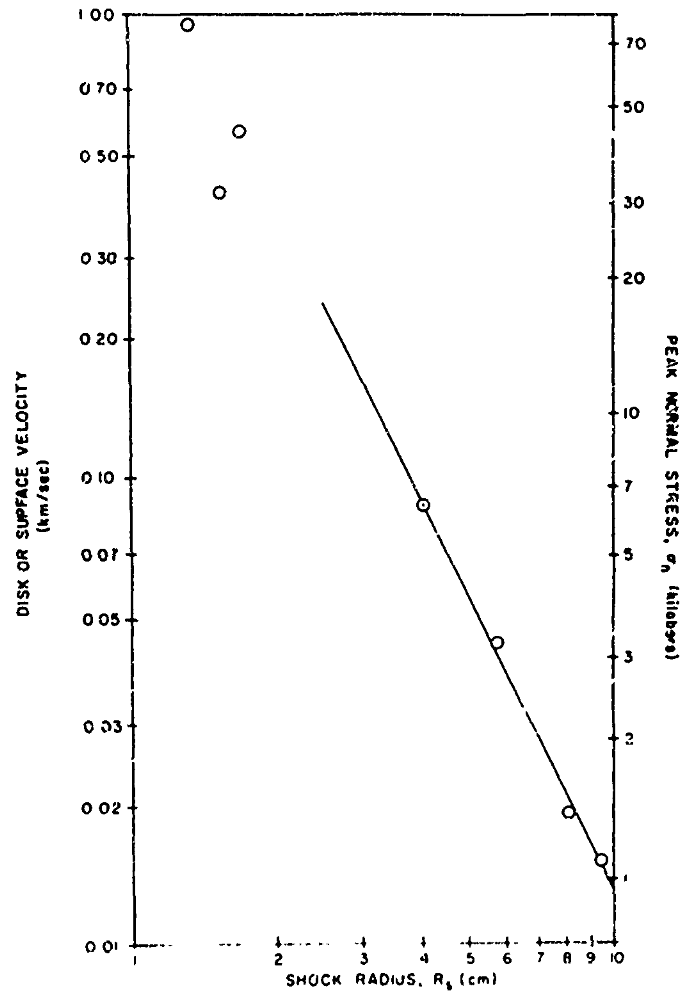

Fig. 84. Variation of Free Surface Velocity with Shock Radius -- 6061-T6 Aluminum Alloy 62.5 - 90° Off Axis.

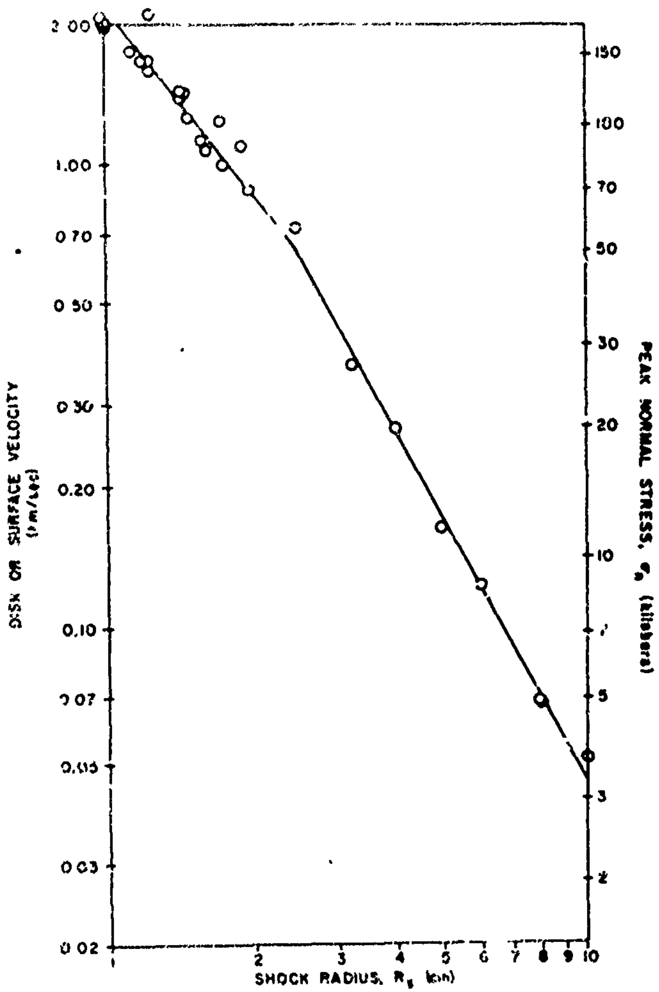

Fig. 85. Variation of Free Surface Velocity with Shock Radius -- 7075-T6 Aluminum Alloy 0 - 17.5° Off Axis.

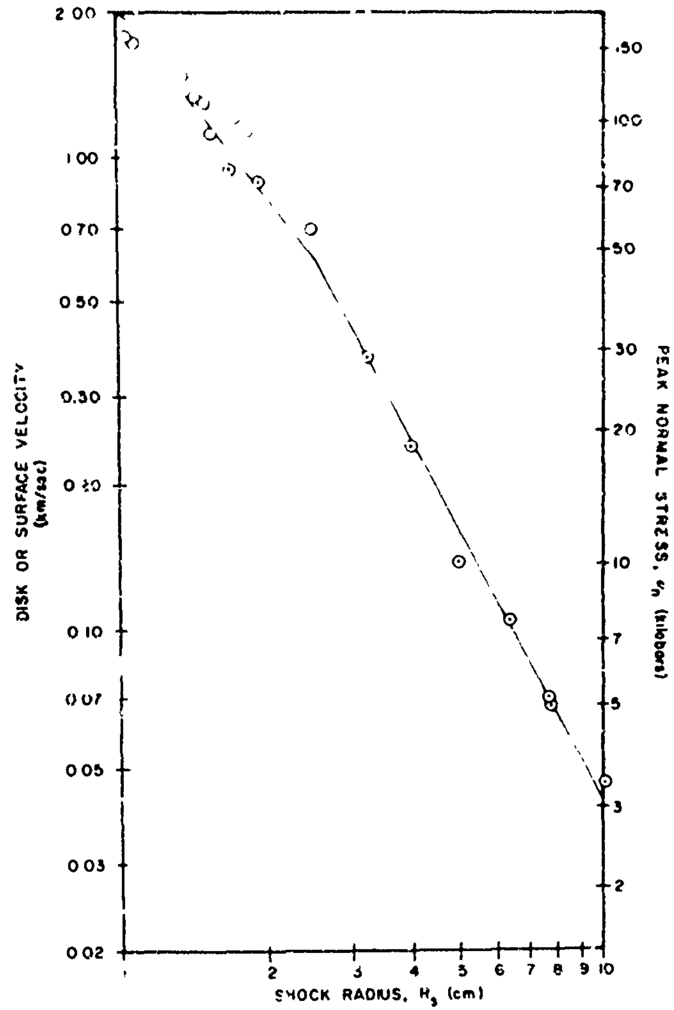

Fig. 86. Variation of Free Surface Velocity with Shock Radius -- 7075-T6 Aluminum Alloy 17.5 - 32.5° Off Axis.

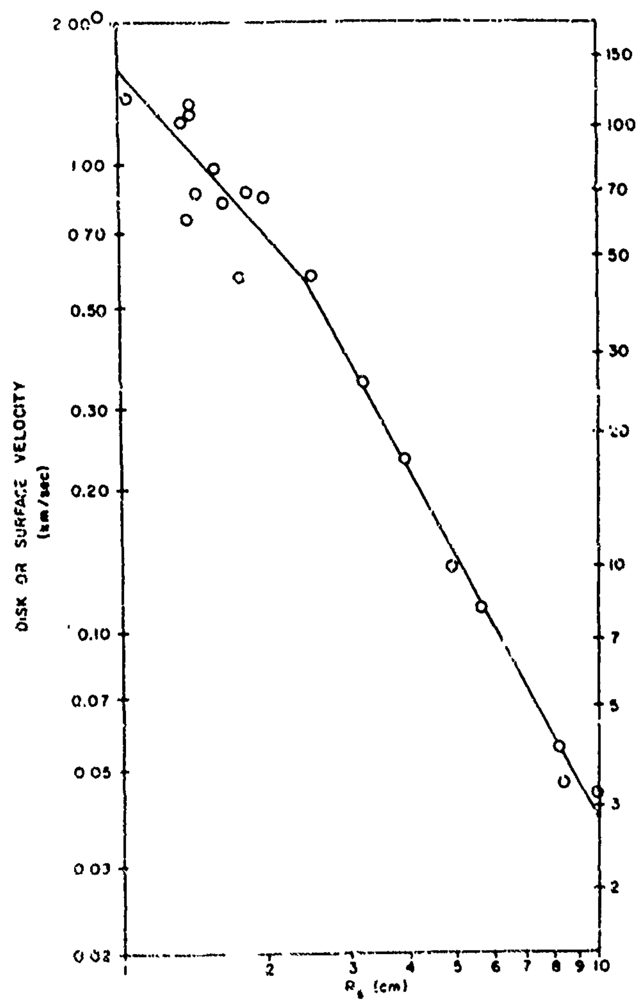

Fig. 87. Variation of Free Surface Velocity with Shock Radius -- 7075-T6 Aluminum Alloy 32.5 - 47.5° Off Axis.

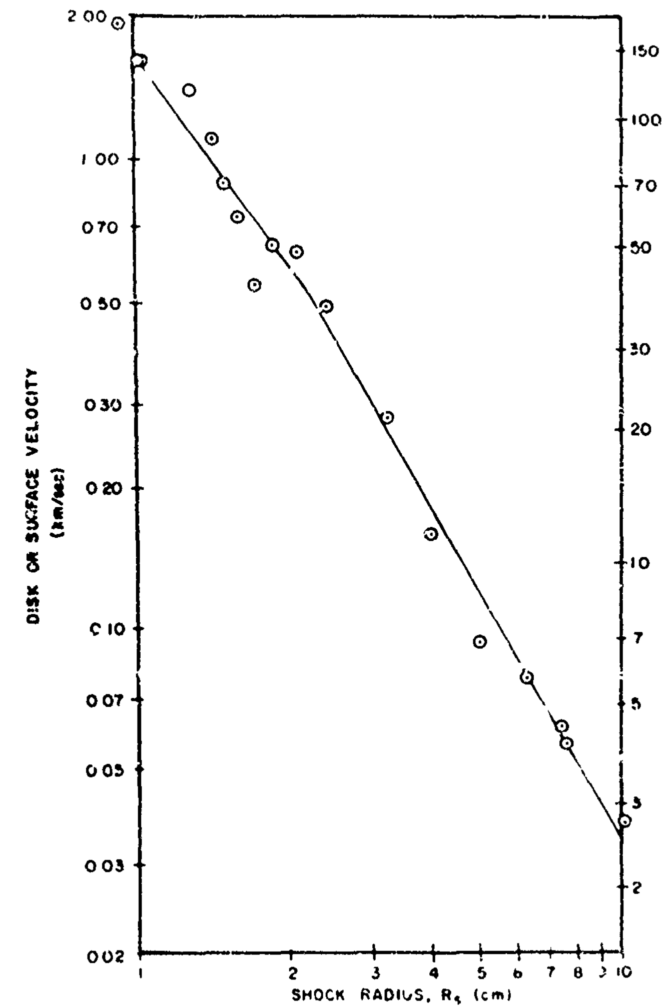

Fig. 88. Variation of Free Surface Velocity with Shock Radius -- 7075-T6 Aluminum Alloy 47.5 - 62.5° Off Axis.

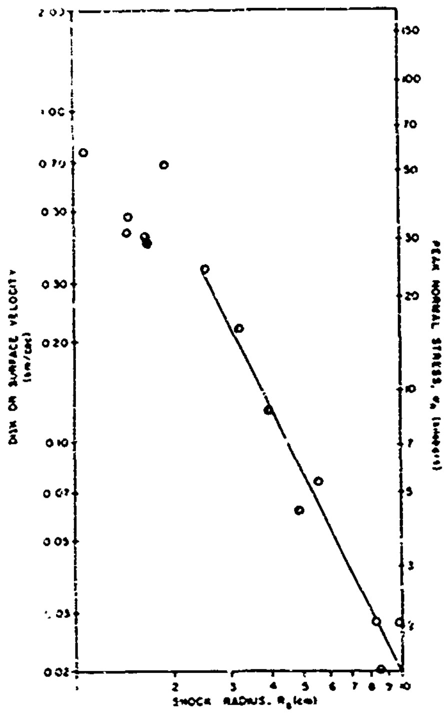

Fig. 89. Variation of Free Surface Velocity with Shock Radius -- 7075-T6 Aluminum Alloy 62.5 - 90° Off Axis.

If the velocity-distance relation is expressed in the form

$$v_{fs} = aR_s^b$$

then each set of data can be characterized by two sets of the constants a and b, each set applying to one section of the decay curve, and by the specification of the value of R_s at which the transition between the two decay laws takes place. This decay law data is shown in Table VIII. The parameter b specifies the slope of the decay curve and is the most important parameter in these relations.

In the angle range 0 - 17.5°, the data indicates similar behavior for all three alloys for those portions of the curve corresponding to the higher free surface velocity; consequently the curve was derived from a composite of the data from all three alloys in this angle range. In this free surface velocity regime, the corresponding peak normal stresses are quite high, ranging from 20 kbar to over 200 kbar. Therefore, it is not surprising that the three alloys behave alike. The overall response of the materials is dominated by the hydrodynamic behavior -- and the strength properties of the different alloys do not affect hydrodynamic behavior.

In the angle range 17.5 - 32.5 degrees the data indicate that the same phenomenon is also occurring. To within experimental error, the slopes of the lines are same for all three alloys again and the curves shown were derived from data t n from all three alloys. For the remaining angle ranges, the data is consistent with nearly identical behavior by all three alloys in the upper pressure range, but there is insufficient data to be conclusive. In these remaining cases, the curves were derived separately (whenever sufficient data was available) for each alloy and angle range.

The Hugoniot relation between the stress and free surface (or disk) velocity is sufficiently non-linear that some curvature can be seen in the stress-shock radius plots, especially in the higher stress range. Up to a stress of roughly 50 kilobars, the free surface velocity-stress relation is nearly linear. Consequently the log-log plots relating peak normal stress to shock radius yield straight lines in the lower stress ranges. The slope of this line is identical to that given in Table VIII (the constant b_2) for the velocity-distance relations.

As an alternative, it is possible to obtain straight line fits to the log stress-log shock radius data. Relatively small differences in the curves result if this approach is taken. In any event, it does not appear possible to make a clear choice of the two curve fitting approaches on the basis of the available data. The choice of the linearized log velocity-log shock radius relations used was quite subjective and based on the opinion that slightly more consistent results were obtained. In addition, the disk velocity is the measured quantity, while stress is a derived quantity here.

Variations With Off-Axis Angle. It is a common observation that the shock wave produced by a hypervelocity impact expands from the source in a nearly spherical manner, e.g., see Ref. 11. Empirical observations, such as spall effects, also indicate that the stress in the expanding shock front must be a

Table VIII

Velocity-Distance Decay Law Parameters

$$v_{fs}\ (\text{km/sec}) = aR_s^{\,b}$$

Target Alloy	Off-Axis Angle Range (deg)	Multiplier a_1	Exponent b_1	Est Exponent Variance	Approximate R_t (cm) at Transition	Multiplier a_2	Exponent b_2	Est Exponent Variance
1100-0	0-17.5	0.345	-1.335	0.027	4.8	0.990	-2.267	0.031
	17.5-32.5	0.304	-1.306	0.062	4.8	0.975	-2.312	0.047
	32.5-47.5	0.278	-1.346	0.035	5.0	1.191	-2.635	0.090
	47.5-62.5	0.167	-1.305	0.093	5.1	1.517	-3.222	0.086
	62.5-90	0.176	-1.587	0.178	-	-	-	-
6061-T6	0-17.5	0.345	-1.335	0.027	2.6	0.660	-2.075	0.372
	17.5-32.5	0.304	-1.306	0.062	2.5	0.602	-2.037	0.038
	32.5-47.5	-	-	-	-	0.549	-2.035	0.143
	47.5-62.5	-	-	-	-	0.513	-2.122	0.178
	62.5-90	-	-	-	-	0.257	-2.142	0.094
7075-T6	0-17.5	0.345	-1.335	0.027	2.5	0.579	-1.922	0.062
	17.5-32.5	0.304	-1.306	0.062	2.6	0.570	-1.943	0.066
	32.5-47.5	0.211	-1.157	0.232	2.5	[illegible]	-1.960	0.070
	47.5-62.5	0.215	-1.416	0.147	2.2	0.345	-1.803	100
	62.5-90	-	-	-	-	0.317	-2.023	0.180

relatively slowly varying function of angle off axis. These facts form the basis for attempts to simplify analytical studies of hypervelocity impact cratering by assuming that the problem has a one-dimensional spherical geometry. This suggests physically that a hypervelocity impact into a thick target is equivalent to a sudden, confined energy release in a small region of an infinite medium.

Using this type of assumption Rae (Ref. 18) applied point source blast wave theory to studying the hypervelocity impact problem. His approximate methods for solving the symmetric problem are discussed in Chapter VII. In addition, he explored the effects of asymmetry (i.e. the existence of the free surface at the target face) and showed that, for this approximate theory, the variations in shock variables such as peak pressure off axis had only a minor effect on those same variables measured on axis.

Physically, it would be expected that the maximum peak normal stress would occur on axis, that the stress would decrease slowly with increasing angle off axis, and that it would then drop more rapidly to zero as the region of the free surface is reached. This general trend is confirmed by the data obtained here -- see Fig. 90 which compares the results of the experimental data reported earlier for 1100-0 aluminum for the various angle ranges and Fig. 91 which makes the same comparison for the 7075-T6 alloy. These results indicate that the velocity decay (or stress decay) does not change with angle in the higher stress region to within the accuracy of the experimental data, although the absolute velocity (stress) does drop in about the expected way as a function of angle off axis. In the lower stress range, the magnitude of the curve varies with off-axis angle in roughly the same manner as before, but here the stress seems to decay at a higher rate as the off-axis angle gets large. There was not sufficient experimental data obtained to determine the desired decay curves for the large-angle case ($\sim 70^{\circ}$ off-axis) for 1100-0 aluminum or for the high stress range of the 7075-T6 aluminum. The individual data points actually obtained are plotted, with several typical error bars, to illustrate that the data follows the qualitative trend discussed.

The variation of peak normal stress (normalized to the on-axis value) with angle is shown in Figs. 92 and 93 for three shock radii, 2, 4, and 8 cm for 1100-0 and 7075-T6 aluminum targets respectively. The approximate curves drawn through the data points show the type of behavior discussed earlier. The disk velocity (or peak stress) varies only a few percent from its on-axis value out to off-axis angles as high as 25-30 degrees. The stress then drops smoothly with increasing angle to zero at ninety degrees which corresponds to the free front surface.

An anomalous behavior is displayed by the data from the 1100-0 aluminum at a shock radius of 8 cm when the stress decreases toward zero with increasing angle very suddenly at about 40 degrees. This peculiar behavior implies that the stress decay rate changes with the angle off axis at large shock radii. One explanation is that rarefaction waves originating along the free front surface have overtaken the shock wave by this time and are creating further attenuation. It is

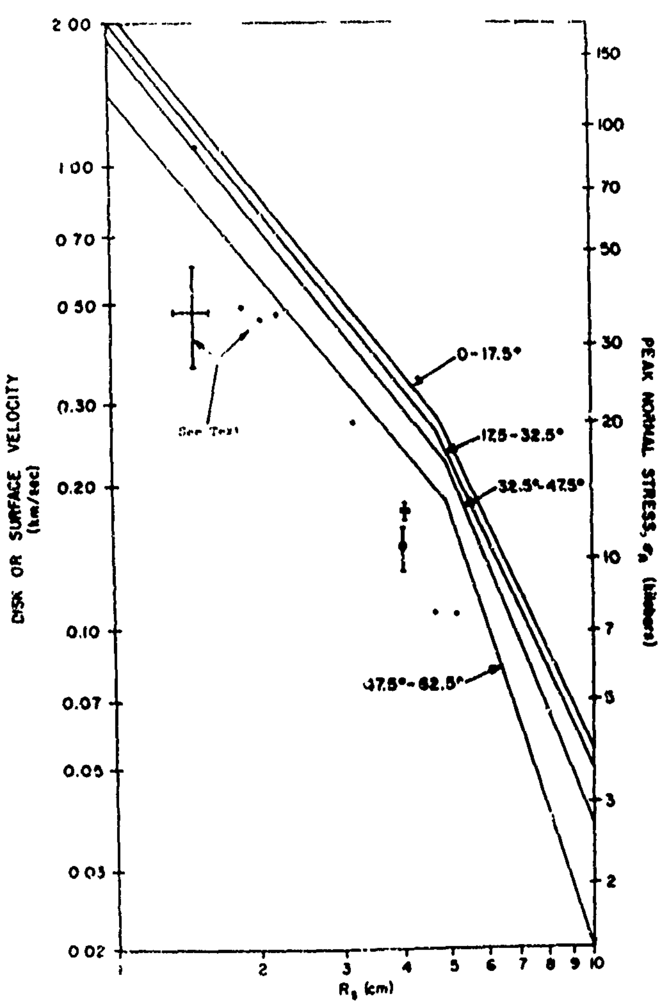

Fig. 90. Variation of Disk Velocity Decay as a Function of Angle Off Axis -- 1100-0 Aluminum.

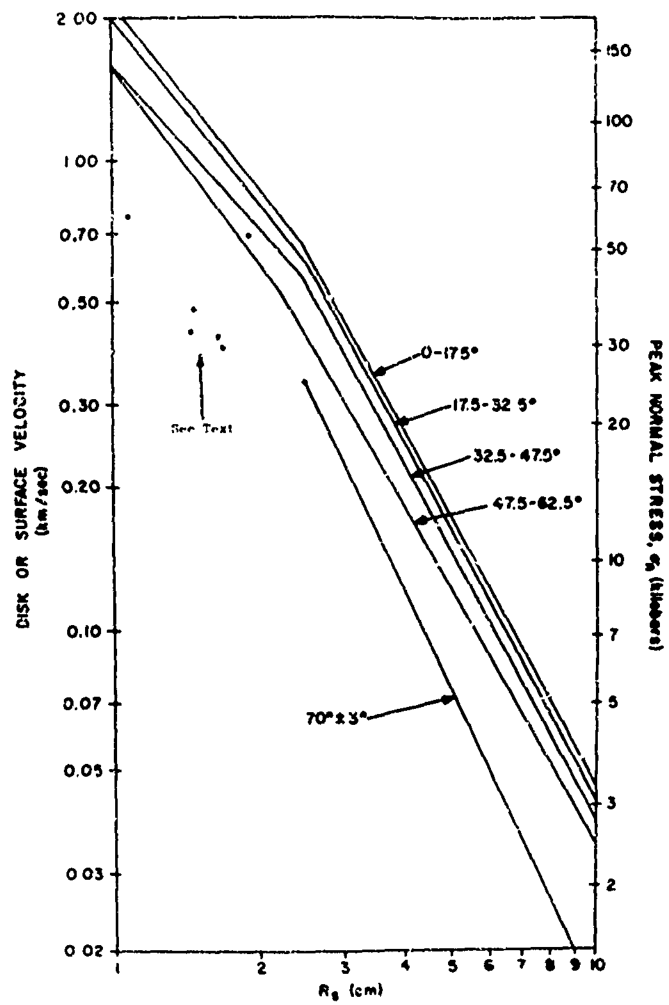

Fig. 91. Variation of Disk Velocity Decay as a Function of Angle Off Axis -- 7075-T6 Aluminum.

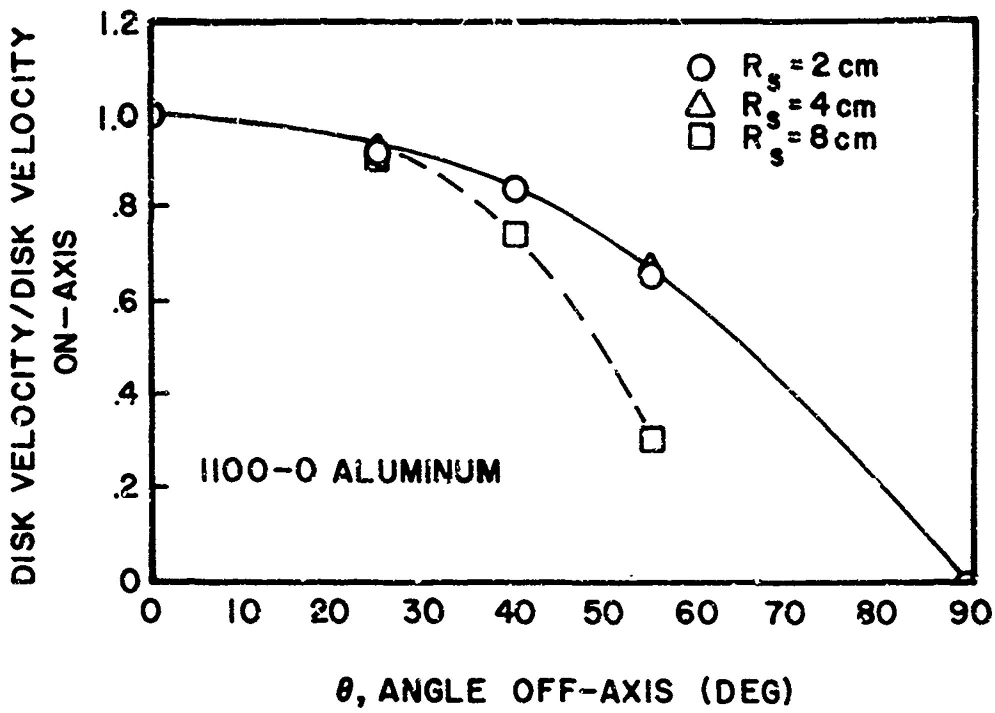

Fig. 92. Variation of Normalized Surface Velocity with Angle Off Axis for Three Shock Radii in 1100-0 Aluminum.

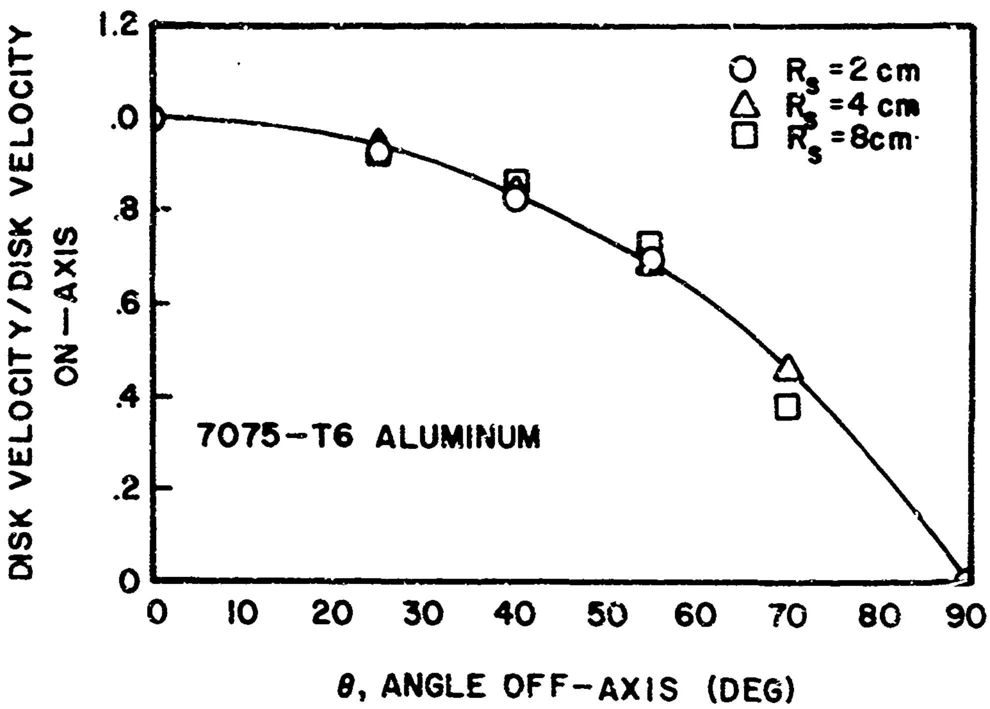

Fig. 93. Variation of Normalized Surface Velocity with Angle Off Axis for Three Shock Radii in 7075-T6 Aluminum.

not clear why the other alloys do not show this behavior.

Previous Experimental Results

Results of Charest. The earliest direct measurements of stresses from hypervelocity impacts into a metallic target were those obtained by Charest (Ref. 13) who used a fly-off disk technique similar to the one described in Chapter V to obtain the measurements. All impacts were 0.476 cm diameter aluminum spheres into 1100-0 aluminum targets at a velocity of approximately 7 km/sec, and only on-axis measurements were made. For years, this has been the only direct experimental data on stresses in a metallic target available to researchers for correlation with theoretical or analytical studies. Charest's data has been scaled linearly with size to the nominal 0.635 cm diameter projectile used here and has been scaled with projectile velocity to the nominal 7 km/sec in accordance with the procedure of Appendix E. The scaled results are compared with those obtained in this study in Fig. 94.

The agreement is quite good, especially at the higher stresses. In the shock radius range of $2.5 < R_s < 5$ cm, Charest's data tends to fall slighrly lower than that obtained in this study. The net result is that the change in slope of the stress decay curve reported here is not apparent in Charest's data. The consistent results shown earlier for various angles with respect to the trajectory covering three separate aluminum alloys strongly substantiates the conclusion that the knee in the decay curve actually exists. Charest's results are consistent with the curve of Fig. 94, but display more scatter than the data from which the curve was derived.

Based upon his data, Charest derived the following expression for the decay of the peak normal stress, σ_n :

$$\sigma_n / \sigma_H = 1.234 \left[\frac{R_s}{R_{so}} \right]^{-1.6} \quad \text{for } R_s \geq 1.14\, R_{so}$$

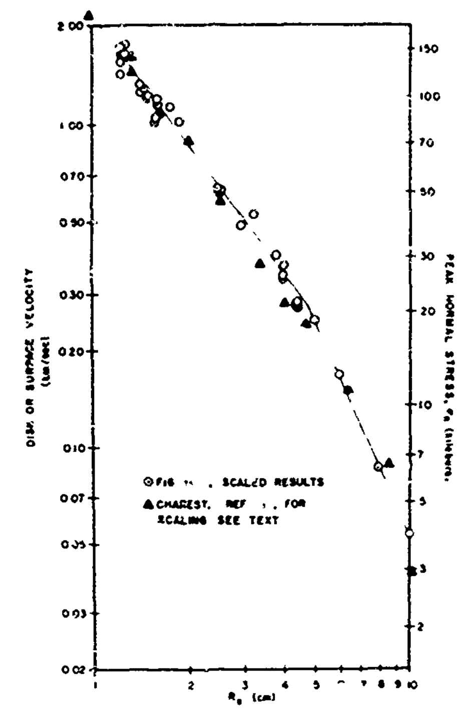

Fig. 94. Comparison of Data with Results of Charest (On Axis).

where σ_H is the one-dimensional Hugoniot pressure at impact, and R_{so} $(=d/2)$ is the projectile radius. The upper limit of validity was obtained by simply extrapolating this equation to the point at which $\sigma_n = \sigma_H$.

Expressed in the same form, the results of this study are as shown in Table IX. For these experiments, $\sigma_H = 962$ kilobars and $R_{so} = 0.3175$ cm. To derive these decay laws, the experimental data reported earlier (Figs. 75, 80 and 85) was converted to log stress versus log shock radius and straight lines were least squares fitted to these data points over the various ranges of interest. For the lower stresses, the results (i.e. the exponents) compare closely with those obtained in Table VIII. For the higher stresses, the increasingly non-linear relation between disk (or free surface) velocity and peak normal stress leads to a slightly altered exponential decay law. The results of Table VIII displaying the velocity versus distance decay law is preferred here over the stress versus distance decay law since the former appears to be the more fundamental quantity.

Table IX

On-Axis Stress Decay Laws

1100-0 Aluminum

$$(\sigma_n/\sigma_H) = 1.116\,(R_s/R_{so})^{-1.464} \qquad 2.1 < (R_s/R_{so}) < 15.1$$

$$(\sigma_n/\sigma_H) = 11.39\,(R_s/R_{so})^{-2.303} \qquad 15.1 < (R_s/R_{so}) < 31$$

6061-T6 Aluminum

$$(\sigma_n/\sigma_H) = 1.116\,(R_s/R_{so})^{-1.464} \qquad 3.1 < (R_s/R_{so}) < 8.2$$

$$(\sigma_n/\sigma_H) = 4.54\,(R_s/R_{so})^{-2.132} \qquad 8.2 < (R_s/R_{so}) < 31$$

7075-T6 Aluminum

$$(\sigma_n/\sigma_H) = 1.116\,(R_s/R_{so})^{-1.464} \qquad 3.1 < (R_s/R_{so}) < 7.9$$

$$(\sigma_n/\sigma_H) = 3.125\,(R_s/R_{so})^{-1.975} \qquad 7.9 < (R_s/R_{so}) < 31$$

Results of Billingsley. More recently Billingsley (Ref. 14) reported on-axis measurements for the impact of aluminum spheres onto 6061-T6 aluminum targets. He obtained two sets of data, one involving 0.476 cm diameter projectiles with a nominal velocity of 7.32 km/sec, the other using 0.635 cm diameter projectiles with a nominal velocity of 7.63 km/sec. (Billingsley also obtained data for impacts into 6061-T6 and 2024-0 aluminum at impact velocities of 4.42 km/sec and 1.52 km/sec respectively as well as data on copper onto copper impacts at 6.1 km/sec. Not being of direct interest here, this additional data will not be discussed.)

The technique employed by Billingsley was to measure directly the rear surface velocity of the flat plate target with a high speed framing camera. This procedure is valid for relatively thin targets, but at some point the strength of the material will retard the rear surface motion and destroy the validity of the experiment. In this study, experiments with fly-off disks showed clear separation between the target rear surface and the disk for shock radii as small as 1.75 cm. It therefore appears unlikely that the procedure employed by Billingsley can yield valid data for shock radii of greater than about 2 cm for a 0.635 cm diameter projectile. Applying linear size scaling to adjust the 0.476 cm projectile diameter data to the nominal 0.635 cm diameter, and applying velocity scaling in accordance with Appendix E, a portion of Billingsley's data is presented in Fig. 95 along with the on-axis 6061-T6 aluminum alloy data obtained here and presented earlier in Fig. 80. A plot of all the 6061-T6 aluminum on-axis data on a different scale is shown in Fig. 96. In each case the curve is obtained from the decay law data of Table VIII.

For $R_s < 1.0$ cm, Billingsley's data agrees well enough with the expected behavior of the decay curve, while for $R_s > 2.5$ cm the agreement with the results of this study is fair, with Billingsley's data tending to fall below the decay curve measured here. This is as expected, since his measurement technique should lead to low results at these shock radii. In the middle region, 1.0 cm $< R_s <$ 2.5 cm, where the results should be at maximum accuracy the agreement is at its worst. The agreement with Charest's data is no better. Billingsley notes this latter difference (Ref. 14:8) and attributes the difference to material strength effects. The data obtained in this study on the 6061-T6 aluminum refute this interpretation and indicate that at least this portion of Billingsley's data must be reevaluated.

Billingsley also reports the results of several numerical calculations corresponding to his experiments performed with a pure hydrodynamic (no strength) formulation. These results will be discussed in Chapter VII.

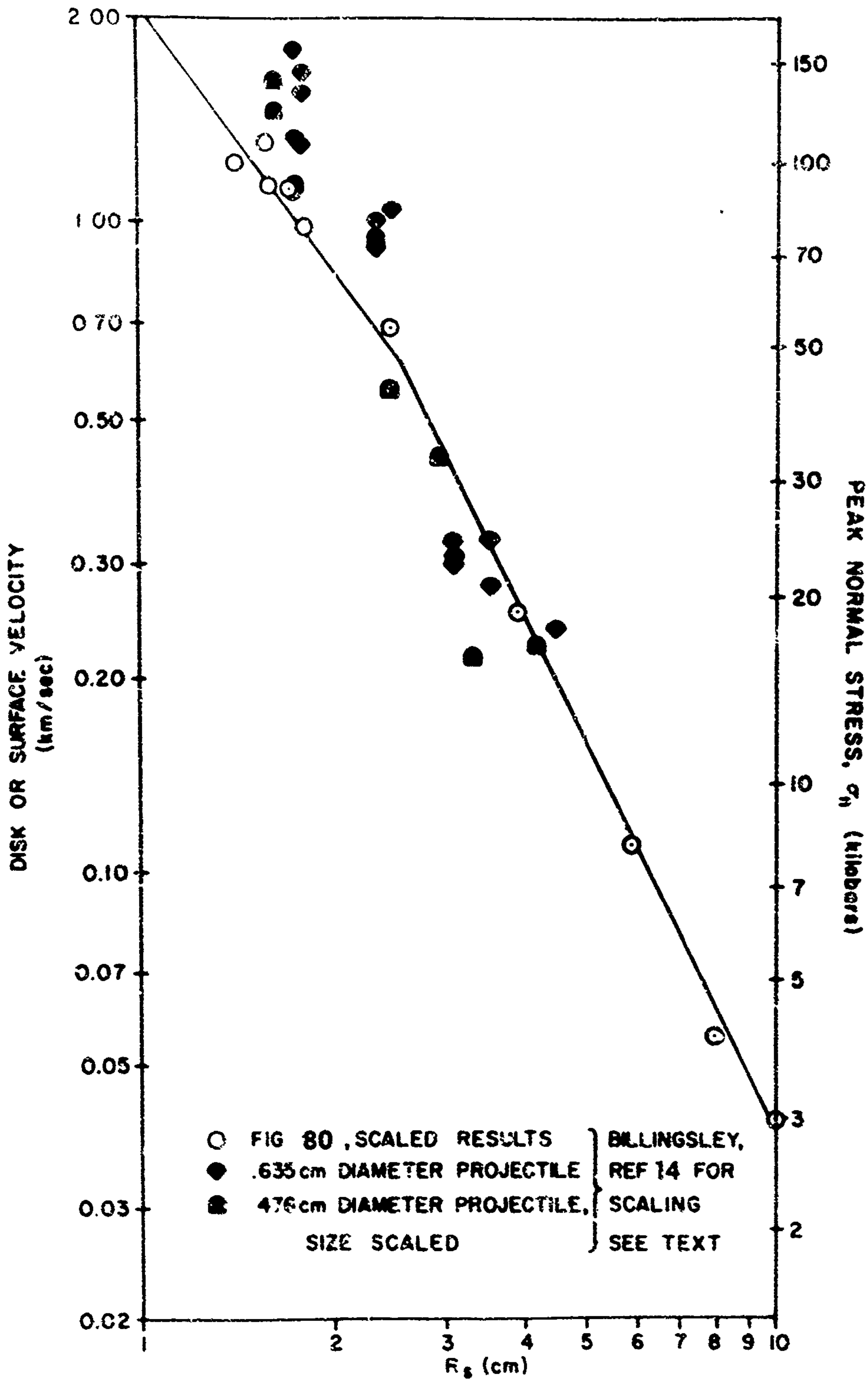

Fig. 95. Comparison of Data with Results of Billingsley (On Axis).

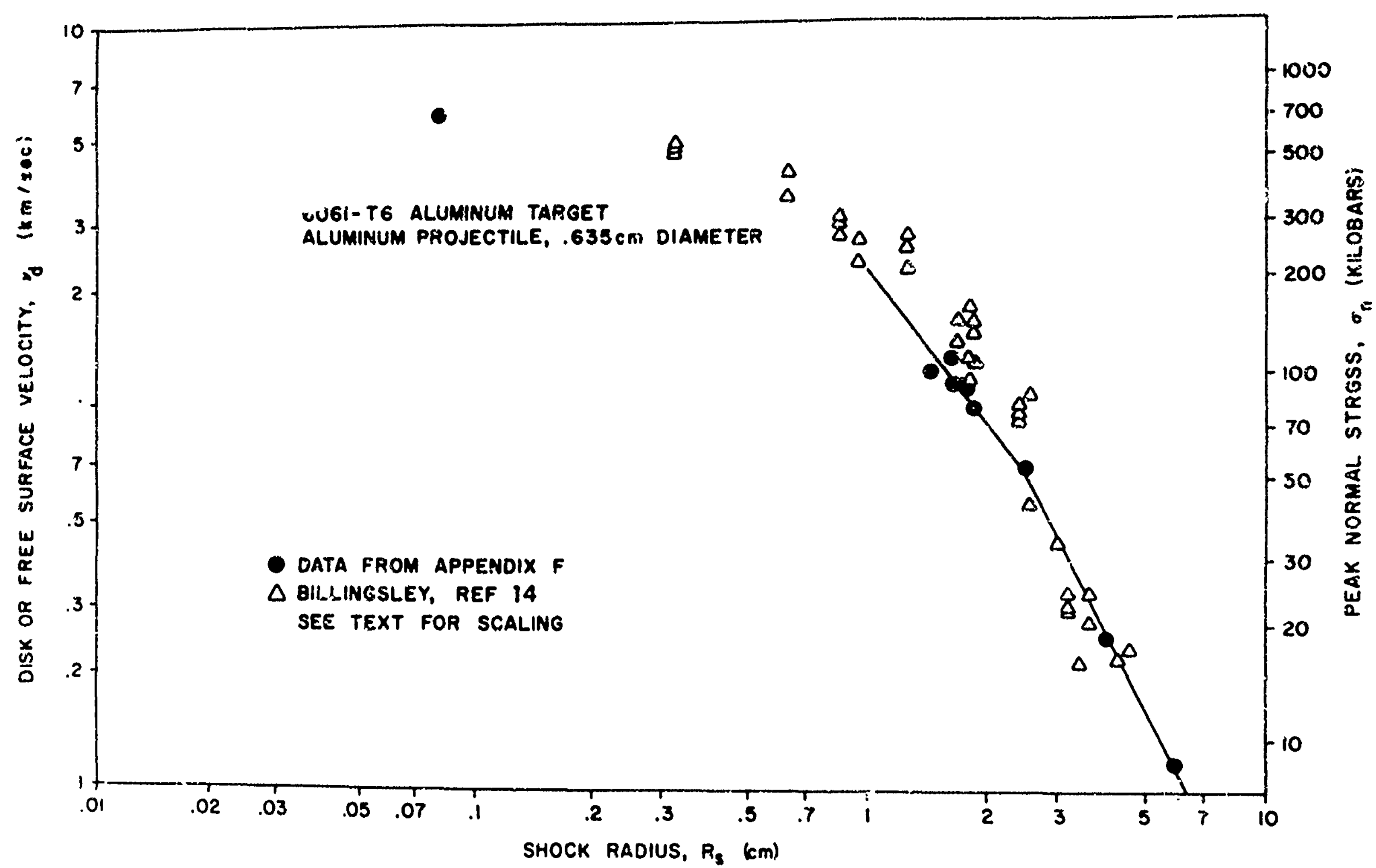

Fig. 96. Wide Range Comparison of Data with Results of Billingsley (On Axis).

Effects of Material Properties on Stress Attenuation

The effect of material strength upon the propagation and attenuation of stress waves was of prime interest in this portion of the experimental program. Little experimental work on this subject has been accomplished previously in hypervelocity impact studies although considerable work has been completed in one-dimensional (plate slap) impact research. In the following section the results obtained in this aspect of the study are described, some of the implications of previous one-dimensional research are discussed, and finally an attempt is made to explain some of the effects evident in the two-dimensional hypervelocity impact case.

Stress Attenuation Results. For discussion purposes, curves derived from the experimental data presented earlier in this chapter (Figs. 75 through 89) are given here again in a form more convenient for direct comparison of the behavior of the three aluminum alloys. The curves derived from on-axis data are shown in Fig. 97, while the curves for 25°, 40°, and 55° off axis are shown in Figs. 98, 99, and 100, respectively. Although the data is less reliable and exists for only the 6061-T6 and 7075-T6 alloys, the information for the 70° off-axis case is also shown in Fig. 100.

The main features of the stress decay are quite apparent for each alloy and show considerable similarity in the decay behavior for the various off-axis angles. In each case, the stress shows two distinct regions of different rates of stress attenuation. In the upper region where the stresses are relatively high, the behavior appears to be hydrodynamic in the sense that the decay for the three alloys is identical to within experimental error. As mentioned previously, the curves in the higher stress region in Figs. 97 and 98 were derived from a composite of data from all three alloys. At the higher angles (Figs. 99 and 100) there was not sufficient data to justify this procedure and only the results of the data obtained from 1100-0 aluminum are shown.

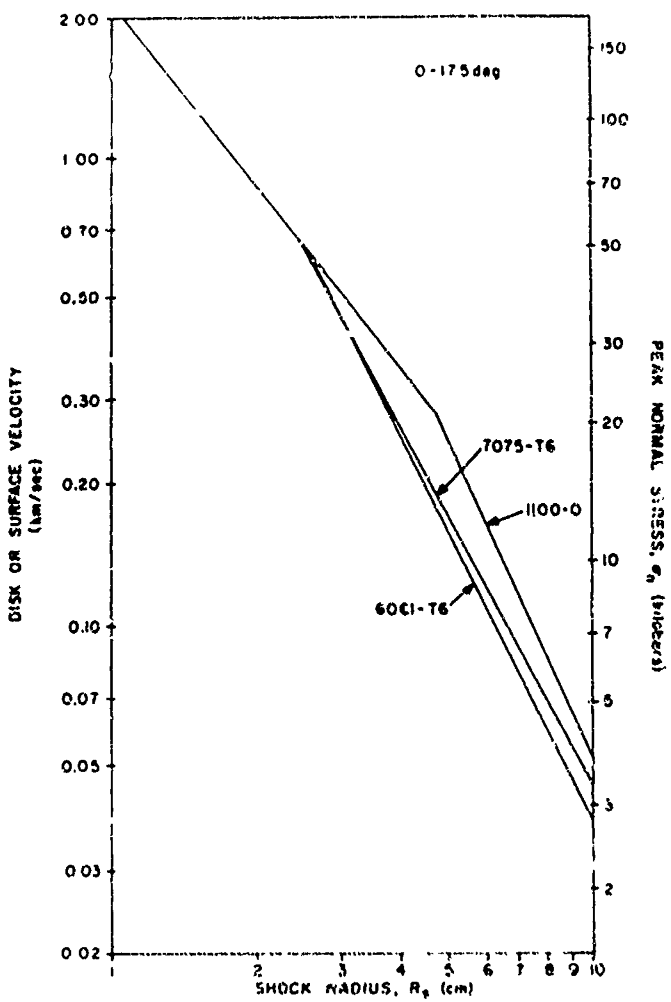

Fig. 97. Comparison of Stress Attenuation for Three Aluminum Alloys (On Axis).

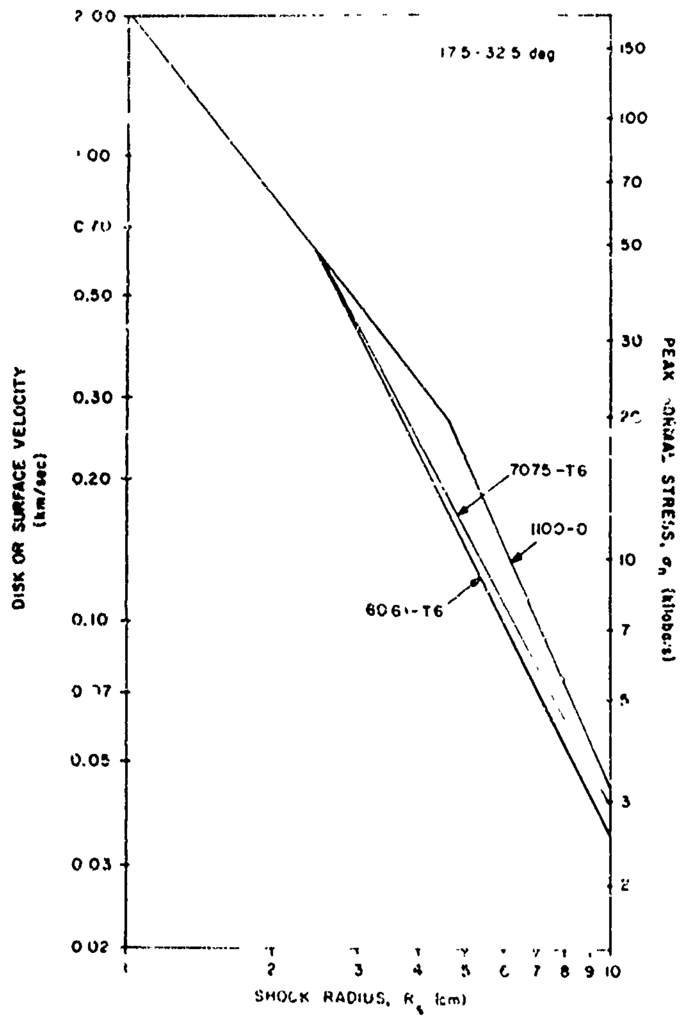

Fig. 98. Comparison of Stress Attenuation for Three Aluminum Alloys (25° Off Axis).

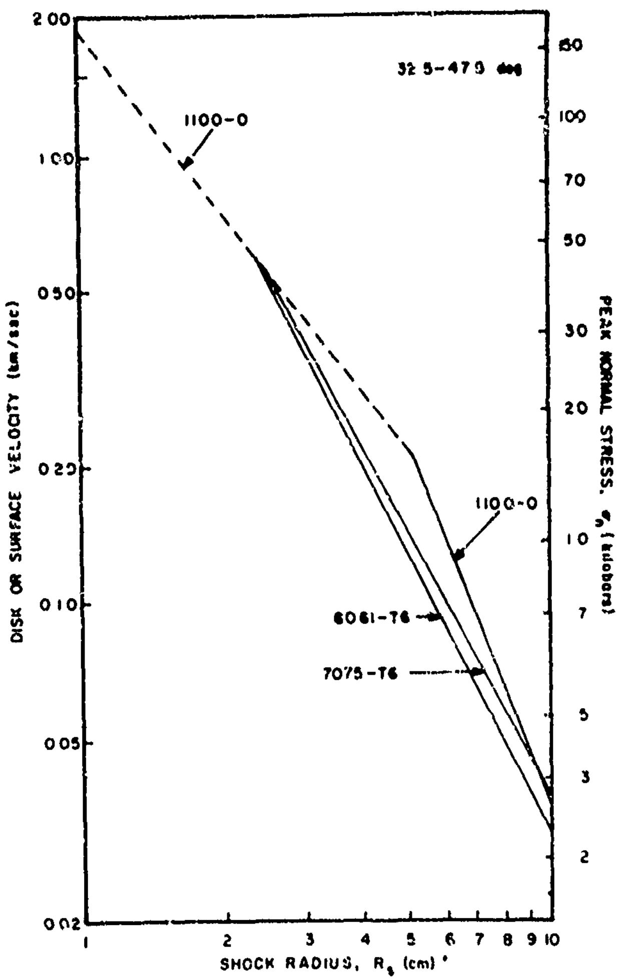

Fig. 99. Comparison of Stress Attenuation for Three Aluminum Alloys (40° Off Axis).

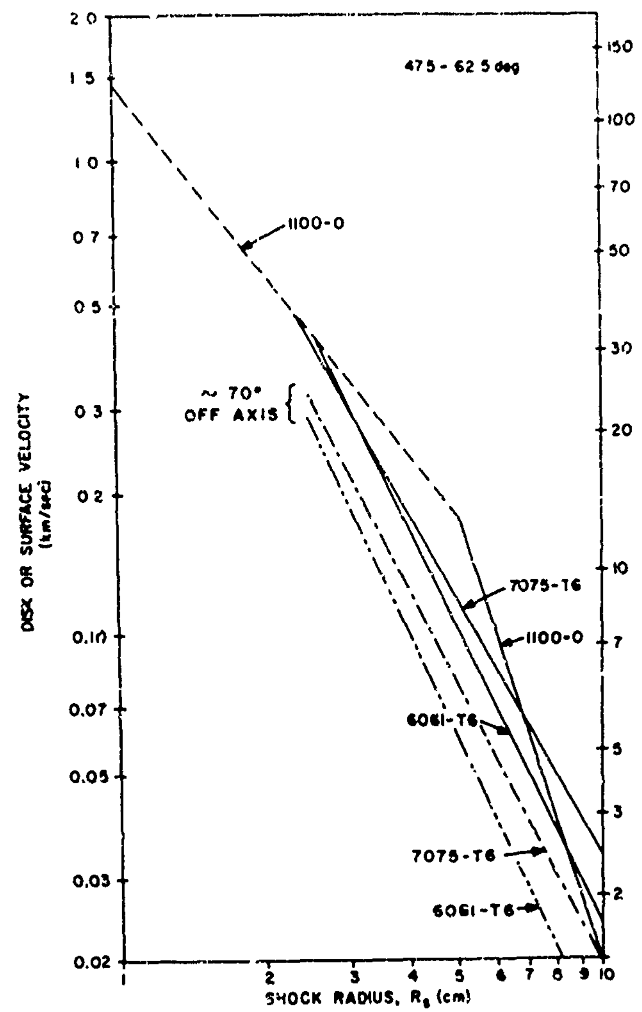

Fig. 100. Comparison of Stress Attenuation for Three Aluminum Alloys (55° and 70° Off Axis).

At a specific shock radius which does not change as a function of angle off axis (to within experimental accuracy) there is a distinct change in the shape of the decay curve for each alloy. Beyond this knee in the curve, the attenuation rate is then larger for each alloy, being greatest for the soft 1100-0 alloy and smallest for the very hard 7075-T6 aluminum. It would appear, therefore, that the experimental data shows significant non-hydrodynamic behavior in the attenuation of the shock wave produced in aluminum by a hypervelocity impact.

The effects of variation in the angle off axis, briefly discussed before, are quite evident in the experimental data. The net effect appears to be simply a shift (lowering) of the curve on the log-velocity/log-shock-radius plots as the off-axis angle is increased. To first order, the decay rates observed (the slope of the curve) do not change with increasing angle for the 6061-T6 and 7075-T6 alloys, but show a rather substantial increase with increasing angle for the 1100-0 alloy.

Several possible sources of error have been examined to ensure that the above phenomena really exist and are not simply created by the experimental methods:

a. Instrumentation. At a target thickness of approximately 2.5 cm, a transition was made from the use of the Model 300 camera to the Dynafax Model 326 camera for measuring the fly-off disk velocity. There was a region near $R_s = 2.5$ cm where there was overlap in the camera coverage and the results were consistent. The use of two cameras could not account for the knee in the curve for the 1100-0 alloy since only the Dynafax camera was used in the region of $R_s = 5$ cm.

b. Experimental Error. It is possible that scatter in the experimental data coupled with the error associated with each data point might lead to the behavior shown. This is highly unlikely. The errors associated with each data point, particularly at the lower pressures, are substantially smaller than the differences in the curves noted. Likewise, the scatter of the data in this region is small and has been taken into account, at least partially, by the statistical technique used to derive the curves. The consistent behavior between the data taken at various angles -- which constitute essentially separate experiments -- also speaks strongly against random errors in the data leading to the observed behavior.

c. Fly-Off Disks. The performance of the fly-off disk technique in the presence of a two-wave structure (i.e., an elastic precursor) has been questioned. This subject is treated in Appendix D and the two-wave structure was found not to significantly affect the fly-off disk velocity. Likewise, spall in the target will not affect the measurement of peak rear surface velocity by the fly-off disks since no tensile forces can be transmitted across the target-disk interface.

Based on these facts, it is felt that the experimental data obtained and the method used to present that data here represent an accurate portrayal of the true attenuation of the peak of the stress waves as they propagate into thick aluminum targets. It now remains to explain the various features of the results.

One Dimensional Planar Stress Attenuation. The attenuation of shock waves in a planar, one-dimensional strain situation has been studied by various researchers in an effort to develop models of the material behavior under the shock loading conditions. Some of the basic results of this research are reviewed here and will be used later in discussing the hypervelocity impact results.

The early models of shock loaded material behavior assumed purely hydrodynamic behavior, i.e., that the material had no shear strength. Among the earliest documented evidence of the elastic-plastic behavior of materials at high stress levels was the work of Fowles (Ref. 49) who performed plate slap experiments in aluminum (2024) at stresses up to 200 kilobars. He used several techniques to monitor the velocity of the rear surface of the target. The results indicated an attenuation of the stress pulse that was premature when compared to hydrodynamic theory. The application of simple elastic-plastic theory yielded satisfactory agreement with experiment provided the yield strength of the material was allowed to be a linear function of the compression of the material.

The basic mechanisms by which this non-hydrodynamic attenuation occurs are illustrated in Fig. 101. Upon impact, both elastic and plastic waves of compression are created and travel in the x-direction through the target and in the negative x-direction through the impacting plate. Upon reflection off the free surface of the plate at A, an elastic unloading wave travels back into the target at local sound speed in the compressed medium, which is higher than the speed of the compressive plastic wave in the target. Eventually, the elastic unloading wave catches the plastic compressive wave at the point B, unloading it partially and reflecting to the left. In addition, a series of plastic unloading waves was created at the point A (the plastic rarefaction fan) and the components propagate in the x-direction at velocities greater than that of the plastic compressive wave. Eventually, multiple reverberations of the elastic relief wave occur between the head of the rarefaction fan and the plastic compression wave, further decreasing the amplitude of the latter in stepwise fashion.

Shortly thereafter, the head of the rarefaction fan catches the plastic compression wave, resulting in further attenuation as more of the fan overtakes the wave. In the purely hydrodynamic case, nothing analogous to the elastic waves exists and attenuation does not commence until the head of the unloading wave from point A catches the compressive wave and starts to unload the pressure continuously.

The general situation encountered in terms of stress attenuation in the planar one-dimensional situation is further illustrated in Fig. 102 which gives a general picture of the type of results obtained by Curran (Ref. 50) and others (Refs. 51 and 52). The figure is not intended to present any specific data, only to illustrate trends.

With this background, the basic effects can be understood, but further complications arise. Curran (Ref. 50) found that to predict correctly the magnitude of the experimentally observed attenuation using simple elastic-plastic

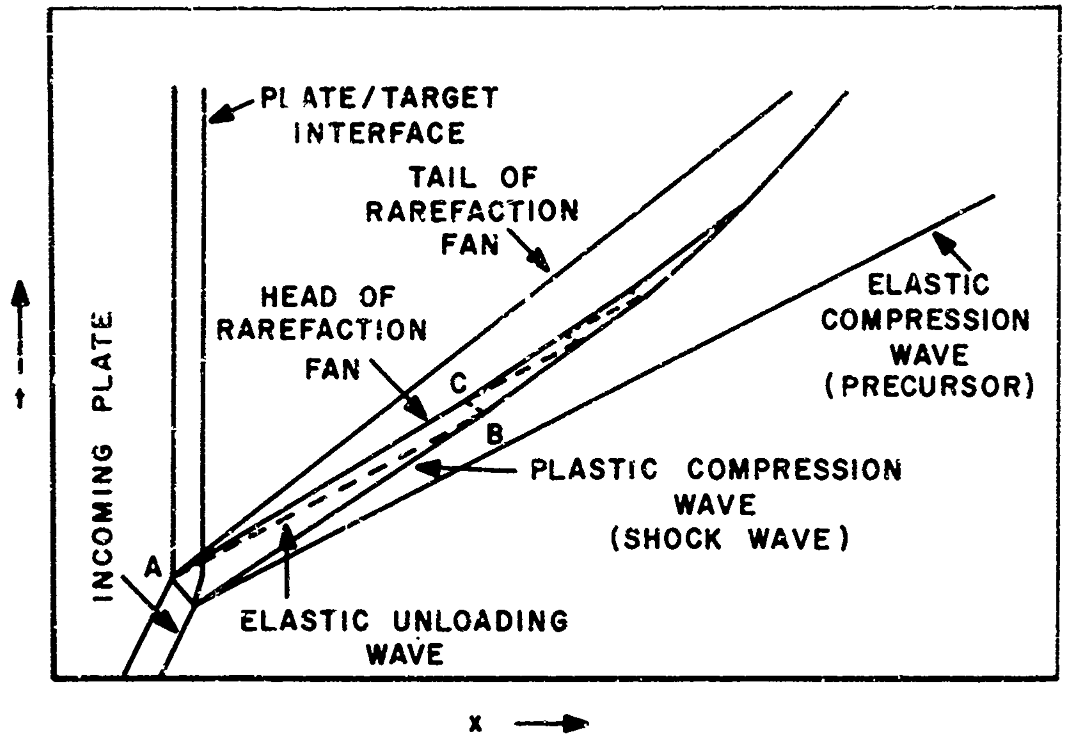

Fig. 101. Illustration of Wave Interactions in Elastic-Plastic Material Impacted by Flat Plate.

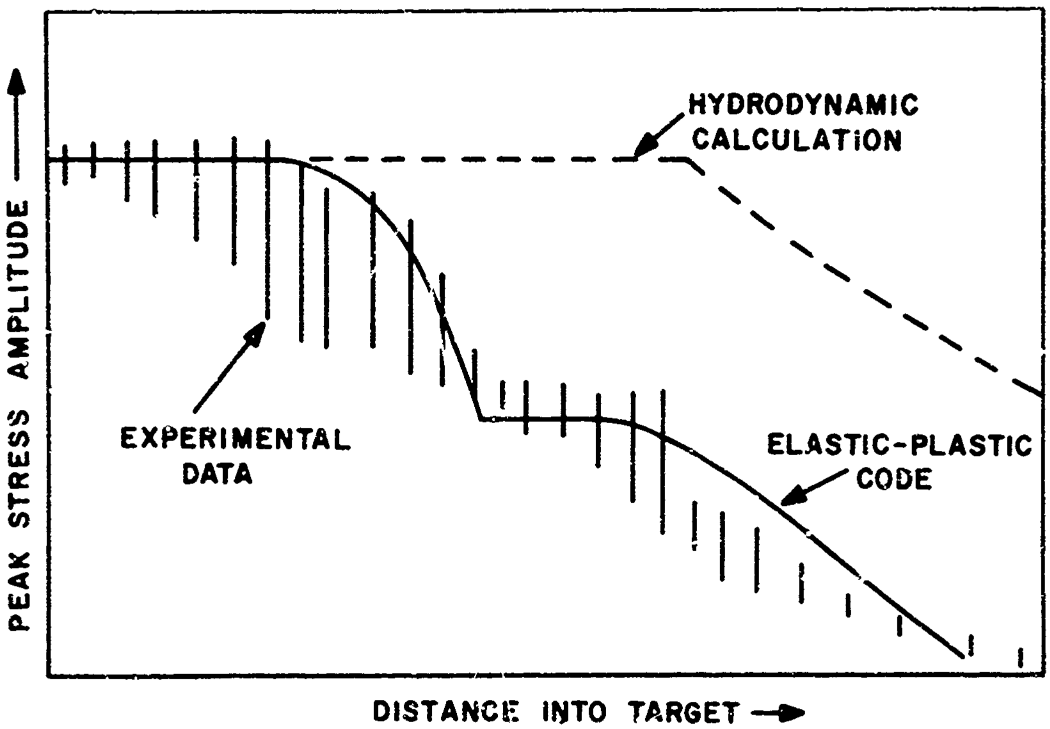

Fig. 102. Typical Results of One-Dimensional Attenuation Experiments in Aluminum.

theory, it was necessary to assume that the yield strength of the 2024 aluminum used varied with the compression of the material. He proposed that the tensile yield strength varied linearly from its value of less than 1 kilobar at zero pressure to over 12 kilobars at an imposed pressure of over 200 kilobars. Similar results were also reported by Mader (Ref. 53) who obtained good agreement between elastic-plastic calculations using a variable yield strength model and detailed measurements of the stress wave shapes obtained experimentally with capacitor gauge techniques.

Erkman, et al (Ref. 52) performed additional attenuation experiments in 2024 and 1060 aluminum and confirmed the essential correctness of an elastic-plastic treatment of the shock wave attenuation in addition to exploring the effects of a shear modulus that varied with compression. As shown in Fig. 102, calculations with the usual elastic-plastic theory show a rounded, step-like decrease in the stress at the point where the elastic relief wave overtakes the plastic compression wave. Further, there is a region of constant stress associated with a distinct separation between the elastic relief wave and the plastic rarefaction fan that follows. Erkman et al., found no evidence of the existence of this step-like behavior in their experimental data. On the basis of his evidence, Erkman concluded that a Bauschinger effect (lack of distinct yield point upon relief) in the aluminum was spreading the elastic relief wave so that the attenuation became one smooth process. In addition, Erkman discovered significant differences in the behavior of the 2024-T351 and 1060 aluminum alloys employed in the experiments. The 1060 alloy indicated a more fluid-like behavior at the higher pressures.

Somewhat better agreement between the theory and the experimental determination of the point at which attenuation starts can be obtained by allowing the elastic modulii to vary as a function of the hydrostatic pressure (Ref. 54:86). This results in an increase in the bulk modulus, K, and consequently in the speed at which the elastic relief wave propagates.

More recent experiments by Seaman, et al (Ref. 55) were conducted in measuring the complete stress-time profile of the wave at various positions in targets of 2024-T8 and 6061-T6 aluminum with manganin transducers. They concluded that (Refs. 55:92 and 98):

a. A pronounced Bauschinger effect in both alloys governed the speed of the rarefaction waves and the stress attenuation rate. A gradual transition from elastic to plastic behavior, rather than a specific yield point, was observed upon unloading, with a continuously decreasing shear modulus.

b. No stress relaxation effects were observed, although this does not preclude their existence at early times.

c. A large elastic-plastic transition region was also observed upon loading for both alloys. This leads to a gradually rising non-steady-state profile between the precursor and main wave.

The variety of studies cited above serves to illustrate the complexity of the shock wave propagation and attenuation processes, even in the simple, planar geometry of the plate impact experiment. It has been amply demonstrated that elastic-plastic theory leads to a relatively good description of the propagation, but the details depend upon the behavior of the material. Even in such a simple material as aluminum, such things as the Bauschinger effect, strain hardening, strain-rate effects, and a non-linear transition between elastic and plastic states may affect the shock wave.

Spherical Geometry. The divergent geometry typical of the hypervelocity impact of a compact projectile onto a large target severely complicates the situation. Here it is more difficult to visualize the events since the nearly spherical symmetry imposes a geometric attenuation on top of that produced by material effects. The initial loading conditions are also much more complicated than in the plate impact case. In the latter, one-dimensional strain can be assumed, while a hypervelocity impact creates a crater that grows in the presence of flowing material right in the region where the loading that will create a shock wave is taking place. Few really complete analytical or numerical studies of strength dependent shock wave propagation in this complicated hypervelocity case have been carried out.

By making several simplifying assumptions regarding geometry, Mok (Ref. 56) was able to provide some insight into the wave propagation phenomena. He assumed a one-dimensional, spherical geometry. The inside of a spherical cavity in the medium was assumed to be loaded by a pressure pulse of finite amplitude and fixed duration. The equations of motion and an elastic-plastic material model were then solved numerically (finite difference techniques) to determine the subsequent material motion. In this situation it is, unfortunately, impractical to construct a reasonably accurate r-t plot of the wave interactions to check the numerical calculations (as was done by Curran[Ref.50] in the planar case), since the characteristics of the equations of motion are curved paths due to the geometry.

The features of the stress attenuation results obtained by Mok (Ref. 56:35) are illustrated in Fig. 103. No scales are shown since only the shape of the curves and relative slopes are of interest. The upper portion of the decay curve represents the propagation of the plastic (or hydrodynamic) wavefront prior to its being overtaken by unloading waves. In this region the slope of the curve is nearly -1, implying that the free surface velocity (or particle velocity, u) varies as $1/R_s$. The approximate slopes of these curves are shown in parentheses.

Assume that the shock thickness remains constant in this regime and that the energy within the shock wave is conserved. If the shock pulse is sufficiently uniform that it can be assumed to be at constant density, the specific internal energy, e, of the shocked material is proportional to $1/R_s^2$. Likewise, it can be shown from the Rankine-Hugoniot jump conditions that, behind the shock front, $e = (1/2)u^2$. Consequently

$$u \propto 1/R_s \qquad \text{(Eq. 10)}$$

agreeing with the results of Mok's calculations. This result is also obtained at much lower pressures, where acoustic approximations may be employed.

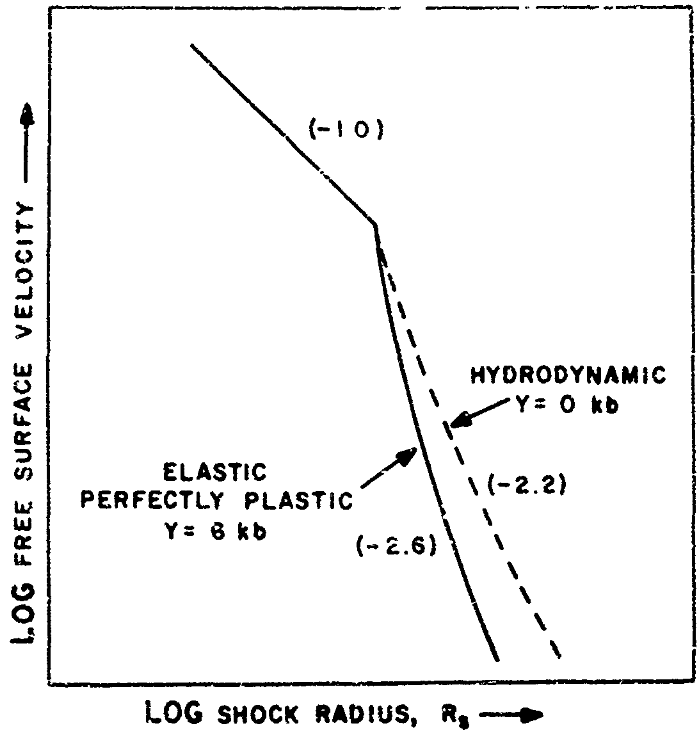

Fig. 103. Shock Wave Attenuation Results for One-Dimensional Spherical Geometry According to Calculations by Mok.

The numerical results reported by Mok are, unfortunately, not of sufficiently fine resolution that the behavior of the stress waves in the region of the knee of the curve can be examined in detail. The change in slope at this point is clearly due to release waves catching the main compressive wave, but the distinction between the elastic and plastic unloading waves and the separation between the two are not apparent in the results reported. This might have been affected by the size of the zones used in the numerical calculations.

The lower portions of the attenuation curves show a substantial difference in slope due to the variation in the postulated material strength. Mok (Ref. 56:39) notes that: "This difference in pressure is about the same order as the yield stress of the material and appears to be nearly constant throughout the propagation. Accordingly, the influence of the yield strength becomes more significant as the strength of the shock wave becomes weaker." This is apparently caused by the fact that the strength dependent attenuation is caused by the elastic unloading wave and that the amplitude of this wave is related to the tensile yield strength of the material.

The net affect is that for two materials with the same Hugoniot, the material with greater yield strength exhibits a lower stress at large shock radii once the elastic rarefaction wave has overtaken the plastic compression front.

Comparison with Experimental Results. In view of the descriptions of strength dependent wave propagation just given, the experimental shock attenuation results obtained here will be discussed in more detail. The reader is again referred to Figs. 97 through 100, particularly the first of these where the on-axis attenuation is displayed.

In the high stress region, the behavior of the attenuation is substantially different (more severe) than that calculated by Mok for his idealized one-dimensional simulation of a hypervelocity impact. The higher attenuation recorded in the experiments probably indicates that the loading history is unlike that described by Mok due to the processes occurring in the cratering region. The experiments appear to produce a stress pulse whose amplitude drops sharply with distance behind the shock front, whose components travel at different velocities and which, hence, tends to spread out as it progresses, leading to increased attenuation. The two-dimensional aspects of the impact, the lateral flow in the crater and rarefactions originating from the edges of the deformed projectile, are undoubtedly the source of these differences. The results indicate that constant pressure loading, such as that studied by Mok, is not a good simulation of the hypervelocity impact loading. The technique developed by Mok is, however, extremely useful in studying and understanding the hypervelocity impact behavior. It would be very interesting to explore further the effects of different loading histories on the subsequent wave propagation and, with fixed loading history, to study the effects of different models of the materials behavior.

In each case, the change in slope of the stress attenuation curve appears to be due to the overtaking of the plastic compression wave by an unloading wave.

For the 1100-0 aluminum, the strength is so small that the material apparently behaves plastically (nearly hydrodynamically) down to very low pressures. The point of catch-up is about 5 cm into the target. This corresponds to a time of about 8.3 μsec after impact -- see Fig. 104 later in this chapter. Assuming that during the impact the projectile deformed such that it was roughly 0.5 cm thick, the rarefaction must travel about 6 cm in the 8.3 μsec period, representing an average velocity of about 7.2 mm/ μsec. This is not an unreasonable number considering the highly compressed material that the rarefaction had to traverse.

Similarly, it appears that the knee in the stress attenuation curves for the 6061-T6 alloy represents the arrival of the elastic unloading wave at the compression front. In this case, the knee is about 2.5 cm into the target, requiring the elastic unloading wave to travel a distance of roughly 3.5 cm. According to Fig. 104 again, this occurs at a time of about 3.7 μsec after impact. This represents an average elastic unloading wave speed of slightly under 10 mm/ μsec, which again is reasonable (see Ref. 52:45).

Once unloading has occurred, the slopes of the stress attenuation curves are more difficult to explain. In fact, the slopes lie in inverse order of what would be expected on the basis of Mok's results, i.e., the soft 1100-0 alloy shows the highest attenuation rate, while the strong 7075-T6 alloy shows the lowest attenuation rate. In all likelihood, this phenomena is related to the unloading history of the original stress pulse in each material. The flow of material and two-dimensional rarefaction effects in the region of the impact point vary greatly for the soft and hard alloys (see Chapter IV, for example) so that the stress unloading is also probably quite different. There does not seem to be enough information available here, at least without employing additional computer calculations, to verify the effects of loading history on the wave propagation.

Note that in none of the data is there any evidence of the ramp behavior (see Fig. 102) discussed earlier for the one-dimensional case. This seems to confirm the earlier findings that no specific yield point exists in unloading for these alloys.

The behavior of the attenuation in the 1100-0 alloy as a function of the angle off axis is remarkably different from the other alloys. This effect may be at least partly related to the apparently unusual unloading history of the 1100-0 material in the crater region, although it is unlikely that this unloading history continues to manifest itself at such large distances from the impact point.

The experimental results obtained in this study have led to a more thorough description of the attenuation process and their strength dependence in the hypervelocity impact situation. Certainly, not all the observed behavior has been satisfactorily explained. Mok (Ref. 56:39) pointed out that, due to the sensitivity to loading history, spherical shock wave experiments represent a complicated configuration for examining the basic effects of material behavior upon shock wave propagation. The results presented above confirm his proposition. It must be pointed out, however, that experiments such as these are essential to the full understanding of two-dimensional wave propagation (as opposed to studies dealing solely with material models) where the load history is not known a priori and it is in this context that the results are believed to be valuable. In reality, practical problems must employ computer codes that calculate all the processes, including the load history, and experimental confirmation of proper operation of these extremely complex codes must be available.

Shock Wave Arrival Time Results

The arrival time instrumentation described in Chapter V was applied to many of the experiments cited in Table VII, either as an add-on, or in some cases as the primary experiment. Some 28 experiments yielded decipherable data. The data obtained is contained in Appendix F, Table XXI.

It was the original intent of these experiments to measure the shock trajectories in each of the three aluminum target alloys, 1100-0, 6061-T6, and 7075-T6 and to use this data to study differences in the shock propagation behavior of these materials. In each case, it was desirable to measure the arrival time of the steep fronted plastic wave if a complex wave structure were present.

The results obtained have not been completely consistent with this objective, although much useful information has been obtained.

The shock trajectory is not a sensitive measure of shock propagation phenomena (as will be discussed in Chapter VII), consequently extreme accuracy is required to separate the effects of alloys of the same basic material based upon the trajectory of the plastic front alone. It would not appear from the data obtained that such accuracy is possible with the techniques employed. In fact, it is probably impossible to perform this task with any realistic experimental technique that does not resolve the structure of the wave front.

A variety of phenomena, some experimental, some physical, affected the shock wave arrival time results. These effects are most easily discussed by inspecting the data obtained -- shown in Fig. 104. The data for all three alloys has been shown on one plot to make the discussion easier. The solid line is the theoretical shock trajectory for a hydrodynamic shock wave as derived from a blast wave model of the impact due to k[illegible]v -- see Chapter VII and Ref. 11. This shock trajectory agrees well with similar data obtained from the "variable energy" model developed in Chapter VII. The shock trajectory data obtained from pure hydrodynamic (OIL code) numerical results from Ref. 14, and from the STEEP code calculations of Ref. 32 also show good agreement, although reliable results are available only for the region $R_s < 3$ cm. The dashed line indicates the approximate expected trajectory of an elastic precursor traveling at the acoustic sound speed in aluminum, approximately 6.40 mm/ μsec.

If the instrumentation were properly sensing the arrival time of the plastic shock front at the target rear surface, the data should all fall near the hydrodynamic trajectory shown. Obviously, much of the data does not. Several different effects must be invoked to explain these discrepancies. First, the groups of data that lie to the left of the plastic wave trajectory at about $R_s \approx 2$ cm and $R_s \approx 4$ cm were apparently caused by the early closure of the foil switch used to signal impact and to trigger the oscilloscopes. It is likely that small particulate debris hit the switch ahead (< 2 μsec) of the projectile. The quartz probe records of

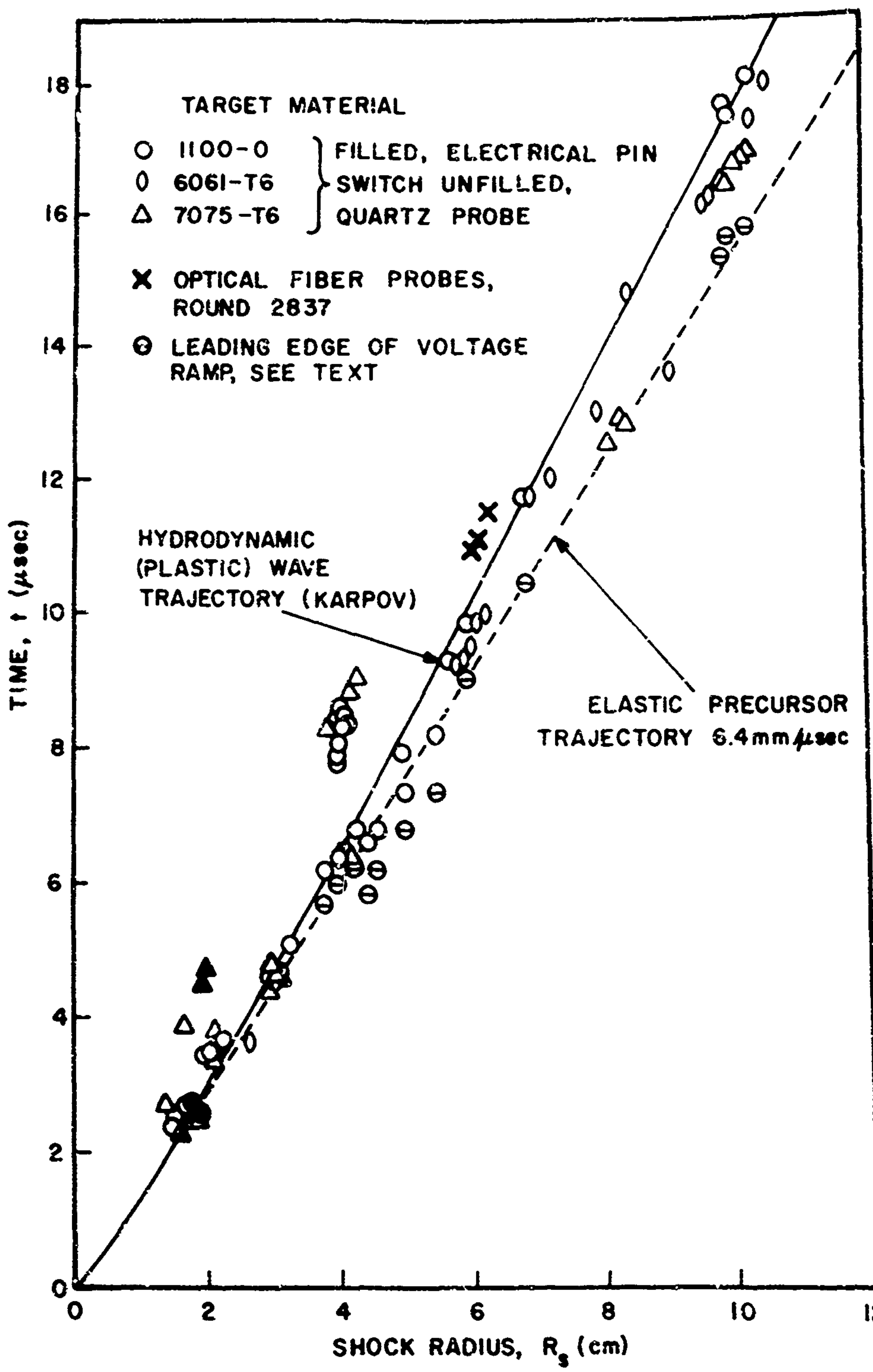

Fig. 104. Shock Front Arrival Time Data, All Target Materials.

several of these events yield some plausible confirmation of this phenomenon -- a small pressure pulse (apparently) precedes the main pulse caused by the projectile-generated shock wave. This debris may have been caused by the worn gun parts employed during a portion of the experimental program.

The optical fiber probe data is internally consistent, but does not agree well with quartz probe data obtained on the same round (2837). This is probably due to difficulties in interpreting what constitutes light cut-off from the fiber optic probe. Further development would be necessary before this type of probe could be used with confidence.

The remaining data does indicate significant trends if certain assumptions are made regarding errors or inconsistencies in the oscilloscope records. First of all, the electrical pin switch probes yield data that is consistent with the theoretical shock trajectory and, also, the results of the quartz probes in the region $R_s < 3$ cm when those rounds involving gross early switch closure are rejected. The record obtained on round 2811 at $R_s \approx 4$ cm where both electrical switch and quartz probes were mounted on the same target shows that, at this stress level, the electrical switch probe is responding more slowly than it should. It yielded signals about 1/2 μsec late with respect to the quartz probe signal. At higher stress levels, no such delay in closure was detected.

At small shock radii and high stress ($R_s < 4$ cm) the quartz probes generally yielded good data that is consistent with the predicted shock radius. There is scatter in the data in this region, probably due largely to errors in measuring the value of the shock radius R_s. The exact impact point was hard to determine accurately for the small targets, all of which suffered severe deformation or penetration during the impact process. Errors in measuring R_s of at least ± 0.15 cm are quite realistic.

The quartz probe records at the larger shock radii are the most interesting. As explained earlier, the signal omitted by the quartz crystal is proportional to the stress induced in the crystal. The existence of edge effects, combined states of stress created by the divergent shock wave geometry, and multiple reflections in the thin crystal all combine to preclude the use of the quartz probe device to measure directly the stress amplitude.

The probe does, however, give a qualitative picture of the stress amplitude history and yields surprisingly consistent results. Typical oscilloscope traces for each of the target materials obtained at shock radii of $R_s \approx 10$ cm are shown in Fig. 105. The shape of the waveform is characteristic of the target alloy, although there is little difference between the results for 6061-T6 and 7075-T6 aluminum. The shape of the waveform persists all the way down to the smaller shock radii. In particular, the voltage ramp that appears on the leading edge of the pulse in 1100-0 aluminum has the characteristics of an elastic precursor: (1) the length of the ramp increases with increasing shock radius; (2) the ratio of the amplitude of the ramp to the voltage peak increases with increasing shock radius and (3) the leading edge of the ramp travels at the acoustic wave speed in aluminum, 6.4 mm/μsec. The latter effect can be observed from those data points on Fig. 104 marked with the symbol $\ominus$. Likewise, the data for the leading edge of the main voltage spike, marked O, agrees well with the predicted shock trajectory, so that the main pulse is seen to correspond to the plastic wavefront.

The set of four pairs of data points from Round 2851 lying to the right of the dashed line are believed to be off by about one μsec based on other quartz data from the same round. When adjusted by this amount, the results are consistent with the remainder of the data on 1100-0 aluminum.

There is no evidence of any well defined "precursor" on the quartz probe records for the 7075-T6 and 6061-T6 alloy targets. The leading edge of the pulse rises quickly, but not discontinuously, to the peak value. The rise time is slightly faster in the 7075-T6 aluminum. For both alloys the rise time becomes longer as the shock radius increases. The bulk of the data indicates that the trajectories of these waves lie somewhere between the calculated shock trajectory of a hydrodynamic wave and an elastic wave. The data lying in the region 7.9 cm $\leq R_s \leq$ 9.1

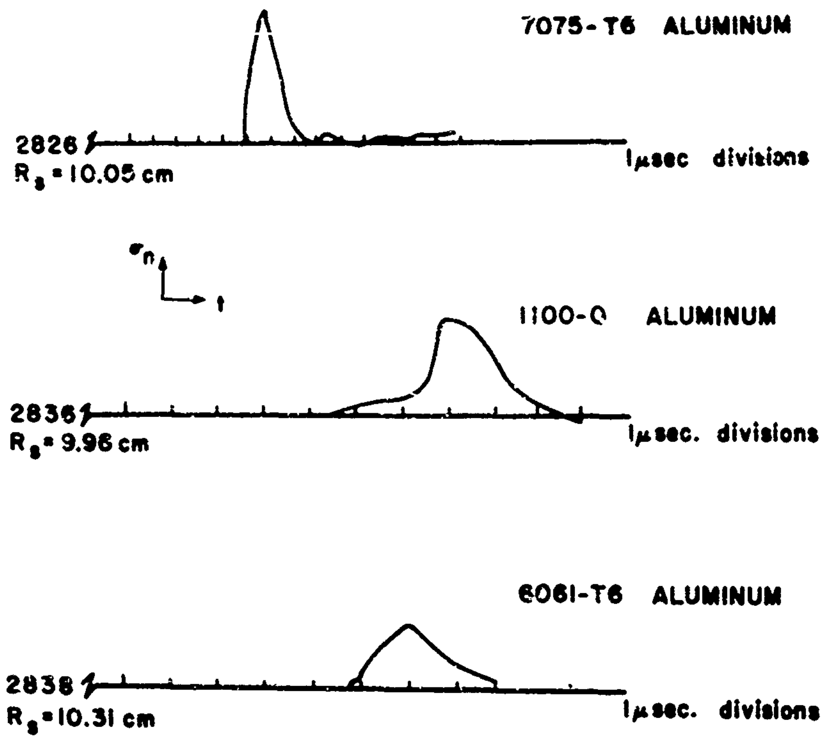

Fig. 105. Waveforms at Large Shock Radii Measured with Quartz Crystal Probes.

cm does not appear to be consistent with these conclusions, but is believed to be in error. No explanation can be derived from the available records.

The quartz probes have a good time response, and the slopes of the leading edges of the stress pulses observed are probably realistic even though the crystal cannot reach stress equilibrium until the wave has traversed the crystal and reflected off the aluminum interface at least once. The time resolution of these probes should have been about 0.1 μsec and appeared to be that good. The leading edge of the stress wave in the 7075-T6 aluminum was characterized by a very fast, almost discontinuous, rise to about half amplitude followed by a slower rise to the peak value. In the 6061-T6 alloy, the rise was more continuous and smooth (and possibly slightly slower) to the full amplitude. The stress decay measured by the quartz probes is consistent with the general picture of the wave shape expected from this type of impact, i.e., a roughly triangular shaped wave. No attempt has been made to analyze the details of the stress history from these records.

The difference in waveform detected for the three alloys is significant. The soft 1100-0 aluminum displays a distinct elastic precursor while the hard alloys -- where any elastic component would be expected to be of higher amplitude if present at all -- exhibit no precursor at all. The latter two do seem to exhibit some stress relaxation in the rising portion of the wavefront, however. Since the 1100-0 aluminum is considerably more strain rate sensitive than the other alloys, it may be that strain rate effects are influencing the structure of the rising portion of the stress pulse.

In any event, the quartz probe data has pointed out wave propagation phenomena that are worthy of additional study with more quantitative instrumentation. The experience gained in this study can furnish several valuable guidelines for such efforts: (1) the sensor chosen should have a small area to avoid errors in the calculation of the shock radius; (2) the sensor should be calibrated over a wide range of stress; (3) the sensor should be chosen, and the instrumentation designed, so that both shock time of arrival and stress history information are obtained; and (4) orthogonal image converter photographs (or similar arrangement) should be taken viewing the projectile at the time the impact switch closes, thereby yielding precise information on the impact point and precise timing of the impact with respect to the sensor signals. The most promising candidates for sensors at this time are either the laser velocity interferometer or the use of piezoresistive foil gauges compensated for divergent flow conditions if necessary.

<u>Summary</u>

A series of seventy hypervelocity impact experiments was completed in a program designed to study the propagation (trajectory) and attenuation of stress waves in aluminum alloys. Aluminum projectiles of .635 cm diameter were launched at a velocity of about 7 km/sec and allowed to impact targets of 1100-0, 6061-T6, and 7075-T6 aluminum. Measurements were then made at various angles

and distances from the impact point of the wave arrival time and its peak amplitude employing the techniques previously described.

The variation of peak stress with angle off axis has been measured and found to be in general agreement with the qualitative picture of a hypervelocity impact as being similar to a point source wave expansion. Beyond 40° off axis, this picture breaks down rapidly.

Measurements of the attenuation of the peak normal stress in the wave with distance demonstrated the existence of a knee in the attenuation curves associated with significant non-hydrodynamic attenuation in the 6061-T6 and 7075-T6 alloys. The 1100-0 alloy exhibits essentially hydrodynamic behavior down to relatively low stress levels. The behavior of these alloys is interpreted in terms of existing one-dimensional shock wave propagation theory and experiments.

Measurements of the shock wave arrival time at various distances, although not completely successful due to timing inaccuracies, yielded confirmation of the postulated elastic-plastic behavior of the materials. The data demonstrated the substantial difference in behavior among the three aluminum alloys employed.

VII. Comparison of Experimental Shock Pressure Results with Hydrodynamic Theory and Numerical Results

The experimental program just described has yielded a large quantity of data relating the peak normal stress in the shock wave to the distance into the target and the angle away from the projectile trajectory. This information has been sufficiently complete to establish detailed stress decay laws for three aluminum alloys of widely varying strength: 1100-0, 6061-T6, and 7075-T6. Additional information has been obtained on the shock wave trajectory and, in a very limited fashion, on the wave shape. The results have been interpreted in terms of the physical processes occurring during the wave propagation. It now remains to compare these results with selected theoretical predictions of this hypervelocity impact situation.

An impact such as that described here is quite complicated--as was discussed in Chapter II and elsewhere. Consequently, attempts to treat this problem with moderately simple analytic theory have been either unsuccessful or of limited applicability. The most promising approach to treating the hydrodynamic portion of the impact has been to use the similarity method for solving the point source blast wave problem in a perfect gas and to modify this method to make it more pertinent to the actual solid material of interest. This method is described in some detail in the first part of this Chapter. Modifications to the basic theory by several authors and a new modification proposed by Torvik and this author are discussed. The results are compared with the available experimental results.

Currently, the most complete way to treat the entire impact process is numerically, through the use of a computer program to solve the pertinent equations by applying finite difference techniques. The second portion of the Chapter is devoted to a comparison of the experimental results with the limited number of computer calculations that are available for direct comparison.

Emphasis is placed upon the results of the STEEP code (see Chapter II) for those problems that were designed specifically to correspond to the experiments conducted in this study. The actual performance of these computer calculations was not a part of this effort.

Blast Wave Solutions to the Impact Problem

Analytical solutions of even the simplest impact problems are most difficult because the equations are non-linear. One of the most detailed analytical approaches was taken by Rae and Kirchner (Ref. 18, 19, and 20) who adapted gas dynamic solutions of the point source blast wave problem to impacts into solids. Their approach assumes that the materials involved behave as perfect fluids (no heat conduction, no viscosity) with a hydrodynamic equation of state, and spherical symmetry. The hydrodynamic or fluid-like behavior of the material, at least during the early phases of a hypervelocity impact, is justified on the basis that the pressures greatly exceed the yield or shear strength of the material. During the later stages of the impact process, this will not be true. A point source release of energy at the center of the coordinate system is then assumed to approximate an impact -- and the results are used to help justify this assumption. In the following sections, the essential elements of Rae and Kirchner's approach are outlined and the results are applied to the impact of a 0.635 cm diameter aluminum projectile with a velocity of 7.0 km/sec upon an infinite halfspace of aluminum. The discussion here is based primarily upon Ref. 18. Modifications to Rae and Kirchner's approach are formulated and discussed and the results are compared with experimental data.

Similarity--The Perfect Gas Solution. The approach is founded upon the concept of similarity which states that (for certain problems) properly normalized quantities (pressure, density, etc.) at any instant are the same when viewed on a scale defined by the shock radius at that instant. That is, each quantity depends upon the ratio

$$\eta = \frac{r}{R_S(t)}$$

(Eq. 11)

where r is the distance from the impact point and $R_s(t)$ is the distance from the impact point to the shock front, rather than upon r and t, the time, explicitly. The quantity η is called the similarity variable, and in certain cases may be used to eliminate the explicit time dependence from the problem.

The dynamical equations of motion in spherical coordinates with no angular dependance are:

$$\frac{\partial \rho}{\partial t} + u \frac{\partial \rho}{\partial r} + \rho \left(\frac{\partial u}{\partial r} + \frac{2u}{r} \right) = 0$$

$$\frac{\partial u}{\partial t} + u \frac{\partial u}{\partial r} + \frac{1}{\rho} \frac{\partial p}{\partial r} = 0$$

$$\frac{\partial e}{\partial t} + u \frac{\partial e}{\partial r} - \frac{p}{\rho^2} \left(\frac{\partial \rho}{\partial t} + u \frac{\partial \rho}{\partial r} \right) = 0 \qquad \text{(Eq. 12)}$$

obtained from conservation of mass, momentum, and energy respectively and where

ρ = density

u = r - component of velocity vector for a particle

p = pressure

e = specific internal energy

In addition, an equation of state in the form $e = e(p, \rho)$ is required to complete the set of equations, and the Rankine-Hugoniot conditions at the shock front represent a boundary condition on the problem.

Next, a set of dimensionless similarity functions is defined.

$$\phi(\eta, R_S) = u / \dot{R}_S$$

$$f(\eta, R_S) = p / \rho_0 \dot{R}_S$$

$$\psi(\eta, R_S) \qquad \rho/\rho_o$$

$$g(\eta, R_S) = (e - e_o)/\dot{R}_S^2$$

(Eq. 13)

where $\dot{R}_s$ = D the shock velocity. Substituting into Eq. 12 then:

$$(\phi - \eta)\frac{\partial \psi}{\partial \eta} + \psi\left(\frac{\partial \phi}{\partial \eta} + \frac{2\phi}{\eta}\right) = -R_S \frac{\partial \psi}{\partial R_S}$$

$$(R_S \ddot{R}_S/\dot{R}_S^2)\phi + (\phi - \eta)\frac{\partial \phi}{\partial \eta} + \frac{1}{\psi}\frac{\partial f}{\partial \eta} = -R_S \frac{\partial \phi}{\partial R_S}$$

$$(2R_S \ddot{R}_S/\dot{R}_S^2)g + (\phi - \eta)\frac{\partial g}{\partial \eta} - \frac{f}{\psi^2}(\phi - \eta)\frac{\partial \psi}{\partial \eta} = -R_S \frac{\partial g}{\partial R_S} + \frac{f}{\psi^2} R_S \frac{\partial \psi}{\partial R_S} \qquad \text{(Eq. 14)}$$

For similarity to apply, the variables of Eq. 13 must not be a function of the scale of the problem, R_s. The basic assumption of self-similar flow then requires that $\phi = \phi(\eta)$, $f = f(\eta)$, etc. and consequently that the right hand side of Eqs. 14 must be identically zero. In addition, to reduce this set of partial differential equations to a set of ordinary differential equations there must be no explicit time dependence in the equations, hence in the similarity solution it is further assumed that the term $\beta = R_s \ddot{R}_s / \dot{R}_s^2$ must be constant. Double integration shows that this requires $R_s \sim t^N$ where N need not be an integer. For the similarity case, the final form of the ordinary differential equations of motion are:

$$(\phi - \eta)\psi' + \psi(\phi' + 2\phi/\eta) = 0$$

$$\left(\frac{N-1}{N}\right)\phi + (\phi - \eta)\phi' + \frac{1}{\psi} f' = 0$$

$$2\left(\frac{N-1}{N}\right)g + (\phi - \eta)g' - \frac{f}{\psi^2}(\phi - \eta)\psi' = 0$$

(Eq. 15)

where the prime denotes differentiation with respect to η. In terms of the similarity functions the Rankine-Hugoniot conditions become $[\psi_H \equiv \psi(\eta = 1, R_s)]$

$$\rho_o D = \rho (D - u) \quad \rightarrow \quad \psi_H (1 - \phi_H) = 1$$

$$p - p_o = \rho_o D u \quad \rightarrow \quad f_H = \phi_H + p_o / \rho_o \dot{R}_S^2$$

$$e = \frac{p + p_o}{2} \left(\frac{1}{\rho_o} - \frac{1}{\rho} \right) \quad \rightarrow \quad g_H = \frac{f + f_o}{2} \left(1 - \frac{1}{\psi_H} \right)$$

(Eq. 16)

In addition, when the equation of state has the general form $e = e(p, \rho)$, explicit time dependence may enter into the equation of state $\dot{R}_s^2 g = F(\rho_o \dot{R}_s^2 f, \rho_o \psi)$ through the existence of the $\dot{R}_s$ term. If the equation of state takes the form $e = p\,\zeta(\rho)$, then $g = \rho_o f \zeta(\psi)$ and the explicit time dependence disappears. In the case of a perfect gas, the equation of state satisfies this condition taking the form

$$e = \frac{p}{(\gamma - 1)\rho}$$

(Eq. 17)

where $\gamma = c_p/c_v$ is the ratio of specific heats of the gas. Explicit time dependence may enter the problem also when the term $p_o / \rho_o \dot{R}_s^2$ is of the order of ϕ_H. Consequently at low enough pressure ratios, a gas dynamics problem is <u>not</u> similar.

In solids it is safe to assume that p_o, the pressure in the undisturbed material, is negligible compared to the pressure behind the shock wave. Eq. 17 can then be used in conjunction with Eqs. 16 to obtain

$$\psi_H (1 - \phi_H) = 1$$

$$f_H = \phi_H$$

$$\psi_H = \frac{1}{1 - 2\rho_o \zeta(\psi)}$$

(Eq. 18)

Given the function $\zeta(\psi)$ this set can be solved explicitly for ϕ_H, ψ_H, and f_H which means that the density ratio $\psi_H = \rho/\rho_o$ at the shock front is constant for the problem. This result is a consequence of assuming a similarity solution and implies that the solution is exact only in the region of limiting compression, corresponding to a strong shock wave in a gas. The result is categorically not true for solids except at extreme pressures (tens of megabars).

Eq. 17 rewritten in similarity variables can be differentiated with respect to η and solved for g'. This result can then be used to eliminate g' from Eq. 15 reducing these to three linear equations in the three unknowns ψ', ϕ', and f'. The set can then be solved for the unknown derivatives in the form:

$$\psi' = \psi'(\eta, \phi, \psi, f)$$
$$\phi' = \phi'(\eta, \phi, \psi, f)$$
$$f' = f'(\eta, \phi, \psi, f)$$

(Eq. 19)

Using N as a parameter these equations may then be solved to determine ψ, ϕ, and f. For any value of γ, the equations may be integrated numerically using Eq. 18 as starting conditions. The set of equations has an acceptable, single-valued solution only for N = 2/5 and, for that situation, an analytic solution has been worked out by several authors as discussed by Rae in Ref. 20:26. This is the classical blast wave problem as first described by G. I. Taylor. (Ref. 57).

The results for various values of γ ranging from 2 to 100 are displayed in Fig. 7 a-j of Ref. 20 and Fig. 12 a-c of Ref. 18.

The relation between R_s and t may then be obtained as follows. The total energy in the system is (assuming only a hemisphere):

$$E = 2\pi \int_0^{R_s} \left[e + \frac{u^2}{2} \right] \rho \, r^2 \, dr \qquad \text{(Eq. 20)}$$

In terms of the similarity variables this yields

$$E = 2\pi \rho_0 \dot{R}_s^2 R_s^3 I(\gamma) \qquad \text{(Eq. 21)}$$

where

$$I(\gamma) = \int_0^1 \left[\left(\frac{1}{\gamma - 1} \right) \frac{f}{\psi} + \frac{\phi^2}{2} \right] \psi \, \eta^2 \, d\eta \qquad \text{(Eq. 22)}$$

Hence, once $f(\eta)$, $\phi(\eta)$, and $\psi(\eta)$ are known for a given γ, this integral may be evaluated for that value of γ. The shock trajectory is then found by integrating Eq. 21 to obtain

$$R_s(t) = \left[\frac{25 E}{8 \pi \rho_0 I(\gamma)} \right]^{1/5} t^{2/5} \qquad \text{(Eq. 23)}$$

the classical result for a strong blast wave in a perfect gas. Equation 23 also determines $\dot{R}_s(t)$ which, when combined with the equation of state and Eq. 18 allows a direct calculation of ϕ_H, ψ_H, and f_H.

<u>Application to a Solid</u> -- <u>The Equation of State</u>. As noted above, the use of similarity to treat the blast wave problem implies that the density ratio across the shock front is a constant--a state which is known to be incorrect for shock wave propagation in solid materials. To see how the non-similar nature of flow in solids arises, consider the Mie-Gruneisen form of the equation of state for solids:

$$e(p,\rho) - e_H(\rho) = \frac{1}{\rho \Gamma(\rho)} \left[p - p_H(\rho) \right] \qquad \text{(Eq. 24)}$$

where the Gruneisen factor $\Gamma(\rho)$ depends only weakly on ρ and the subscript H refers to the value on the shock Hugoniot. This can be rewritten in the form:

$$e = \frac{p}{\rho\,\Gamma(\rho)} - \Delta(\rho)$$

(Eq. 25)

where

$$\Delta(\rho) = \frac{p_H(\rho)}{\rho\,\Gamma(\rho)} - e_H(\rho)$$

(Eq. 26)

Equation 25 has the desired form for a similarity treatment of the problem provided $\Delta(\rho)$ is very small. Except at extreme pressures (many megabars) the term $\Delta(\rho)$ is <u>not</u> small compared to $p/\rho\Gamma$ and consequently the problem of shock propagation in solids is characteristically <u>non-similar.</u> In a solid, the density ratio across the shock front will vary considerably as the pressure changes.

In what follows it will be convenient to employ a simplified form of the functional relation that describes the Hugoniot or shock adiabat states of the material. This expression relates the shock speed to the particle speed in a linear manner:

$$D = c + s\,u$$

(Eq. 27)

Rae terms any material whose Hugoniot obeys this relation a c,s medium. The relation itself is usually termed simply the "linear Hugoniot." A wide variety of materials have Hugoniots that are well approximated by this equation, although in every case the relation fails at very high pressures. In particular, Eq. 27 yields good results for aluminum at pressures up to roughly 200 kilobars, and yields only modest errors up to pressures of a megabar. Physically, the constant c represents the low pressure limit of the bulk sound speed of the material. The interpretation of s is more complicated, but it is related to the zero pressure Gruneisen parameter, Γ_0 .

<u>Quasi-Steady Solution</u>. One approximate method for treating the non-similar nature of impacts in solids is termed the "quasi-steady" method and was developed by Rae and Kirchner (Ref. 19). The method employs the

basic results of the similarity solution for a perfect gas, but forces the results to match properly the Hugoniot of the solid material at the shock front by letting the γ of the "gas" vary as a function of shock radius. This varying γ introduces non-similar features into the results as desired and ensures that the flow variables take on mutually consistent values at the shock front.

An important result arising from the perfect gas equation of state is that, for any fixed value of γ, there is associated only one value of the density--that is, the density across the shock front is constant and uniquely determined as mentioned before. Combining Eq. 17, the perfect gas equation of state, with the third member of Eq. 16 the Rankine-Hugoniot jump conditions:

$$\frac{p}{(\gamma-1)\rho} = \frac{p}{2}\left[\frac{1}{\rho_o} - \frac{1}{\rho}\right] \qquad \text{(Eq. 28)}$$

If the compression, μ, is defined by

$$\mu \equiv \frac{\rho}{\rho_o} - 1 \qquad \text{(Eq. 29)}$$

then the above can be solved to yield the relation:

$$\gamma = \frac{\mu+2}{\mu} \qquad \mu = \frac{2}{\gamma-1} \qquad \text{(Eq. 30)}$$

One obvious way to account for the varying compression that occurs during the propagation of a shock wave in a solid is to let γ vary. Conversely, note that when γ is specified, Eq. 28 is indeterminate in the pressure, p. A perfect gas may have any number of pressure states corresponding to a given compression if the compression is created by a strong shock ($p_o = 0$). This sort of behavior does not exist in a solid except at extreme pressures.

The employment of the linear Hugoniot form (Eq. 27) now allows the convenient use of dimensionless flow variables which are defined as follows (see Appendix H for a dimensional analysis justification for these variables):

μ -- compression, related to density

u/c -- dimensionless particle velocity

D/c -- dimensionless shock velocity

$p/\rho_o c^2$ -- dimensionless pressure

$c\,t/R_o$ -- dimensionless time, where R_o is a scale length defined below

These arise naturally when the linear Hugoniot form is combined with the Rankine-Hugoniot jump conditions to obtain the following expressions which are termed the "Hugoniot values" and which are valid at the shock front in the solid:

$$D/c = \frac{\mu + 1}{\mu + 1 - \mu s} \qquad \text{(Eq. 31)}$$

$$u/c = \frac{\mu}{\mu + 1 - \mu s} \qquad \text{(Eq. 32)}$$

$$p/\rho_o c^2 = \frac{\mu(\mu + 1)}{(\mu + 1 - \mu s)^2} \qquad \text{(Eq. 33)}$$

For a given value of γ, the most important relation derived from similarity theory is Eq. 27:

$$E = 2\pi \rho_o D^2 R_s^3 I(\gamma)$$

If the projectile energy is defined as E_o and a scale length, R_o, is defined by

$$R_o \equiv \left[\frac{E}{2\pi \rho_o c^2}\right]^{1/3} \qquad \text{(Eq. 34)}$$

this relation can be written in dimensionless form as

$$\left(\frac{E}{E_o}\right) = \left(\frac{D}{c}\right)^2 \left(\frac{R_s}{R_o}\right)^3 I(\gamma) \qquad \text{(Eq. 35)}$$

where E is the energy chosen for the similarity solution and where the option is left open here to let E differ from the actual projectile energy, E_o. This feature of the solution is new with this author's discussion of the problem. Its ramifications will be discussed later.

The following description of the quasi-steady model represents the author's interpretation of the processes involved and is believed to be consistent with Rae's presentation. This particular approach to discussing the quasi-steady model leads conveniently into the discussions of modifications to this basic model.

For a similarity solution, E/E_o and γ are constant, while D/c and R_s/R_o vary. Note that the shock speed varies even though the compression remains fixed. Combining the first and second Rankine-Hugoniot jump conditions across the shock front (of the perfect gas), the following is obtained:

$$\frac{p}{\rho_o c^2} = \frac{\mu}{\mu+1} \left(\frac{D}{c}\right)^2 \qquad \text{(Eq. 36)}$$

Now, since μ is assumed a constant for this process, combining this with Eq. 35 yields

$$\frac{p}{\rho_o c^2} = \text{constant} \left(\frac{R_s}{R_o}\right)^{-3} \qquad \text{(Eq. 37)}$$

along the similar expansion. This shows that for fixed γ (or μ) the similar solution yields straight lines of slope -3 on a log ($p/\rho_o c^2$) vs log (R_s/R_o) plot. These straight lines vary only in separation as μ or E/E_o are changed.

The method developed by Rae for applying this perfect gas similarity solution in an approximate way to a solid is illustrated in Fig. 106. Starting at some point A which corresponds to a compression μ_A, the shock front can be thought of as being allowed to follow the path A B, at constant compression, obeying the similarity solution for a perfect gas and with a γ that corresponds to μ_A through Eq. 30. The values $(p/\rho_o c^2)_A$ and $(p/\rho_o c^2)_B = (p/\rho_o c^2)_C$ are found from Eq. 33 knowing μ_A and $\mu_c = \mu_A + \Delta\mu$.

Next the quantity $(R_s/R_o)_B$ is determined from Eq. 37 which yields:

$$(R_s/R_o)^3_B = (R_s/R_o)^3_A \left[\frac{(p/\rho_o c^2)_A}{(p/\rho_o c^2)_B}\right] \qquad \text{(Eq. 38)}$$

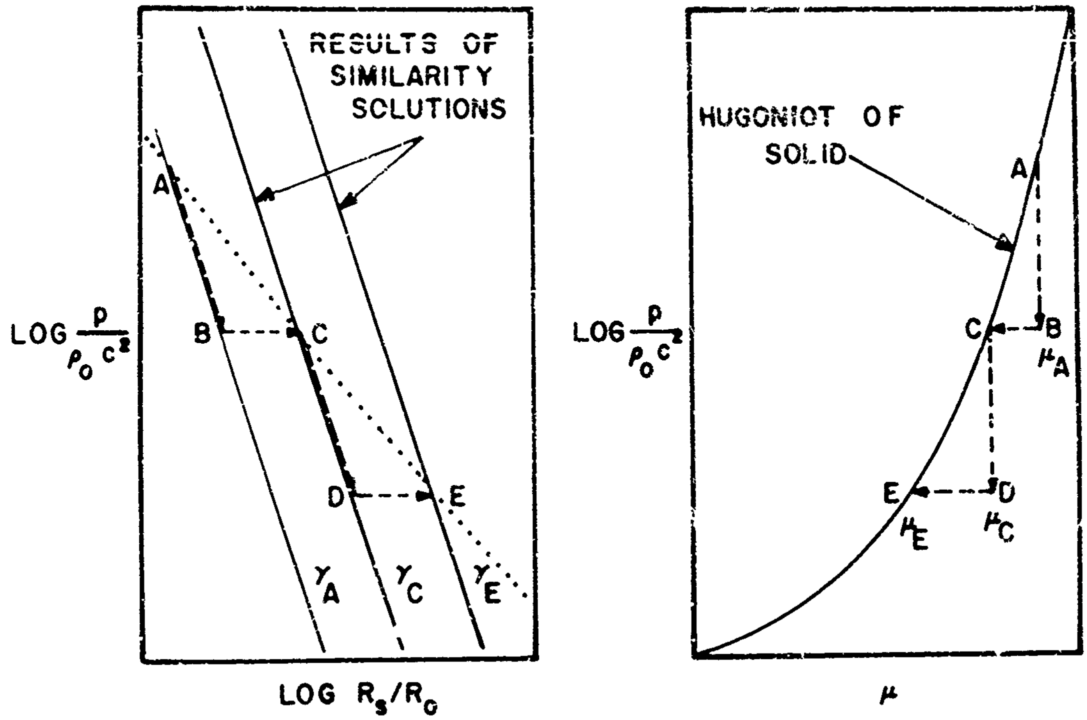

Fig. 106. Illustration of Method for Introducing Non-Similar Corrections for Applying Blast Wave Calculations in a Solid Material.

The shock speed at B is determined by using Eq. 35. Then the transit time for the shock wave between the points $(R_s/R_o)_A$ to $(R_s/R_o)_B$ is given approximately by

$$\Delta\left(\frac{ct}{R_o}\right)_{AB} \cong \left\{\left(\frac{R_s}{R_o}\right)_B - \left(\frac{R_s}{R_o}\right)_A\right\} \left\{\frac{2}{\left(\frac{D}{c}\right)_A + \left(\frac{D}{c}\right)_B}\right\} \qquad \text{(Eq. 39)}$$

At this stage, the process has followed a similar expansion at constant compression and now lies at a state B off the Hugoniot of the material. Rae and Kirchner then proposed to correct this false state by forcing the process back to the Hugoniot along the path BC at constant pressure. In the pressure-shock radius plane this implies that the process is now moved along BC to a new similarity curve characterized by a new γ_C derived from μ_C.

After adjustment along the path B C, the new variables must satisfy the similarity Eq. 35, but now with the new value γ_C, yielding

$$\left(\frac{R_s}{R_o}\right)_C = \left[\frac{(E/E_o)}{(D/c)_C^2 \; I(\gamma_C)}\right]^{1/3} \qquad \text{(Eq. 40)}$$

where $(D/c)_C$ is obtained from Eq. 31 using the new value μ_C for the compression. If Eq. 40 is evaluated at $(R_s/R_o)_B$ using the new value $\gamma = \gamma_C$, the value for $(D/c)_B$ will, of course, not agree with that obtained previously when $\gamma = \gamma_B$. Hence, it can be said that the quasi-steady model leads to a variation in the shock speed over the path BC. The time taken for the shock to "traverse" this path is given approximately by

$$\Delta\left(\frac{ct}{R_o}\right)_{BC} = \left\{\left(\frac{R_s}{R_o}\right)_C - \left(\frac{R_s}{R_o}\right)_B\right\}\left\{\frac{2}{\left(\frac{D}{c}\right)_B + \left(\frac{D}{c}\right)_C}\right\} \qquad \text{(Eq. 41)}$$

The net result of this procedure is that the value of γ used is continuously changed to force the solution to lie on the solid material Hugoniot curve. The large variation in γ actually encountered is the result of accounting for non-similarity. The actual pressure variation calculated by this method is as indicated by the dotted curve in Fig. 106.

The results of one step as described above, then yield the necessary starting condition for the next step. Except for the calculation of shock trajectory, the step size is unimportant because the flow quantities turn out to be dependent only upon the end points of the step.

The starting conditions for the first step can be obtained from the initial (one-dimensional) shocked states. For like material impact where the impact velocity is given by v,

$$\left(\frac{u}{c}\right) = \frac{1}{2}\left(\frac{v}{c}\right) \qquad \text{(Eq. 42)}$$

Applying the Rankine-Hugoniot equation at the shock front and using the linear Hugoniot for the material:

$$\mu_{impact} = \frac{(v/c)}{2 + (s-1)(v/c)} \qquad \text{(Eq. 43)}$$

Values for the remaining flow quantities at impact may then be obtained from Eq. 31 and 33. The quasi-similar method will predict infinite shock speed and pressure at $R_s = 0$, consequently this unrealistic situation can be avoided by assuming that the one-dimensional impact conditions described above are maintained out to that shock radius where the quasi-similar solution corresponds to these conditions. The shock radius corresponding to this transition can be obtained from Eq. 35 where the values of D/c and γ used are derived from Eq. 43.

<u>Varying Energy Method.</u> The method just described involves the self-consistent joining of a sequence of similarity solutions by varying the values of γ. The variation of the energy, E, driving the similarity solution produces the same sort of effect. In fact, it seems reasonable that the quantity E/E_o is as valid an adjustable parameter as is γ. It is therefore proposed that an alternative development can be achieved by letting both γ and E/E_o vary in a plausible manner.*

Referring again to Fig. 106, the process starts at a given compression μ_A and a value of $(E/E_o)_A$ determined from the previous step. The first part of the process, from A to B, is the same as explained for the quasi-steady method.

In the varying energy method, the expansion over the path B to C is calculated somewhat differently. It is assumed that the shock velocity remains constant over the path, assuming the value it must have at the point C to be consistent with the solid material Hugoniot, $(D/c)_C$. A discontinuous change is made in the energy at the point B. Along the path AB, the energy remains constant at the value $(E/E_o)_A$. At the point B, the energy is changed to $(E/E_c)_C$ and remains at that value over the interval B to C. Applying Eq. 35 at points B and C with $(E/E_o)_B = (E/E_o)_C$ and $(D/c)_B = (D/c)_C$ and noting that $\gamma_B = \gamma_A$ the following expression for the shock radius at the point C is obtained:

*This approach was suggested by Prof. P. Torvik, AF Institute of Technology. Helpful discussions with him on this theory are hereby gratefully acknowledged.

$$\left[\frac{R_s}{R_o}\right]_C = \left[\frac{R_s}{R_o}\right]_B \left\{\frac{I(\gamma_A)}{I(\gamma_B)}\right\}$$

(Eq. 44)

Once this is solved for $(R_s/R_o)_C$, Eq. 35 can be used to obtain the new value of $(E/E_o)_C$. This new energy is then used to start the next step in the solution of the problem.

One additional alteration affecting the selection of γ for any given expression was made in arriving at the varying energy model. It may be observed that the perfect gas equation of state (Eq. 17) when combined with the energy Rankine-Hugoniot condition (Eq. 16) results in the elimination of both the specific internal energy and the pressure from the equation. This means that for a specified γ and compression, μ, the pressure is indeterminate; a number of pressure states may correspond to any given compression. This is the same as stating that all strong shocks in a perfect gas, no matter what their pressure, propagate at the limiting compression of the medium. This feature of the perfect gas equation of state is distinctly incorrect when applied to solids. In a normal solid, the Hugoniot curve represents a unique, single valued functional relation between the pressure and the compression.

The use of an equation of state in other than the $e = pf(\rho)$ form would destroy the requirements for a similarity solution in this development. There is, however, a simple way to ensure a one-to-one correspondence between the pressure and compression as is required for adequate treatment of a solid. In complete form, the energy Rankine-Hugoniot condition takes the form:

$$(e/c^2) - (e_o/c^2) = (p/\rho_o c^2)\left\{\frac{\mu/2}{\mu + 1}\right\}$$

(Eq. 45)

The second term on the left side has been ignored to this point, but can be used to accomplish the task described above. In this application let e_o/c^2 be defined as a parameter, A, and the normal physical interpretation is ignored. Given this form, the combination of Eq. 45 with the perfect gas equation of state yields

$$\frac{(p/\rho_0 c^2)}{(\gamma-1)(\mu+1)} = A + (p/\rho_0 c^2)\left[\frac{\mu/2}{\mu+1}\right] \qquad \text{(Eq. 46)}$$

Although it may be necessary to change A as a function of μ, this equation can be solved uniquely for $(p/\rho_0 c^2)$ in terms of μ when γ is given. In the application to the problem of an impact into a solid, the equation of the Hugoniot curve for the solid was known, and it was desired to solve Eq. 46 for γ when some value of μ was specified. To accomplish this, once μ was specified the values of $(p/\rho_0 c^2)$ at the points $\mu = \mu + \delta\mu$ and $\mu = \mu - \delta\mu$ was calculated from the known Hugoniot, keeping $\delta\mu$ very small. This yields two equations that can be solved simultaneously to yield approximate values of γ and A at the point μ. In particular,

$$\gamma = \frac{h(\mu_2 + 2) - (\mu_1 + 2)}{h\mu_2 - \mu_1} \qquad \text{(Eq. 47)}$$

where

$$h = \frac{(p/\rho_0 c^2)_2\ (\mu_1 + 1)}{(p/\rho_0 c^2)_1\ (\mu_2 + 1)} \qquad \text{(Eq. 48)}$$

The above revised method was used to calculate γ as a function of μ in the varying energy model. The result is that a local piecewise fit to the Hugoniot has been obtained in the perfect gas equation of state form.

Quasi-Steady and Varying Energy Model Results. The blast wave expansion models discussed above were calculated with a digital computer program. The values for $I(\gamma)$ used were obtained from Figure II of Ref. 18 using a combination of table interpolation and algebraic functional form to generate the desired values. The problem considered was the impact of a 0.635 cm diameter aluminum sphere traveling at 7.0 km/sec and impacting an aluminum target. Other data is shown in Table X. The results of these calculations are shown in Fig. 107. The experimental results shown are those from Chapter VI for 1100-0 aluminum targets measured on-axis, see Fig. 75.

Table X

Properties at Impact

Aluminum Density	2.765 g/cm^3
Linear Hugoniot Constants	
c	5.25×10^5 cm/sec
s	1.3718
Scaled Projectile Energy, E_o/c^2	.332
Scaling Length, R_o	.267 cm
Scaling Pressure, $\rho_o c^2$	768 kb
Impact Conditions	
D/c	1.915
u/c	.667
$P/\rho_o c^2$	1.276
μ	.534

The quasi-steady model produces results that do not agree particularly well with the experimental results, especially in predicting the slope of the pressure-distance curve. Changing the value of E/E_o used does not change the slope; it merely translates the curve to the right or left. Beyond the value of $R_s/R_o \approx 20$, the experimental results show that non-hydrodynamic behavior of the target is severely affecting the pressure decay. Since none of the similarity models discussed here include any non-hydrodynamic behavior, no agreement with experiment in this region should be expected. The apparent agreement between the quasi-steady model results and experiments in the region $10 < R_s/R_o < 25$ is believed to be simply fortuitous and physically without significance.

Some experimental evidence (see Fig. 96) suggests that the pressure curve slope becomes smaller (less steep) at values of $R_s/R_o < 4$. Consequently, the results of the quasi-steady model and experiments will differ even more in the region $R_s/R_o < 4$ than they do in the region shown. This is somewhat disappointing since the quasi-steady model should work best in the higher pressure regime. Agreement at R_s/R_o less than roughly 2 should not be expected since at this small radius the actual impact-generated stress field has not smoothed out

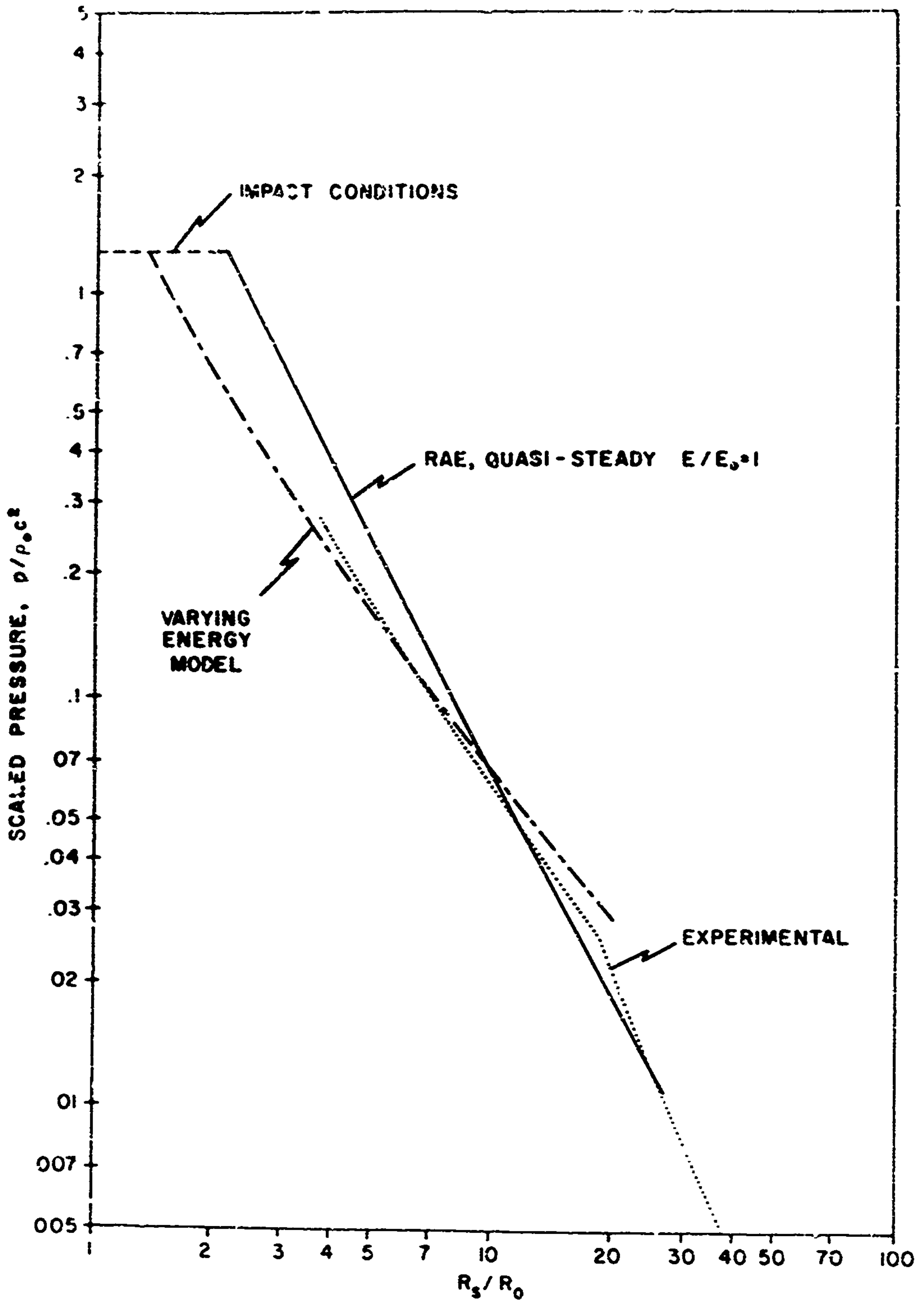

Fig. 107. Blast Wave Theory Results Obtained With Quasi-Steady and Varying Energy Models.

to look like it was created by an apparent point source.

The varying energy model yields improved agreement between theory and experiment, although deviations are apparent at either end of the pressure regime illustrated. The slope of the pressure-distance curve (the pressure decay law) is improved over that produced by the quasi-steady model.

The application of the varying energy model requires, as does the quasi-steady method, a knowledge of the value of E/E_o used to start the problem. There is no clearcut physical basis for choosing this parameter, unfortunately, other than empirically. For this calculation, the following line of reasoning was used to select E/E_o: Consider the spherical projectile of radius r_o to be approximated by an L/D = 1 right circular cylinder of the same volume and equivalent radius r_c, that impacts the target end-on. At the center of the cylinder, the shocked state is a region of one-dimensional flow until such time as rarefactions from the edge of the cylinder reach the axis of the propagating shock wave. It can be shown that for the impact condition treated here, the rarefaction starts to attenuate the on-axis pressure after the shock wave has reached a distance of $R_s/R_o = 1.61$. If the one-dimensional impact conditions are used to calculate D/c and γ, this corresponds to $(E/E_o)_{initial} = 0.87$. Because of the shape difference, rarefactions will start earlier in the process and the on-axis pressure should be affected at smaller radius for the spherical projectile actually used. Consequently, there is at least some justification in choosing an $(E/E_o)_{initial}$ with a value less than 0.87. Based upon the agreement with the experimental data, $(E/E_o)_{initial}$ was chosen to be 0.5, a number that is at least plausible based upon the above argument.

Even though the selection of the parameter $(E/E_o)_{initial}$ has to be chosen empirically, the varying energy model does succeed in improving the agreement between theory and experiment at the higher pressure region and yields better agreement in the pressure-distance curve slope out to a shock radius of about $R_s/R_o = 18$ where non-hydrodynamic processes become important. Further investigation of the selection of the starting energy parameter will be required before this model can be used with any confidence for other materials or projectile velocities.

Karpov Model. In evaluating Rae and Kirchner's quasi-steady model, Karpov (Ref. 11) examined Eq. 35 and noted that it involves a physically unrealistic singularity in the shock velocity at $R_s/R_o = 0$. He therefore suggested that the coordinates be shifted such that the shock velocity remains finite at $R_s = 0$:

$$E/E_o = (D/c)^2 \left[\frac{R_s}{R_o} - \frac{R_s'}{R_o}\right]^3 I(\gamma) \qquad \text{(Eq. 49)}$$

where R'_s/R_o is a constant whose value is to be determined by the one-dimensional impact conditions, i.e.

$$R_s'/R_o = \sqrt[3]{\frac{E/E_o}{(D/c)^2_{impact}\; I(\gamma_{impact})}} \qquad \text{(Eq. 50)}$$

If the quantity R'_s/R_o is calculated as indicated, and Eq. 49 is used in lieu of Eq. 35 in the quasi-steady model, the results of Fig. 108 are obtained for the impact problem defined in Table X. The results are presented for several values of E/E_o since again this is a parameter that can be varied, although once chosen it does not change during the calculation. The "natural" value $E/E_o = 1$ yields poor results. The more or less arbitrary selection of $E/E_o = 2$, however, yields surprisingly good results. The agreement between the $E/E_o = 2$ curve and the experimental results is excellent except at the high pressure end and, of course, at radii of $R_s/R_o > 20$ where non-hydrodynamic processes alter the behavior. Even in the region $R_s/R_o < 4$, the agreement between this model and experiment is relatively good since the few experimental points available in this region predict roughly the behavior demonstrated by the $E/E_o = 2$ curve.

Again, however, good agreement between experiment and theory is obtained only when the parameter E/E_o is properly chosen empirically. Applications to

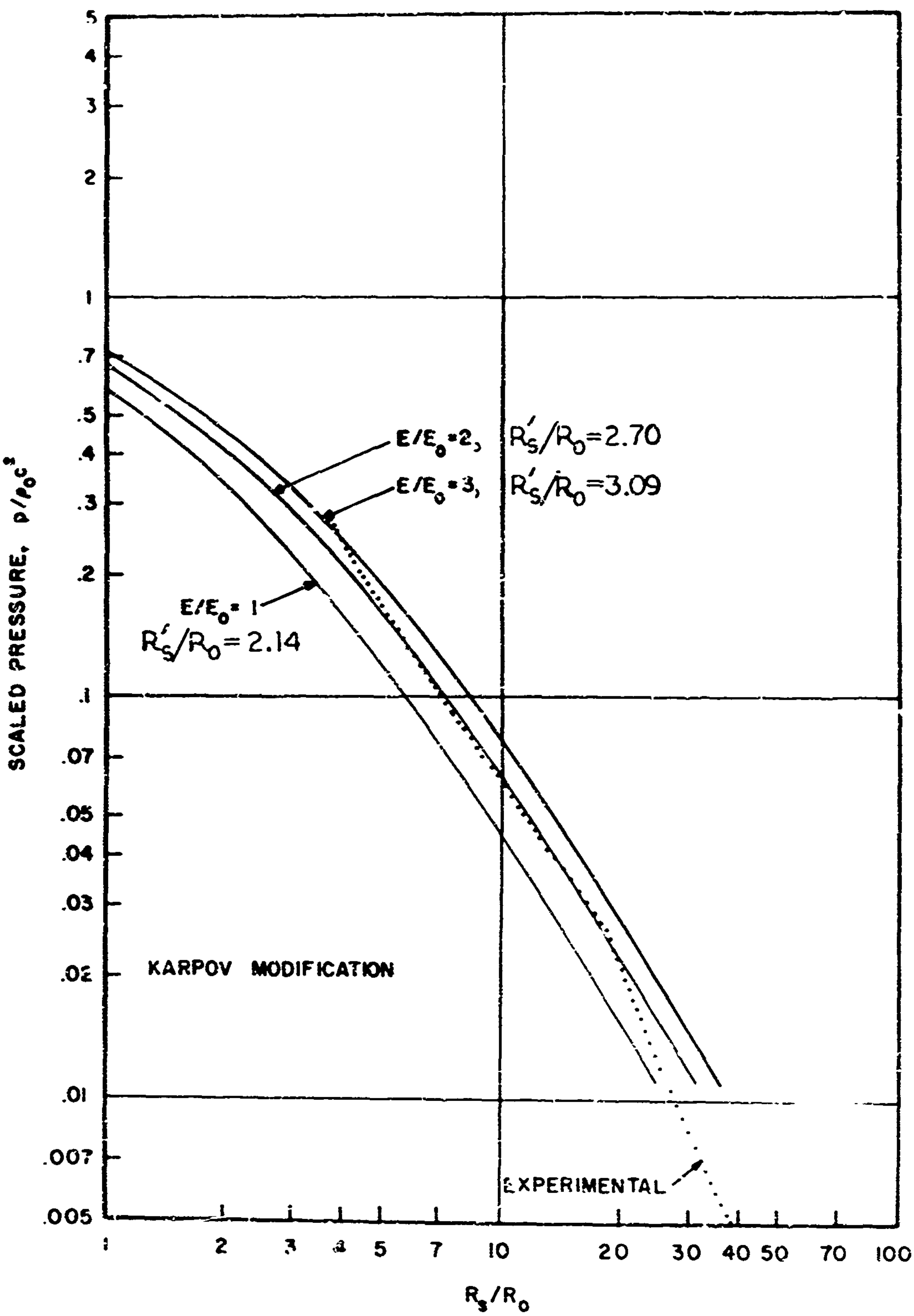

Fig. 108. Blast Wave Theory Results Obtained with Karpov Modification to Quasi-Steady Model.

different impact cases are required to establish a more rational basis for the selection of this parameter.

Other Results. In each of the similarity models discussed, the value of γ used in the perfect gas equation of state has been allowed to vary to compensate for the fact that a solid does not really obey this form of the equation of state. Figure 109 illustrates the large changes in γ required by each of the models to account for, in an approximate way, the non-similar effects in the hydrodynamic flow in a solid. Extremely large values of γ are encountered in the Rae and Karpov solutions, while the varying energy model developed here exchanges a portion of the variation in γ for changes in the driving energy, E. In explanation of the variation in E/E_o, the interpretation is made that increases in E/E_o do not imply energy is being created, but that a similarity solution corresponding to a higher energy is necessary to match the behavior of the solid at larger shock radii.

Among the models, the behavior of the shock speed is different at small shock radii. As mentioned before, for the quasi-steady and varying energy models, the shock speed is somewhat artifically limited so that it does not exceed the shock speed predicted at impact with one-dimensional theory. If left unconstrained, the shock speed in these models would tend toward infinity as R_s approaches zero -- a situation which does not occur in real impacts. The fundamental assumption of the approach taken by Karpov removes the singular behavior of the sound speed for this model. For each model, the shock speed approaches the bulk wave speed, c, at large shock radii as would be expected. These effects are shown in Fig. 110.

As shown in Fig. 111, the shock trajectories predicted by the various models are very similar. Measurements of shock trajectory do not, therefore, represent a very sensitive test of the relative merits of these models.

Cylindrical Blast Wave Model. An additional similarity-type model was developed by Heyda (Ref. 23) based upon a semi-empirical combination of

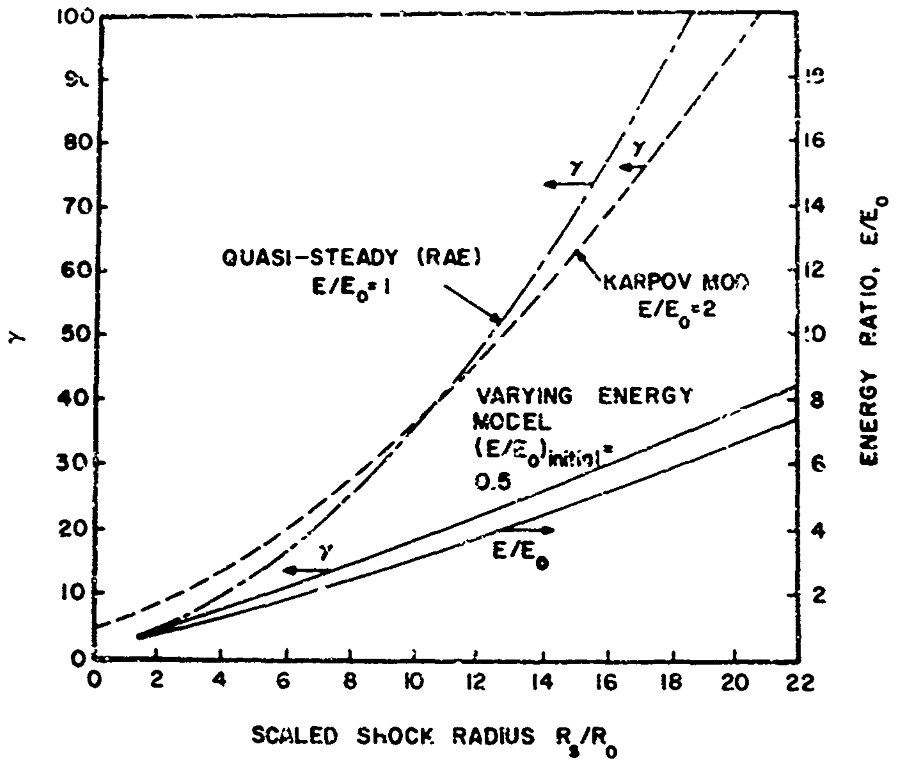

Fig. 109. Behavior of Energy and γ in Blast Wave Similarity Models.

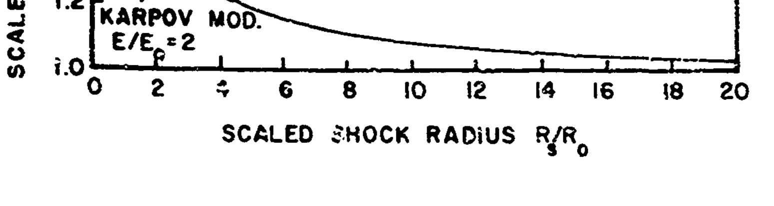

Fig. 110. Behavior of Shock Speed in Blast Wave Similarity Models.

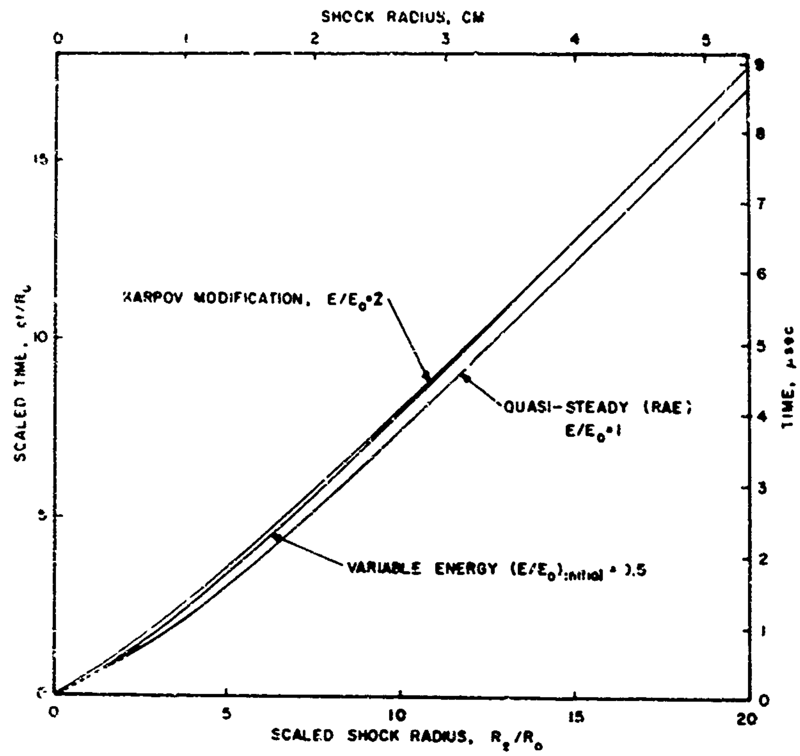

Fig. 111. Shock Trajectory Predicted Using Three Approximate Blast Wave Similarity Models.

cylindrical and spherical blast wave solutions. The model was derived on the basis of a cylindrical projectile of length L_p and radius R_p impacting the target normally. If it is assumed that $L_p = 2R_p$ and the resulting cylinder is replaced with a spherical projectile of equal volume and diameter $d=\sqrt[3]{3/2}\ L_p$, then Heyda's results, in dimensionless form, are as follows:

$$D/c = 4\,\tilde{a}\,\tilde{k}\,(Z^{-1/2} - \tilde{k}/Z) \tag{Eq. 51}$$

$$\text{where } Z = \frac{R_s}{R_o} - \frac{R_{so}}{R_o} \tag{Eq. 52}$$

$\tilde{a} = 1.055\ (\frac{D}{c})_{impact}$ as obtained from the one-dimensional result

$(\frac{D}{c})_{impact} = 1 + \frac{s}{2}\ (\frac{v}{c})$ derived from Eq. 43

$$\tilde{k} = 0.368 \left[\frac{(d/R_o)}{6} \right]^{1/6} \left(\frac{v}{c}\right)^{-1/3} \quad \text{(Eq. 53)}$$

$$\frac{R_{so}}{R_o} = \frac{R_{si}}{R_o} - 6.717\,\tilde{k}^2 \quad \text{(Eq. 54)}$$

$$\frac{R_{si}}{R_o} = \left(\frac{ct_1}{R_o}\right)\left(\frac{D}{c}\right)_{impact} \quad \text{(Eq. 55)}$$

$$\frac{ct_1}{R_o} = \frac{\sqrt[3]{2/3}\;(d/R_o)}{(c_H/c)^2 - [(D/c)_{impact} - 1/2\,(v/c)]^2} \quad \text{(Eq. 56)}$$

c_H = speed of the rarefaction wave behind the shock front at impact conditions.

The shock trajectory is given by

$$\frac{ct}{R_o} = \frac{1}{2\tilde{a}\tilde{k}} \left[Z^{3/2}/3 + \frac{\tilde{k}}{2}\; Z + \tilde{k}^2 Z^{1/2} + \tilde{k}^3 \ln (Z^{1/2} - \tilde{k}) + 2\tilde{a}\tilde{k}\left(\frac{ct_1}{R_o}\right) - \tilde{k}^3\; (6.67 \ln 1.59\tilde{k}) \right] \quad \text{(Eq. 57)}$$

The required empirical constants were derived from the results of numerical calculation of hypervelocity impacts.

The results of the above method applied to the impact described in Table X are shown in Fig. 112. Several values of c_H/c have been used since good data is not available on this parameter. The values obtained with $c_H/c = 3$ correspond closely to those obtained by Billingsley (Ref. 14:23), although this appears to be physically unrealistic.

The results are clearly quite inaccurate for this impact situation no matter what value of c_H is chosen. While the $c_H/c = 3$ curve may provide a reasonably accurate fit of the data at very early times ($R_s/R_o < 5$) it fails

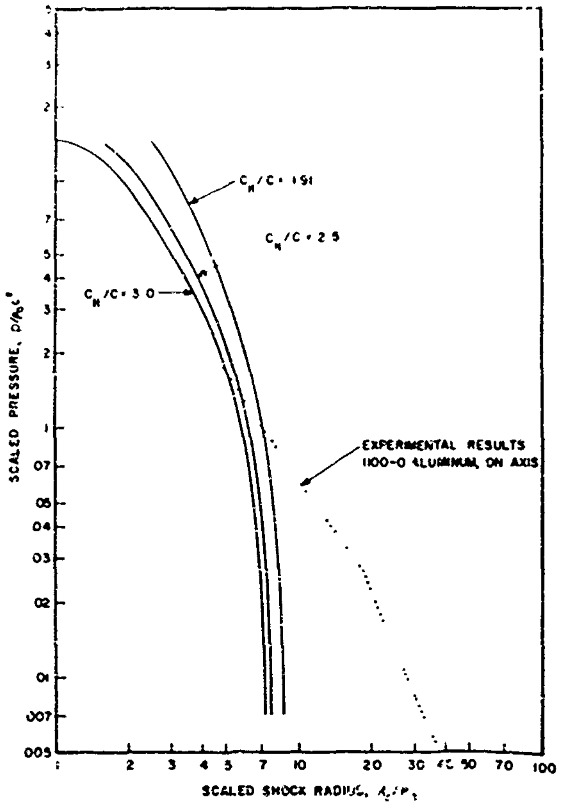

Fig. 112. Results of Cylindrical Blast Wave Model (Heyda).

catastrophically at this point yielding unrealistic behavior in terms of the shock decay. It appears, therefore, that this model does not properly describe the impact except possibly at very early time and in regions of very high stress -- a regime not investigated experimentally in this study.

Remarks. The similarity-like models are useful in understanding the processes involved in certain regimes of the shock propagation -- and in determining at what point and to what extent some of the simplifying assumptions fail. The results obtained here describe the major features of the wave propagation phenomena out to a shock radius in the region of $R_s/R_o \approx 15$ or so relatively accurately and indicate the relevance of the hydrodynamic model of the behavior of this solid. The breakdown of the model when strength and multi-dimensional factors became important is also shown. The data has also been valuable in the evaluation of the experimental shock trajectory data -- see chapter VI.

The three models described above clearly illustrate the difficulty in trying to predict analytically from reasonably tractable models the results of a hypervelocity impact into a thick target. The quasi-steady solution first proposed by Rae and Kirchner does not appear to yield accurate results, although it represents a dramatic improvement over a straight similarity solution (constant γ) to the problem. The modification of Karpov and the varying energy model proposed here yield substantially improved results, but each involves the use of an empirical constant to obtain good agreement. All of these models are based upon several simplifying assumptions discussed earlier. As pointed out, they cannot properly predict (1) behavior near the origin, (2) multi-dimensional effects such as the values of the variables off the axis or the results of oblique impact, (3) effects of rarefaction waves originating at free surfaces or material interfaces, (4) flow properties far behind the shock front, as is required to study crater growth, (5) any effects where material strength properties are important. The more complete description of the hypervelocity impact cratering and shock propagation problem requires the application of modern finite-difference numerical methods where many of the above restrictions can be removed. The price paid is very dear, though, since numerical solutions are orders of magnitude more complicated and expensive and are still subject to a variety of restrictions and uncertainties.

Comparison of Experimental and Numerical Results

The similarity theory developments just discussed have clearly indicated the extremely difficult problem of describing the complex hypervelocity impact event using an analytic approach. When complex geometries and strength of materials are considered, the problem becomes absolutely intractable in that fashion. The alternative -- numerical solution of the equations of motion by finite difference methods -- has produced fruitful results and is the foundation of much of our current understanding of hypervelocity impact and multi-dimensional shock wave propagation phenomena. These numerical techniques are currently finding wide practical application beyond the study of hypervelocity impacts into thick targets. The concepts, applications and limitations of the computer programs based upon these numerical techniques have been discussed briefly in Chapter II and will not be repeated here. It is merely noted again that the ultimate test of the numerical techniques is their correlation with experiments.

The remainder of this chapter deals with the comparison of the experimental data on shock wave propagation and attenuation generated in this study with those few numerical results available in a form suitable for such direct comparison. These calculations have already been examined to some extent in Chapter IV where comparisons with experimental crater growth were made. Here the region of interest is in the vicinity of the shock front and, except for a very short time after impact, is far removed from the growing crater. The variation of the peak stress at the shock front as a function of shock radius is of primary importance because of the available experimental data and the overall check this provides on the performance of the numerical scheme. Additional parameters, such as peak stress variation with angle off axis and the shape of the stress pulse are discussed insofar as available data allows.

Results of OIL/RPM Codes. The OIL code (Ref. 58) represented the first in a family of two-dimensional continuum mechanics codes written in Eulerian coordinates and designed specifically to calculate impacts into solid materials. OIL is a one-material code that treats only hydrodynamic behavior. A later member of this family, called RPM, incorporated a rigid plastic model of strength behavior. Many of the best theoretical studies of hypervelocity impact phenomena by Walsh, Dienes, and Johnson (Ref. 8, 59, and 60) were based upon the application of these codes.

Fortunately, two sets of calculations that correspond roughly to portions of the experiments conducted here have been reported in sufficient detail to allow direct comparison. The first was an OIL code calculation (Ref. 14) of the impact of a .435 cm aluminum sphere onto an aluminum target at a velocity of 7.63 km/sec. The results of the predicted variation of particle velocity (taken in the form $v_{fs} = 2u$) with distance into the target, R_s, on axis are shown in Fig. 113. In addition to applying linear size scaling, each point has been scaled to a projectile velocity of 7.0 km/sec by the technique developed in Appendix E. The on-axis experimental data is from Fig. 75 and Fig. 80 for impacts into 1100-0 and 6061-T6 aluminum at a projectile velocity of 7.0 km/sec. Since this calculation was purely hydrodynamic and only extended to a shock radius of 2.15 cm the choice of alloy for comparison is unimportant since the data from 1100-0, 6061-T6, and 7075-T6 alloys are indistinguishable in this region.

Although the OIL results lie slightly below the experimentally derived curve, they agree quite well with the experimental results, predicting both the magnitude of the particle velocity and the rate of decay with distance quite well. The behavior at $R_s < 1$ cm is roughly as expected, though no experimental data is available in this region. This comparison is quite pleasing in that the expected purely hydrodynamic behavior at pressures above approximately 75 kilobars is verified.

The second set of results presented on the same figure are from an RPM calculation by Dienes (Ref. 40) of the impact of a .4763 cm diameter aluminum sphere into an 1100-F aluminum target at 7.39 km/sec. The results were linearly size scaled to the .635 cm diameter projectile size of the experiments and the data was adjusted as before to correspond to the 7.0 km/sec projectile impact velocity condition.

In the purely hydrodynamic regime, $R_s < 2$ cm, only two calculated points are available, but the agreement with the experimental data is excellent. At lower pressures ($R_s > 3$ cm) the calculated values of the particle velocity are some 25-30 percent lower than the experimental values for the 1100-0 alloy. However, the most striking feature of the data is the apparent agreement with the slope of the experimental curves in the region $R_s > 5$ cm. Not enough compu-

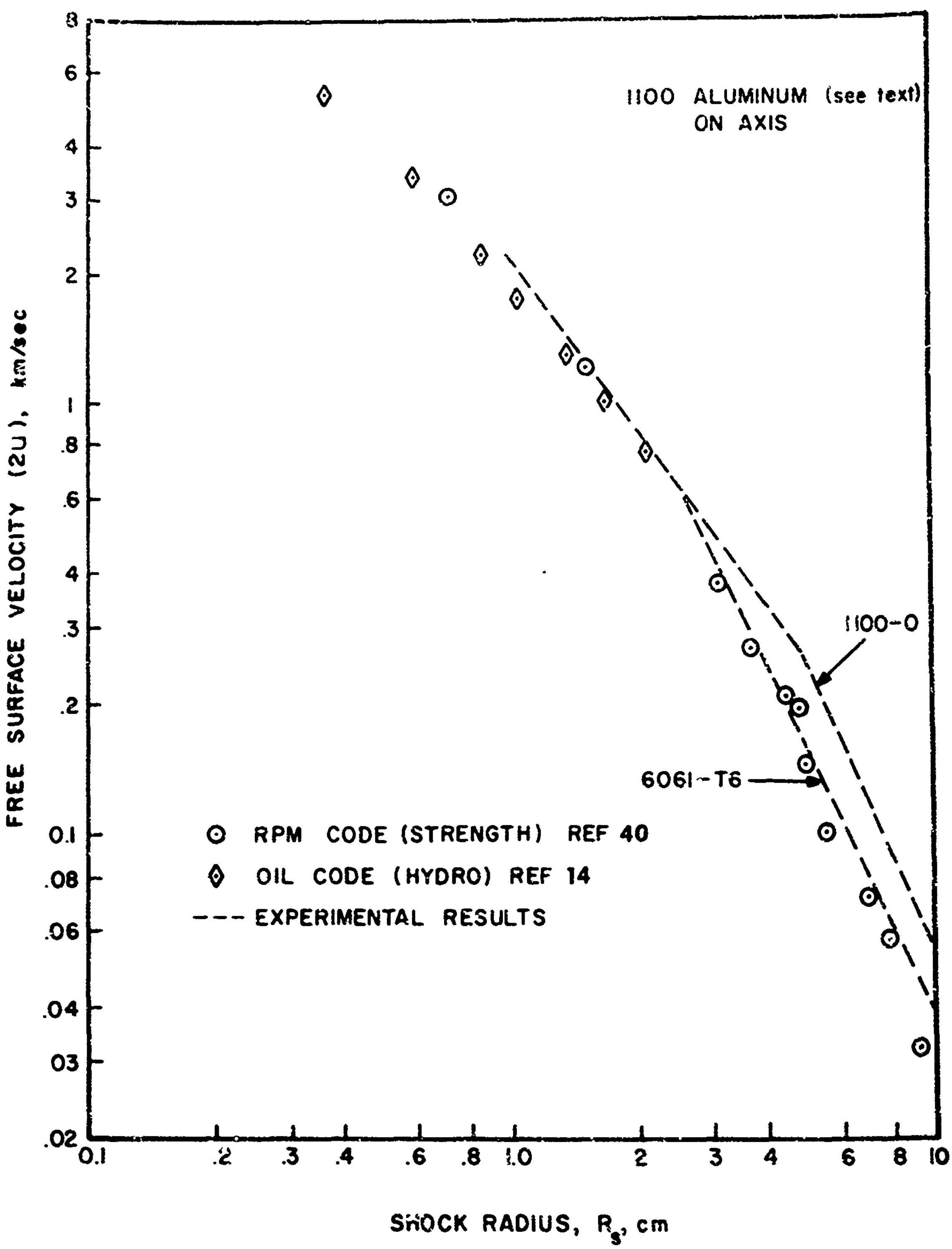

Fig. 113. Comparison of On-Axis Experimental Results with OIL and RPM Code Results -- 1100 Aluminum.

tational results were reported to determine the exact slope of the computer predicted curve in the region 2 cm $< R_s <$ 5 cm or to determine if there is a relatively abrupt change in the slope of the curve in the region of $R_s \approx 5$ cm.

The yield strength of the 1100-F aluminum used in Dienes' calculations was taken to be 1.3 kilobars while the yield strength of the 1100-0 (annealed) aluminum used in the experiments was 0.26 kilobars and that of the 6061-T6 alloy was 2.76 kilobars. Consequently, while the correlation is not perfect by any means, it does appear likely that the RPM code is predicting the strength-dependent attenuation in a fashion similar to that described in Chapter VI. The sources of the somewhat large scatter in the region $R_s > 4$ cm of the computer-generated data points may be due partly to coarser zoning used in this region and is affected by this author's transcription of the data. It is somewhat unfortunate that more RPM data points are not available in the transition region, 2 cm $< R_s <$ 3 cm, since this would help to decide just to what extent the RPM and experimental results agree. Indeed, additional calculations with altered material yield strength would be most useful in interpreting the meaning of the numerical results.

Based upon the available information, however, the on-axis predictions of particle velocity (or pressure) as a function of shock radius by the OIL and RPM codes are quite good. There seems to be a slight (roughly 10 percent) tendency to underestimate the pressure at any given position. Later members of the OIL family of computer codes treat elastic as well as plastic material behavior and may be expected to yield even better results.

Results of STEEP Code. Another series of continuum mechanics codes based upon the numerical finite difference approach has been developed and applied by Bjork, Rosenblatt, Kryenhagen, and others (Ref. 41) to a variety of impact problems. One member of this group, the STEEP code, was used by Rosenblatt (Ref. 32) to calculate impact problems for direct comparison with the shock wave propagation experiments described herein. The STEEP code is written in a two-dimensional Eulerian coordinate system with cylindrical symmetry.

It includes an elastic-plastic model of material strength behavior and a variety of other advanced features related to models of material behavior. The general features of this code as well as the problems calculated are described in Chapter II.

Specifically, the STEEP results include the impact of .635 cm diameter spheres at a velocity of 7.0 km/sec onto both 1100-0 and 7075-T6 aluminum targets at normal incidence. The yield strength used in the calculations varied slightly from those reported in Table II: 0.31 kb instead of 0.26 kb for the 1100-0 alloy and 4.14 kb instead of 4.86 kb for the 7075-T6 alloy.

The results obtained are shown in Fig. 114 which describes the position history of the peak normal stress in the target, on axis. The experimental data was derived from that presented in Fig. 75 and Fig. 85 of Chapter VI. In the high stress region, $R_s < 1.1$ cm, the numerical results for the 1100-0 and 7075-T6 alloys are nearly identical, confirming the essentially hydrodynamic behavior of the materials at these stresses.

For the 1100-0 alloy, the STEEP code results tend to underestimate the measured peak normal stress by roughly 20 percent. Except for this offset, however, the agreement between the theory and experiment for this alloy is quite good for the on-axis data, i.e., the slope of the stress decay curve is predicted quite accurately out to $R_s \approx 5$ cm. At this point, a change in the slope of the decay curve is expected, but is not apparent in the numerical calculation. Unfortunately, the numerical calculation had to be terminated at $R_s \approx 6$ cm for economic reasons and the zoning was rather course at this radius, so it is not possible to either confirm or deny the proper behavior of the code in this region.

In similar fashion, the STEEP results for the 7075-T6 alloy are offset from the experimental results by 10 to 15 per cent. Aside from this, the agreement with the experimental results is good. Even the expected change in slope of the stress decay curve at about 2.5 cm depth is predicted well, although the slope changes smoothly and not in the more abrupt manner indicated by the experiments. Again it would have been instructive to have carried the 7075-T6

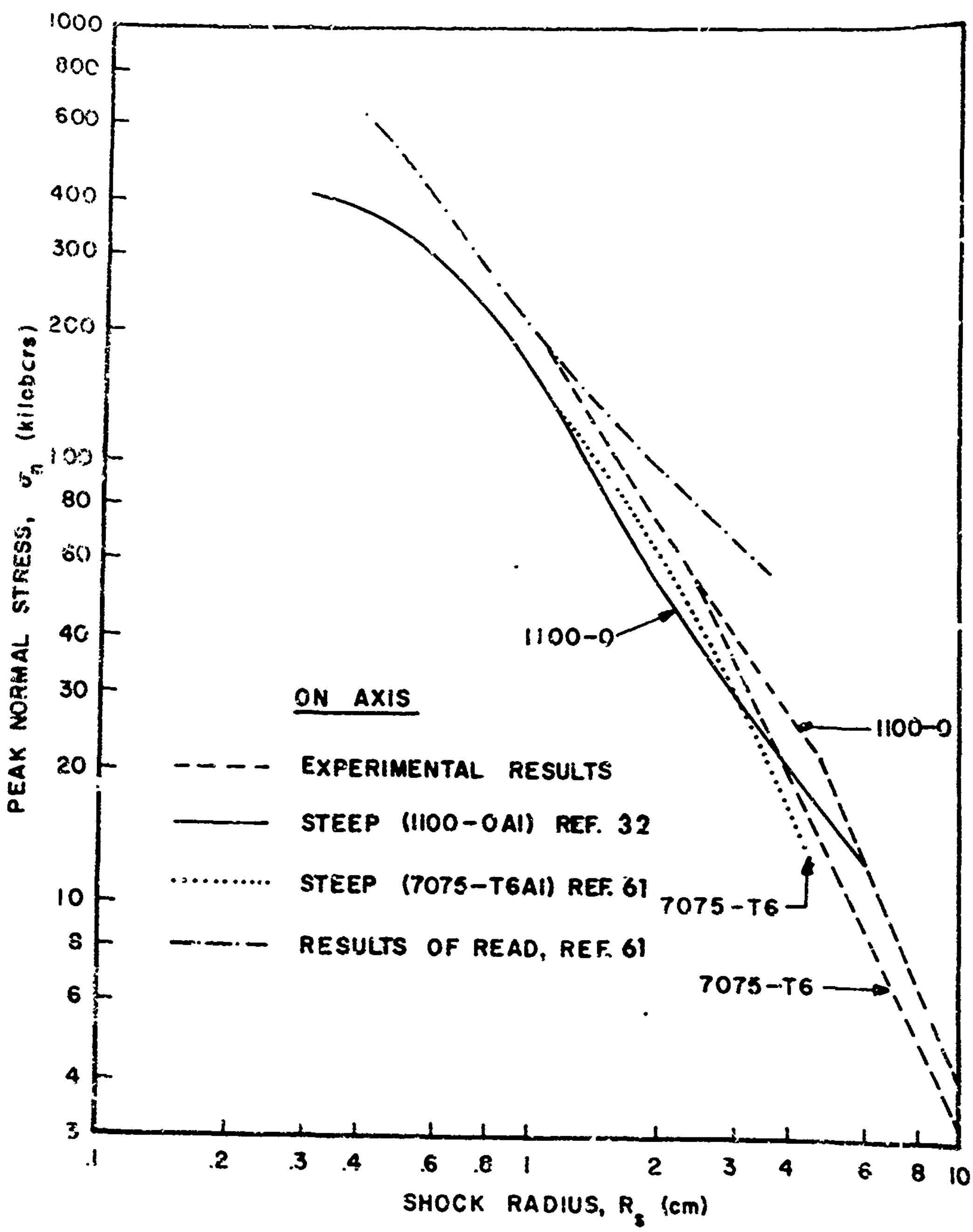

Fig. 114. Comparison of On-Axis Experimental Results with STEEP Code Results -- 1100-0 and 7075-T6 Aluminum.

calculation out to a larger shock radius. Since only partial results are available on the STEEP calculations at this time, it is not possible to interpret these calculations, other than in an overall sense, in terms of the behavior discussed in Chapter VI.

Finally, the results of a very early strength code calculation by Read (Ref. 61) has been included for comparison. This calculation was performed for the impact of an aluminum projectile onto a hard (believed to have been 6061-T6) aluminum target at 7.35 km/sec. The results have again been size scaled and adjusted to an impact velocity of 7.0 km/sec as before. The results show poor comparison with either the experiments of this study or the later, more sophisticated calculations by Rosenblatt shown on the same figure, at least in the region $R_s > 1$ cm. It was, however, the comparison of the results of this calculation with the experimental results of Charest (Ref. 13; see also Fig. 94) that led Read to postulate that the existence of a two-wave structure in the target was causing the fly-off disk technique to record a reduced and unrealistic stress measurement. Had the more recent numerical results been available, the question of the response of the fly-off disks to the two-wave structure would probably never have been raised. This phenomenon is discussed from a different point of view in Appendix D.

At this time, there are not sufficient details of the calculations available to construct complete peak normal stress vs shock radius plots as in Fig. 114 for angles off the axis. Results are available, however, at several selected shock radii and are presented for an 1100-0 aluminum target in Fig. 115 and for a 7075-T6 aluminum target in Fig. 116. The light data points are from the numerical results, while the dark data points were taken from the straight line fits to the experimental data. Where error bars are shown, the points have been obtained by extrapolation of these straight line fits into a region of nonexistent or unreliable experimental results. The error bars indicate a crude estimate of the reliability of these particular points, but are not

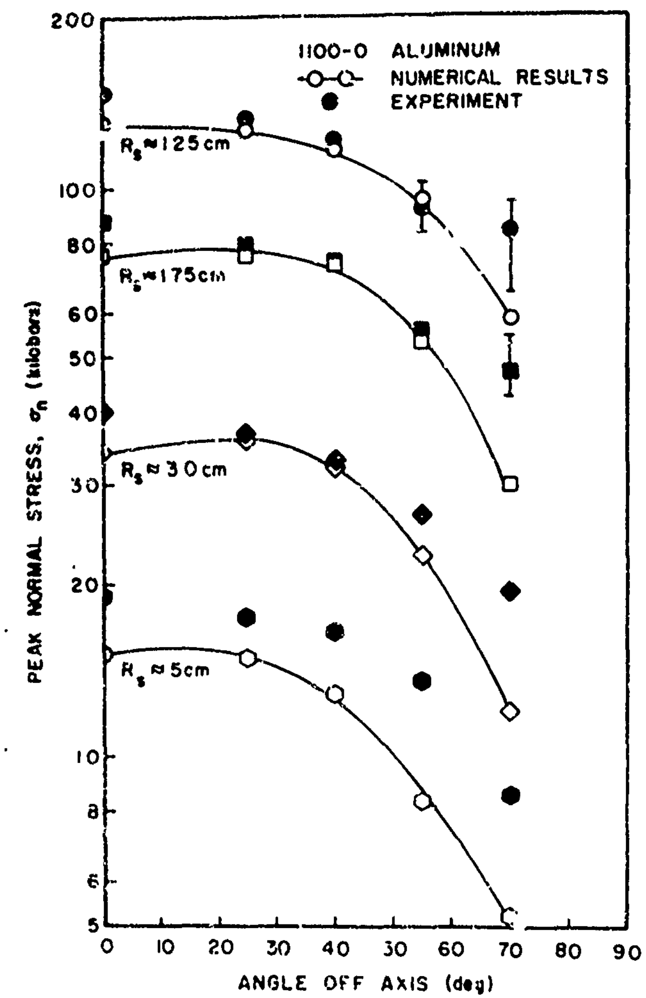

Fig. 115. Peak Normal Stress in 1100-0 Aluminum at Selected Shock Radii as a Function of the Angle Off Axis.

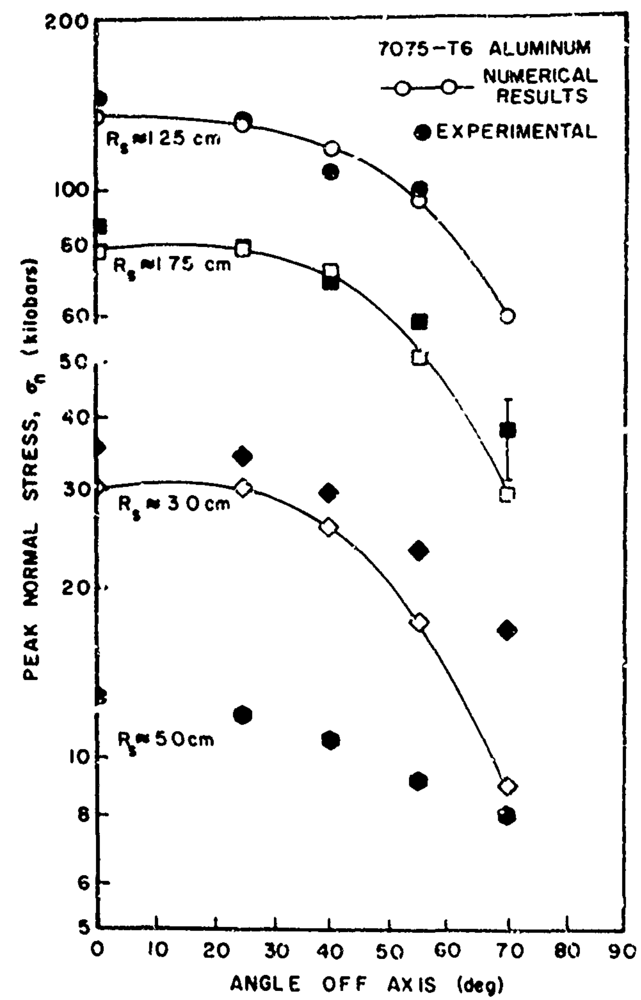

Fig. 116. Peak Normal Stress in 7075-T6 Aluminum at Selected Shock Radii as a Function of the Angle Off Axis.

intended to be typical of errors associated with regions where actual data existed; there the errors are much smaller.

For the 1100-0 alloy, the results for the on-axis case again show the roughly constant percentage difference between the experimental and numerical results previously indicated on Fig. 114. The percentage difference becomes somewhat larger at $R_s \approx 5$ cm after the decay curve has changed slope. At the 25°, 40°, and 55° stations the agreement between the numerical results and experiments is even better than it was on axis, except at the largest shock radius where some deviation occurs. Since there seems to be no physical reason why the stress should ever be larger anywhere than it is on axis in this geometry, it may be that the boundary conditions imposed at the position of the axis in the numerical calculation are disturbing the results slightly. In any event, the effect is quite minor.

At the highest off-axis angle measured, 70°, the experiments measured stresses substantially higher than those predicted numerically. This indicated that the code is not properly treating the effects of release waves in the problem. At the larger shock radii, 3 cm and 5 cm, this same type of deviation may be occurring even at smaller off-axis angles. More details of the numerical results are required before this can be confirmed, however.

The results for the 7075-T6 aluminum targets tell almost the same story and are surprisingly consistent. Again the agreement between theory and experiment is improved at the intermediate off-axis angles and again the code predicts results at large angles which are too low by a substantial margin. In this case, the calculations were not carried out to a shock radius of 5 cm, but the trend is clear and the experiments are consistent.

Finally, an attempt has been made in two cases to compare the complete stress history obtained from the numerical calculations with the records obtained from the quartz disk arrival time probes. Since the quartz probes were not calibrated for measuring stress, the results have been normalized to the peak value in each case and should be viewed with some caution. The first case, involving measurements at 40° off axis in an 1100-0 alloy target is shown in Fig. 117. The agreement between theory and experiment in the central portion of the pulse is extremely good -- in fact, it is probably too good since there is a difference of about 4 mm between the positions at which calculations and measurements were made. Nevertheless, the agreement in waveform is quite encouraging, especially since the quartz probes were not designed with this type of measurement in mind.

There is a substantial difference in the behavior of the precursor part of the stress pulse. It is difficult to say which is more correct, the gauge or the calculation, since the uncalibrated gauge might be responding non-linearly in this region. On the other hand, it is at least equally likely that the code is incorrect. Finite difference schemes such as those used in STEEP tend to smear the leading edge of a pulse like this over several zones, and here the zoning was large enough that this effect could have produced the longer precursor. Likewise, models of material behavior -- such as work hardening -- can affect the structure of the elastic precursor. Based upon the available data it is not possible to assign reasons for the discrepancies, but these records do point out the desirability of performing well controlled stress history measurements for comparison with the calculations.

The second records compared are shown in Fig. 118. Here, as indicated previously, no well defined elastic precursor is evident in the hard 7075-T6 alloy. The agreement between the calculations and gauge records is obviously not very good in this case. This is probably due to the fact that the probe measured the wave at 84° off axis, an extremely high angle where the stress is substantially lower than that at 70° off axis. Rosenblatt (Ref. 32) notes the apparent existence of several well defined and separated waves emanating from the region of the impact in the STEEP code results; this is rather obvious in the code results shown in Fig. 118. The quartz record does indicate the possible existence of a second wave, although the behavior of these gauges upon stress relief is much in

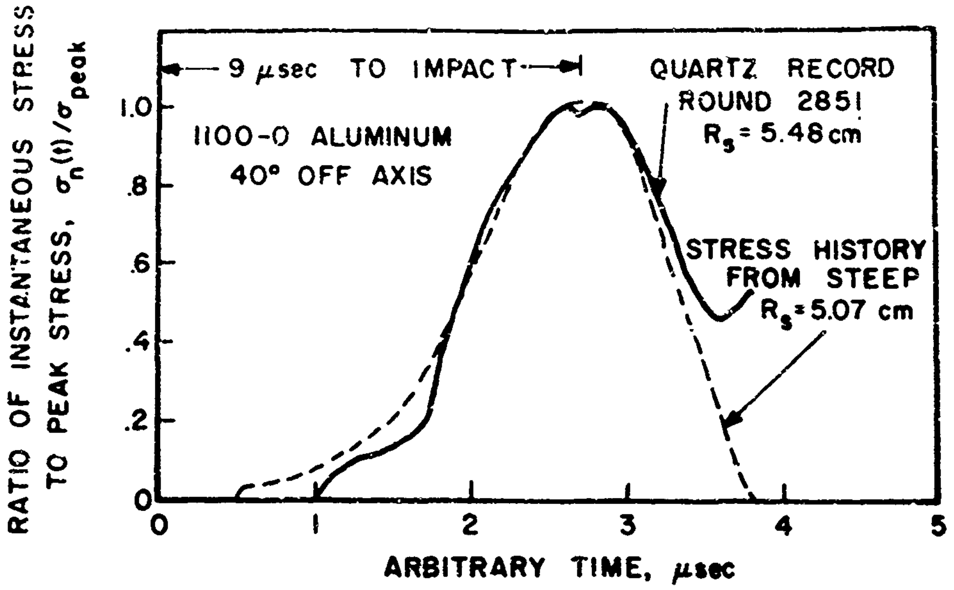

Fig. 117. Comparison of Stress History from Quartz Gauge with STEEP Code Predictions -- 1100-0 Aluminum.

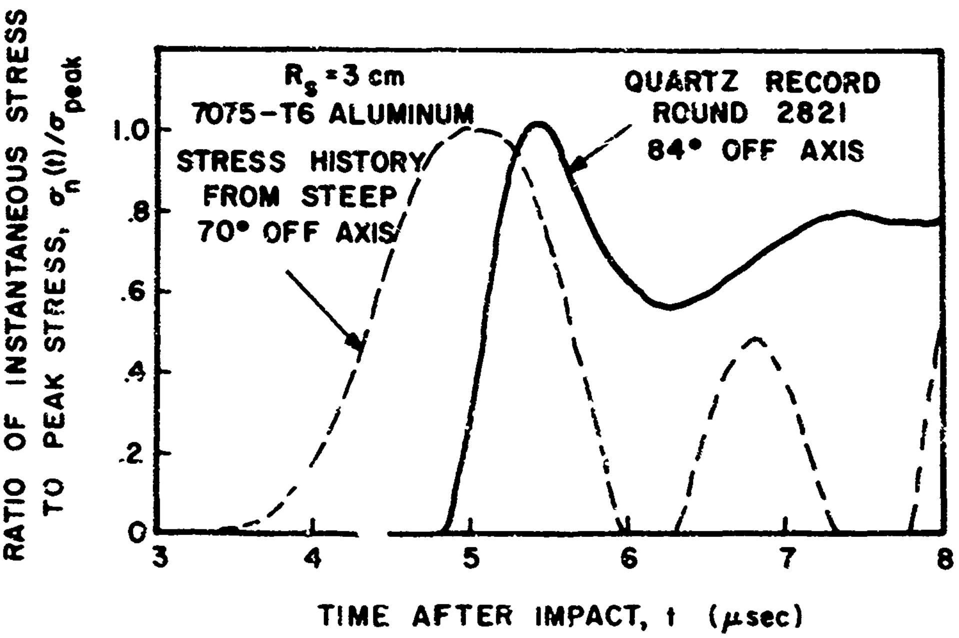

Fig. 118. Comparison of Stress History from Quartz Gauge with STEEP Code Predictions -- 7075-T6 Aluminum.

doubt. The question of whether the multiple waves are real or numerically generated oscillations is still unanswered, but worthy of further investigation.

Summary

Existing analytical techniques based upon the similarity theory of gas dynamics have been applied to the hydrodynamic behavior of solids and the results have been compared to the experimental results of this study. The similarity-like models employed are useful in understanding the processes involved in certain regimes of the shock propagation and in determining at what point and to what extent some of the simplifying assumptions fail. In the intermediate stress regime, down to within roughly an order of magnitude of the material yield strength, either the Karpov or varying energy model yield respectable agreement with experiments, provided one constant in the calculation is correctly chosen. Extensive modifications to the basic theory were necessary to get even the most rudimentary agreement with experiments because of the basic non-similar behavior of solid materials. Even so, the models describe purely hydrodynamic behavior and are unable to account for any of the many potential effects of material strength upon the shock wave propagation.

Fairly detailed comparisons have been made between available numerical calculations (particularly the STEEP code) and the experiments with favorable results. Although differences in stress magnitude exist, the numerical techniques were able to predict with fair accuracy the attenuation of the on-axis peak normal stress in the target as a function of depth, including the effects of target strength. The results were compared for several angles off axis and found to be good except for the higher angles ($\sim 70^\circ$) where the code predicts stresses that are much too low. Two quartz probe records of stress history were compared to numerical results and found to be in good agreement, although these results must be considered preliminary.

VIII. Conclusions and Recommendations

Conclusions

The primary objective of this research study, to determine experimentally the role played by material strength in an idealized hypervelocity impact situation, has been successfully accomplished. Experimental data regarding the phenomena associated with the region of the crater, including crater growth rates, have been obtained for three alloys of aluminum under varying conditions. Similarly, accurate experimental measurements of the propagation of the shock wave (the peak normal stress) into the target have been made for the same three alloys. An analysis of the results has yielded reasonable explanations for the phenomena observed. Correlation with numerical calculations has shown that the computer codes produce generally valid results, but that many of the details are in question.

The following specific conclusions apply to the results of this research:

1. The experimental techniques developed have yielded highly accurate results describing the time variation of the geometry of craters produced in aluminum by hypervelocity impacts. The techniques are applicable to future studies with other geometries or materials provided the target is sufficiently transparent to the x-rays to provide a good image.
2. The history of crater growth (either diameter or penetration) in all the aluminum alloys studied can be approximated quite accurately by a simple exponential growth law of the form D/d or $p/d = A - Be^{-t/\tau}$ where τ is the exponential period characteristic of the impact such that, to first order, D_{final}/τ and p_{final}/τ are constants independent of material strength.
3. In aluminum, rebound of the crater dimensions at late times did not occur to within experimental error.

4. Measurement of the growth of the outside diameter of the crater lip in the cases investigated yields an approximate measure of the exponential period, τ, for that case, but caution is urged in applying this conclusion outside the range of velocities and materials investigated.
5. Computer calculations (STEEP) tended not to predict crater growth rates accurately, particularly at intermediate times. Predictions of final crater dimensions were generally not much better, yielding results in several cases that would appear to be in error by ten to twenty percent.
6. As expected, the experiments show different crater growth rates in materials of different strengths. This is the first experimental evidence on transient cratering behavior demonstrating the details of these growth rate differences.
7. The fly-off disk technique coupled with a statistical treatment of the results yields an accurate, reproducible, and relatively convenient method for measuring peak normal stresses in solids. It can measure a wide range of stress levels, usually would not require direct calibration, and could be applied to a variety of situations.
8. The results show that, for the cases treated, the peak normal stress varies as the shock radius to some power to high accuracy once the initial projectile penetration has ceased. The stress varies only weakly with angle off axis out to about 30°. The stress then drops monotonically with increasing angle reaching the required value of zero at 90° off axis.
9. Definite non-hydrodynamic stress attenuation has been detected in the experiments. To the author's knowledge, this is the first experimental evidence of such material strength dependence obtained in a diverging geometry (the effect has been observed in plane geometry, see Ref. 49).

10. The quartz arrival time probes proved effective and demonstrated the existence of considerable structure on the leading edge of the propagating stress pulses. The results obtained are consistent with the elastic-plastic model of wave propagation described in the text.

11. The comparison of Mok's one-dimensional calculations (Ref. 56) and the results obtained here show that the stress attenuation is sensitive to the loading history in the crater region as well as to material effects.

12. The results of analytic methods (modified similarity theory) for calculating shock wave propagation in this impact situation have been compared with experimental results and found to yield good results only in limited regions.

13. Comparisons of numerical calculations of shock propagation have been made with the experimental results with generally acceptable agreement. Again, many of the details are in question. In particular, the numerical calculations fail to predict correctly the stress attenuation at large angles off axis and do not clearly indicate the point at which elastic or plastic unloading alters the stress attenuation. It is extremely difficult to determine why certain effects are (or are not) occurring when only a very few calculations are available.

Recommendations

Two types of additional studies are feasible and would contribute materially to extending the mainstream of the effort reported herein. The first is the development of techniques for monitoring the complete stress history (rather than merely the peak) at various positions in the target. Techniques which are at the forefront of the state of the art, such as compensated Manganin wire gauges and laser velocity interferometers, have become available only very recently and could be applied directly to this problem. Secondly, it would appear useful to extend Mok's work (one-dimensional spherical calculations) to explore the effects of both loading history and various material models on the stress attenuation history. This type of study is far too complicated and expensive to perform using the two-dimensional computer codes. Theoretical parameter studies are very important in interpreting the results of experiments in this field.

In addition, the following specific studies could be performed using the techniques developed herein (or minor variations thereof):

1. Studies of oblique hypervelocity impacts could be performed and transient measurements taken. Very little is known about shock wave propagation under these conditions, yet the phenomena are of practical interest.
2. Normal impacts into composite and/or porous materials could be studied. In many instances, it is the details of the shock wave propagation through materials such as these that is of prime interest.
3. Dynamic measurements of impacts with projectiles moving at ballistic velocities (armor impacts, etc.) are of increasing importance. Many of the techniques described herein, both experimental and numerical, are directly applicable to such problems. In particular, one such study involving the determination of the effects of projectile strength upon target response (at ballistic velocities) is already being performed under AFML and AFIT sponsorship.
4. Further experiments should be performed to determine if flat plate targets could be used when additional shock wave propagation experiments are desired -- see Appendix E.

IX. References

Much of the literature in the hypervelocity impact field is contained in the Proceedings of the various Hypervelocity Impact Symposia held from time to time up through 1965. In particular, the material in the 6th and 7th Symposia, cited as References 1 and 2 below, is both abundant and useful. It has, therefore, been found convenient to abbreviate these references to the Symposia, e.g., HVIS-7, and to cite the individual contributions separately:

1. --------. Proceedings of the Sixth Symposium on Hypervelocity Impact. Cleveland, Ohio: The Firestone Tire and Rubber Co., 1963.

2. --------. Proceedings of the Seventh Hypervelocity Symposium. Orlando, Florida: The Martin Co., 1965.

3. Cosby, W. A., and R. G. Lyle. The Micrometeoroid Environment and Its Effect on Materials and Equipment. NASA SP-78. Washington: National Aeronautics and Space Administration, 1965.

4. Hermann, Walter, and A. H. Jones. Survey of Hypervelocity Impact Information. ASRL 99-1. Cambridge, Mass: Massachusetts Institute of Technology, 1961.

5. Bouma, D. D., and W. C. Burkitt. Multivariable Analysis of the Mechanics of Penetration of High Speed Particles. NASA CR-664. Denver, Colo: The Martin Co., 1966.

6. Eichelberger, R. J. "Summary: Theoretical and Experimental Studies of Crater Formation" in HVIS-6, Vol. II, Pt 2, pp. 683-705 (1963).

7. --------. Study of the Phenomena of Hypervelocity Impact. NASA CR-55266 (N64-13393). Santa Barbara. Calif: General Motors Defense Research Laboratories, 1963.

8. Kineke, J. H., Jr., "Observations of Crater Formation in Ductile Materials" in Proceedings of the Fifth Symposium on Hypervelocity Impact, Vol. 1, Part 2. Golden, Colo: Colorado School of Mines, 1962.

9. Kineke, J. H., Jr., and R. Vitali. "Transient Observations of Crater Formation in Semi-Infinite Targets" in HVIS-6, Vol. II, Part 2, pp. 457-512 (1963).

10. Frasier, J. T., and B. G. Karpov. "Hypervelocity Impact Studies in Wax" in HVIS-5, Vol. 1, Part 2, pp. 371-388 (1961).

11. Frasier, J. T., B. G. Karpov, and L. S. Holloway. "The Behavior of Wax Targets Subjected to Hypervelocity Impacts" in HVIS-7, Vol. V, pp. 123-160 (1965).

12. Gehring, J. W., C. L. Meyers, and J. A. Charest. "Experimental Studies of Impact Phenomena and Correlation with Theoretical Models" in HVIS-7, Vol. V, pp. 161-211 (1965).

13. Charest, J. A. Measurement of Shock Wave Pressures Generated by Hypervelocity Impacts in Aluminum. NASA CR-78399 (N66-37523). Santa Barbara, Calif: General Motors Defense Research Laboratories, 1964.

14. Billingsley, J. P. Comparison of Experimental and Predicted Axial Pressure Variation for Metallic Targets Impacted by Metallic Spheres. AEDC TR 69-49 (AD690492). Tullahoma, Tenn: ARO, Inc., 1969.

15. Billingsley, J. P. "Comparison of Experimental and Predicted Axial Pressure Variation for Semi-Infinite Metallic Targets" in Proceedings of the AIAA Hypervelocity Impact Conference. Cincinnati, Ohio, 1969.

16. Kinslow, R. "Observations of Hypervelocity Impact of Transparent Plastic Targets" in HVIS-7, Vol. VI, pp. 49-107 (1965).

17. Stepka, F. S., et al. Investigation of Characteristics of Pressure Waves Generated in Water Filled Tanks Impacted by High Velocity Projectiles. NASA TN-D-3143. (1965)

18. Rae, W. J. Nonsimilar Solutions for Impact-Generated Shock Propagation in Solids. NASA CR-54251. Buffalo, N.Y.: Cornell Aeronautical Lab, Inc. (1965)

19. Rae, W. P., and H. P. Kirchner. "A Blast Wave Theory of Crater Formation in Semi-Infinite Targets" in HVIS-6, Vol. II, Part 1, pp. 163-227 (1963).

20. Rae, W. J., and H. P. Kirchner. Final Report on a Study of Meteoroid Impact Phenomena. NASA CR-50171. Buffalo, N.Y.: Cornell Aeronautical Lab, Inc., 1963.

21. Zaker, T. A. Point Source Explosion in a Solid. ARF 4132-6. Chicago, Ill.: Armour Research Foundation, 1959.

22. Bach, G. G., and J. H. Lee. "Shock Propagation in Solid Media" in Proceedings of the AIAA 5th Aerospace Sciences Meeting (AIAA Paper 67-141), 1967.

23. Heyda, J. F., and T. D. Riney. "Peak Axial Pressures in Semi-Infinite Media Under Hypervelocity Impact" in HVIS-7, Vol. III, pp. 75-122 (1965).

24. Bjork, R. L. Effect of Meteoroid Impact on Steel and Aluminum in Space. RAND Paper P-1662. Santa Monica, Calif.: The RAND Corp., 1959.

25. Evans, M. W., and F. H. Harlow. The Particle-in-Cell Method for Hydrodynamic Calculations. LA-2139. Los Alamos, N. Mex.: Los Alamos Scientific Laboratory of the University of California, 1957.

26. Walsh, J. M., and J. H. Tillotson. "Hydrodynamics of Hypervelocity Impact" in HVIS-6, Vol. II, Part 1, pp. 59-104 (1963).

27. Walsh, J. M., and W. E. Johnson. "On the Theory of Hypervelocity Impact" in HVIS-7, Vol. II, pp. 1-75 (1965).

28. Riney, T. D. "Visco-Plastic Solution of Hypervelocity Impact Cratering Phenomena" in HVIS-6, Vol. II, Part 1, pp. 105-140 (1963).

29. Dienes, J. K. "Late-Stage Equivalence and Similarity Theory for One-Dimensional Impacts" in HVIS-7, Vol. II, pp. 187-219 (1965).

30. Bjork, R. L., et al. Analytical Studies of Impact Effects as Applied to the Meteoroid Problem. NASA CR-757. Sherman Oaks, Calif: Shock Hydrodynamics, Inc., 1967.

31. Wilkins, M. L. Calculations of Elastic-Plastic Flow. UCRL-7322. Livermore, Calif.: University of California Lawrence Radiation Laboratory, 1963.

32. Rosenblatt, M. Numerical Calculations of Hypervelocity Impact Crater Formation in Hard and Soft Aluminum Alloys. (In Publication) Sherman Oaks, Calif.: Shock Hydrodynamics, Inc., 1970.

33. Gehring, J. W., Jr. "Observations of the Phenomena of Hypervelocity Impact" in Hypervelocity Impact: Fourth Symposium. Eglin AFB, Fla: Air Proving Ground Center, 1960.

34. Smith, R. H. Investigation of Crater Growth and Ejecta Cloud Resulting from Hypervelocity Impact of Aluminum Sphere on Thick Aluminum Targets. AFML TR 68-175, prepared from thesis performed for the Air Force Institute of Technology. Wright-Patterson AFB, Ohio: AF Materials Laboratory, 1968.

35. Swift, H. F. The Air Force Materials Laboratory Hypervelocity Ballistic Range. AFML TR 67-2. Wright-Patterson AFB, Ohio: University of Dayton Research Institute, 1967.

36. Swift, H. F., and E. Strader. "Flash X-Ray Actuated Trigger Switch." Review of Scientific Instruments, 39 (5): 728-730 (May 1968).

37. Preonas, D. D., and H. F. Swift. "High Intensity Point Light Source" in Proceedings of the 9th International Congress on High Speed Photography. Denver, Colo., Aug. 1970.

38. Rolsten, R. F., and W. A. Dean. Metallurgy of Aluminum Ingots for Hypervelocity Impact Targets. AFML TR 66-109. Wright-Patterson AFB, Ohio: AF Materials Laboratory, 1966.

39. Preonas, D. D., H. F. Swift and G. S. Williams. "An Inexpensive Automatic Digital Film Reader." Journal of the SPIE, 8(5):184-186 (1970).

40. Dienes, J. Cratering Calculations with a Hydrodynamic Strength Code. GAMD-7369. San Diego, Calif.: Gulf General Atomic, 1966.

41. Rosenblatt, M., and R. Bjork. Multi-Dimensional and Multi-Material Analytical Methods for Computer Solution of Hypervelocity Impact and Wave Propagation Problems. Sherman Oaks, Calif.: Shock Hydrodynamics, Inc., undated.

42. Walsh, J. M., et al. Summary Report on the Theory of Hypervelocity Impact. GA-5119. San Diego, Calif.: General Atomic Div., 1964.

43. Halperson, S. M. "Comparison Between Hydrodynamic Theory and Impact Experiments" in HVIS-7, Vol. 5, pp. 235-257 (1965).

44. Holloway, L. S. Observations of Crater Growth in Wax. BRL MR-1526. Aberdeen PG, Md.: Ballistics Research Laboratory, 1963.

45. Rinehart, J. S. Practical Countermeasures for the Prevention of Spall. AFSWC TR 60-7. Golden, Colo.: Colorado School of Mines, 1960.

46. Swift, H. F., D. D. Preonas and W. C. Turpin. "Dissection Methods for Measuring the Characteristics of Expanding Clouds." Review of Scientific Instruments, 41 (5): 746-751 (May 1970).

47. Prater, R. F., H. R. Taylor and H. F. Swift. "Piezoelectric Shock Wave Arrival Time Sensor" in the proceedings of the Aeroballistic Range Association. Dayton, Ohio: University of Dayton Research Institute, Nov. 1969.

48. Kohn, B. J. Compilation of Hugoniot Equations of State. AFWL TR 69-38. Kirtland AFB, N. Mex.: AF Weapons Laboratory, 1969.

49. Fowles, G. R. "Shock Wave Compression of Hardened and Annealed 2024 Aluminum." Journal of Applied Physics, 32 (8), 1475-1487 (1961).

50. Curran, D. R. "Nonhydrodynamic Attenuation of Shock Waves in Aluminum." Journal of Applied Physics, 34 (9), 2677-2685 (1963).

51. Erkman, J. O., and G. E. Duvall. "Elastoplasticity and the Attenuation of Shock Waves" in Proceedings of 9th Midwest Mechanics Conference. Madison, Wisc.: University of Wisconsin, 1965.

52. Erkman, J. O., A. B. Christensen and G. R. Fowles. Attenuation of Shock Waves in Solids. AFWL TR 66-12 (AD 482942). Menlo Park, Calif: Stanford Research Institute, 1966.

53. Mader, C. L. One-Dimensional Elastic-Plastic Calculations for Aluminum. LA-3678. Los Alamos, N. Mex.: Los Alamos Scientific Laboratory of the University of California, 1967.

54. Keller, D. V. Shock Propagation in Solids and Foams and Studies of Non-Hydrodynamic Attenuation. ARD 66-31R (AD 636271). Los Angeles, Calif.: Nortronics, Div. of Northrop Corp., 1966.

55. Seaman, L., et al. Classification of Materials by Shock Properties. AFWL TR 69-96. Menlo Park, Calif.: Stanford Research Institute, 1969.

56. Mok, C. H. The Effects of Solid Strength on the Propagation and Attenuation of Spherical and Plane Shock Waves. BRL R-1375 (AD 663820). Aberdeen PG, Md.: Ballistic Research Laboratory, 1967.

57. Taylor, G. I. "The Formation of a Blast Wave by a Very Intense Explosion." Proceedings of the Royal Society, Series A, 201, pp. 1959ff (1950).

58. Johnson, W. E. OIL, A Continuous Two-Dimensional Eulerian Hydrodynamic Code. GAMD-5580. San Diego, Calif.: General Atomic Div., 1964.

59. Dienes, J. K. "Late Stage Equivalence and Similarity Theory for One-Dimensional Impacts" in HVIS-7, Vol. II, pp. 187-220 (1965).

60. Walsh, J. M., and W. E. Johnson. "On the Theory of Hypervelocity Impact" in HVIS-7, Vol. II, pp. 1-76 (1965).

61. Private Communication, Dr. H. Read (Systems, Science and Software), San Diego, Calif.

62. Summers, J. L., and A. C. Charters. "High-Speed Impact of Metal Projectiles in Targets of Various Materials" in Proceedings of the Third Symposium on Hypervelocity Impact, Vol. I, pp. 101-110. Chicago, Ill.: Armour Research Foundation, 1958.

63. Clough, N., S. Lieblein, and A. R. McMillan. Crater Characteristics of 11 Metal Alloys Under Hypervelocity Impact Including Effects of Projectile Density and Target Temperature NASA TN D-5135. Cleveland, Ohio: Lewis Research Center, 1969.

64. Christman, D. R. "Target Strength and Hypervelocity Impact." AIAA Journal, 4(10), 1872-1873. (1966)

65. Denardo, B. P., J. L. Summers and C. R. Nysmith. Projectile Size Effects on Hypervelocity Impact. NASA TN D-4067. Ames Research Center, 1967.

66. Rinehart, J. S. and J. Pearson. Behavior of Metals Under Impulsive Loads. New York: Dover, 1965.

67. Zeldovich, Ya. B., and Yu. P. Raizer. Physics of Shock Waves and High Temperature Hydrodynamic Phenomena. Ed. by W. D. Hayes and R. F. Probstein. New York: Academic Press, 1967. Vol. II.

68. Walsh, J. M., and R. H. Christian. "Equation of State of Metals from Shock Wave Measurements." Physical Review, 97, 1544-1556 (1955).

69. Morgan, D. T., et al. Measurement of Gruneisen Parameter and the Internal Energy Dependence of the Solid Equation of State for Aluminum and Teflon. AVCO RAD TR 65-24. (AD 624320). Wilmington, Mass.: AVCO Corp., 1965.

70. Preonas, D. D., and R. F. Prater. "Quantitative Motion Analysis for Rotating Mirror Framing Camera Records." Journal of the Society of Motion Picture and Television Engineers, 79 (7), 586-589 (1970).

71. Bridgman, P. W. Dimensional Analysis. New Haven, Conn.: Yale University Press, 1931.

Appendix A

Reduction of Data Obtained From Crater Growth Flash X-Radiographs

In this appendix, two problems associated with the reduction of x-ray data on crater growth are discussed. The first of these problems occurs because the x-ray source, target, and film were not arranged identically for the various channels; consequently the apparent magnification in each radiograph was different and separate calibration was required. The second problem arises because it was necessary to use small, thin targets to obtain an accurate measure of the crater size at early times. For such targets, the size can actually affect the crater growth process. Methods were devised as described below to properly account for each of these problems in the data reduction.

During each impact event in the crater growth study a sequence of flash radiographs was taken at predetermined times after impact. The difference in magnification on each x-ray created by the geometrical arrangement of the x-ray sources, target, and film holders was such that some distance reference in the field of view was necessary for calibrating each flash x-ray. Each x-ray channel had a substantially different magnification at the plane of the crater and small changes in the placement of the target on the experiment holder could change the magnification from round to round. The use of an x-ray of the final crater for each round obtained after the event, but before the target was moved in any way, proved an expedient way of obtaining the desired reference data. Whenever possible the data from the flash x-ray films was expressed as a ratio of the instantaneous crater dimensions to the dimensions measured in a post-event x-radiograph. In certain cases where target damage precluded obtaining valid post-event x-ray data, the diameter of the target in the instantaneous x-radiograph was employed as a distance reference.

An inherent problem in hypervelocity impact studies is that identical impacts into identical targets display a characteristic scatter in the final crater dimensions. The ratio technique of data reduction used also contributes to reducing such scatter in the crater growth data since the data for a given round is normalized to the actual final dimensions for that round.

Certain applications require that the data be presented directly as the crater diameter, D(t), or the crater depth, p(t), as functions of time. These are usually ratioed to the projectile diameter, d, so that the impact of different sized projectiles can be compared. The procedure is to multiply the ratio of the diameter $D(t)/D_f$, by a "standard" final diameter, D_{fo}, for that material, i.e.

$$\frac{D(t)}{d} = \left[\frac{D(t)}{D_f}\right] \cdot \frac{D_{fo}}{d} \qquad \text{(Eq. 58)}$$

D_{fc} is a mean value obtained from many measurements. The use of D_f instead of D_{fo} in this expression would fail to provide the reduction in scatter mentioned above. In addition, measurement of a single crater diameter D_f (or depth p_f) implies inherent inaccuracies due to the slight irregularities of individual craters coupled with the fact that for any given x-ray the D_f required would be that in the plane through the crater center and perpendicular to the line between x-ray source and film holder. This is a different plane for each x-ray a given round.

There are exceptions to the above procedure. In several cases it was necessary to use thin targets to obtain adequate contrast in the x-ray pictures at very early times when the forming crater was still quite small. In these cases, the final crater produced was not representative of craters in truly quasi-infinite targets. Absolute measurements of the instantaneous crater size were made and compared to a "standard" final diameter to obtain the ratio $D(t)/D_{fo}$. Also for sufficiently small targets, edge effects may alter D(t) after some critical value of t; all data after that time must be disregarded.

The situation described above required that a "standard" final or post-event depth and diameter be defined for each aluminum alloy tested. Over the years vast quantities of experimental information has been gathered on impacts into quasi-infinite targets. Unfortunately, the descriptions of the exact experimental conditions and the characteristics of the target materials were many times not well documented. Certain empirical formulas that describe the crater depth have been developed. One of the earliest was that due to Charters (Ref. 62):

$$\frac{p}{d} = \zeta \left(\frac{\rho_p}{\rho_t}\right)^{2/3} \cdot \left(\frac{v}{\bar{c}_t}\right)^{2/3} \qquad \text{(Eq. 59)}$$

where ρ_p and ρ_t are the projectile and target densities respectively, v is the projectile velocity and $\bar{c}_t$ is the bulk sound speed in the material, $(E_t/\rho_t)^{1/2}$, where E_t is the target modulus of elasticity. The material cratering coefficient ζ varies slightly from material to material but always lies near the value of 2.0. Clough (Ref. 63) indicates that for 7075-T6 aluminum, $E_t = 6.96 \times 10^{11}$ dynes/cm^2 and $\zeta = 2.00$. Using these figures, for a 7075-T6 aluminum target, an aluminum projectile, and an impact velocity of 7.00 km/sec, p/d assumes the value 2.50.

Halperson (Ref. 43) develops the formula $p/d = 2.36\, v^{1/3} - 1.60$ for 1100-F aluminum (Brinnell Hardness Number 25), however he only claims good results up to a projectile velocity of 6 km/sec. Indeed the $v^{1/3}$ is no longer the accepted scaling law for hypervelocity impacts although it may well fit the data in the range Halperson discusses. In any event, application of this formula with v = 7.00 km/sec yields p/d = 2.91 for 1100-F aluminum.

More recently Christman (Ref. 64) obtained another relation where the target strength was accounted for by a parameter B_{max} which is the maximum Brinnell Hardness Number (BHN) measured in the vicinity of the sectioned target crater after the impact:

$$\frac{p}{d} = 2.05 \left(\frac{\rho_p}{\rho_t}\right)^{2/3} \left[\frac{\rho_t v^2}{B_{max}}\right]^{1/3} \qquad \text{(Eq. 60)}$$

For 1100-0 aluminum (BHN25) the B_{max} was found to be 45 kg/mm^2. Then for 7.00 km/sec projectile velocity, a p/d of 2.97 is obtained.

Unfortunately, the material parameters for the other alloys in this study were not available in the literature surveyed nor was information on crater diameters. Consequently, it was decided to analyze all the pertinent impacts that had been performed at the AFML facility in order to determine reasonable a averages for crater depths and diameters, to determine the scatter in this data, and to demonstrate the changes created by target thickness. Table XI shows the results obtained. Selected well documented results obtained by Denardo (Ref. 65) and Halperson (Ref. 43) were added to the AFML data for analysis. Projectile sizes lay between 0.318 cm and 0.635 cm and velocities between 6.0 and 7.5 km/sec. In each case the projectile was aluminum. A scaling law of $v^{2/3}$ was used to adjust all of the data to a nominal velocity of 7.0 km/sec while linear scaling was used to compare results obtained with different projectile sizes.

The quantities σ_p and σ_D represent the root mean square deviation from the mean for the p/d and D/d ratios respectively. The values in this table obtained from recent experimental data agree satisfactorily with the values obtained above from the relations of Halperson, and Christman for 1100 aluminum. The value obtained using the Charters equation does not agree well at all. Indeed, the value is more nearly that obtained at AFML for 7075-T0 aluminum. Table XII presents the raw data upon which these averages are based. Targets displaying massive spall or complete penetration were not included.

Note also that for the case of 7075-T6 aluminum, the diameter is very difficult to define due to brittle fracture of the crater lips and adjacent material late in the crater formation. This same effect accounts for the large scatter in

Table XI

Standard Crater Dimensions for Aluminum Alloys-1

Aluminum Alloy	Average p/d	σ_p	No. of Data Points	Average D/d	σ_D	No. of Data Points
1100-0	2.89	0.08	49	5.20	0.08	48
6061-T6	2.07	0.06	8	4.14	0.31	8
7075-T0	2.48	0.03	8	4.27	0.13	8
7075-T6	1.87	0.09	14	--	--	--

the 6061-T6 diameter data. For the 7075-T6 alloy, absolute values of the diameter were determined directly from each x-ray.

Figures 119 and 120 present the data as a function of the target thickness, T. Whenever the target rear surface was not parallel to the front surface, the distance from the impact point to the nearest point on the rear surface was used. This data indicates that the target thickness has little effect upon the crater depth or diameter until some critical thickness is reached -- a thickness corresponding to massive rear surface spall or complete target penetration. For each of these aluminum alloys the threshold appears to lie near a T/d value of 6, although the data is sparse in most cases.

Several other projectile and target combinations are required for this study although there is not sufficient data available to study the behavior of these materials as a function of target thickness. This additional data is presented in Tables XIII and XIV.

This data indicates that the use of the ratio technique of reducing the flash x-ray photographs should remain valid down to the target thickness threshold point described above. For cases below this threshold, or for those events where massive target spall or complete penetration occurred an absolute measurement of the crater dimensions and separate evaluation of the validity of each x-ray must be made.

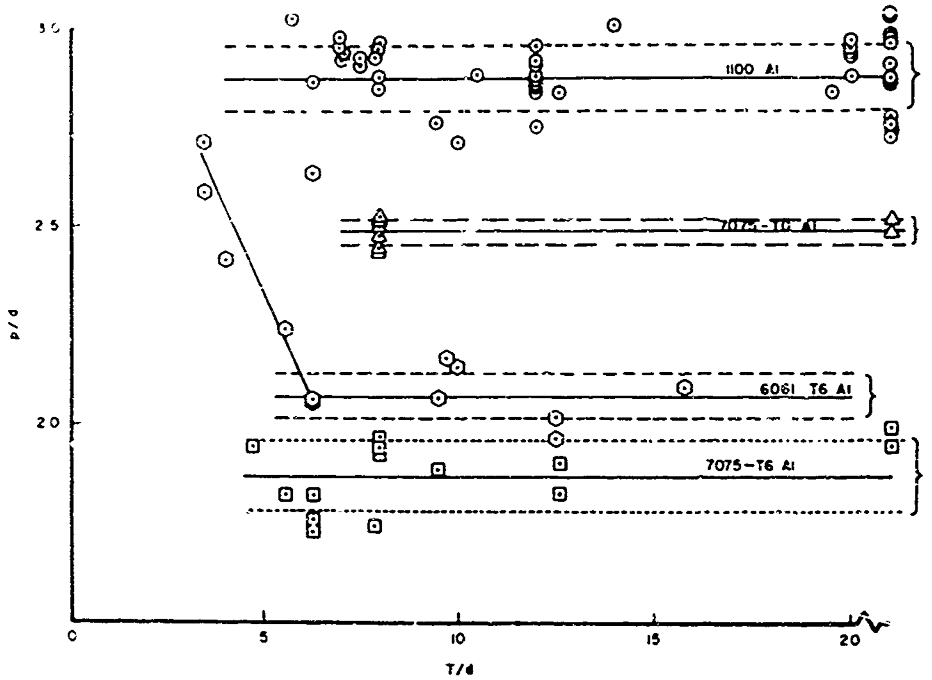

Fig. 119. Hypervelocity Impact (7 km/sec) Crater Penetration versus Target Thickness in Scaled Coordinates for Aluminum Alloys.

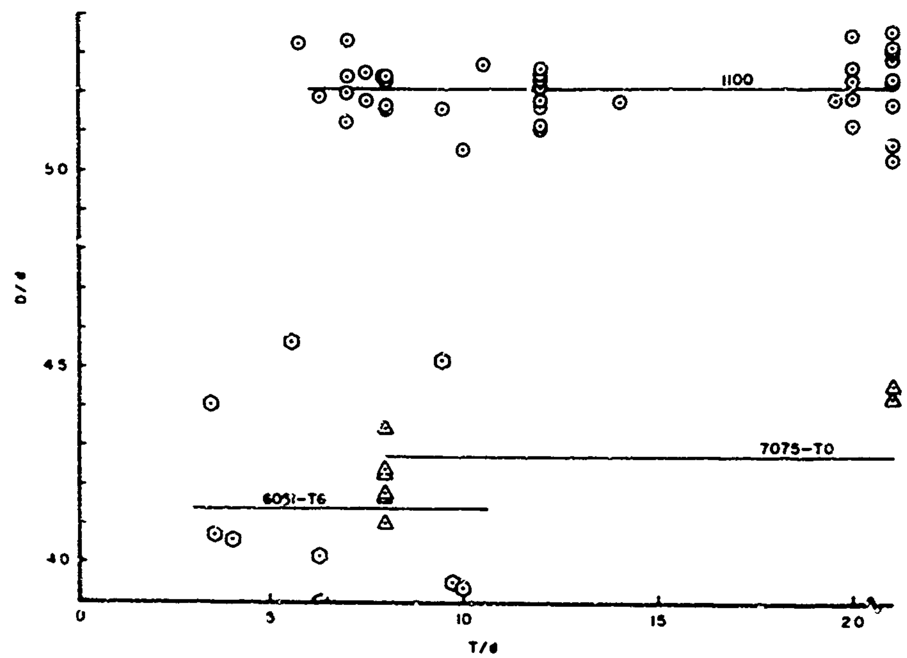

Fig. 120. Hypervelocity Impact (7 km/sec) Crater Diameter versus Target Thickness in Scaled Coordinates for Aluminum Alloys.

Table XII

Crater Dimension Data-I

Round Number	Projectile Velocity (km/sec)	Projectile Diameter (cm)	Scaled Depth (p_s/d)	Scaled Diameter (D_s/d)	Target Thickness (T/d)
1100-0 Aluminum					
2002	6.86	0.3175	2.93	5.21	20.0
2003	6.69	0.3175	2.94	5.10	20.0
2004	6.90	0.3175	2.96	5.25	20.0
2005	6.69	0.3175	2.92	5.33	20.0
2093	6.84	0.3175	2.75	5.15	>20
2238	7.16	0.3175	2.83	5.17	19.5
2239	7.32	0.3175	2.87	5.17	20.0
2384	6.90	0.3175	2.87	5.26	10.5
2385	7.05	0.3175	2.92	5.24	7.5
2386	7.03	0.3175	2.90	5.17	7.5
2387	7.01	0.3175	2.71	5.05	10.0
2455	7.10	0.3175	2.83	5.10	12.0
2456	7.01	0.3175	2.86	5.20	12.0
2457	7.01	0.3175	2.74	5.24	12.0
2459	6.90	0.3175	2.90	5.17	12.0
2460	6.91	0.3175	2.87	5.11	12.0
2461	6.80	0.3175	2.84	5.15	12.0
2462	6.90	0.3175	2.95	5.22	12.0
2463	6.76	0.3175	2.91	5.25	12.0
2464	6.87	0.3175	2.85	5.11	12.0
2503	7.16	0.3175	2.87	5.15	8.0
2504	7.22	0.3175	2.84	5.16	8.0
2505	7.14	0.3175	2.94	5.23	8.0
2521	7.30	0.3175	2.96	5.22	8.0
2589	6.37	0.635	2.94	5.32	7.0
2639	7.14	0.635	2.92	5.19	7.0
2640	7.06	0.635	2.97	5.23	7.0
2641	7.01	0.635	2.94	5.12	7.0
2676	6.80	0.635	3.02	5.32	5.75
2719	6.96	0.635	3.00	5.17	14.0
2811	6.99	0.635	2.86	5.18	6.3
2851	6.43	0.635	2.92	5.23	7.9
2860	6.70	0.635	2.83	-	12.6
2864	6.70	0.635	2.75	5.15	9.45

Table XII (Continued)

Round Number	Projectile Velocity (km/sec)	Projectile Diameter (cm)	Scaled Depth (p_s/d)	Scaled Diameter (D_s/d)	Target Thickness (T/d)
76*	6.85	0.4763	2.86	5.29	†
77*	6.54	0.4763	2.90	5.34	†
94*	7.20	0.4763	2.95	5.22	†
614*	7.52	0.3175	2.71	5.02	†
615*	7.02	0.3175	2.73	5.05	†
620*	6.36	0.635	2.90	5.21	†
854*	6.90	0.3175	2.77	5.17	†
909*	6.25	0.3175	2.87	5.27	†
44**	6.57	0.635	2.98	5.30	†
45**	6.72	0.635	2.85	5.22	†
48**	6.87	0.635	2.97	5.30	†
277**	6.74	0.4763	2.98	5.22	†
278**	7.13	0.4763	3.03	5.17	†
280**	7.38	0.4763	2.96	5.16	†
284**	7.01	0.4763	3.02	5.29	†
6061-T6 Aluminum					
2006	7.18	0.3175	2.14	3.94	10.0
2007	7.14	0.3175	2.16	3.94	9.75
2008	7.19	0.3175	2.42	4.06	4.06
2012	6.50	0.3175	2.58	4.07	3.60
2014	6.67	0.3175	2.72	4.41	3.50
2688	6.70	0.635	2.63	3.60	6.32
2694	6.80	0.635	2.24	4.56	5.6
2806	6.70	0.635	2.06	-	6.3
2837	6.25	0.635	2.06	4.51	9.45
2838	5.93	0.635	2.09	-	15.75
2842	5.88	0.635	2.01	-	12.6
2863	6.70	0.635	2.01	-	12.6
2865	6.70	0.635	2.06	4.15	6.3
7075-T0 Aluminum					
2240	6.95	0.3175	2.51	4.48	>20

* Ref. 66

** Ref. 42

† Quasi-infinite, exact value not cited. Taken as >20.

Table XII (Continued)

Round Number	Projectile Velocity (km/sec)	Projectile Diameter (cm)	Scaled Depth (p_s/d)	Scaled Diameter (D_s/d)	Target Thickness (T/d)
2245	7.20	0.3175	2.48	4.41	>20
2503	7.45	0.3175	2.43	4.17	8.0
2506	7.15	0.3175	2.52	4.10	8.0
2508	7.16	0.3175	2.49	4.23	8.0
2519	7.27	0.3175	2.44	4.18	8.0
2522	7.34	0.3175	2.47	4.34	8.0
2523	7.28	0.3175	2.52	4.23	8.0
7075-T6 Aluminum					
2242	7.15	0.3175	1.94	-	>20
2247	7.17	0.3175	1.99	-	>20
2509	7.29	0.3175	1.96	-	8.0
2510	7.20	0.3175	1.93	-	8.0
2511	7.24	0.3175	1.94	-	8.0
2693	6.97	0.635	1.82	-	5.6
2804	6.70	0.635	1.73	-	6.3
2823	7.00	0.635	1.90	-	12.6
2824	6.95	0.635	1.83	-	12.6
2825	6.41	0.635	1.88	-	9.5
2832	6.96	0.635	1.95	-	4.75
2854	6.61	0.635	1.74	-	7.9
2857	6.44	0.635	1.76	-	6.3
2859	6.44	0.635	1.82	-	6.3

Table XIII
Standard Crater Dimensions for Aluminum Alloys-II

Aluminum Alloy	Projectile Material	Nominal Projectile Velocity (km/sec)	Average p/d	Average D/d
1100-0	2017 Al	2.30	1.56	2.60
1100-0	2017 Al	5.20	2.52	4.42
1100-0	2017 Al	4.10	2.27	3.94
1100-0	Steel	5.20	5.02	6.03

Table XIV

Crater Dimension Data-II

Round Number	Projectile Velocity (km/sec)	Projectile Diameter (cm)	Scaled Depth (p_s/d)	Scaled Diameter (D_s/d)	Target Thickness (T/d)
1100 Aluminum Target (Scaled to 2.30 km/sec)					
1044	2.34	0.3175	1.49	2.62	8.0
1045	2.32	0.3175	1.53	2.57	8.0
1049	2.29	0.3175	1.67	2.61	7.1
1100 Aluminum Target (Scaled to 5.20 km/sec)					
2515	5.40	0.3175	2.53	4.39	8.0
2516	5.03	0.3175	2.49	4.43	8.0
2517	5.07	0.3175	2.59	4.40	8.0
2524	5.16	0.3175	2.52	4.40	8.0
2642	5.42	0.635	2.44	4.51	7.0
1100 Aluminum Target (Scaled to 4.10 km/sec)					
2698	4.19	0.635	2.36	3.96	4.75
2700	4.03	0.635	2.14	3.96	7.0
2701	4.09	0.635	2.21	3.94	5.2
2702	4.08	0.635	2.30	3.94	5.2
2703	4.10	0.635	2.28	3.94	5.2
2704	4.23	0.635	2.35	3.87	5.2
1100 Aluminum Target--Steel Projectile (Scaled to 5.20 km/sec)					
2526	5.26	0.358	4.96	6.02	14.2
2527	5.03	0.358	5.01	6.13	14.2
2528	5.13	0.358	5.08	5.95	14.2

Appendix B

Experimental Crater Growth Data

All the usable crater growth data acquired in this effort has been processed and is reported in this appendix. The results discussed in Chapter IV are based upon this data. The characteristics of each round fired may be obtained by referring to Table IV.

The data obtained from flash x-radiographs is shown in Table XV. In some cases, a given x-ray channel may have failed to yield useful results either because of unreadable x-radiographs or because of failure to record the timing signals. These points have been eliminated from the data presented. Likewise, the small percentage of rounds fired that failed to yield any useful information -- usually due either to a broken projectile or a gross failure in the timing system -- are not reported.

In Table XV, the normalized time used, t/d, has units of μ sec/cm. The timing method refers to the type of equipment generating the signal that indicated x-ray firing; H.S. refers to the "head switches," X-TRIG to the output from the x-ray thyratrons, and OTHER to signals derived from less accurate sources, generally a measurement of the time between impact and the output of an electronic time delay generator. The estimated accuracy of the x-ray firing time is based upon actual measurements of the relative times of activation of the switch, time delay generator, x-ray thyratron driver, and x-ray tube head switches for those rounds where complete timing data was available. The data was averaged separately for each channel to arrive at an average time delay and rms deviation from this mean time delay. This rms deviation was used to obtain the estimated accuracy of the timing signal.

The information on image quality is an average of the subjective evaluation of each film by at least three readers. Even th e films rated poor yielded remarkedly consistent results.

The data on the growth history of the front surface plume was acquired with a high speed framing camera. The processed results are shown in Table XVI. The column labeled "case" refers to the type of experiment -- the key is provided in Table III.

Table XV. Flash X-Ray Crater Growth Data.

ROUND NUMBER	PROJECTILE DIAMETER (CM)	X-RAY NUMBER	TIME RATIO (t/d)	TIMING METHOD	ESTIMATED ACCURACY (Δt/d)	DIAMETER RATIO (D/d)	IMAGE QUALITY	PENETRATION RATIO (p/d)	IMAGE QUALITY
1044	0.318	1	25.80	OTHER	2.83	2.340	FAIR		
		2	29.60	X-TRIG	1.26	2.420	FAIR		
		4	20.80	H. S.	0.63	2.350	POOR	1.120	POOR
		5	36.90	X-TRIG	1.26	2.230	FAIR	1.560	FAIR
		6	67.40	X-TRIG	1.26	2.570	FAIR	1.450	FAIR
1045	0.318	3	55.70	H. S.	0.63	2.730	FAIR	1.420	FAIR
		4	52.30	H. S.	0.63	2.470	FAIR	1.510	POOR
		5	18.60	X-TRIG	4.40	2.200	POOR	1.060	FAIR
		6	26.50	H. S.	0.63	2.210	FAIR	1.370	POOR
1049	0.318	1	41.60	OTHER	3.14	2.450	FAIR		
		3	28.70	OTHER	1.89	2.520	FAIR	1.400	FAIR
		4	23.00	OTHER	1.89	2.280	FAIR	1.140	FAIR
		5	41.30	OTHER	3.14	2.460	FAIR	1.340	FAIR
		6	58.60	OTHER	1.89	2.440	POOR	1.390	POOR
2384	0.318	1	13.82		1.57	3.380	FAIR		
		2	13.98	OTHER	2.52	3.480	FAIR		
		3	16.70		1.57			2.000	GOOD
		4	15.75		1.57			2.020	GOOD
		5	10.65		1.57	3.330	GOOD	0.	
2385	0.318	1	42.20		1.57	4.840	FAIR		
		2	45.60		1.57	5.100	FAIR		
		3	49.40		1.57	4.950	GOOD	2.860	GOOD
		4	42.50		6.29	5.040	GOOD	2.800	GOOD
		5	41.00		1.57	5.040	FAIR		
2387	0.318	3	161.30	OTHER	6.29	5.200	FAIR	2.770	FAIR
		4	116.70	OTHER	6.29	5.070	GOOD	2.830	GOOD
		5	69.40	OTHER	6.29	5.200	FAIR		
2502	0.318	3	43.50	X-TRIG	1.26	4.090	POOR	2.410	POOR
		5	74.30	H. S.	0.63	4.270	FAIR	2.420	FAIR
2503	0.318	1	103.70	OTHER	3.14	5.080	GOOD		
		2	93.00	X-TRIG	1.26	5.260	FAIR		
		4	41.90	H. S.	0.63	4.940	GOOD	2.780	GOOD
2504	0.318	2	1.26	X-TRIG	1.57	2.000	FAIR		

Table XV (Continued)

ROUND NUMBER	PROJECTILE DIAMETER (CM)	X-RAY NUMBER	TIME RATIO (t/d)	TIMING METHOD	ESTIMATED ACCURACY (Δt/d)	DIAMETER RATIO (D/d)	IMAGE QUALITY	PENETRATION RATIO (p/d)	IMAGE QUALITY
		4	4.73	H. S.	0.47	2.440	FAIR	1.270	FAIR
		5	8.29	H. S.	0.47	2.910	GOOD	1.590	GOOD
		6	5.17	H. S.	0.47	2.390	FAIR	1.440	FAIR
2505	0.319	1	133.00	OTHER	4.40	5.300	GOOD		
		4	64.30	X-TRIG	1.57	5.100	GOOD	2.890	GOOD
		5	180.20	H. S.	0.94	5.150	GOOD	3.010	FAIR
		6	103.70	X-TRIG	..57	5.290	FAIR	2.890	FAIR
2506	0.318	4	41.00	H. S.	0.94	4.010	FAIR	2.510	FAIR
		6	97.40	H. S.	0.94	4.140	POOR	2.530	POOR
2507	0.318	1	20.50	X-TRIG	1.26	3.590	GOOD		
		2	37.50	X-TRIG	1.26	4.100	GOOD		
		3	4.22	H. S.	0.47	1.980	FAIR	0.820	FAIR
		4	5.70	H. S.	0.47	2.110	FAIR	1.040	FAIR
		5	6.96	H. S.	0.47	2.360	FAIR	1.070	FAIR
		6	8.31	H. S.	0.47	2.740	FAIR	1.540	FAIR
2508	0.318	3	22.70	X-TRIG	1.26	3.590	FAIR	2.130	FAIR
		4	31.80	H. S.	0.63	4.020	FAIR	2.360	FAIR
		6	67.40	H. S.	0.63	4.140	FAIR	2.550	POOR
2509	0.318	3	18.30	X-TRIG	1.26	3.230	FAIR	1.510	POOR
		4	34.60	H. S.	0.63	3.500	FAIR	1.640	POOR
		5	49.10	X-TRIG	1.26	3.400	FAIR	1.620	FAIR
		6	69.90	X-TRIG	1.26	3.430	POOR	1.590	POOR
2510	0.318	4	6.93	H. S.	0.31	2.340	POOR	1.190	POOR
		5	10.30	H. S.	0.31	2.670	FAIR	1.470	FAIR
		6	12.10	X-TRIG	1.10	2.870	FAIR	1.510	FAIR
2511	0.318	3	3.40	X-TRIG	1.10	1.680	POOR	0.800	POOR
		4	5.98	H. S.	0.31	2.210	FAIR	1.170	FAIR
		6	128.50	X-TRIG	1.26	3.290	FAIR	1.620	FAIR
2515	0.317	1	73.10	H. S.	0.63	4.290	GOOD		
		2	53.90	H. S.	0.63	4.420	GOOD		
		3	9.51	X-TRIG	1.10	2.390	FAIR	1.280	FAIR
		4	12.60	X-TRIG	1.10	3.050	FAIR	1.660	FAIR
		5	18.90	H. S.	0.31	3.540	GOOD	1.940	GOOD

Table XV (Continued)

ROUND NUMBER	PROJECTILE DIAMETER (CM)	X-RAY NUMBER	TIME RATIO (t/d)	TIMING METHOD	ESTIMATED ACCURACY (Δt/d)	DIAMETER RATIO (D/d)	IMAGE QUALITY	PENETRATION RATIO (p/d)	IMAGE QUALITY
		6	35.30	OTHER	1.89	4.150	GOOD	2.540	GOOD
2516	0.319	1	73.10	H. S.	0.63	4.330	FAIR		
		2	8.28	H. S.	0.31	2.340	POOR		
		4	6.08	X-TRIG	1.10	1.990	FAIR	1.160	FAIR
		5	12.70	H. S.	0.31	3.090	FAIR	1.790	FAIR
		6	34.60	X-TRIG	1.26	4.240	FAIR	2.540	FAIR
2517	0.318	1	138.70	H. S.	0.63	4.290	FAIR		
		2	19.50	X-TRIG	1.57	4.240	FAIR		
		3	7.02	H. S.	0.31	2.120	FAIR	1.030	FAIR
		4	10.70	H. S.	0.63	2.839	FAIR	1.510	FAIR
		5	51.00	X-TRIG	1.26	4.510	FAIR	2.599	FAIR
		6	59.30	H. S.	0.63	4.460	FAIR	2.470	FAIR
2519	0.318	5	42.20	OTHER	1.89	4.019	POOR		
		6	86.37	OTHER	2.83	4.230	FAIR	2.600	POOR
2520	0.318	5	32.10	OTHER	1.89	3.340	FAIR	1.620	FAIR
		6	78.40	OTHER	1.89	3.259	POOR	1.690	POOR
2521	0.318	5	125.40	OTHER	1.89	5.200	GOOD	2.830	FAIR
		6	106.50	OTHER	1.89	5.160	GOOD	2.860	GOOD
2524	0.358	1	39.70	H. S.	0.56	4.240	FAIR		
		3	5.89	OTHER	1.40	2.570	POOR	2.210	POOR
		4	6.71	X-TRIG	1.40	1.930	GOOD	1.620	GOOD
		5	40.30	X-TRIG	1.12	4.440	GOOD	3.960	GOOD
		6	17.00	X-TRIG	1.12	3.070	GOOD	2.760	GOOD
2525	0.358	3	19.20	OTHER	1.40	3.140	GOOD	3.310	GOOD
		4	12.90	X-TRIG	0.98	2.710	GOOD	2.660	GOOD
2527	0.359	3	24.90	OTHER	1.40	3.680	FAIR	3.660	GOOD
		4	5.92	X-TRIG	0.98	1.819	FAIR	1.410	GOOD
		5	31.50	X-TRIG	1.12	4.160	FAIR	4.220	GOOD
		6	40.93	X-TRIG	1.12	4.580	GOOD	4.370	GOOD
2529	0.358	3	66.50	OTHER	1.68	5.450	GOOD	5.090	GOOD
		4	49.40	X-TRIG	1.12	4.970	GOOD	4.720	GOOD
		6	79.70	H. S.	0.56	5.800	FAIR	5.060	GOOD

Table XV (Continued)

ROUND NUMBER	PROJECTILE DIAMETER (CM)	X-RAY NUMBER	TIME RATIO (t/d)	TIMING METHOD	ESTIMATED ACCURACY (Δt/d)	DIAMETER RATIO (D/d)	IMAGE QUALITY	PENETRATION RATIO (p/d)	IMAGE QUALITY
		6	96.10	X-TRIG	1.12	5.900	FAIR	5.020	GOOD
2484	0.635	2	12.00	X-TRIG	0.79	3.320	FAIR		
		3	9.18	H. S.	0.31	2.370	FAIR	1.300	POOR
		5	14.00	X-TRIG	0.54	3.360	GOOD	1.980	GOOD
		6	12.00	H. S.	0.31	3.320	GOOD	1.770	GOOD
		7	5.77	X-TRIG	0.94	2.670	FAIR		
		9	11.50	X-TRIG	1.10	3.320	FAIR		
		10	13.40	X-TRIG	1.10	3.580	GOOD		
2485	0.635	2	82.40	X-TRIG	0.79	3.930	FAIR		
		3	35.30	H. S.	0.31	2.860	POOR	1.470	POOR
		5	65.80	X-TRIG	0.54	4.220	GOOD	2.010	GOOD
		6	83.60	X-TRIG	1.42	3.970	FAIR	2.070	FAIR
		7	64.00	H. S.	0.31	4.260	FAIR		
		8	65.20	X-TRIG	0.79	4.300	FAIR		
		9	93.20	X-TRIG	1.10	4.020	FAIR		
		10	114.80	X-TRIG	1.10	3.970	FAIR		
2486	0.635	3	11.80	X-TRIG	0.63	3.480	FAIR	1.680	FAIR
		4	23.50	H. S.	0.31	3.850	FAIR	2.030	POOR
		8	28.70	H. S.	0.31	4.180	FAIR		
		9	35.60	X-TRIG	1.10	4.220	FAIR		
		10	45.20	X-TRIG	1.10	4.100	POOR		
2493	0.635	1	70.00	X-TRIG	1.49	4.180	FAIR		
		2	70.60	X-TRIG	0.79	4.140	FAIR		
		3	25.50	H. S.	0.31	4.020	FAIR	2.030	FAIR
		4	41.90	H. S.	0.31	4.270	POOR	2.050	POOR
		5	71.70	H. S.	0.31	4.060	FAIR	2.070	FAIR
		6	70.30	H. S.	0.31	3.890	POOR	1.950	POOR
		7	13.70	H. S.	0.31	3.480	FAIR		
		8	27.30	X-TRIG	0.79	3.940	FAIR		
		9	44.10	X-TRIG	1.10	4.220	FAIR		
		10	76.60	X-TRIG	1.10	4.180	POOR		
2497	0.635	3	8.82	H. S.	0.31	2.700	FAIR	1.530	FAIR
		4	12.30	H. S.	0.31	3.430	FAIR	1.820	FAIR
		5	23.80	H. S.	0.31	3.950	FAIR	2.400	FAIR
		6	29.80	H. S.	0.31	4.210	GOOD	2.540	GOOD
		8	19.70	H. S.	0.31	3.800	FAIR		

Table XV (Continued)

ROUND NUMBER	PROJECTILE DIAMETER (CM)	X-RAY NUMBER	TIME RATIO (t/d)	TIMING METHOD	ESTIMATED ACCURACY (Δt/d)	DIAMETER RATIO (D/d)	IMAGE QUALITY	PENETRATION RATIO (p/d)	IMAGE QUALITY
		9	25.70	X-TRIG	1.10	4.260	POOR		
2692	0.635	2	11.90	X-TRIG	0.79	2.910	FAIR		
		3	4.57	H. S.	0.31	2.940	FAIR	0.750	FAIR
		4	9.75	H. S.	0.31	2.700	FAIR	1.250	FAIR
		5	13.20	H. S.	0.31	3.110	FAIR	1.470	FAIR
		6	12.10	X-TRIG	1.42	2.930	GOOD	1.490	GOOD
		7	5.82	H. S.	0.31	2.070	FAIR		
		8	5.82	H. S.	0.31	2.090	FAIR		
		9	17.20	X-TRIG	1.10	3.270	GOOD		
		10	21.70	X-TRIG	1.10	3.380	FAIR		
2693	0.635	3	25.00	H. S.	0.31	3.360	POOR	1.610	FAIR
		5	44.10	H. S.	0.31	3.400	POOR	1.610	FAIR
		6	59.80	H. S.	0.31	3.360	POOR	1.780	POOR
2694	0.635	3	8.82	H. S.	0.31	2.780	FAIR	1.370	FAIR
		4	16.40	H. S.	0.31	3.520	POOR	1.900	POOR
		5	44.90	H. S.	0.31	4.140	FAIR	2.030	FAIR
		6	109.60	H. S.	0.31	4.140	FAIR	2.070	FAIR
		7	9.29	H. S.	0.31	3.230	FAIR		
		8	15.90	H. S.	0.79	3.730	FAIR		
		9	59.50	H. S.	1.10	4.100	FAIR		
		10	2 0.00		15.75	4.180	FAIR		
2696	0.635	3	37.20	H. S.	0.31	4.520	POOR	2.780	POOR
		4	60.60	H. S.	0.31	5.200	FAIR	2.800	POOR
		5	83.10	H. S.	0.31	5.150	GOOD	2.860	GOOD
		7	39.40	H. S.	0.31	4.780	FAIR		
		8	58.40	X-TRIG	0.79	5.290	FAIR		
		9	73.50	X-TRIG	1.10	5.300	POOR		
		10	95.40	X-TRIG	1.10	4.990	POOR		
2698	0.635	4	1.48	H. S.	0.31	1.340	POOR		
		5	4.55	H. S.	0.31	1.930	FAIR	0.700	FAIR
		8	3.58	H. S.	0.31	2.130	FAIR		
		9	6.14	X-TRIG	1.10	2.250	FAIR		
		10	11.30	X-TRIG	1.10	2.800	FAIR		
2700	0.635	3	28.80	H. S.	0.31	3.630	POOR	2.540	POOR
		4	34.60	H. S.	0.31	3.900	FAIR	2.180	FAIR

Table XV (Continued)

[illegible] NUMBER	PROJECTILE DIAMETER (CM)	X-RAY NUMBER	TIME RATIO (t/d)	TIMING METHOD	ESTIMATED ACCURACY (Δt/d)	DIAMETER RATIO (D/d)	IMAGE QUALITY	PENETRATION RATIO (p/d)	IMAGE QUALITY
		5	37.00	H. S.	0.31	3.900	FAIR	2.250	FAIR
		6	15.40	H. S.	0.31	3.040	FAIR	1.500	FAIR
		7	28.80	H. S.	0.31	3.630	FAIR		
		8	34.50	H. S.	0.31	3.890	FAIR		
		9	39.40	H. S.	0.31	3.860	FAIR		
270	0.635	2	13.50	X-TRIG	0.79	2.440	FAIR		
		3	11.70	H. S.	0.31	2.760	FAIR	1.390	FAIR
		4	11.70	H. S.	0.31	2.800	GOOD	1.450	GOOD
		5	15.00	H. S.	0.31	3.040	GOOD	1.500	GOOD
		7	4.57	H. S.	0.03	1.890	GOOD		
		8	5.83	H. S.	0.31	2.130	GOOD		
		9	7.69	X-TRIG	1.10	2.440	FAIR		
		10	8.98	X-TRIG	1.10	2.480	FAIR		
2704	0.635	2	9.29	H. S.	0.31	2.450	FAIR		
		3	4.25	H. S.	0.31	1.380	POOR	0.610	POOR
		4	5.83	H. S.	0.31	1.970	FAIR	0.660	FAIR
		5	8.98	H. S.	0.31	2.330	GOOD	1.070	GOOD
		7	13.10	H. S.	0.31	2.800	FAIR		
		8	15.70	H. S.	0.31	3.040	FAIR		
		9	18.40	X-TRIG	1.10	3.310	POOR		

Table XVI

Framing Camera Data on Plume Diameter Minimum and Plume Base Growth

Round Number	Case	Projectile Diameter, d (cm)	Frame Number	Scaled Time, t/d (μsec/cm)	Scaled Plume Minimum, D_m/d	Scaled Plume Base D_b/d
1043	4	0.318	35	2.39	1.38	1.53
			36	4.71	1.60	1.90
			37	7.10	1.96	2.18
			38	9.46	2.31	2.48
			39	11.83	2.42	2.65
			40	14.00	2.56	2.84
			42	18.83	2.80	3.07
			44	23.67	-	3.28
			46	28.38	3.13	3.28
2520	8	0.318	27	7.27	2.95	3.84
			28	11.01	3.69	4.79
			29	14.71	4.15	5.21
			30	18.26	4.45	5.25
			31	22.14	4.65	5.31
			32	25.70	4.87	5.40
			33	29.55	4.96	5.52
			34	33.04	4.95	5.35
			35	36.75	5.11	5.53
			36	40.34	5.04	5.57

Table XVI (Continued)

Round Number	Case	Projectile Diameter, d (cm)	Frame Number	Scaled Time, t/d (μsec/cm)	Scaled Plume Minimum, D_m/d	Scaled Plume Base D_b/d
2521	1	0.318	37	2.80	1.88	2.44
			38	4.63	2.31	3.30
			39	6.52	2.70	4.13
			40	8.19	2.96	4.35
			42	11.94	3.55	5.33
			44	15.69	-	6.03
			46	19.37	4.46	6.44
			2	25.20	4.99	7.05
			4	28.88	5.25	7.68
			6	32.63	5.48	-
			8	36.75	5.72	8.20
2523	7	0.318	13	1.41	1.49	1.64
			14	2.82	1.95	2.29
			15	4.28	2.22	2.86
			16	5.61	2.54	3.36
			17	7.13	2.86	3.71
			18	8.45	3.06	4.00
			19	9.92	3.31	4.31
			20	11.33	3.54	4.57
			23	15.73	4.13	-
			26	19.92	4.62	6.04

Table XVI (Continued)

Round Number	Case	Projectile Diameter, d (cm)	Frame Number	Scaled Time, t/d (μsec/cm)	Scaled Plume Minimum, D_m/d	Scaled Plume Base D_b/d
			28	22.82	4.89	6.11
			30	25.62	5.13	6.47
			32	28.49	5.35	6.64
			34	31.31	5.55	6.78
			36	34.12	5.78	-
			38	36.97	5.92	-
2524			2	2.14	1.74	2.01
			3	3.56	2.02	2.59
			4	5.01	2.38	3.04
			5	6.49	2.60	3.55
			6	7.91	2.80	3.80
			7	9.35	2.99	3.96
			8	10.65	3.15	4.24
			9	12.13	3.35	4.80
			10	13.54	3.51	5.03
			11	14.99	3.67	5.10
			12	16.35	3.84	5.12
			13	17.76	3.88	5.19
			15	20.63	4.02	5.69
			17	23.46	4.31	5.68
			19	26.24	4.47	-
			21	29.10	4.64	5.97

Appendix C

Determination of Geometry for Multi-Faceted and Half-Cylinder Targets

The experiments conducted on shock wave propagation into the aluminum targets required that an accurate determination be made of the various geometric factors involved in accurately describing the impact and the point at which a measurement was taken. Specifically it was necessary to determine the distance from the point of impact to the point of measurement, the angle between the projectile trajectory and the line connecting the impact point to the point of measurement, and the angle between the shock front and the target surface at the point of measurement. This appendix describes the details of how these geometric measurements were made for the several types of targets used.

Each multi-faceted target was designed so that the distances from the "nominal" impact point to each rear surface along the line perpendicular to that surface were identical. The thin aluminum fly-off disks were placed on these rear surfaces at the points just described and time-of-arrival probes were slightly displaced from these points. It is a characteristic of light-gas guns that the point of impact cannot be predicted exactly *a priori*. Consequently the "nominal" impact point just described did not in general correspond to the real impact point. The actual measurement of required distances and angles had to be performed after the round was fired. For these experiments the actual impact point was always within one projectile diameter of the nominal impact point and usually closer.

The geometry of the multi-faceted target is illustrated in Fig. 121. A system of coordinates is defined upon the target front face such that looking down the gun barrel toward the target, the x-axis is to the right, the y-axis up, and the z-axis back along the projectile trajectory. The origin is located at the

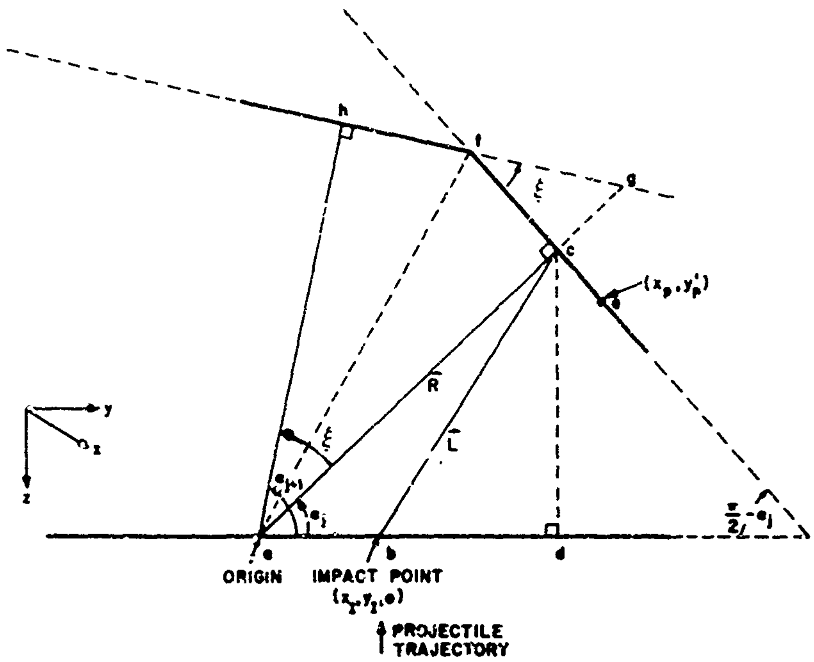

Fig. 121. Multi-Faceted Target Geometry.

"nominal" impact point (a); the actual impact point (b) has coordinates $(x_I, y_I, 0)$. The component of the vector from the origin to (b) that lies along the y-axis is called $\overrightarrow{ab}$.

$\vec{R}$ is the vector connecting the origin with the j^{th} surface such that the vector is normal to the j^{th} surface. $\vec{R}$ intersects the j^{th} surface at the point (c). The angle α_j refers to the angle between the y-axis and the vector $\vec{R}$, which lies in the y-z plane. Then

$$\vec{R} = R \cos \alpha_j \hat{e}_y - R \sin \alpha_j \hat{e}_z \qquad \text{(Eq. 61)}$$

where $\hat{e}_x$, $\hat{e}_y$, and $\hat{e}_z$ are unit vectors. Also the vector $\overrightarrow{ab} = y_I \hat{e}_y$ so that

$$\vec{L} = \vec{R} - \overrightarrow{ab} = (R \cos \alpha_j - y_I)\, \hat{e}_y - R \sin \alpha_j \hat{e}_z \qquad \text{(Eq. 62)}$$

Then the vector from the impact point to the point (c), namely $\vec{D}$, is given by

$$\vec{D} = -x_I \hat{e}_x + (R \cos \alpha_j - y_I)\, \hat{e}_y - R \sin \alpha_j \hat{e}_z \qquad \text{(Eq. 63)}$$

and

$$|\vec{D}| = \sqrt{x_1^2 + y_1^2 + R^2 - 2 y_1 R \cos \alpha_i} \qquad \text{(Eq. 64)}$$

The unit vector along $\vec{D}$ is $\vec{D}/|\vec{D}|$ while the unit vector along the direction $\vec{cd}$ which is the normal to the front surface, is $-\hat{e}_z$. Consequently the angle ϕ between the trajectory and $\vec{D}$ is given by

$$\cos\phi = \frac{\vec{D}}{|\vec{D}|} \cdot (-\hat{e}_z) \qquad \text{(Eq. 65)}$$

or

$$\phi = \cos^{-1}\left[\frac{R \sin \alpha_i}{|\vec{D}|}\right] \qquad \text{(Eq. 66)}$$

In many cases, instrumentation was located other than at the nominal point "c" on the target. Now consider a point p located at an arbitrary position on the i^{th} surface. In a primed coordinate system lying on that surface with origin at c, the point p has coordinates (x'_p, y'_p):

From the geometry shown in Fig. 122 $\angle cad = \angle d\ \ = \alpha_i$ and the x'-axis lies along the x-axis. Then the vector $\vec{l}$ from c to p lying in the i^{th} surface is

$$\vec{l} = x_p \hat{e}_x + y'_p \sin \alpha_i \hat{e}_y + y'_p \cos \alpha_i \hat{e}_z \qquad \text{(Eq. 67)}$$

expressed in the unprimed system. The distance from the impact point b to the point on the i^{th} surface is then given by $\vec{d} = \vec{D} + \vec{l}$ such that

$$d = |\vec{d}| = \sqrt{(x_p - x_1)^2 + (R \cos \alpha_i - y_1 + y_p \sin \alpha_i)^2 + (y_p \cos \alpha_i - R \sin \alpha_i)^2} \qquad \text{(Eq. 68)}$$

and if θ is the angle between $\vec{d}$ and the unit inward normal to the front surface (i.e. the trajectory) then $\cos\theta = \frac{\vec{d}}{d} \cdot (-\hat{e}_z)$ or

$$\theta = \cos^{-1}\left[\frac{-y_p \cos \alpha_i + R \sin \alpha_i}{d}\right] \qquad \text{(Eq. 69)}$$

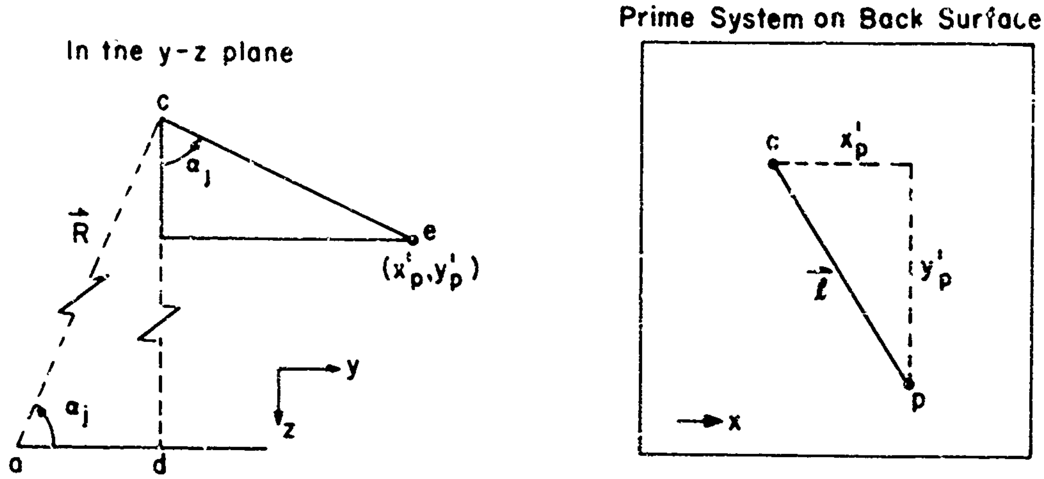

Fig. 122. Rear Face Geometry.

Likewise the angle β between the vector $\vec{d}$ and the i^{th} surface is given by $\cos\beta = (\vec{d}/d)\cdot\hat{n}$ where $\hat{n}$, the unit outward normal to the i^{th} surface is

$$\hat{n} = \cos\alpha_i \hat{e}_y - \sin\alpha_i \hat{e}_z \qquad \text{(Eq. 70)}$$

Consequently

$$\beta = \cos^{-1}\left[\frac{R - y_I \cos\alpha_i}{d}\right] \qquad \text{(Eq. 71)}$$

In practice, it was necessary to measure the placing of flyers and probes on the surfaces with respect to the "corner" f between the i^{th} and $i+1^{th}$ surfaces. In order to convert to the primed coordinate system centered at c, it is necessary to determine the distance $\overline{fc}$. From the geometry:

$$\cos(\alpha_{i+1} - \alpha_i) = R/(R + \overline{cg}) \qquad \text{(Eq. 72)}$$

since $\overline{ah} = \overline{ac} = R$ by construction. Then

$$\overline{cg} = \frac{R}{\cos(\alpha_{i+1} - \alpha_i)} - R \qquad \text{(Eq. 73)}$$

since $\overline{gh} \perp \overline{ha}$ and $\overline{fc} \perp \overline{ac}$, $\xi = \alpha_{i+1} - \alpha_i$. Consequently

$$\tan \xi = \frac{\overline{gc}}{\overline{fc}} \qquad \text{(Eq. 74)}$$

yielding

$$\overline{fc} = R\left(\frac{1 - \cos \xi}{\sin \xi}\right) \qquad \text{(Eq. 75)}$$

In practice, the measurements of the location of flyer disks and time-of-arrival probes on the rear facets were made immediately after the target was prepared and were recorded on standard forms. Measurements were made carefully with a scale and are believed to be accurate to within about ±0.2 mm. After the round was fired, the coordinates of the impact were measured with respect to the nominal impact point which was marked on the target prior to impact. The impact point was measured using a reticle consisting of a series of concentric circles and perpendicular lines on a small transparent plastic plate.

The reticle was placed over the crater and moved manually until the center of the crater was best determined visually. This simple method was checked using a more accurate method where cross hairs were optically projected onto the target face. The techniques gave very consistent results. The accuracy of determining the impact point is estimated to be about ±0.3 mm, although the accuracy was somewhat less in those targets which were badly deformed by the impact or where fracture, especially in the 7075-T6 aluminum, created uneven cratering.

The equations derived above were implemented in a computer program which used the coordinates of the impact point and of each flyer or probe as inputs. Additional data such as the angles α_i, the "radius" R, and other information identifying the shot and type of target were also required.

Calculation of the geometry for the cylindrical targets was somewhat less straightforward. These targets were used only for short impact-to-surface distance events where pressures were so high that free surface velocities could be monitored in place of loosely attached fly-off disks. In every case, the pressures were so high that the target was completely penetrated; it was impossible to determine the impact point by inspecting the target remnants. In fact, all geometric measurements were obtained from the Beckman &Whitley Model 300 camera photographic records of the event.

The major features of the standard framing camera data reduction program are described in Chapter V. In essence, it provides a statistical analysis to determine the velocity and direction of motion of some "particle" whose coordinates are obtained from several frames of the record. A subroutine was added which allowed the determination of the mean coordinates of a fixed point whose coordinates are provided from several frames. This is considerably more accurate than data taken from a single frame. The results of a variety of tests indicated that the position of any clearly defined point could be determined to within 0.1 cm with respect to a reference system included within the field of view, even when the camera was located more than 35 feet from the subject. By reading different points along some straight line in space, the program is also able to provide accurate information regarding the angular position of that line.

When a cylindrical target is impacted near its centerline, the entire rear surface expands at high velocity and in a very even and generally symmetric fashion, forming a cloud or bubble of debris. To determine the velocity of any point upon this surface, it is necessary to be able to follow the same point from frame to frame, i.e. to distinguish a given point on the rear surface from its neighbor through a sequence of photographs. In general, the smoothness of the expansion makes the identification of individual points impossible. Fig. 56 shown previously illustrates a typical expanding cloud.

It was necessary, early in the program, to perform altered experiments aimed at studying the characteristics of the expanding cloud and at identifying the trajectory of individual small portions of the leading edge of the debris. The technique used was based upon a series of experiments conceived by Swift, et al., (Ref. 46) at this facility and used in several studies to explore the expansion characteristics of debris clouds created by hypervelocity impacts into thin plate targets. The essence of the technique is that solid material is placed in the path of the expanding debris, stopping some of the debris and allowing other portions to pass by unhindered -- that is, the debris is split into identifiable components without affecting their subsequent behavior. A variety of experiments have proved that the splitting process does not alter the debris cloud characteristics of interest here.

As implemented for this study, the "cylindrical" target is placed with its flat face toward the gun barrel and its long axis parallel to the optical axis of the camera which views the back-lighted target in silhouette. A series of pairs of closely spaced copper wires was then located on a circle centered on the target axis and placed parallel to the axis. The typical frame from the record of Round 2730 is shown in Fig. 123 while a photograph of the target setup was given in Fig. 54. Photographs were obtained from 3 μ sec before impact to about 35 μ sec after impact. For those frames taken prior to impact, points were read at the position of the corners and surfaces of the target, the position of each copper rod, and the position of the incoming projectile. After impact, the position of various identifiable points on the expanding debris front were recorded in as many frames as possible.

The computer program then yielded, in a coordinate system tied to the reference grid, the mean position of the corners of the target and each copper rod as well as the line representing the projectile trajectory. This data was plotted and used to determine the point of impact on the target. Note that the position of impact along the axis of the cylinder is unimportant since both the target and expanding debris were viewed in silhouette. Fig. 124 was generated from the computer printout of the data read from the framing camera films.

Fig. 123. Typical Frame from Round 2730.

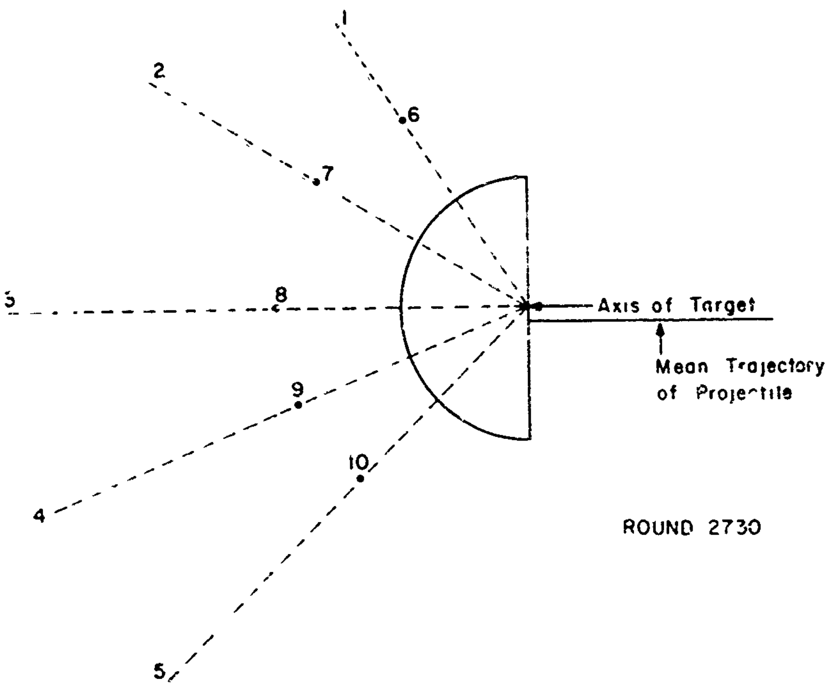

Fig. 124. Analysis of Debris Expansion -- Round 2730.

In this figure the location of the target was determined from the mean coordinates generated by the data reduction program and the projectile trajectory was determined in like manner as were the points 6-10 which represent the center of the pairs of wires placed in the path of the expanding debris. Points 1-5 represent the mean position of the narrow "beam" of debris which passed through the center of each pair of wires. The dotted lines then indicate the trajectory of the debris at each point. When extrapolated back toward the target, these trajectories appear to originate at a point near the axis of the target -- a fact which was used in the data reduction for later shots. The velocities obtained for portions of the debris cloud far away from any wires when compared with the velocities for the debris beam that went between the wire pairs indicated that the wires do not affect the velocity of this beam. The correspondence of the origin of particle trajectories with the target axis was tested in several other rounds including 2728 and 2729 where solid .16 cm diameter brazing rods were used to split the cloud in lieu of pairs of fine wires. The results obtained from these rounds was consistent with the trajectory origin discussed above within measurement error.

In later rounds the splitting technique was replaced by simply placing a plastic sheet in front of the field of view with lines drawn emanating at predetermined angles from the target axis. The camera to subject distance was so large that parallax was no problem.

For either type of experiment, the target geometry factors of distance from impact to point of origin of a given particle on the back surface and of the angle between the projectile trajectory and the line from the impact point to the point on the rear surface were determined as follows:

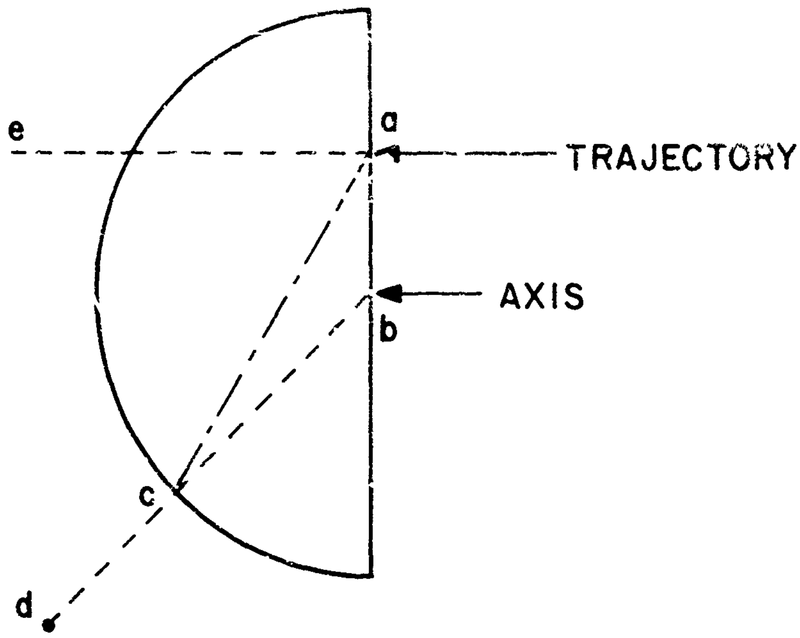

Fig. 125. Geometry for Data Reduction.

The position of the target and the projectile trajectory, both obtained from computer output, were plotted to obtain the impact point "a". The point "d" represents the mean position of a series of readings of a given particle whose motion was followed by the framing camera. Using the assumption that the particle trajectory passes through the axis of the target, a straight line extrapolation from "d" to "b" was used to obtain the point "c" on the rear surface of the target at which the particle in question originated. The distance from impact to the particle origin was obtained by measuring the distance $\overline{ac}$. The angle eac corresponds to the trajectory of the shock wave from the impact point to the particle of interest. The angle at which the shock wave impinges upon the rear surface at the point "c" is the angle acb.

The overall accuracy of determining the geometry of the cylindrical targets by this method is not as good as that used for the multi-faceted targets.

Indeed, this undoubtedly accounts for a portion of the larger scatter obtained in those experiments where the small half cylinders were used as targets. The camera yields position information which is on the average good to less than 0.1 cm. For those targets where the impact was near the axis, the final measurements of distances were probably good to about 0.1 cm, while angles could be measured to about $\pm 1^{\circ}$. In a few rounds, the impact was more than one-third projectile diameter off dead center. In very small targets this resulted in a non-symmetric expansion of the debris cloud -- making the photographs more difficult to read and interpret -- and possibly negating the assumption that particle trajectories pass through the target axis.

Appendix D

Pressure Measurements by Fly-off Disks

Hopkinson Fly-off Disks

The fly-off disk method of determining peak stress in a shock wave is based upon the technique developed by Hopkinson (Ref. 66:78-80) in 1914. The technique was first applied to hypervelocity impact measurements by Charest (Ref. 13) who obtained data describing the shock decay on-axis in 1100 aluminum. In essence, the disk is used to trap a portion of the momentum available in an incident stress pulse. The measured velocity of the disk is then sufficient to allow determination of the magnitude of the stress pulse incident on the disk. Errors in determining stresses from the disk velocity data can arise from several sources including oblique wave incidence, edge effects, two-wave structures, etc. Each of these subjects is discussed in Chapter V. Two aspects are discussed in more detail here: (1) the use of Hugoniot data to provide the relation between the disk velocity and the stress at the rear surface of the target, and (2) the possible effects of a two-wave structure on the interpretation of the fly-off disk velocity.

Theory of Operation. Assume that a plane wave of constant amplitude is incident upon a free surface to which a thin disk of thickness T has been attached with a zero strength adhesive (see Fig. 126).

The momentum per unit area M_d trapped in the disk is then given by:

$$M_p = \int_0^{\tau} \sigma_n(t)\, dt \qquad \text{(Eq. 76)}$$

where σ_n is the stress normal to the interface and $\tau = 2T/D$, twice the transit time of the wave through the disk because the wave reflects off the free surface at the right. This result assumes that the reflected release wave acts as a negative amplitude shock wave travelling at shock speed D for the short distance T in

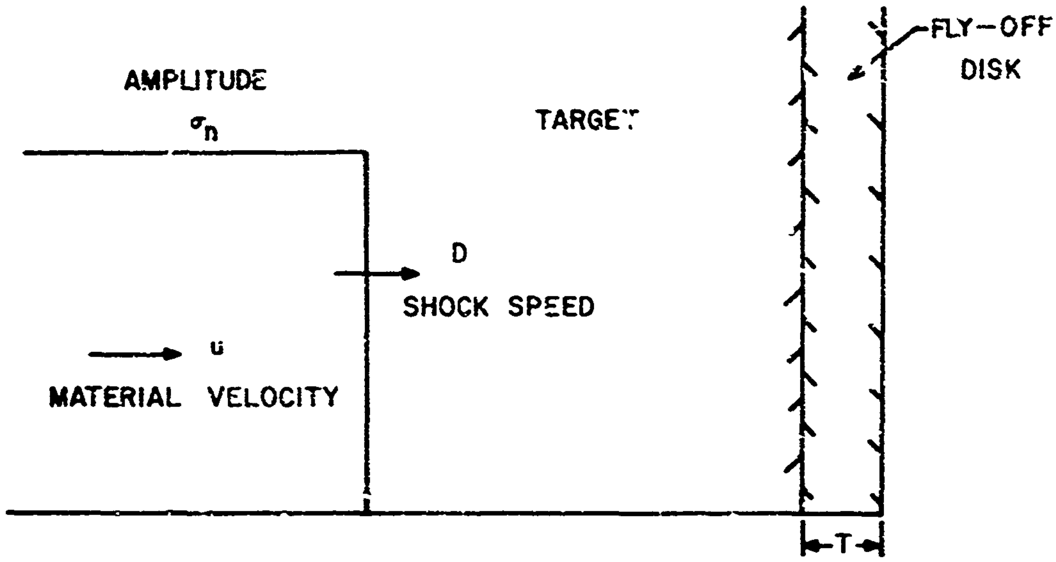

Fig. 126. Shock Interaction with Fly-Off Disk.

question. Provided the pulse is of constant amplitude for time τ, this becomes

$$M_d v_d = \sigma_n (2T/D) \qquad \text{(Eq. 77)}$$

where M_d and v_d are the mass per unit area and velocity of the fly-off disk respectively. Note then that $M_d = \rho_o T$ and from conservation of momentum across the shock front $\sigma_n = \rho_o Du$. These then yield the result

$$v_d = 2u \qquad \text{(Eq. 78)}$$

that is, the disk velocity is twice the material velocity at the rear surface -- a well known approximate result.

Stress Wave Shape. This analysis assumed a constant stress behind the incident shock wave. In reality, the stress decreases behind the steep fronted shock. If the duration of the shock wave is less than twice the transit time through the disk, the total momentum -- not the peak stress -- is actually measured. At the other extreme, for very thin disks, a good measure of peak stress is obtained. If the stress varies significantly during the time it takes a shock wave to make a double transit through the disk, an error will occur in the stress measurement since the average rather than peak stress will be obtained. As outlined in Chapter V, care was taken to keep the fly-off disks sufficiently thin that the stress wave decayed only very little during a double shock transit across the disk, thereby assuring that peak stresses were measured.

Free Surface Approximation. The analysis above is simplified in that it treats the wave reflection by superposition (a linear process) and treats a rarefaction wave as a shock wave. In reality, the process is non-linear and the rarefaction is an isentropic relaxation process. The rear surface velocity is correctly given by (Ref. 67:718)

$$v_d = u + \int_0^P \frac{dp}{\rho c} \qquad \text{(Eq. 79)}$$

where c is the local sound speed and the integration takes place down an isentrope from the shocked state to zero pressure. At low pressures

$$\int_0^P \frac{dp}{\rho c} \approx \frac{p}{\rho_o c_o} = \frac{V_o p}{c_o} \qquad \text{(Eq. 80)}$$

But the sound speed c_o is:

$$c_o = V_o \left(- \frac{\partial p}{\partial V}\right)_s^{1/2} \approx V_o \left(\frac{p}{V_o - V}\right)^{1/2} \qquad \text{(Eq. 81)}$$

hence

$$\int_0^P \frac{dp}{\rho c} = \sqrt{p\,(V_o - V)} \qquad \text{(Eq. 82)}$$

However, from the Rankine-Hugoniot condition at the shock front:

$$u^2 = p\,(V_o - V) \qquad \text{(Eq. 83)}$$

Consequently $\int_0^p \frac{dp}{\rho c} \approx u$ at low pressures and $v_d \approx 2u$ as cited above. At higher pressures, this approximation fails and the velocity doubling rule must be treated in a more exact manner.

It is a remarkable fact, however, that for most materials the velocity doubling rule holds to within a few percent up to very high pressures, generally several hundred kilobars (Ref. 68). For aluminum, in particular, the error in using the velocity doubling rule amounts to less than 2% at a pressure of nearly 400 kilobars and is considerably better at lower pressures. In view of this result, the relation $v_d = 2u$ has been used throughout this study. The errors created by this approximation are less than one percent in any of the pressure measurements made.

<u>Hugoniot Data</u>

Given the velocity of a fly-off disk and the velocity doubling rule it is then possible to determine the stress magnitude (assumed to be the hydrodynamic pressure) if the Hugoniot curve of the material, $p_H = p_H(u)$ is known. Rather extensive data is available for several of the aluminum alloys. The data used for the conversion of fly-off disk velocities to pressures in this study are shown as the solid line in Figure 127. The broken lines indicate how little difference there is between several aluminum alloys. Data from other sources, for these alloys and for pure aluminum, agree very well with the data plotted for 2024 aluminum. In particular, the Los Alamos equation of state used in the numerical cratering calculations described in Chapter VII produces Hugoniot data that differs from the 2024 aluminum Hugoniot by less than 0.1% up to 100 kilobars and 0.5% at 250 kilobars. In any event, the differences in Hugoniot data are less than the experimental errors in measuring fly-off disk velocities.

All other quantities behind the shock front, such as ρ_H and D, can then be calculated by applying the Rankine-Hugoniot equations.

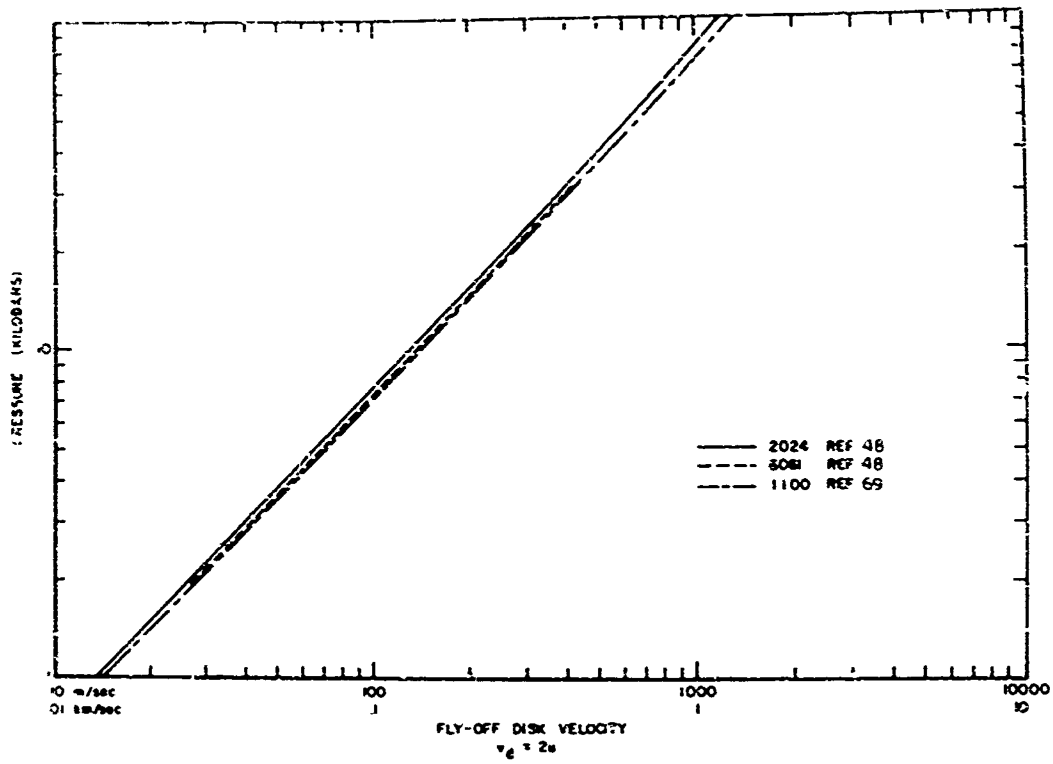

Fig. 127. Aluminum Hugoniot Data.

Effects of Two-Wave Structure

Several studies (Refs. 49 and 50) indicate that a two-wave structure may exist in aluminum due to elastic-plastic effects. There is a region of pressures above the Hugoniot elastic limit but below roughly 100 kb where the shock speed (plastic wave) is subsonic with respect to the undisturbed medium through which it is propagating. This can lead to the type of situation depicted in Fig. 128 where an elastic "precursor" travelling at sonic velocity can lead the plastic portion of the wave. The amplitude of the precursor is determined by the dynamic yield strength of the material.

It has been suggested by Read (Ref. 61) that this two-wave structure might alter the performance of a fly-off disk used to measure pressures. This was proposed as a possible explanation of the discrepancy noted between the results

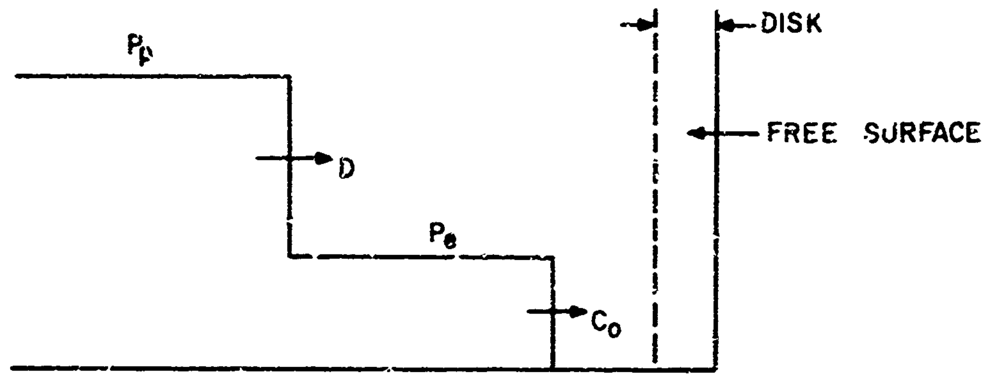

Fig. 128. Two Wave Structure.

of Charest (Ref. 13) and computer predictions of a similar problem. The purpose here is to perform a first order, simplified analysis of fly-off disk performance when subjected to a simple two-wave input.

For this analysis, the shock wave is assumed to be planar. All shocks are assumed to travel at the same speed. This is slightly inaccurate since elastic and plastic waves travel at different speeds. However, only short shock travel distances are to be considered here, so the errors generated by this assumption are quite small. Waves reflected in tension at an interface are assumed to travel as tensile shock waves. Referring to Fig. 128, the right-travelling elastic precursor is reflected in tension from the free surface. The reflected tensile wave then interacts with the oncoming compressive plastic front, producing reflected and transmitted waves. It is this and subsequent interactions that could affect the ultimate velocity of the rear surface (i.e., the disk).

In analyzing the interaction of the tensile elastic wave and the plastic wave, it is assumed that to the incoming wave (either the plastic or elastic wave depending on the point of view), the other wave front merely represents a change in medium with a different density, sound speed, etc. The resulting interactions are then calculated using linear superposition, both for pressures and material velocities. Although shock propagation in solids is basically a non-linear process, this procedure produces only small errors so long as the pressures are relatively low.

The interaction of a shock wave at the interface between two media is depicted in Fig. 129. The incident wave has amplitude p_I; its interaction with the interface creates reflected and transmitted waves, p_R and p_T, respectively.

To avoid separation at the material boundary, the pressures must be equal on each side of the boundary:

$$p_I + p_R = p_T \qquad \text{(Eq. 84)}$$

and the material velocities must yield

$$u_I - u_R = u_T \qquad \text{(Eq. 85)}$$

Defining the shock impedance by $Z = \rho_o D$ and applying the conservation of momentum relation $p = \rho_o Du$ at the shock front the following are obtained

$$\frac{p_R}{p_I} = \frac{Z_B - Z_A}{Z_A + Z_B} \qquad \text{(Eq. 86)}$$

and

$$\frac{p_T}{p_I} = \frac{2Z_B}{Z_A + Z_B} \qquad \text{(Eq. 87)}$$

which are the well known impedance relations. Note that at a free surface, $Z_B = 0$ yielding $p_T = 0$ and $p_R = - p_I$ for the reflected tensile wave. Likewise the following relations can be obtained for the material velocities:

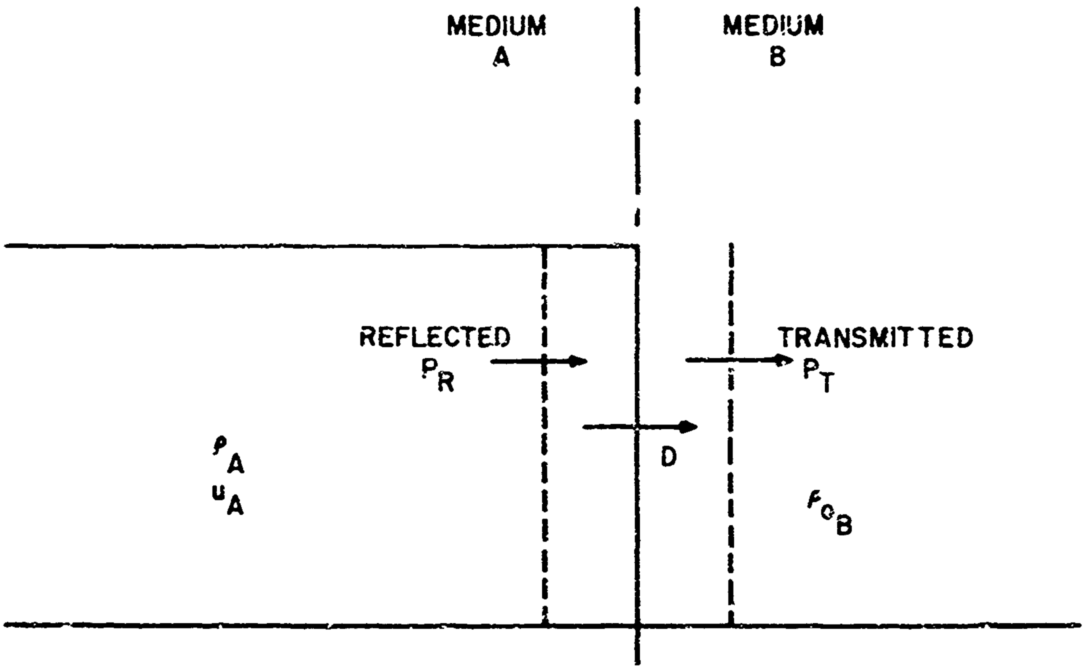

Fig. 129. Wave Interaction at Material Interface.

$$\frac{u_R}{u_I} = \frac{Z_B - Z_A}{Z_A + Z_B} \qquad \text{(Eq. 88)}$$

$$\frac{u_T}{u_I} = \frac{2Z_A}{Z_A + Z_B} \qquad \text{(Eq. 89)}$$

In this case, at a free surface with $Z_B = 0$, $u_R/u_I = -1$ implies that the material velocity in the reflected tensile wave is opposite to the direction of the wave propagation while $u_T/u_I = 2$ recovers the free surface approximation discussed above.

Now again consider the two-wave structure pictured in Fig. 128. An x-t plot of the interactions of these waves is depicted in Fig. 130. Each wave is numbered and identified as to whether its origin was elastic or plastic and to whether it is a compressive or tensile wave. Assuming that the amplitudes of

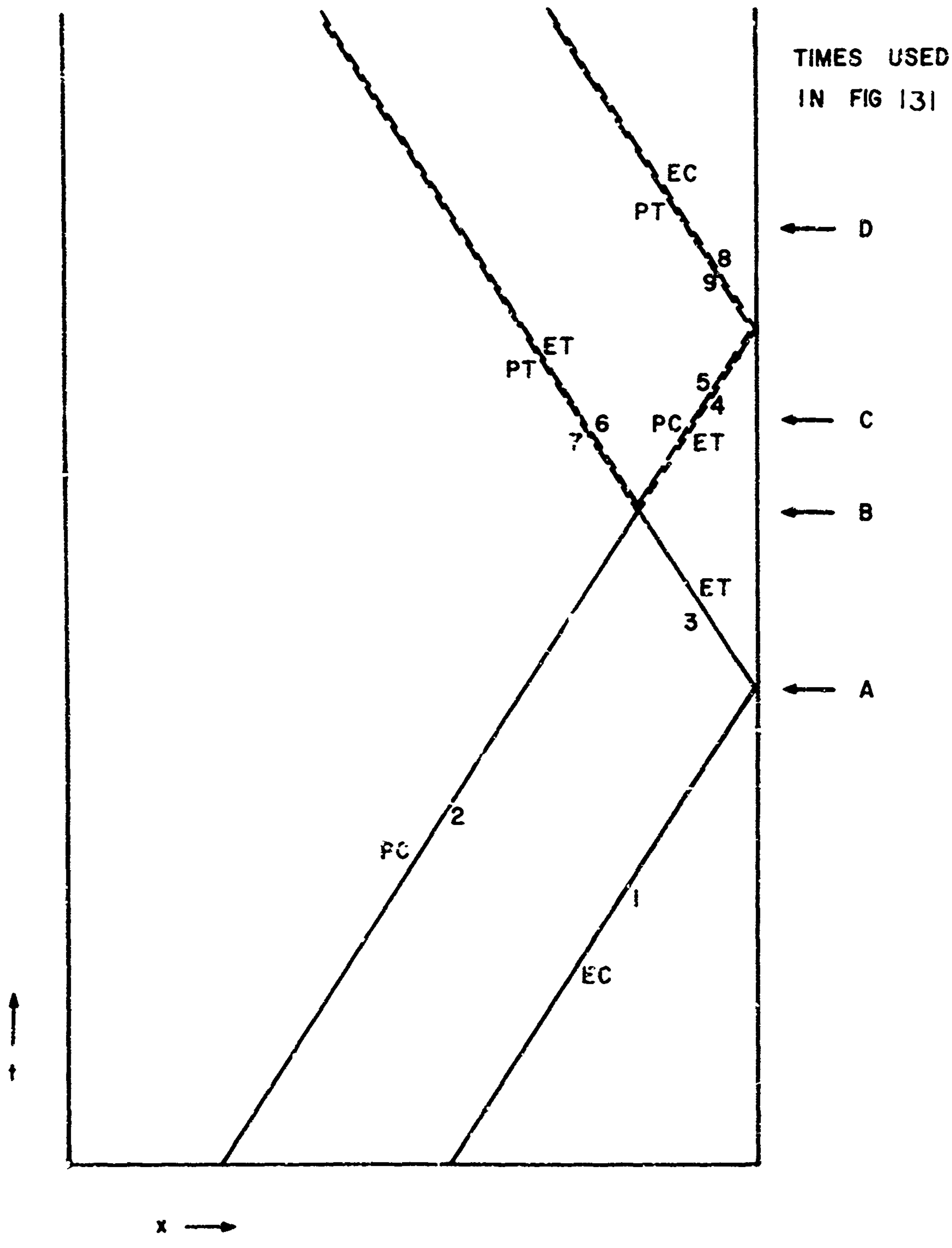

Fig. 130. x - t Plot for Dual Wave Interaction.

Table XVII

Results of Wave Interactions

No.	Type	Pressure (kb)	Material Velocity (mm/μsec)
1	EC	7.000	.047
2	PC	20.000	.132
3	ET	-7.000	.047
4	ET	-.131	-.001
5	PC	19.626	.134
6	ET	-7.131	.046
7	PT	-.374	.002
8	EC	.131	-.047
9	PT	-19.626	.134

the incident elastic and plastic waves are 7 kilobars and 20 kilobars respectively (for a total stress of 27 kb) the values shown in Table XVII are obtained for the wave interactions.

The results of applying this analysis to the interacting wave system shown in Fig. 130 is that the final velocity of the free surface (or the fly-off disk) is altered very little by the presence of the elastic precursor. The final free surface velocity calculated is .360 mm/μsec as opposed to the value of .358 mm/μsec that would have been obtained if the elastic precursor did not exist. If no precursor had existed, the pressure near the rear surface would simply have been cancelled by the reflected tensile wave. As panel D of Fig. 131 shows, the elastic procursor has drastically altered the shape and amplitude of the pressure pulse in the region of the target rear, but has made little if any change in the ultimate velocity of the rear surface. Provided the incident pressure pulse monotonically increases to the peak, the ultimate rear surface velocity will not be affected by the details of the shape of the rising part of the pressure pulse.

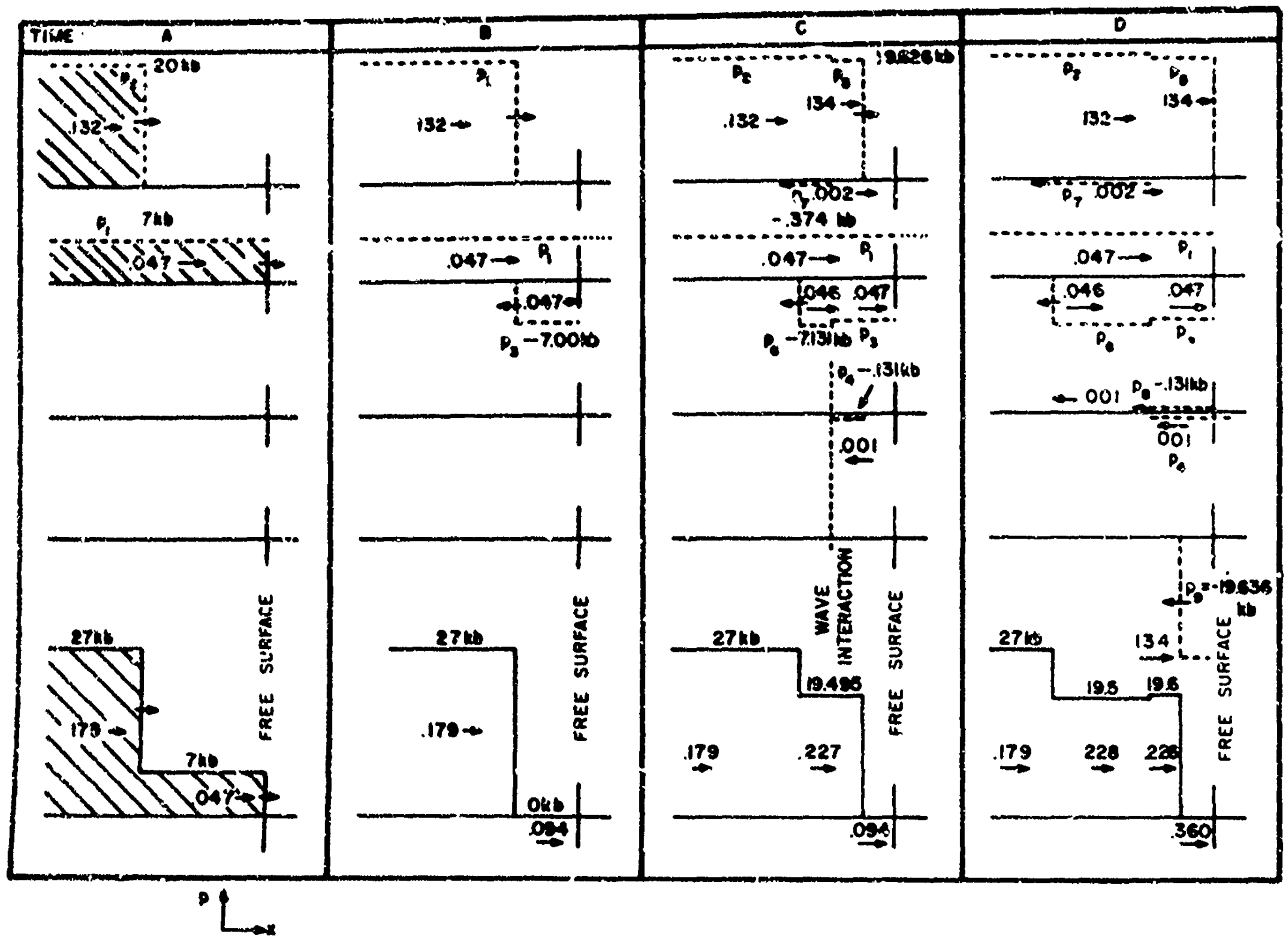

Fig. 131. Analysis of Dual Wave Reflection at Free Surface.

This effect is illustrated by a set of numerical calculations performed by Read (Ref. 61) although he interpreted the results differently. Several sketches of his computer output, corresponding roughly to the situations depicted in Fig. 131 are shown in Fig. 132. Note that Read's results show considerably more structure in the wave form. By Panel D again, the pressure pulse has been drastically altered by the presence of the elastic precursor. The last panel shows the time history of the velocity of the material in a zone near the target rear surface. The velocity increases monotonically, although with some structure, to a peak velocity that corresponds to that of the peak pressure in the incident wave.

Using an analytical approach, Fowles (Ref. 49:1481-1482) studied the effect of elastic-plastic behavior on rear surface motion due to a stress wave created by a planar impact. He approximated the release path of the material and determined that the effect of elastic unloading on the rear surface velocity was quite small, a few percent in the worst case.

The above calculations and results strongly support the conclusion that a dual wave structure has little effect, if any, upon the pressure values obtained from experimental fly-off disk data. The discrepancies such as those cited by Read that exist between numerical and experimental results cannot be explained on the basis of the mechanisms discussed here.

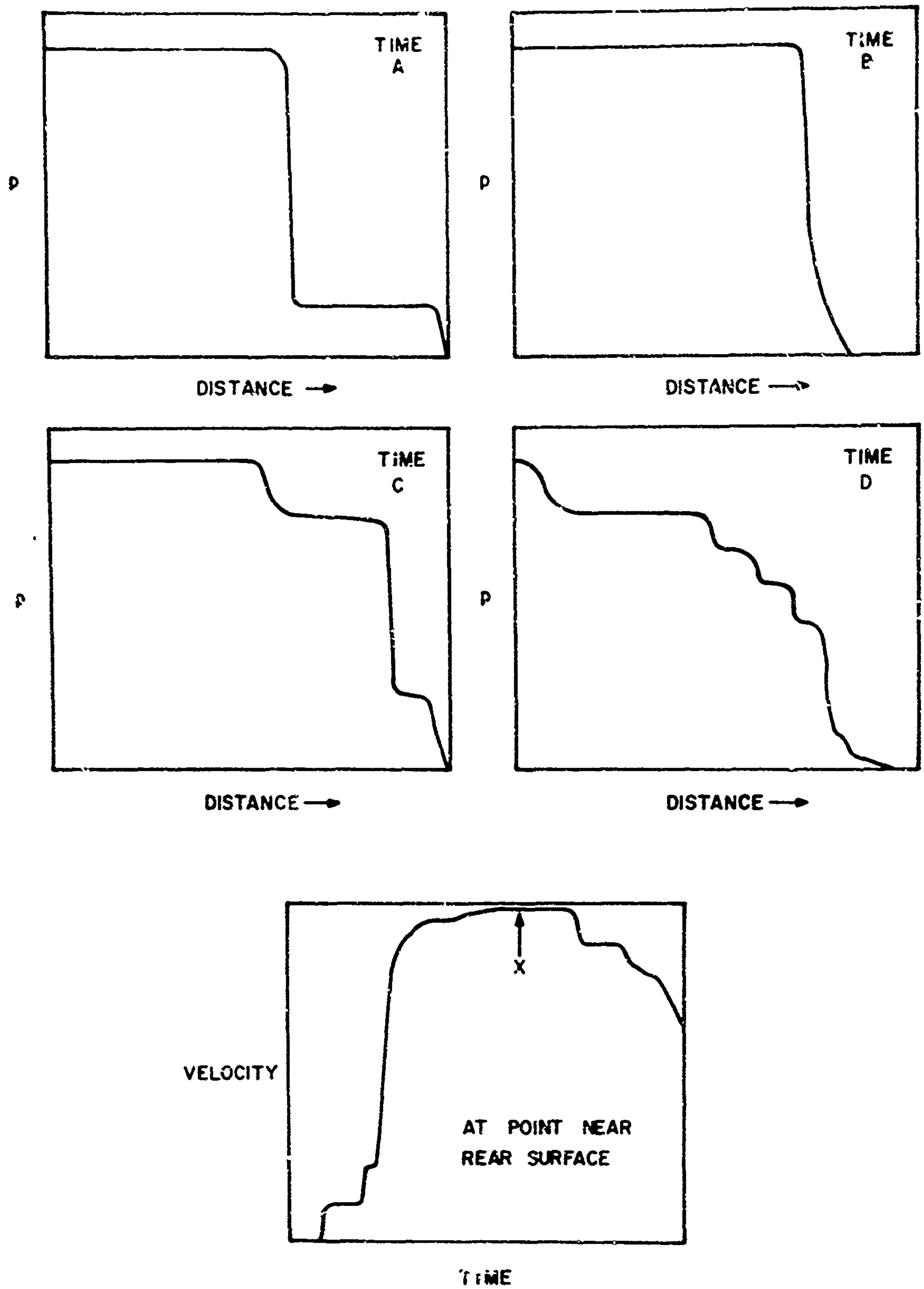

Fig. 132. Numerical Results -- Dual Wave Interaction
From Ref. 61.

Appendix E

Adjustment of Rear Surface Velocity Data for Variations in Projectile Velocity and Shock Incidence Angle

The experimental results described in Chapter VI were obtained under carefully controlled conditions where as many variables as possible were held fixed. However, there is inevitably some small scatter in the projectile velocities generated by the light-gas gun launcher. In each experiment, the nominal projectile velocity was 7 km/sec, but actual projectile velocities varied between 5.9 km/sec and 7.3 km/sec with nearly 75% of the experiments having projectile velocities in the range of 6.6 km/sec to 7.2 km/sec.

Likewise the point of impact upon the target cannot be controlled exactly. The targets were designed so that, if the impact were at the nominal aiming point, the shock wave would be normally incident on each rear surface where a measurement was being made. This assumes, of course, that the expansion of the shock wave is spherical and centered at the impact point. Whenever the actual impact was off the aiming point, the shock wave was incident upon the rear surface at a slight angle. In each case this angle was measured (indirectly) again assuming a spherical shock front) after the event. The angle was found to vary from zero degrees (normal incidence) to a maximum of 14°.

This appendix describes techniques for adjusting the experimental data to account for small variations in projectile velocity and angle of incidence of the shock wave with target free surfaces.

Angle Variation

To obtain a first order correction for the free surface velocity produced by a shock wave impinging upon the surface at some angle, δ, consider the following situation. Assume that a plane wave is incident upon a flat surface and that the wave has a particle velocity vector $\vec{u}$ with direction along the direction of wave motion. The components of $\vec{u}$ are $u_T = u \sin \delta$ and $u_n = u \cos \delta$ representing the projection of $\vec{u}$ tangent to and normal to the free surface respectively. In an experiment, the component $v_{fs} \approx 2u_n$ is actually measured, since only motion normal to the surface is monitored (see Appendix D for discussion of the velocity doubling rule). This is also true if fly-off disks are used since the extremely low strength attachment of the disk to the target effectively prevents the transmission of the tangential component of the particle velocity, u_T. Experiments conducted where disks were placed on flat plate targets verify the statement that, even at rather high incidence angles ($> 30^{\circ}$), the disk acquires a velocity almost normal to the rear surface. In either case, a first order adjustment to the observed disk or free surface velocity can be obtained by simply taking the adjustment law to be:

$$u_{adjusted} = u_{measured} / \cos \delta \qquad \text{(Eq. 90)}$$

This is, of course, only a first order correction since such effects as surface waves and shear waves generated upon reflection are ignored. In every case, the angle of incidence of the shock wave is nearly normal, so first order effects should dominate.

Reinhart (Ref. 66:11-14) considers a more accurate analysis of the reflection of a plane elastic wave incident upon a free surface at angle δ. His analysis includes consideration of the reflected shear wave and his results indicate that the "correction factor" due to oblique incidence lies within a few per cent of $1/\cos \delta$ out to δ of sixty degrees whereupon the $1/\cos \delta$ law fails. This conclusion applies only to a material (such as aluminum) with Poisson's ratio near 0.34. Further investigation would be required before applying this simple angle scaling law to materials whose Poisson's ratio differ substantially from 0.34.

Projectile Velocity Variation

Four rounds were fired at reduced velocity (~5.5 km/sec) to provide data for the empirical adjustment of disk or free surface velocity as a function of projectile velocity. Each of these rounds consisted of a series of fly-off disks placed upon the rear of a flat plate target in the manner described in

Chapter V for the fly-off disk development experiments. These results are then directly comparable with the results obtained in the development series at higher velocity (7 km/sec). The characteristics of these four experiments are shown in Table XVIII.

Table XVIII

Velocity Scaling Experiments

Round	Target Thickness (cm)	Projectile Velocity (km/sec)
2879	1.00	5.8
2880	2.54	6.1
2642	4.44	5.4
2870	6.83	5.2

The results of round 2642 were the most complete and have therefore been used to establish the scaling law. The results of this round as well as the results of several of the experiments performed at higher velocity are shown in Fig. 133. The solid line is a least - squares fit to the data acquired from $\sim$7 km/sec impact experiments onto 1100-0 aluminum targets (Table XIX). To within the experimental error, the dashed line through the data from Round 2642 is parallel to the solid line. This indicates that an adjustment or scaling of the fly-off disk velocity data from the lower impact velocity $v_p(a)$ to the nominal velocity $v_p(b)$ can be accomplished by simple multiplication by a scale factor:

$$v_{p_{scaled}} = v_{p_{measured}} \cdot k(v_p) \qquad \text{(Eq. 91)}$$

where the scale factor k is a function of the projectile velocity, v_p. A simple linear variation of the scale factor with projectile velocity has been chosen for ease of application. At $v_p = 5.48$ km/sec, the data of Fig. 133 yields $k = 1.537$

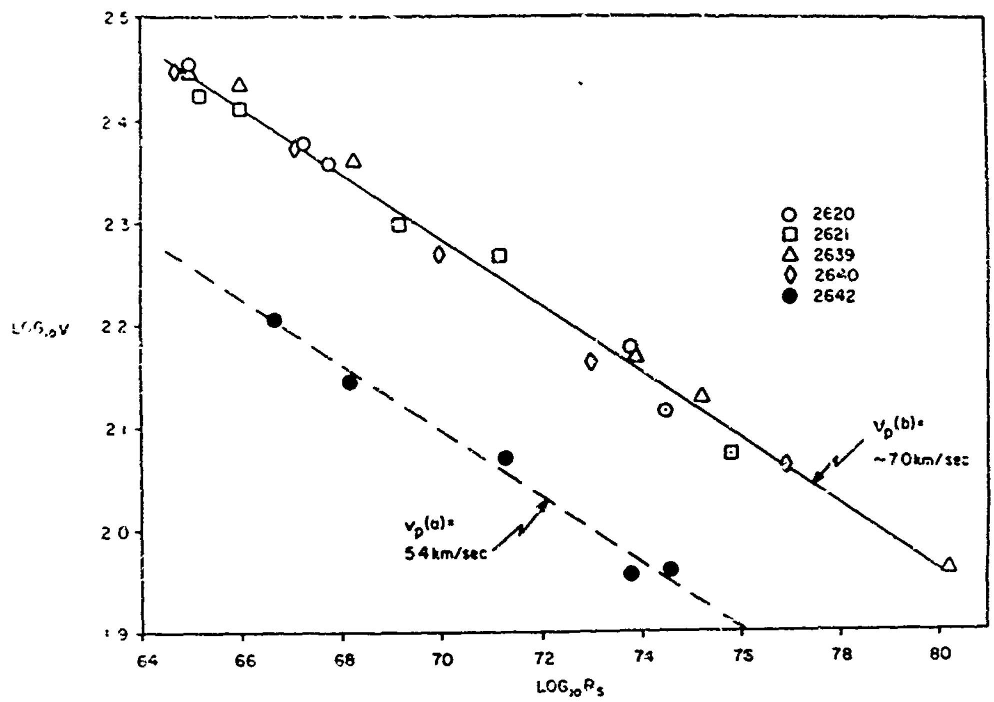

Fig. 133. Variation of Fly-Off Disk Velocity with Shock Radius and with Projectile Velocity as a Parameter.

while at $v_p = 7.0$ km/sec, it must be true that $k = 1$. The linear function $k(v_p)$ is then defined by

$$k(v_p) = 1 + \{[7.0 - v_p]/(7.0 - 5.48)\} \cdot 0.537 \qquad \text{(Eq. 92)}$$

or

$$k(v_p) = 3.47 - 0.353\, v_p \qquad \text{(Eq. 93)}$$

An exponential functional form for k (linear in $\log_{10} k$) yields very similar results. In practice, this scale factor was applied to experimental data only in the range 6.6 km/sec $< v_p <$ 7.2 km/sec. It was assumed to apply to those measurements made on free surface velocities as well as those made from fly-off disks.

The decrease in measured free surface or disk velocity with increasing R_s displayed in Fig. 133 is due to three separate effects: (1) the usual decrease of stress in the target with distance from impacts; (2) the increasing angle of incidence, δ, between the expanding shock front and the free surface; and (3) the increasing angle off the trajectory, θ. The slope of the line in Fig. 133 should not, then, be expected to correspond to the results of the on-axis measurements of Chapter VI (specifically Fig. 75) where the incidence angle δ was always small and where the angle off trajectory, θ, was also near zero. As expected, the results do not agree as evidenced in Fig. 134 where the results of the impacts onto 1100-0 aluminum on-axis are shown by the solid line. The data from the pertinent flat plate development rounds (2610, 2614, and 2618) are included for comparison as well as the data from the lower velocity rounds described in Table XVIII.

The effectiveness of the incidence angle and projectile velocity scaling laws developed here are illustrated in Fig. 135 where the data of Fig. 134 has simply been scaled according to the relation:

$$v_{d_{scaled}} = [k(v_p)/\cos\delta]\, v_{d_{measured}}$$

The agreement with the data obtained in Chapter VI is substantially improved. Those data points at the larger values of R_s for a given round correspond to large angles off axis and do deviate from the solid line as was expected since the scaling does not include any consideration of this angle. The correlation, although not perfect, is substantially improved by this scaling procedure.

It should be noted that the development data of Fig. 135 has been scaled over a wide range of the variables v_p and δ. The final data of Chapter VI has, however, been scaled over much smaller ranges of these variables. Consequently, errors in the scaling laws are less important for that application.

The unexpectedly good results obtained by correcting the data for shock incidence angle with a simple cosine law raise an interesting possibility -- that of performing production experiments in the future with flat plate targets instead of the multi-faced targets actually used. This would result in considerably less

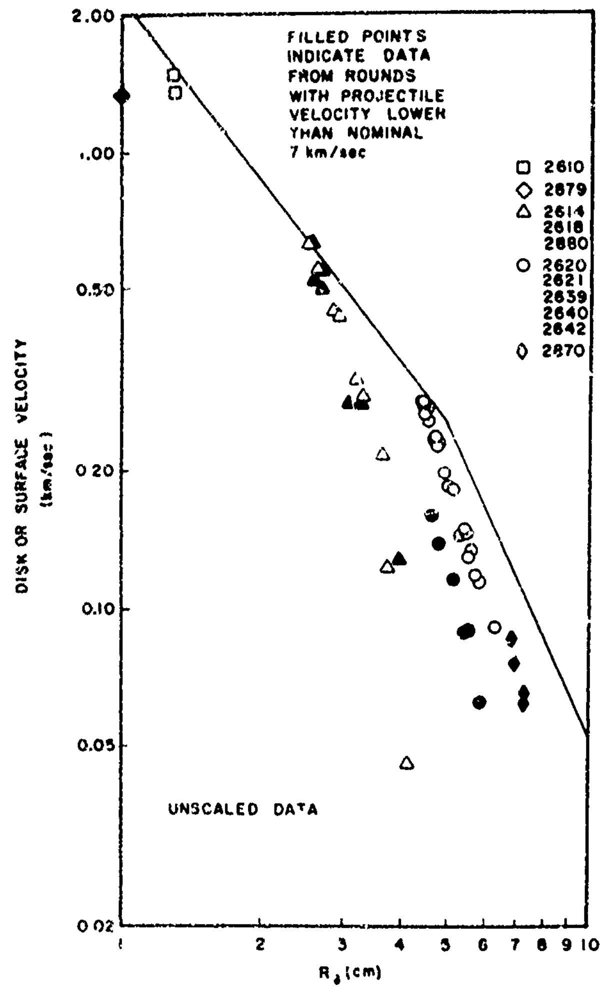

Fig. 134. Comparison of Flat Plate Fly-Off Disk Data with On-Axis Results from Multi-faceted Targets, Unscaled.

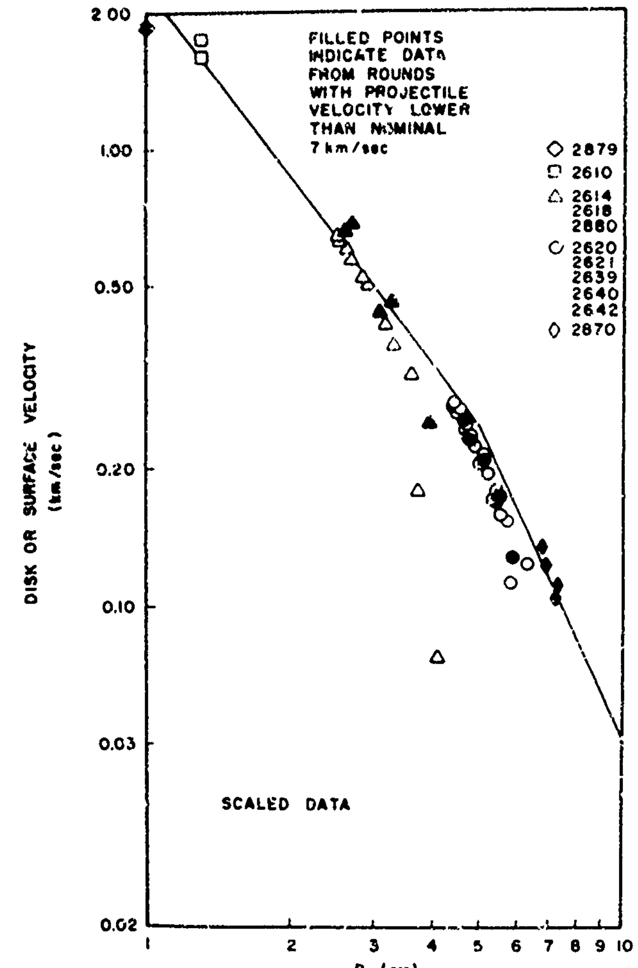

Fig. 135. Comparison of Flat Plate Fly-Off Disk Data with On-Axis Results from Multi-faceted Targets, Scaled.

difficult and less expensive experiments. While the results described here are promising, they are not sufficient to justify such an approach. A small number of additional flat plate experiments might well provide convincing evidence for or against this proposition.

Appendix F

Experimental Data On Shock Wave Arrival Times and Fly-Off Disk Velocities

This appendix contains information on the experimental data points generated during the phase of the program devoted to studying shock wave propagation. The details of the experiments used to acquire this data are in Chapter V. With that chapter as background, little further explanation of the data is required here.

Table XIX presents the data acquired during the early development shots when only flat plate targets were used. In every case, the target was 1100-0 aluminum. The parameter r_p refers to the distance along the rear surface of the target between the center of the disk and the point at which the line representing the projectile trajectory would intersect the rear surface.

Table XX contains the production fly-off disk data analyzed in Chapter VI. Similarly, Table XXI presents the shock wave arrival data obtained during the production program. The numbers in parentheses in the "Arrival Time" column refer to the earliest signal (precursor), while the other numbers refer to the arrival time of the main signal.

Table XIX

Fly-Off Disk Data From Flat Plate Development Rounds

Round No.	Proj. Velocity (km/sec)	Target Thickness (cm)	Disk Velocity (km/sec)	R_s, Impact to Disk Distance (cm)	r_p, Trajectory to Disk Distance (cm)	Angle Off Axis (deg)	Flyer Thickness (cm)
2587	6.69	4.51	0.053	6.49	4.67	46.4	0.063
			0.207	4.63	1.04	13.1	0.063
			0.234	4.52	0.23	2.9	0.063
			0.220	4.61	0.94	11.9	0.063
			0.187	4.95	2.04	24.6	0.063
2610	6.56	1.27	0.015	4.43	4.24	74.0	0.061
			0.048	3.61	3.38	70.0	0.061
			0.131	2.88	2.59	64.4	0.061
			0.289	2.19	1.78	55.0	0.061
			0.580	1.56	0.91	35.9	0.061
			1.486	1.30	0.30	13.4	0.030
			1.350	1.31	0.33	14.7	0.030
			0.201	2.27	1.88	56.4	0.030
			0.171	3.20	2.94	67.2	0.030
2614	6.93	2.49	0.093	4.40	3.63	56.0	0.061
			0.145	3.78	2.84	49.2	0.061
			0.233	3.21	2.03	39.5	0.061
			0.385	2.76	1.19	25.8	0.061

TABLE XIX (continued)

Round No.	Proj. Velocity (km/sec)	Target Thickness (cm)	Disk Velocity (km/sec)	R_s, Impact to Disk Distance (cm)	r_p, Trajectory to Disk Distance (cm)	Angle Off Axis (deg)	Flyer Thickness (cm)
			0.525	2.53	0.43	9.9	0.061
			0.621	2.53	0.46	10.6	0.030*
			0.551	2.65	0.91	20.3	0.030*
			0.448	2.86	1.40	29.6	0.030*
			0.316	3.19	2.00	39.1	0.030*
			0.217	3.63	2.64	47.1	0.030*
			0.046	4.12	3.28	53.3	0.030*
2618	7.02	2.54	0.024	4.67	3.92	57.6	0.061
			0.074	4.09	3.20	52.0	0.061
			0.135	3.50	2.41	43.9	0.061
			0.268	2.99	1.58	32.2	0.061
			0.394	2.68	0.85	18.7	0.061
			0.624	2.56	0.29	6.6	0.030*
			0.625	2.59	0.51	11.5	0.030*
			0.545	2.70	0.93	20.3	0.030*
			0.434	2.95	1.51	31.0	0.030*
			0.291	3.31	2.12	40.2	0.030*
			0.123	3.73	2.73	47.5	0.030*
2619	7.20	4.42	0.033	6.01	4.07	43.0	0.061
			0.112	5.47	3.22	36.4	0.061

TABLE XIX (continued)

Round No.	Proj. Velocity (km/sec)	Target Thickness (cm)	Disk Velocity (km/sec)	R_s, Impact to Disk Distance (cm)	r_p, Trajectory to Disk Distance (cm)	Angle Off Axis (deg)	Flyer Thickness (cm)
			0.148	5.06	2.46	29.4	0.061
			0.195	4.74	1.71	21.3	0.061
			0.215	4.53	0.98	12.6	0.061
			0.235	4.43	0.27	3.5	0.061
			0.188	4.70	1.61	20.2	0.061
			0.163	4.98	2.29	27.6	0.061
			0.119	5.43	3.15	35.8	0.061
2620	7.04	4.45	0.130	5.56	3.34	37.2	0.030
			0.149	5.15	2.59	30.5	0.061
			0.227	4.77	1.73	21.4	0.030
			0.224	4.55	0.93	11.9	0.061
			0.284	4.46	0.25	3.2	0.030
			0.226	4.52	0.81	10.4	0.061
			0.237	4.71	1.54	19.3	0.030
			0.158	5.00	2.29	27.5	0.061
			0.150	5.45	3.14	35.5	0.030
			0.092	5.97	3.98	42.2	0.061
2621	6.94	4.45	0.119	5.49	3.22	36.2	0.061
			0.183	5.15	2.59	30.5	0.030
			0.187	4.80	1.80	22.2	0.061

TABLE XIX (continued)

Round No.	Proj. Velocity (km/sec)	Target Thickness (cm)	Disk Velocity (km/sec)	R_s, Impact to Disk Distance (cm)	r_p, Trajectory to Disk Distance (cm)	Angle Off Axis (deg)	Flyer Thickness (cm)
			0.257	4.57	1.02	13.0	0.030
			0.295	4.46	0.30	3.9	0.015
			0.265	4.48	0.51	6.6	0.030
			0.257	4.64	1.30	16.4	0.015
			0.198	4.91	2.08	25.3	0.030
			0.178	5.25	2.79	32.4	0.015
			0.118	5.73	3.61	39.4	0.030
2639	7.14	4.44	0.092	6.33	4.51	45.8	0.030
			0.116	5.88	3.86	41.4	0.030**
			0.147	5.49	3.23	36.3	0.030
			0.188	5.12	2.54	30.0	0.030**
			0.228	4.82	1.88	23.1	0.030
			0.278	4.47	0.48	6.2	0.030
			0.311	4.45	0.33	4.3	0.030**
			0.272	4.56	1.03	13.2	0.030
			0.218	4.74	1.65	20.6	0.030**
			0.194	4.94	2.16	26.2	0.030**
			0.174	5.26	2.82	32.7	0.030
			0.134	5.65	3.50	38.6	0.030**
2640	7.07	4.44	0.115	5.88	3.86	4.44	0.025

TABLE XIX (continued)

Round No.	Proj. Velocity (km/sec)	Target Thickness (cm)	Disk Velocity (km/sec)	R_s, Impact to Disk Distance (cm)	r_p, Trajectory to Disk Distance (cm)	Angle Off Axis (deg)	Flyer Thickness (cm)
			0.235	4.69	1.52	19.1	0.025
			0.231	4.50	0.74	9.5	0.061
			0.280	4.44	0.20	2.6	0.025
			0.185	5.01	2.33	27.9	0.025
			0.145	5.37	3.02	34.5	0.025
2641	7.0	4.45	0.087	6.19	4.32	44.6	0.025**
			0.096	5.77	3.68	40.0	0.055
			0.136	5.42	3.10	35.2	0.025**
			0.148	5.08	2.46	29.2	0.055
			0.195	4.80	1.83	22.6	0.025**
			0.224	4.61	1.25	15.9	0.025**
			0.180	4.82	1.88	23.1	0.055
			0.165	5.10	2.51	29.7	0.025**
			0.115	5.42	3.10	35.2	0.055
			0.108	5.80	3.73	40.4	0.025**
2642	5.42	4.44	0.063	5.90	3.89	41.6	0.030
			0.090	5.46	3.18	35.9	0.030
			0.139	4.81	1.85	22.8	0.030
			0.160	4.65	1.37	17.3	0.030
			0.117	5.16	2.62	30.8	0.030

TABLE XIX (continued)

Round No.	Proj. Velocity (km/sec)	Target Thickness (cm)	Disk Velocity (km/sec)	R_s, Impact to Disk Distance (cm)	r_p, Trajectory to Disk Distance (cm)	Angle Off Axis (deg)	Flyer Thickness (cm)
			0.091	5.56	3.35	37.4	0.030
2870	5.22	6.83	0.062	7.27	2.48	20.0	0.025
			0.076	6.94	1.21	10.0	0.025
			0.086	6.83	0.06	0.0	0.025
			0.077	6.96	1.33	11.0	0.025
			0.066	7.31	2.60	21.0	0.025
2879	5.78	1.0	1.330	1.00	0.0	0.0	0.025
2880	6.13	2.54	0.280	3.29	2.09	39.3	0.025
			0.500	2.71	0.91	19.7	0.025
			0.510	2.61	0.60	13.3	0.025
			0.280	3.09	1.77	35.0	0.025
			0.130	3.94	3.02	49.0	0.025

* 0.476 cm diameter.
** 0.318 cm diameter.

Table XX

Fly-Off Disk and Free Surface Velocity Data

ROUND NO.	TARGET MATERIAL	TARGET TYPE	PROJECTILE VELOCITY (KM/SEC)	SHOCK RADIUS (CM)	φ, ANGLE OFF TRAJECTORY (DEG)	θ, SHOCK/SURFACE INTERACTION ANGLE (DEG)	UNSCALED DISK/SURFACE VELOCITY (M/SEC)	SCALED DISK/SURFACE VELOCITY (M/SEC)	VEL. ERROR (%)
2601	6061-T6	PLATE	7.39	0.08	0.	0.	6580.	5742.	0.3
2610	1100	PLATE	6.55	1.30	13.4	13.4	1466.	1753.	10.0
2614	1100	PLATE	6.95	2.53	10.6	10.8	621.	643.	0.7
2618	1100	PLATE	7.05	2.56	6.6	6.6	624.	617.	1.1
				2.59	11.5	11.5	625.	626.	0.7
2620	1100	PLATE	7.03	4.46	3.2	3.2	284.	281.	0.7
2621	1100	PLATE	6.94	4.48	6.6	6.6	265.	272.	0.7
2639	1100	PLATE	7.14	4.47	6.2	6.2	278.	267.	1.2
2640	1100	PLATE	7.07	4.44	2.7	2.7	280.	274.	0.8
2659	6061-T6	PLATE	7.26	0.08	0.	0.	6170.	5626.	0.3
2661	6061-T6	PLATE	7.23	0.08	0.	0.	6120.	5713.	0.7
2719	1100	5-FCT	6.96	3.57	54.5	3.1	234.	236.	2.1
				3.99	20.5	3.0	299.	304.	1.3
				4.01	3.0	3.0	335.	340.	1.5
				4.03	40.0	3.0	288.	292.	0.9
				4.05	68.7	3.2	170.	173.	1.7
2720	1100	5-FCT	6.31	3.82	10.8	11.2	312.	392.	0.9
				4.08	11.0	11.0	291.	366.	1.3
				4.51	47.0	7.9	193.	240.	0.7
				4.71	72.8	4.7	85.	105.	1.8
2726	1100	HF-CYL	6.92	1.63	24.3	2.7	800.	923.	5.5
				1.60	3.9	2.9	970.	998.	3.9
				1.57	22.8	2.7	950.	977.	5.9
2728	1100	HF-CYL	6.64	1.80	52.0	5.7	530.	597.	9.5
				1.75	39.0	7.3	730.	924.	3.4
				1.64	13.0	9.2	1040.	1190.	5.3
				1.54	8.0	9.3	1070.	1214.	1.8
				1.52	13.0	9.2	1060.	1203.	2.2
				1.44	34.0	7.8	1050.	1187.	1.5

Table XX (Cont'd.)

ROUND NO.	TARGET MATERIAL	TARGET TYPE	PROJECTILE VELOCITY (KM/SEC)	SHOCK RADIUS (CM)	θ, ANGLE OFF TRAJECTORY (DEG)	δ, SHOCK/SURFACE INTERACTION ANGLE (DEG)	UNSCALED DISK/ SURFACE VELOCITY (M/SEC)	SCALED DISK/ SURFACE VELOCITY (M/SEC)	VEL. [illegible] (%)
				1.38	56.0	5.4	947.	945.	[illegible]
2729	1100	HE-CYL	6.97	1.50	52.6	1.3	840.	872.	7.5
				1.49	30.0	1.2	1140.	1143.	[illegible]
				1.46	6.9	1.9	1200.	1246.	3.4
				1.45	15.8	2.0	1280.	1329.	2.7
				1.42	39.0	1.6	1180.	1225.	3.4
				1.41	55.6	1.2	930.	965.	4.3
				1.51	65.5	0.	460.	477.	2.6
2730	1100	HE-CYL	6.81	1.37	40.0	3.2	780.	811.	2.6
				1.35	42.0	4.4	1240.	1323.	3.8
				1.28	13.0	6.3	1540.	1648.	2.1
				1.29	2.0	6.5	1600.	1712.	2.3
				1.19	27.0	6.0	1650.	1764.	2.2
				1.15	46.0	4.7	1500.	1601.	1.9
2733	1100	3-FCT	6.17	1.66	75.0	6.0	760.	978.	10.2
				1.61	6.4	6.3	810.	1043.	11.1
				1.53	70.3	8.7	850.	1101.	13.7
2734	1100	5-FCT	6.52	2.75	58.5	7.2	320.	375.	10.2
				2.61	24.0	7.2	510.	597.	7.3
				2.52	7.8	7.8	540.	632.	5.5
				2.34	35.2	7.2	580.	679.	2.6
				2.25	67.7	5.7	400.	457.	10.2
2750	7075-T6	HE-CYL	6.07	1.09	61.0	0.	510.	1198.	4.7
				1.05	30.0	4.9	1350.	1783.	3.1
				1.01	0.	5.7	1520.	2310.	5.4
				0.99	15.0	5.8	1570.	2077.	3.3
				0.95	46.0	5.1	1520.	2338.	1.5
2752	7075-T6	HE-CYL	6.11	1.30	54.0	5.6	1070.	1339.	6.2
				1.37	22.5	7.5	1130.	1493.	3.0
				1.47	7.0	7.9	1060.	1419.	3.2
				1.52	20.0	7.3	980.	1286.	2.7
				1.61	46.0	4.5	750.	979.	5.3
				1.67	82.0	0.	320.	417.	22.7
2760	7075-T6	PLATE	5.79	1.35	0.	0.	1460.	2057.	0.9
2763	1100	PLATE	6.55	1.29	0.	0.	1230.	1616.	2.1

Table XX (Cont'd.)

ROUND NO.	TARGET MATERIAL	TARGET TYPE	PROJECTILE VELOCITY (KM/SEC)	SHOCK RADIUS (CM)	θ, ANGLE OFF TRAJECTORY (DEG)	β, SHOCK/SURFACE INTERACTION ANGLE (DEG)	UNSCALED DISK/ SURFACE VELOCITY (M/SEC)	SCALED DISK/ SURFACE VELOCITY (M/SEC)	VEL. ERROR (%)
2766	7075-T6	HF-CYL	6.76	1.38	45.7	7.4	1120.	1222.	2.4
				1.50	12.6	10.2	1140.	1253.	2.2
				1.63	11.4	10.3	970.	1066.	2.1
				1.80	45.7	7.2	530.	578.	11.2
2767	7075-T6	HF-CYL	6.05	1.44	53.0	0.7	1000.	1114.	2.8
				1.46	46.0	0.7	1140.	1270.	2.4
				1.44	38.0	0.7	1220.	1359.	3.7
				1.45	23.0	0.8	1200.	1337.	3.0
				1.45	10.0	0.8	1290.	1437.	2.7
				1.47	0.	0.8	1240.	1382.	4.4
				1.47	39.0	1.3	780.	869.	3.1
				1.48	68.0	0.	430.	479.	11.4
2769	7075-T6	HF-CYL	6.4[illegible]	1.02	53.0	5.0	1500.	1609.	3.3
				1.03	49.2	6.1	1490.	1601.	2.5
				1.09	31.4	9.1	1580.	1710.	1.7
				1.14	17.0	10.9	1610.	1752.	2.1
				1.20	3.2	11.6	1510.	1647.	3.1
				1.28	7.9	11.6	1520.	1658.	4.5
				1.34	26.8	10.4	1100.	1195.	3.3
				1.41	44.0	8.4	710.	767.	3.5
				1.47	68.8	5.1	400.	429.	10.6
2772	6061-T6	HF-CYL	6.98	1.60	49.0	1.2	600.	604.	8.6
				1.62	19.4	1.8	1020.	1027.	4.5
				1.65	4.0	2.1	1120.	1128.	3.7
				1.68	42.0	1.8	880.	886.	5.7
				1.70	71.6	1.1	580.	584.	10.8
2774	7075-T6	HF-CYL	6.71	0.93	57.5	1.3	1780.	1958.	1.9
				0.98	20.0	3.9	1920.	2116.	1.2
				1.01	5.6	4.0	1800.	1984.	1.6
				1.07	44.0	1.3	1250.	1375.	3.0
				1.09	72.2	0.	850.	759.	6.5
2775	6061-T6	3-FCT	6.77	1.63	12.3	13.6	1190.	1320.	2.5
				1.80	13.8	13.8	990.	1099.	2.3
				2.09	61.4	6.9	440.	478.	5.4
2776	6061-T6	3-FCT	6.92	1.55	23.1	6.9	800.	828.	4.1
				1.87	9.4	9.4	940.	979.	2.3

Table XX (Cont'd.)

ROUND NO.	TARGET MATERIAL	TARGET TYPE	PROJECTILE VELOCITY (KM/SEC)	SHOCK RADIUS (CM)	φ, ANGLE OFF TRAJECTORY (DEG)	θ, SHOCK/SURFACE INTERACTION ANGLE (DEG)	UNSCALED DISK/SURFACE VELOCITY (M/SEC)	SCALED DISK/SURFACE VELOCITY (M/SEC)	VEL. CHNGE (%)
				1.70	51.5	7.8	900.	933.	3.7
2777	7075-T6	3-FCT	6.77	1.85	19.7	13.8	1020.	1133.	4.6
				1.94	12.[illegible]	12.1	990.	1092.	5.1
				2.14	60.2	10.5	580.	636.	15.[illegible]
2778	7075-T6	3-FCT	6.55	1.75	24.7	0.3	1050.	1209.	[illegible]
				1.75	0.3	0.3	1070.	1232.	1.9
				1.75	55.1	0.1	470.	541.	6.7
2779	1100	3-FCT	6.80	1.64	19.6	9.4	940.	1015.	1.8
				1.91	6.6	6.6	950.	1022.	1.7
				2.07	59.1	5.8	730.	784.	3.7
2780	1100	3-FCT	7.01	1.67	17.4	13.0	1050.	1073.	1.8
				1.79	12.4	12.4	1100.	1122.	1.6
2781	7075-T6	PLATE	7.01	1.25	0.	0.	1600.	1594.	1.4
2796	6061-T6	5-FCT	7.04	1.93	56.2	3.2	910.	899.	7.4
				1.87	34.0	9.4	1150.	1149.	1.
				1.77	8.1	8.1	1120.	1115.	2.
				1.63	32.8	8.2	820.	817.	1.
				1.55	67.7	4.4	420.	415.	5.0
2797	7075-T6	5-FCT	6.99	1.62	50.7	9.1	740.	754.	8.0
				1.65	23.6	7.9	920.	935.	3.3
				1.77	9.1	9.1	970.	989.	3.8
				1.85	46.4	9.0	860.	876.	5.1
				1.93	70.2	6.5	680.	689.	20.5
2798	1100	PLATE	6.70	1.25	0.	0.	1410.	1555.	1.6
2799	6061-T6	5-FCT	7.01	2.28	52.4	7.9	520.	523.	6.4
				2.40	22.4	7.9	670.	674.	2.7
				2.52	[illegible]	8.0	680.	664.	5.1
				2.71	45.3	7.9	460.	463.	4.4
2801	7075-T6	5-FCT	6.65	2.46	54.8	1.2	410.	485.	20.2
				2.48	28.4	1.2	590.	698.	3.7
				2.50	1.9	1.9	610.	721.	5.1
				2.13	41.9	2.1	490.	580.	6.2
				2.55	70.6	1.3	280.	331.	14.8

Table XX (Cont'd.)

ROUND NO.	TARGET MATERIAL	TARGET TYPE	PROJECTILE VELOCITY (KM/SEC)	SHOCK RADIUS (CM)	θ, ANGLE OFF TRAJECTORY (DEG)	θc SHOCK/SURFACE INTERACTION ANGLE (DEG)	UNSCALED DISK/ SURFACE VELOCITY (M/SEC)	SCALED DISK/ SURFACE VELOCITY (M/SEC)	VEL. ERROR (%)
2809	1100	5-FCT	6.77	4.02	54.6	6.2	229.	249.	3.6
				4.02	30.6	6.2	292.	317.	1.0
				4.02	6.3	6.2	305.	331.	1.8
				4.02	40.4	6.2	251.	272.	2.1
				4.02	70.1	6.2	134.	145.	8.4
2817	1100	PLATE	6.35	1.25	0.	0.	1350.	1647.	6.6
2819	1100	5-FCT	6.83	2.68	60.4	5.4	360.	375.	14.0
				2.65	30.0	9.0	540.	567.	6.3
				2.24	30.1	9.9	520.	548.	8.2
				2.08	70.7	0.7	440.	457.	16.9
2820	1100	HF-CYL	6.19	1.34	41.6	9.3	930.	1201.	3.1
				1.53	10.0	12.5	980.	1279.	2.4
				1.64	14.0	12.4	880.	1149.	2.7
				1.83	46.0	8.9	600.	774.	4.8
				1.91	67.7	5.4	380.	487.	4.7
2822	7075-T6	5-FCT	6.98	1.92	54.6	4.2	650.	650.	3.4
				1.95	22.4	5.1	870.	879.	2.4
				1.99	4.2	4.2	870.	878.	2.2
				2.04	30.0	5.7	850.	860.	3.7
2823	7075-T6	5-FCT	7.00	7.45	52.7	5.7	61.	61.	4.9
				7.73	21.3	6.6	70.	70.	2.4
				9.01	[illegible]	6.7	66.	66.	1.8
				8.40	43.3	5.6	46.	46.	9.1
				8.57	71.9	4.9	20.	20.	6.0
2824	7075-T6	5-FCT	6.95	7.43	53.5	3.2	55.	56.	2.5
				7.80	21.9	4.3	65.	68.	1.0
				7.59	4.4	4.4	66.	68.	1.9
				8.24	42.1	3.3	55.	56.	1.4
				8.37	71.5	3.0	28.	28.	5.3
2825	7075-T6	5-FCT	6.42	6.38	57.7	5.0	65.	78.	1.3
				6.20	29.4	6.1	86.	104.	1.7
				6.01	6.3	6.3	100.	120.	1.5
				5.70	36.2	6.3	93.	112.	1.0
				5.55	68.3	5.3	63.	76.	1.5
2826	7075-T6	5-FCT	6.71	10.18	55.7	2.6	34.	38.	1.4

Table XX (Cont'd.)

ROUND NO.	TARGET MATERIAL	TARGET TYPE	PROJECTILE VELOCITY (KM/SEC)	SHOCK RADIUS (CM)	θ, ANGLE OFF TRAJECTORY (DEG)	δ, SHOCK/SURFACE INTERACTION ANGLE (DEG)	UNSCALED DISK/SURFACE VELOCITY (M/SEC)	SCALED DISK/SURFACE VELOCITY (M/SEC)	VEL. ERROR (%)
				10.13	35.2	2.8	42.	46.	1.2
				10.01	2.8	2.8	46.	51.	1.1
				9.88	39.1	2.9	40.	44.	1.2
				7.91	69.6	2.7	26.	28.	1.5
2829	6061-T6	HF-CYL	6.46	1.60	61.0	0.	440.	520.	7.7
				1.55	37.9	0.	840.	993.	4.7
				1.46	9.8	3.2	1030.	1219.	4.[illegible]
				1.37	32.4	3.5	1050.	1243.	3.1
				1.33	67.1	0.	910.	957.	4.8
2831	7075-T6	HF-CYL	7.10	1.52	54.0	2.2	910.	879.	3.8
				1.56	23.0	3.4	1150.	1112.	3.1
				1.53	1.4	3.6	1160.	1122.	2.5
				1.67	38.0	2.5	860.	831.	3.5
				1.70	68.1	0.	410.	396.	5.3
2834	1100	5-FCT	7.12	2.81	51.1	5.8	410.	395.	12.6
				2.97	4.8	4.8	500.	481.	6.8
				3.10	44.5	5.7	420.	405.	6.8
				3.16	71.8	4.0	340.	327.	9.7
2836	1100	5-FCT	6.45	10.16	55.1	0.3	16.	19.	3.3
				10.07	20.2	0.4	38.	45.	1.1
				10.00	1.1	1.1	45.	53.	1.1
				9.87	39.0	1.1	32.	38.	1.4
2837	6061-T6	5-FCT	6.26	6.21	55.7	4.9	43.	61.	3.3
				6.10	21.6	5.3	83.	104.	1.4
				5.97	9.1	5.[illegible]	95.	119.	2.1
				5.80	36.8	6.0	91.	102.	1.8
				5.77	79.3	10.5	35.	44.	11.9
2838	6061-T6	5-FCT	6.93	10.39	56.7	1.9	19.	25.	3.2
				10.19	27.9	2.9	27.	36.	1.7
				9.56	3.1	3.1	30.	41.	7.4
				9.66	37.5	2.7	28.	39.	3.2
				9.50	69.1	1.2	11.	15.	4.4
2851	1100	5-FCT	6.43	5.55	57.9	6.5	113.	136.	1.5
				5.31	31.6	8.6	163.	197.	1.5
				5.05	19.1	10.1	205.	248.	0.5
				4.63	33.4	10.1	217.	263.	0.9

Table XX (Cont'd.)

ROUND NO.	TARGET MATERIAL	TARGET TYPE	PROJECTILE VELOCITY (KM/SEC)	SHOCK RADIUS (CM)	θ, ANGLE OFF TRAJECTORY (DEG)	δ, SHOCK/SURFACE INTERACTION ANGLE (DEG)	UNSCALED DISK/ SURFACE VELOCITY (M/SEC)	SCALED DISK/ SURFACE VELOCITY (M/SEC)	VEL. ERROR (%)
				4.47	60.4	12.2	138.	166.	[illegible]
2856	7075-T6	5-FCT	6.61	5.08	55.9	4.1	83.	94.	3.[illegible]
				5.04	26.9	4.4	122.	139.	[illegible].7
				4.58	4.2	4.2	142.	161.	[illegible]
				4.51	38.3	4.6	120.	137.	0.5
				4.87	69.8	4.3	54.	62.	1.7
2859	7075-T6	5-FCT	6.44	4.06	55.9	8.2	133.	155.	[illegible]
				4.04	27.0	8.3	202.	243.	[illegible]
				4.01	8.4	8.4	221.	246.	1.[illegible]
				3.57	40.1	8.4	195.	234.	[illegible]
				3.56	69.9	8.4	103.	124.	4.1
2860	1100	5-FCT	6.77	7.82	54.9	1.0	40.	43.	[illegible]
				7.56	1.6	1.6	81.	87.	1.1
				8.07	40.6	1.1	57.	61.	1.[illegible]
2863	6061-T6	5-FCT	6.71	7.85	54.3	2.9	34.	38.	1.5
				7.92	24.0	3.0	51.	56.	1.0
				7.99	3.1	3.1	50.	55.	1.1
				8.10	42.3	3.5	36.	39.	[illegible]
				9.15	70.4	2.8	17.	19.	3.[illegible]
2864	1100	5-FCT	6.66	6.62	59.3	4.5	64.	71.	[illegible]
				6.33	31.9	7.0	120.	135.	[illegible]
				6.01	8.3	8.3	149.	168.	[illegible].5
				5.49	34.0	6.4	158.	177.	1.1
				5.22	67.4	3.3	93.	104.	3.2
2865	6061-T6	5-FCT	6.72	3.50	54.3	3.9	178.	195.	1.6
				3.54	24.0	4.0	222.	244.	[illegible]
				3.58	4.0	4.0	228.	250.	[illegible]
				4.04	41.2	3.8	180.	198.	[illegible]
				4.07	70.5	3.7	80.	88.	[illegible].2
2867	1100	5-FCT	6.49	3.22	57.2	4.9	320.	356.	12.4
				3.29	28.4	5.5	380.	424.	[illegible]
				3.26	4.8	4.8	470.	523.	[illegible]
				3.21	64.4	7.3	240.	269.	[illegible]
2869	7075-T6	5-FCT	6.89	3.25	55.8	3.6	270.	291.	[illegible]
				3.27	25.2	3.5	340.	374.	[illegible]

Table XX (Cont'd.)

ROUND NO.	TARGET MATERIAL	TARGET TYPE	PROJECTILE VELOCITY (KM/SEC)	SHOCK RADIUS (CM)	θ, ANGLE OFF TRAJECTORY (DEG)	δ, SHOCK/SURFACE INTERACTION ANGLE (DEG)	UNSCALED DISK/SURFACE VELOCITY (M/SEC)	SCALED DISK/SURFACE VELOCITY (M/SEC)	VEL [illegible] (%)
				0.26	0.7	3.7	350.	306.	[illegible]
				0.27	30.3	3.7	330.	343.	7.[illegible]
				0.27	59.6	3.6	210.	214.	[illegible]

Table XXI

Shock Arrival Time Data

Round	Target Alloy	Type Sensor	Shock Radius R_s (cm)	Arrival Time t (μsec)	Angle-Off Axis (deg)
2784	7075-T6	E	1.93	4.47*	26
		E	1.95	4.52*	13
		E	1.99	4.73*	58
2785	6061-T6	E	1.94	2.58	26
		E	1.91	2.51	6
		E	1.85	2.58	55
2787	7075-T6	E	1.86	2.45	31
		E	1.77	2.45	8
		E	1.58	2.25	50
2789	6061-T6	E	1.78	2.45	27
		E	1.80	2.50	14
		E	1.84	2.65	57
2791	1100	E	1.78	2.75	27
2799	6061-T6	Q	2.66	3.60	20
2804	7075-T6	Q	3.83	8.22*	40
		Q	4.17	8.79*	16
		Q	4.28	9.00*	34
2807	1100	Q	4.27	(6.20)6.75	37
		Q	4.00	(5.95)6.35	8
		Q	3.79	(5.65)6.15	48
2809	1100	Q	4.13	8.33*	42
			4.09	8.48*	12
		Q	4.09	8.28*	51
2811	1100	Q	4.00	7.74*	50
		Q	4.00	7.84*	6
		Q	4.01	8.04*	46

TABLE XXI (continued)

Shock Arrival Time Data

Round	Target Alloy	Type Sensor	Shock Radius R_s (cm)	Arrival Time t (μsec)	Angle-Off Axis (deg)
		E	4.02	8.49*	62
		E	4.02	8.34*	8
		E	4.02	8.54*	32
2815	1100	Q	2.25	3.66	77
		Q	2.03	3.44	10
		Q	1.93	3.40	63
2821	7075-T6	Q	3.04	4.60	47
		Q	3.00	4.76	11
		Q	2.98	4.78	84
2822	7075-T6	Q	2.11	3.79	80
		Q	2.09	3.52	19
		Q	2.11	3.30	83
2824	7075-T6	Q	8.10	12.50	10
		Q	8.28	12.90	35
		Q	8.39	12.80	65
2826	7075-T6	Q	10.23	17.00	60
		Q	10.16	16.90	32
		Q	10.05	16.80	6
		Q	9.9[illegible]	16.45	34
		Q	9.88	16.50	64
2827	7075-T6	Q	1.66	3.85*	16
		Q	1.36	2.68*	44
2828	6061-T6	Q	3.02	4.75	70
		Q	3.06	4.50	16
2832	7075-T6	Q	2.99	4.33	70
		Q	2.97	4.33	33
		Q	3.11	4.58	15

TABLE XXI (continued)

Shock Arrival Time Data

Round	Target Alloy	Type Sensor	Shock Radius R_s (cm)	Arrival Time t (μsec)	Angle-Off Axis (deg)
		Q	3.15	4.53	28
2833	1100	Q	1.49	2.34	51
		Q	1.52	2.52	17
		Q	1.66	2.67	60
2834	1100	Q	2.95	(4.39) 4.60	73
		Q	3.12	4.65	18
		Q	3.26	(4.75) 5.05	85
2836	1100	Q	10.25	(15.80) 18.10	62
		Q	9.96	(15.65) 17.50	32
		Q	9.88	(15.35) 17.70	63
2837	6061-T6	Q	6.24	9.97	50
		Q	6.10	9.85	28
		Q	6.02	9.47	9
		Q	5.91	9.28	29
		Q	5.78	9.20	61
		OP	6.32	11.52	44
		OP	6.13	11.09	14
		OP	6.07	10.19	23
2838	6061-T6	Q	10.54	(17.70) 18.00	65
		Q	10.31	17.45	34
		Q	10.04	(17.10) 17.45	7
		Q	9.67	16.30	44
		Q	9.58	16.05	63
2842	6061-T6	Q	9.01	13.60	67
		Q	8.42	14.80	26
		Q	7.96	13.00	2
		Q	7.26	12.00	40
		Q	6.94	11.70	72

TABLE XXI (continued)

Shock Arrival Time Data

Round	Target Alloy	Type Sensor	Shock Radius R_s (cm)	Arrival Time t (μsec)	Angle-Off Axis (deg)
2851	1100	Q	5.67	9.25	68
		Q	5.48	(7.30) 8.15	41
		Q	5.02	(6.75) 7.30	7
		Q	4.59	(6.15) 6.73	42
		Q	4.96	7.87	19
		Q	4.44	(5.80) 6.55	78
2857	7075-T6	Q	4.17	6.73	70
		Q	4.07	6.33	35
		Q	4.10	6.46	14
		Q	3.98	6.38	46
		Q	3.99	6.38	79
2864	1100	Q	6.83	(10.40) 11.70	70
		Q	5.95	(9.00) 9.80	2
2865	6061-T6	Q	4.01	6.55	69
		Q	4.07	6.80	13

E---Electrical Pin Switch
Q---Quartz Probe
OP--Optical Fiber Probe
*----Apparent early trigger due to small fragments impacting target slightly ahead of projectile.

Appendix G

Framing Camera Instrumentation

The instruments used to measure the free surface velocity and fly-off velocity of the targets employed in the second phase of this study were high speed framing cameras. Two types were used, a Beckman & Whitley Model 300 and a Beckman & Whitley Dynafax Model 326. The basic operating features of these cameras are listed in the table below while the remainder of this appendix is devoted to a discussion of the special data handling techniques developed to obtain accurate data from the camera records. The details of the experimen that employed these cameras are contained in Chapter V.

Table XXII

Framing Camera Characteristics

	Model 300	Dynafax Model 326
Type	Fixed film with ultraspeed rotating mirror	Film in rotating drum and rotating prism
Maximum Framing Rate	4.5×10^6 fps	2.6×10^4 fps
Minimum Framing Rate	3×10^5 fps	200 fps
Min. Exposure Time at Max. Framing Rate	45 nsec	1.0 μsec
Ratio of Frame Exposure Time to Interframe Time	1:5	1:41
Max. Number of Frames	48	224
Nominal Frame Size	1 cm x 2 cm	.71 cm x .99 cm
Format	24 frames on each of two 8" x 10" sheets of film	Two staggered rows of frames on 35 mm film

The choice of camera was determined by the expected velocity of the object being photographed. The Model 300 camera was used for all free surface measurements and for all experiments where the maximum fly-off disk velocity was expected to exceed 0.4 mm/ μ sec.

Model 300 Camera. Studies of the Model 300 camera performance have been made at this facility by Preonas (UDRI) and the author (Ref. 70). Variations in the time between frames in the camera have been detected and a calibration scheme developed. Likewise the variation in magnification from frame to frame has been calibrated. Optical distortion has been shown to exist, but is rather small and quite difficult to calibrate.

In practice, attempts to obtain velocity data from two or three frames of position data have led to poor results. It appears that the small errors noted above are compounded by small film reading errors, resulting in inaccurate velocity calculations. This problem was effectively solved by using statistical analysis of the position data. A computer program is now available to generate velocity data. The program processes the two-dimensional position data obtained from as many photographic frames as possible. Interframe times and individual frame magnifications are adjusted according to the calibrations mentioned above. A least-squares fit to the position points in x-y-t space then yields a value for the velocity. The data is automatically plotted so that any deviations from unaccelerated rectilinear motion can be detected. In addition, the program can be used to determine the coordinates of a fixed point with respect to a fiducial point located in the field of view by averaging the coordinates from several frames. The net result of this statistical approach is that, with proper techniques, positions can be determined to within the resolution of the camera, and velocities can be determined to within 1-5% depending upon the quality of the film record. The computer program provides the rms deviation for the least-squares fit so that a measure of the velocity accuracy is available in each case.

Almost as important as the data reduction scheme described above has been the development of an automatic digital film reader for accurately obtaining the position data from each frame. The details of this system are described in Ref. 39. This device allows the reading of position points on each frame quickly and accurately, automatically punching the coordinates of each point read on an IBM card ready for use with the data reduction computer program. The net result is that it is feasible to record accurately a large number of data points -- a process which had been an extremely tedious manual procedure.

One potentially troublesome source of systematic error is determining the average magnification in a given event. This was done by placing a fiducial of known length in the field of view, reading position points for the fiducial, and normalizing the coordinates of all other points to the value obtained from the fiducial. The Model 300 camera was in a fixed location for this program and the lens-to-subject distance remained fixed. Consequently a good deal of data on average magnification was obtained from a number of events. The resultant average magnification obtained is felt to be accurate to better than 1.5%. One remaining source of systematic error -- interpretation of the film record -- is a function of the quality of the film record and varied from round to round. In a few cases, errors due to interpretation probably dominated all other errors.

Dynafax Model 326 Camera. The optical design of this drum type framing camera is such that it does not suffer some of the problems described above -- such as variations in interframe time and changes in magnification between frames. Nevertheless, a statistical data reduction program similar to that used with the Model 300 camera is used to reduce the data from this instrument.

The results obtained have been quite good. For good film records with ten or more usable frames of data, velocities can be determined such that the standard deviation from the least-squares fit of position data in x-y-t space is less than 1%. Likewise with a lens-to-subject distance of roughly 300 cm, the position of a fixed point in the field of view can be determined to an accuracy of less than ± 0.05 cm.

With this camera, the lens-to-subject distance was generally changed with each event, resulting in a somewhat greater chance for error in determination of magnification. A fiducial in the field of view of each event was used to determine this magnification. Several tests indicated that the magnification factor was known to an accuracy of approximately 2%.

The two cameras and associated data reduction techniques described above permitted the convenient and accurate determination of fly-off disk and free surface velocities in this study. The application of this instrumentation to the measurement of free surface velocity is described in Chapter V.

Appendix H

Dimensional Analysis

It is usually instructive in the development of analytic theories such as the modified blast wave (similarity) theories discussed in Chapter VII, to present the results in terms of either scaled or dimensionless variables so that the results of one problem may be more easily compared with those of another or so that scaling laws may be explored more directly. The application of the principles of dimensional analysis (Ref. 71 for instance) leads to the definition of consistent sets of such variables and may be used to derive the set of variables employed in Chapter VII.

Assuming that the problem is to calculate the spherical, one-dimensional expansion of a shock wave in a solid material created by a point source explosion (the solid material analogue of the blast wave problem in gas dynamics), the set of physical quantities defined in Table XXIII was selected as being pertinent.

Table XXIII

Blast Wave Problem Variables

Variable	Definition	Dimensions
R_s	Distance from source to shock front	L
R_o	A characteristic length	L
E	Energy characterizing the source	ML^2T^{-2}
p	Pressure	$ML^{-1}T^{-2}$
ρ	Density	ML^{-3}
ρ_o	Undisturbed Density	ML^{-3}
u	Particle Speed	LT^{-1}
D	Shock Speed	LT^{-1}

Table XXIII (Cont'd.)

Variable	Definition	Dimensions
c	Bulk sound speed	LT^{-1}
s	Material constant in linear Hugoniot	---
t	Time	T

Applying the π-theorem of dimensional analysis described in Ref. 71 the following expression is obtained:

$$R_s^{a_1}\ R_o^{a_2}\ E^{a_3}\ p^{a_4}\ \rho^{a_5}\ \rho_o^{a_6}\ u^{a_7}\ D^{a_8}\ c^{a_9}\ s^{a_{10}}\ t^{a_{11}} \qquad \text{(Eq. 94)}$$

Since π is dimensionless by the theorem, the right side of this equation leads to three linear equations relating the exponents for each dimension M, L, and T.

$$a_3 + a_4 + a_5 + a_6 = 0 \qquad \text{(Eq. 95)}$$

$$a_1 + a_2 + 2a_3 - a_4 - 3a_5 - 3a_6 + a_7 + a_8 + a_9 = 0$$

$$-2a_3 - 2a_4 - a_7 - a_8 - a_9 + a_{11} = 0$$

Eliminating a_2, a_6, and a_9 between these equations, substituting the results back into the original π-equation, and collecting terms yields the following set of π-factors:

$$(R_s/R_o),\ (E/\rho_o c^2 R_o^3),\ (p/\rho_o c^2),\ (\rho/\rho_o),\ (u/c),\ (D/c),\ s,\ (ct/R_o)$$

which represent a consistent set of dimensionless groups that may be used in this problem. The second term may be used to define the scaling length, R_o, through the relation

$$R_o^3 \propto E/\rho_o c^2 \qquad \text{(Eq. 96)}$$

The term (R_s/R_o) implies geometric similarity, while those terms containing c indicate how the parameters vary with this fundamental material property. The direct connection with R_o and E in Eq. 96 above is usually termed "energy scaling." Because of the direct implication that $E \propto v_p^2$ here, energy scaling implies that

$$R_o \propto v_p^{2/3}$$

and that all the linear dimensions in the problem can be scaled in this manner. In the true hypervelocity impact regime, where processes such as melting and vaporization may be occurring, numerical studies have shown that the relations $R_o \propto v_p^{.58}$ is more nearly true.

The relation ct/R_o implies that for fixed material (c = constant), the time scales linearly with the characteristic dimensions of the problem. This result was used in Chapter IV in presenting the crater growth data, except the projectile diameter, d, was used in lieu of R_o since these two lengths are linearly related.

By adding the variable Y, the yield strength of the material with dimensions $ML^{-1}T^{-2}$, to the list of parameters above and by again applying the π-theorem, it is possible to obtain the following dimensionless groups:

$$\left(\frac{R}{R_o}\right), \left(\frac{E}{YR_o^3}\right), \left(\frac{p}{Y}\right), \left(\frac{\rho c^2}{Y}\right), \left(\frac{\rho_o c^2}{Y}\right), \left(\frac{u}{c}\right), \left(\frac{D}{c}\right), s, \left(\frac{ct}{R_o}\right)$$

The group that defines $R_o \propto E^{1/3} Y^{-1/3}$ implies that the geometric and time scales in the problem are a function of $Y^{-1/3}$. If this reasoning is applied to the crater growth portion of the problem discussed in Chapter IV, the scaling implies that

$$(p_c/d)_{final} \propto Y^{-1/3}$$ where p_c is the crater penetration, and

$$\tau/d \propto Y^{-1/3}$$ where τ is the time constant for crater growth as discussed in Chapter IV. The experimental results indicated that for each case the exponent was approximately -0.2. The result above is surprisingly close to the experimental value and explains the reasons why both p/d and τ/d vary as the same function of the yield strength.

Unclassified

Security Classification

DOCUMENT CONTROL DATA - R & D

(Security classification of title, body of abstract and indexing annotation must be entered when the overall report is classified)

1. ORIGINATING ACTIVITY (Corporate author) Air Force Materials Laboratory Wright-Patterson AF Base, Ohio 45433	2a. REPORT SECURITY CLASSIFICATION Unclassified 2b. GROUP

3. REPORT TITLE

Hypervelocity Impact -- Material Strength Effects on Crater Formation and Shock Propagation in Three Aluminum Alloys.

4. DESCRIPTIVE NOTES (Type of report and inclusive dates)

Dissertation

5. AUTHOR(S) (First name, middle initial, last name)

Major Ronald F. Prater

6. REPORT DATE	7a. TOTAL NO. OF PAGES	7b. NO. OF REFS
December 1970	290	71

8a. CONTRACT OR GRANT NO.	9a. ORIGINATOR'S REPORT NUMBER(S)
b. PROJECT NO. 7360	AFML-TR-70-295
c. Task 736006	9b. OTHER REPORT NO(S) (Any other numbers that may be assigned this report)
d.	DS/MC/67-2

10. DISTRIBUTION STATEMENT

This document has been approved for public release and sale; its distribution is unlimited.

11. SUPPLEMENTARY NOTES	12. SPONSORING MILITARY ACTIVITY Air Force Materials Laboratory Wright-Patterson AF Base, Ohio 45433

13. ABSTRACT

The effects of material strength upon the transient response of thick aluminum targets to hypervelocity impact has been studied experimentally. Most experiments involved the normal impact of 2017 aluminum spheres at a velocity of about 7 km/sec. Material strength was varied by employing targets of 1100, 6061, and 7075 aluminum alloys. Flash x-ray techniques were used to measure accurately the rate at which the crater grew during the impact process. Crater growth rates were also measured for 1100 aluminum in four separate ranges of projectile velocity from 2.3 km/sec to 7.0 km/sec.

Free surface velocity and Hopkinson fly-off disk techniques were used to measure values of the peak normal stress at various distances from the impact point (between 1 cm and 10 cm) at several related angles away from the projectile trajectory. The measurements of the variation of stress amplitude with distance into the target demonstrated significant non-hydrodynamic stress attenuation believed to be associated with propagation of an elastic relief wave from the rear of the impacting projectile. Numerical calculations yield reasonable agreement with experimental results, but many of the details are in question. Measurement of shock arrival time with quartz disk sensors confirmed the elastic-plastic behavior of the target material.

DD FORM 1 NOV 65 1473

Security Classification

Security Classification

14 KEY WORDS	LINK A		LINK B		LINK C	
	ROLE	WT	ROLE	WT	ROLE	WT
Hypervelocity Impact						
Crater Growth Rates						
Dynamic Pressure Measurements						
Stress Attenuation in Aluminum						
Material Strength Effects in Shock Wave Propagation						
Flash X-Radiography						

Security Classification